PHYSIK

AG MAGNETISMUS

Annual Report 2017

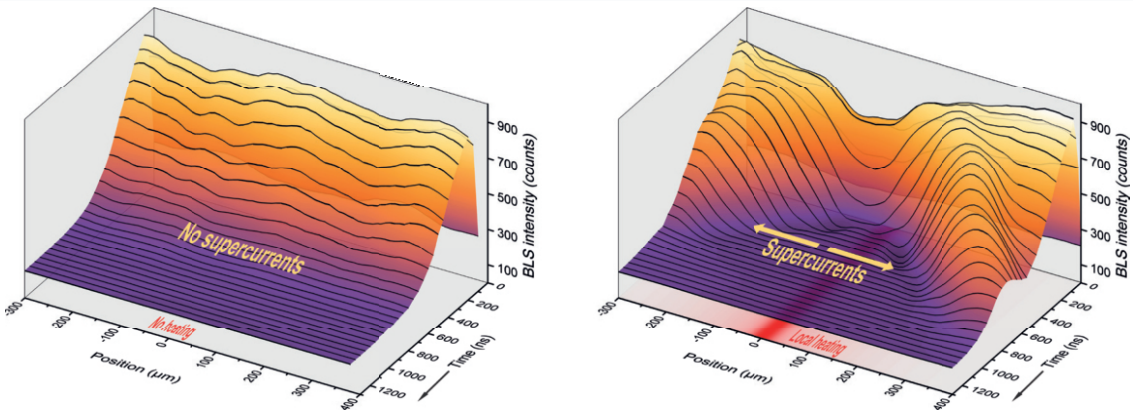

AG MAGNETISMUS TU KAISERSLAUTERN

OPTIMAS

TECHNISCHE UNIVERSITÄT KAISERSLAUTERN

Cover page: Time-space diagrams of magnon Bose-Einstein condensate (BEC) population after termination of a pumping pulse. Left panel - without external heating: after formation of the magnon BEC, it decays uniformly. Right panel - with external heating: immediately after its formation, the magnon BEC is pushed out by a phase gradient created by the non-uniform temperature distribution (the simulated temperature profile is shown in the plane below). A detailed description of the experiment and the results are presented in Article 4.1 of this Report.

Annual Report 2017

Address:	Prof. Dr. Burkard Hillebrands Fachbereich Physik Landesforschungszentrum OPTIMAS Technische Universität Kaiserslautern Erwin-Schrödinger-Straße 56 67663 Kaiserslautern, Germany Tel.: +49-(0)631-205-4228 Fax.: +49-(0)631-205-4095
Postal address:	Postfach 3049 67653 Kaiserslautern, Germany
Internet:	http://www.physik.uni-kl.de/hillebrands/
E-Mail:	hilleb@physik.uni-kl.de

This Annual Report can be downloaded from:
http://www.physik.uni-kl.de/hillebrands/publications/annual-reports/

Our Group

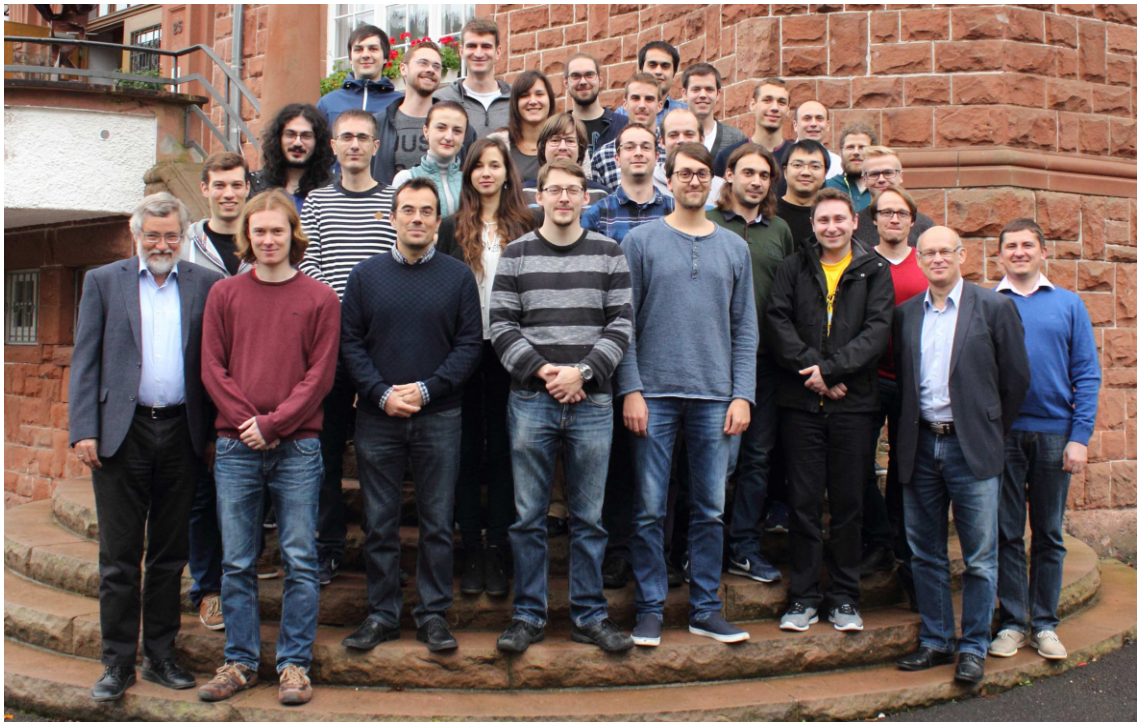

From left to right:

Prof. Dr. Burkard Hillebrands, Tobias Fischer, Ulas Öran, Björn Heinz, Philipp Lang, Dr. Andrés Conca Parra, Timo Noack, Moritz Geilen, Jun. Prof. Dr. Evangelos Papaioannou, Laura Mihalceanu, Halyna Musiienko-Shmarova, Pascal Frey, Dr. Dmytro Bozhko, Laura Scheuer, Matthias Schweizer, Alexander Kreil, Dr. Thomas Langner, Frank Heussner, Morteza Mohseni, Dr. Spyridon Pappas, Michael Schneider, Tobias Jost, Viktor Lauer, Qi Wang, Milan Ender, Dr. habil. Alexander Serga, Dr. Vitaliy Vasyuchka, Dr. Philipp Pirro, Matthias Nabinger, Dr. Thomas Brächer, Jun. Prof. Dr. habil. Andrii Chumak

(The picture was taken at our group retreat in Annweiler in October 2017.)

Not on the picture: Martin Kewenig, Sascha Keller, Dr. Thomas Meyer, Anna Maria Friedel, David Breitbach, Hauke Georg Schäfer, Steffen Steinert, Marjorie Lägel, Sibylle Müller, Dieter Weller, Sven Rebsamen, Rostyslav Serha

Junior Research Group Nano-Magnonics

Group leader: Andrii Chumak, Co-supervisor: Thomas Brächer

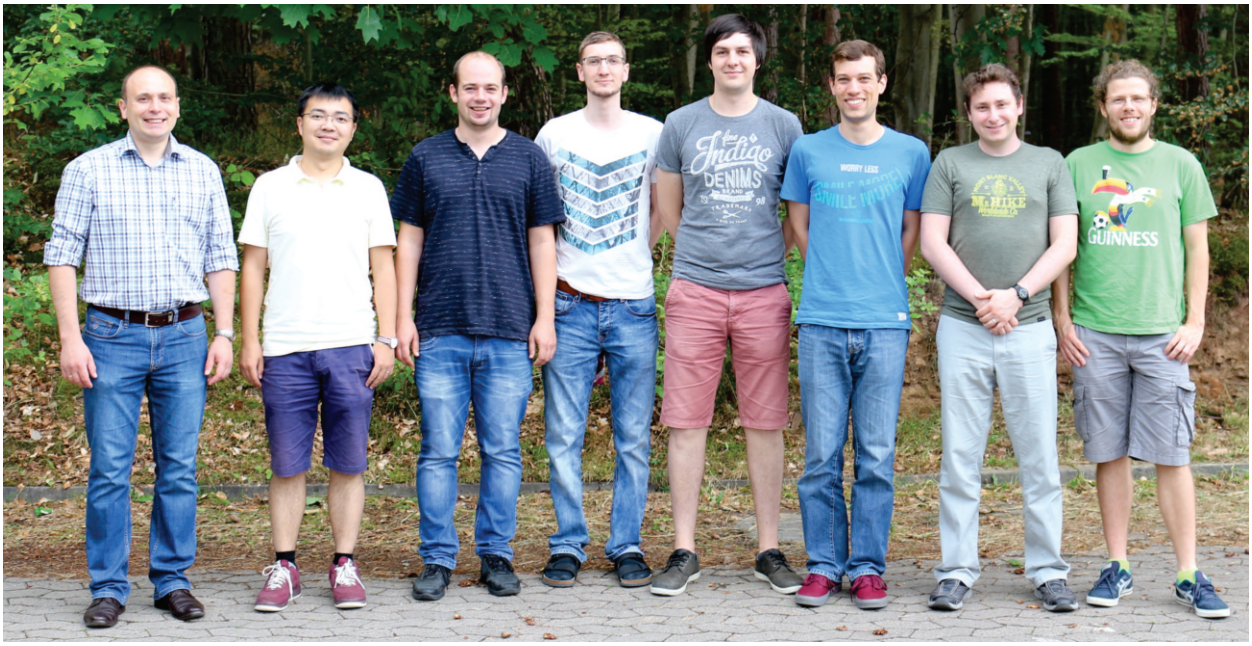

From left to right:

Jun. Prof. Dr. habil. Andrii Chumak, Qi Wang, Michael Schneider,
Martin Kewenig, Björn Heinz, Tobias Fischer, Viktor Lauer, Dr. Thomas Brächer

Nowadays, spin waves and their quanta, magnons, are being considered as future data carriers in novel computing devices. The strategic goal of the Nano-Magnonics Group is to make a transformative change in the data processing paradigm from traditional electronics to magnonics. A set of recent groundbreaking physical discoveries and the revolutionary progress in the fabrication of magnetic nano-structures opened a way to the practical development of magnonic data processing systems. Among the main aims of the Nano-Magnonics Group are the development of two-dimensional magnonic circuits with lateral sizes below 100 nm and to take advantage of novel spintronic phenomena for the excitation and detection of spin waves in these nanostructures. Successful achievement of these aims is essential for the realization of nano-scaled magnonic logic circuits prototypes.

Internet: https://www.physik.uni-kl.de/hillebrands/nano-magnonics-group/
E-Mail: chumak@physik.uni-kl.de

Junior Research Group Spintronics/Spin-Plasmonics

Group leader: Evangelos Papaioannou

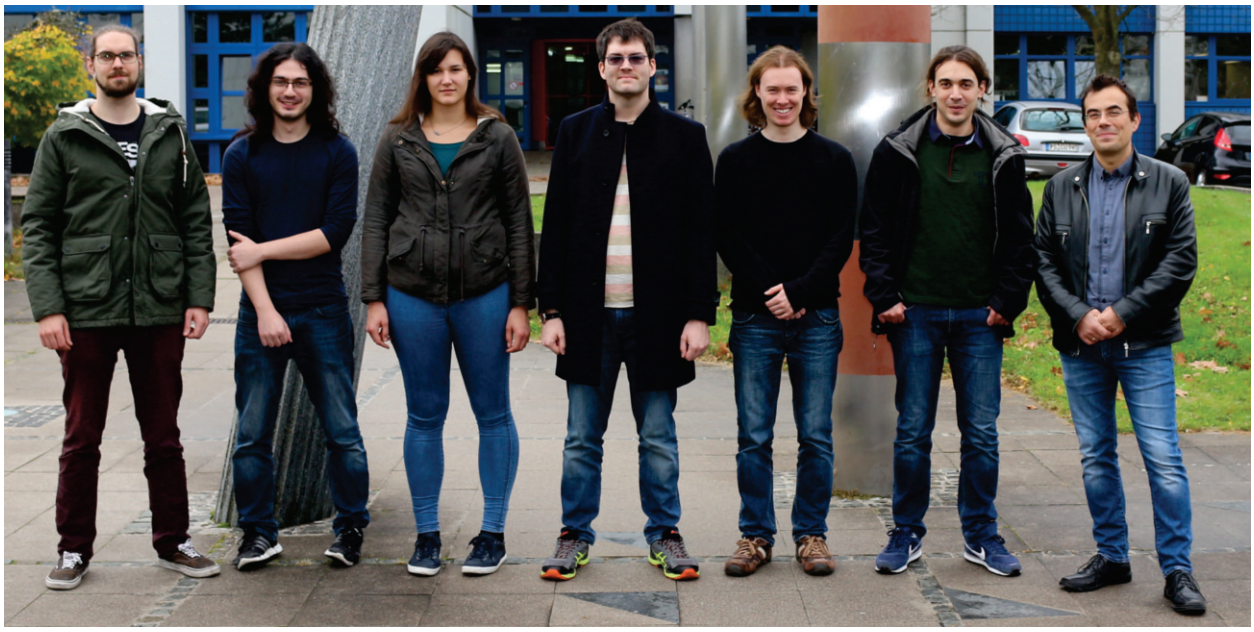

From left to right:

Matthias Schweizer, Ulaş Ören, Laura Scheuer, Sascha Keller, Philipp Lang, Dr. Spyridon Pappas, Jun. Prof. Dr. Evangelos Papaioannou

The strategic goal of the group is to control the magneto-electric spin conversion in magnetic heterostructures by means of atomically controlled interfaces. We focus on the spin pumping effect, spin Hall effect and inverse spin Hall effect for the generation and conversion of spin accumulations and pure spin currents. Equally important objective is the field of spin-plasmonics: our aim is to bring together the fields of Magnonics and Plasmonics. We investigate the emergent properties due to interactions between two collective excitations: plasmons (induced by optical near fields) and magnons. We aim on: (i) the manipulation of magneto-plasmon interaction i.e. the manipulation of surface plasmon properties through the use of magnetic materials and external magnetic fields; (ii) the manipulation of magnon properties by using localized and propagating surface plasmons.

Internet: https://www.physik.uni-kl.de/hillebrands/spintronicsspin-plasmonics-group/
E-Mail: papaio@rhrk.uni-kl.de

Contents

Chapter 1: Preface

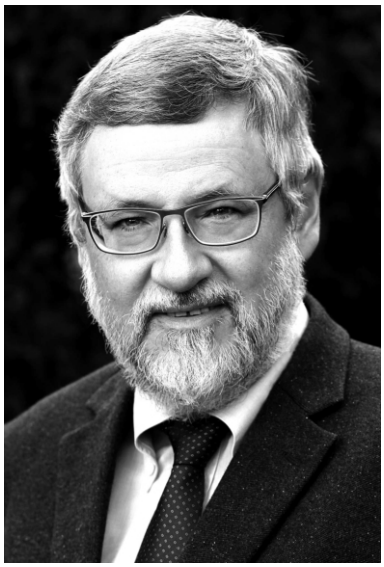

Dear Colleagues and Friends,

We are happy to present our Annual Report 2017. Again, this was a very successful year. This report is covering the period November 2016 to October 2017.

A central strategic issue of this year was the taking off of our two new European Research Council (ERC) projects. The ERC Starting Grant *MagnonCircuits* headed by Andrii Chumak started in summer 2016, and my own ERC Advanced Grant project *Supermagnonics*, started shortly thereafter in October 2016. For each of these two projects, we have installed and commissioned a dedicated Brillouin Light Scattering (BLS) system. Both projects are now productive in generating new results that are described in this report.

Three other projects came to an end: The DFG-funded Priority Program SPP 1538 *Spin Caloric Transport (SpinCaT)* ended, containing two projects from our group addressing *"The magnon Seebeck effect"* and *"Magnon mediated heat and spin transport in magnetic insulators"*. The European Future Emerging Technology (FET) project *Insulator Spintronics (InSpin)* also reached the end of the funding period. Exciting results were obtained from all three projects.

Our overall group size has increased due to the new projects. We have reorganized our group by creating two Junior Research Groups led by Andrii Chumak and by Evangelos Papaioannou, who both are Junior Professors. You will find their descriptions in this report. I sincerely hope that this adds to the scientific visibility of our two young professionals.

This report contains several new research highlights, among them:

• Magnon gases, condensates and supercurrents: We succeeded in performing the first non-local measurement of a magnon supercurrent. We also showed that the mechanism of a kinetic instability can be used for the creation of a magnon Bose-Einstein Condensate (BEC), and we studied the threshold properties in the BEC formation process as well as temperature dependencies. As it relates to the electrical detection of magnons, we could associate the origin of the electric signal to processes of internal pumping. A particular highlight is the observation and the understanding of the obtained BLS spectra of obliquely magnetized YIG films. It is an important prerequisite to extend our studies to new magnonic systems and geometries.

• Magnon computing: We now better understand the pinning conditions in nanoscale magnonic waveguides. We have made progress in using Dzyaloshinskii-Moriya interaction as well as asymmetric magnetic bilayer structures to induce frequency asymmetries between counter-propagating magnons of same absolute wavevector. We investigated back-scattering immune spin-wave modes in thin YIG films as well as spin-wave beams using specifically designed antenna structures. A highlight is the manipulation of spin-wave propagation by controlled thermal gradient structures. Furthermore, we report Frequency-division Multiplexing in magnonic networks utilizing caustic-like spin-wave beams.

• Magnon spintronics: We show progress in several Spin Hall Effect related projects. A highlight is the generation of terahertz radiation in specifically designed Fe/Pt emitters, and another high-

light is the demonstration of two-magnon confluence processes for enhancing the spin pumping efficiency.

• New materials and Heusler compounds: As part of our work we investigated new material systems such as the low damping alloy CoFeAlB. Other aspects were the use of 0-D magneto-plasmonic nanostructures to manipulate the magneto-optic response and the study of the interface properties in Heusler/MgO systems.

In the report period, I celebrated my 60th birthday. My group organized an excellent birthday party including a half-day workshop entitled *"Magnonics – quo vadis"*. Many of the former group members attended, as well as several of my scientific friends. I am particularly thankful to Andrei Slavin, Jürgen Fassbender, Gernot Güntherodt, Martin Aeschlimann, Eiji Saitoh, Gerrit Bauer and John Gregg for their lectures, and in particular for providing answers to the *"quo vadis"* question regarding my research for the coming years. A big "thank you" to my group.

Dmytro Bozhko, Thomas Langner and Thomas Meyer finished their PhD work, Thomas Meyer with distinction. Thomas Brächer joined our group again after a PostDoc period at SpinTec in Grenoble in the Group of Gilles Gaudin. He is now senior PostDoc working on Andrii Chumak's ERC project *MagnonCircuits*.

We welcome Dmytro Bozhko and Spyridon Pappas as new PostDocs, Moritz Geilen, Björn Heinz, Martin Kewenig, Alexander Kreil, Morteza Mohseni and Michael Schneider as new PhD students, Philipp Lang, Laura Scheuer and Matthias Schweizer as new diploma students, and Tobias Jost as new master student. David Breitbach and Matthias Nabinger completed their Bachelors and, continue to be student assistance in the group as they continue with their studies. Ulaş Ören is our new bachelor student. A welcome also to Sven Rebsamen, who joined our group as a technician.

We very much regret that Isabel Sattler, responsible for the science administration in our group, left the group. She accepted an offer as Officer for Research in the Executive Committee of University of Kaiserslautern. We are very happy, that Marjorie Lägel joined the group for this position.

Our work would not have been possible without valuable collaborations with people all over the world. They are too many to list them here all. In particular we would like to thank, in alphabetical order, Christoph Adelmann, Adekunle Adeyeye, Johan Åkerman, Yasuo Ando, Antonio Azevedo, Christian Back, Matthieu Bailleul, Gerrit Bauer, Arne Brataas, Yury Bunkov, Giovanni Carlotti, Florin Ciubotaru, Mairbek Chshiev, Russell Cowburn, Sergej Demokritov, Thibaut Devolder, Bernard Dieny, Oleksandr Dobrovolskiy, Marco Doms, Rembert Duine, Carsten Dubs, Ursula Ebels, Hajo Elmers, Karin Everschor-Sitte, Jürgen Fassbender, Gerhard Fecher, Claudia Felser, Albert Fert, Mark Freeman, Gilles Gaudin, Sebastian Gönnenwein, Olena Gomonay, Gernot Güntherodt, Joachim Gräfe, John Gregg, Dirk Grundler, Gianluca Gubbiotti, Konstantin Gusliyenko, Uwe Hartmann, Thomas Hauet, Michel Hehn, Yves Henry, Jos Heremans, Atsufumi Hirohata, Axel Hoffmann, Koichiro Innomata, Gerhard Jakob, Xiaofeng Jin, Martin Jourdan, Glib Kakazei, Boris Kalinikos, Alexy Karenowska, Sang-Koog Kim, Akihiro Kirihara, Olivier Klein, Mathias Kläui, Yuri Kobljanskyj, Peter Kopietz, Mikhail Kostylev, Maciej Krawczyk, Volodymyr Kruglyak, Takahide Kubota, Ronald Lehndorff, Joseph Losby, Jörg Lösch, Gregoire de Loubens, Victor L'vov, Sadamichi Maekawa, Stéphane Mangin, Gennadiy Melkov, Claudia and Tim Mewes, Shigemi Mizukami, Shuichi Murakami, Hiroshi Naganuma, Oleksii Nechyporuk, Andrei Nikitin, Sergei Nikitov, Jean-Pierre Noziéres, Kevin O'Grady, Hideo Ohno, Tereo Ono, Mikihiko Oogane, Yoshichika Otani, Stuart Parkin, Sébastien Petit-Watelot, Johannes Paul, Anna Pomyalov, Günter Reiss, Sergio Rezende, Vladyslav Romanyuk, Caroline Ross, Manfred Rührig, Eiji Saitoh, John R. Sandercock, Rudi Schäfer, Gerd Schönhense, Helmut Schultheiss, Koji Sekiguchi, Jairo Sinova,

Andrei Slavin, Rolf Slatter, Bob Stamps, Yoshishige Suzuki, Ihor Syvorotka, Koki Takanashi, Vasyl Tiberkevich, Simon Trudel, Yaroslav Tserkovnyak, Ken-ichi Uchida, Alexey Ustinov, Bart van Wees, Martin Weides, Mingzhong Wu and Igor Zavislyak.

Collaborations within the Fachbereich Physik at the University of Kaiserslautern (in particular Martin Aeschlimann, James Anglin, Réné Beigang, Sebastian Eggert, Michael Fleischhauer, Georg von Freymann, Jochen Kuhn, Herwig Ott, Hans-Christian Schneider, Volker Schünemann, and Artur Widera and their groups), Michael Kopnarski and his team from the Institut für Oberflächen- und Schichtanalytik, as well as Sandra Wolff and her team from the Nano Structuring Center have been very stimulating. We are very grateful to be a member of the State Research Center for Optics and Material Sciences OPTIMAS.

We would also like to thank all our sponsors, which are the Deutsche Forschungsgemeinschaft (DFG), the Bundesministerium für Bildung und Forschung (BMBF), the Deutscher Akademischer Austauschdienst (DAAD), the European Community (ERC, EFRE, INTAS, INTERREG), the Carl Zeiss Foundation, the State of Rhineland Palatinate and the University of Kaiserslautern. Concerning our projects in applied research, I would like to express my gratitude to Sensitec GmbH as our strong partner in R&D on spintronic sensors.

Our special thanks go to Halyna Musiienko-Shmarova, Sascha Keller, Morteza Mohseni, Dieter Weller, Marjorie Lägel and Sibylle Müller for their help in preparing this report, and to the team from Photo-Repro-Druck, University of Kaiserslautern.

It is our special pleasure to greet all former group members. May this report help with stay in touch.

With all best wishes for Christmas, and a Happy New Year,

Kaiserslautern, November 2017

Vorwort

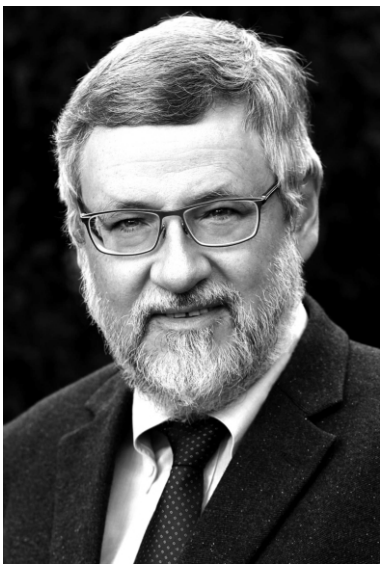

Liebe Kolleginnen und Kollegen, Freundinnen und Freunde unserer Arbeitsgruppe,

wir freuen uns sehr, Ihnen den Bericht über unsere Forschungsaktivitäten 2017 vorlegen zu dürfen. Er deckt den Zeitraum von November 2016 bis Oktober 2017 ab.

Ein zentraler Kernpunkt unserer diesjährigen Forschungsarbeit war es, unsere zwei neuen ERC – Projekte zum Laufen zu bringen. Der ERC Starting Grant *MagnonCircuits* von Andrii Chumak startete im Sommer 2016 und mein eigenes ERC Advanced Grant – Projekt *Supermagnonics* kurz darauf im Oktober 2016. Für jedes der zwei Projekte haben wir einen dedizierten Brillouin-Lichtstreu-Aufbau (BLS) neu konzipiert und installiert. Beide Projekte sind somit in die produktive Phase übergegangen, deren Resultate Teil dieses Berichts sind.

Drei andere Projekte sind ausgelaufen: das DFG – finanzierte Schwerpunktprogramm SPP 1538 *Spinkalorischer Transport (SpinCaT)* mit zwei Projekten unserer Gruppe, welche sich mit dem *"Magnon-Seebeck-Effekt"* und dem *"Wärme - und Spin-Transport durch Magnonen in magnetischen Isolatoren"* befassten, wurden abgeschlossen. Auch die Finanzierungsperiode des europäischen FET Projekts *"Insulator Spintronics (InSpin)"* endete. Alle drei Projekte haben zu stimulierenden Forschungsergebnissen geführt.

Durch die neuen Projekte ist die Größe unserer Gruppe gewachsen. Durch die Einrichtung zweier Nachwuchsgruppen, die von den Juniorprofessoren Andrii Chumak und Evangelos Papaioannou geleitet werden, haben wir deshalb eine Umstrukturierung der Gruppe vorgenommen. Die jeweiligen Beschreibungen, von denen wir hoffen, dass sie zur Sichtbarkeit unserer Nachwuchswissenschaftler beitragen, finden Sie im vorliegenden Bericht.

Unsere diesjährigen Forschungs-Highlights waren:

• Magnonengase, -Kondensate und -Superströme: Wir konnten die erste nicht-lokale Messung eines magnonischen Superstroms durchführen. Ebenso konnten wir zeigen, dass der Mechanismus der kinetischen Instabilität zur Erzeugung eines magnonischen Bose-Einstein-Kondensates (BEK) eingesetzt werden kann. Wir untersuchten die Schwellwerteigenschaften der BEK-Bildung sowie die Temperaturabhängigkeit. Bezüglich der elektrischen Detektion von Magnonen konnten wir das gemessene Signal auf interne Pumpprozesse zurückführen. Ein besonderer Höhepunkt war die Messung und das Verständnis der BLS-Spektren von YIG Filmen, bei denen die Magnetisierung aus der Filmebene ragte. Dies stellt eine wichtige Voraussetzung für die Erweiterung unserer Forschung auf neue magnonische Systeme und Geometrien dar.

• Magnonen-Computing: Wir habe unser Verständnis der Randbedingungen in nanoskopischen magnonischen Wellenleitern verbessert. Auch bei der Verwendung der Dzyaloshinskii-Moriya-Wechselwirkung und asymmetrischer Bilagen zur Erzeugung von Frequenzasymmetrien zwischen gegenläufig propagierenden Magnonen gleicher Wellenlänge haben wir Fortschritte erzielt. Wir haben Spinwellenmoden in YIG untersucht, die gegen Streuung immun sind sowie Spinwellenstrahlen, die durch spezielle Antennenstrukturen angeregt wurden. Ein Höhepunkt ist die Kontrolle der Spinwellenpropagation durch thermische Gradienten. Außerdem berichten wir über Frequenzteilungs-Multiplexer in magnonischen Netzwerken, die Kaustik-ähnliche Strahlen nutzen.

• Magnon-Spintronik: Wir verzeichnen Fortschritte in mehreren sich mit dem Spin-Hall-Effekt befassenden Projekten. Ein Highlight ist die Generation von Terahertzstrahlung in speziell konzipierten Fe/Pt-Emittern, und ein weiteres die Demonstration der Erhöhung der Spin-Pump-Effizienz durch Zwei-Magnonen-Konfluenzprozesse.

• Neue Materialien und Heuslerverbindungen: Wir untersuchten neue Materialsysteme wie z. B. die Verbindung CoFeAlB, die eine geringe Dämpfung aufweist. Weitere Aspekte waren der Einsatz von 0-D magneto-plasmonischen Nanostrukturen und Studien der Grenzflächeneigenschaften in Heusler/MgO-Systemen.

Im von diesem Bericht umfassten Zeitraum feierte ich meinen 60. Geburtstag. Meine Gruppe organisierte eine sehr schöne Feier inklusive eines halbtägigen Workshops mit dem Titel *"Magnonics – quo vadis"*, für die ich ihr an dieser Stelle noch einmal besonders danken möchte. Viele der ehemaligen Gruppenmitglieder sowie mehrere meiner wissenschaftlichen Weggefährten nahmen teil. Ich bin besonders Andrei Slavin, Jürgen Fassbender, Martin Aeschlimann, Eiji Saitoh, Gerrit Bauer, John Gregg und Gernot Güntherodt für ihre Vorträge dankbar, insbesondere für ihre Antworten auf die *"quo vadis"* Frage bezüglich meiner weiteren wissenschaftlichen Arbeit in den nächsten Jahren.

Dmytro Bozhko, Thomas Langner und Thomas Meyer beendeten ihre Doktorarbeiten, Thomas Meyer mit Auszeichnung. Thomas Brächer stieß nach seinem Postdoc bei Spintec in Grenoble in der Gruppe von Gilles Gaudin wieder zu uns. Er ist nun wissenschaftlicher Projektleiter in Andrii Chumaks ERC Projekt *MagnonCircuits*.

Wir begrüßen Moritz Geilen, Björn Heinz, Martin Kewenig, Alexander Kreil, Morteza Mohseni und Michael Schneider als neue Doktoranden, Philipp Lang, Laura Scheuer und Matthias Schweizer als neue Diplomanden, Tobias Jost als neuen Masterstudenten. David Breitbach und Matthias Nabinger haben ihre Bachelorarbeit in unserer Gruppe abgeschlossen und sind weiterhin als studentische Hilfskräfte in unserer Gruppe aktiv. Ferner begrüßen wir Ulaş Ören als neuen Bachelorstudenten und Sven Rebsamen als neuen Techniker in unserer Gruppe.

Wir bedauern sehr, dass Isabel Sattler, die für die wissenschaftliche Verwaltung in der Gruppe verantwortlich war, uns verlassen hat. Sie nahm das Angebot an, als Forschungsreferentin ins Referat für Forschung und Nachwuchsförderung zu wechseln. Wir sind sehr erfreut, dass ihre Position von unserem neuen Gruppenmitglied Marjorie Lägel übernommen wurde.

Unsere Arbeit wäre nicht ohne wertvolle Kooperationen mit Partnern aus der ganzen Welt möglich gewesen. Es sind zu viele um sie alle an dieser Stelle aufzulisten. Insbesondere möchten wir, in alphabetischer Reihenfolge, danken: Christoph Adelmann, Adekunle Adeyeye, Johan Åkerman, Yasuo Ando, Antonio Azevedo, Christian Back, Matthieu Bailleul, Gerrit Bauer, Arne Brataas, Yury Bunkov, Giovanni Carlotti, Florin Ciubotaru, Mairbek Chshiev, Russell Cowburn, Sergej Demokritov, Thibaut Devolder, Bernard Dieny, Oleksandr Dobrovolskiy, Marco Doms, Rembert Duine, Carsten Dubs, Ursula Ebels, Hajo Elmers, Karin Everschor-Sitte, Jürgen Fassbender, Gerhard Fecher, Claudia Felser, Albert Fert, Mark Freeman, Gilles Gaudin, Sebastian Gönnenwein, Olena Gomonay, Gernot Güntherodt, Joachim Gräfe, John Gregg, Dirk Grundler, Gianluca Gubbiotti, Konstantin Gusliyenko, Uwe Hartmann, Thomas Hauet, Michel Hehn, Yves Henry, Jos Heremans, Atsufumi Hirohata, Axel Hoffmann, Koichiro Innomata, Gerhard Jakob, Xiaofeng Jin, Martin Jourdan, Glib Kakazei, Boris Kalinikos, Alexy Karenowska, Sang-Koog Kim, Akihiro Kirihara, Olivier Klein, Mathias Kläui, Yuri Kobljanskyj, Peter Kopietz, Mikhail Kostylev, Maciej Krawczyk, Volodymyr Kruglyak, Takahide Kubota, Ronald Lehndorff, Joseph Losby, Jörg Lösch,

Gregoire de Loubens, Victor L'vov, Sadamichi Maekawa, Stéphane Mangin, Gennadiy Melkov, Claudia and Tim Mewes, Shigemi Mizukami, Shuichi Murakami, Hiroshi Naganuma, Oleksii Nechyporuk, Andrei Nikitin, Sergei Nikitov, Jean-Pierre Noziéres, Kevin O'Grady, Hideo Ohno, Tereo Ono, Mikihiko Oogane, Yoshichika Otani, Stuart Parkin, Sébastien Petit-Watelot, Johannes Paul, Anna Pomyalov, Günter Reiss, Sergio Rezende, Vladyslav Romanyuk, Caroline Ross, Manfred Rührig, Eiji Saitoh, John R. Sandercock, Rudi Schäfer, Gerd Schönhense, Helmut Schultheiss, Koji Sekiguchi, Jairo Sinova, Andrei Slavin, Rolf Slatter, Bob Stamps, Yoshishige Suzuki, Ihor Syvorotka, Koki Takanashi, Vasyl Tiberkevich, Simon Trudel, Yaroslav Tserkovnyak, Ken-ichi Uchida, Alexey Ustinov, Bart van Wees, Martin Weides, Mingzhong Wu und Igor Zavislyak.

Die Zusammenarbeit mit dem Fachbereich Physik der Technischen Universität Kaiserslautern (insbesondere mit Martin Aeschlimann, James Anglin, Réné Beigang, Sebastian Eggert, Michael Fleischhauer, Georg von Freymann, Jochen Kuhn, Herwig Ott, Hans-Christian Schneider, Volker Schünemann und Artur Widera und ihren Arbeitsgruppen), Michael Kopnarski und seinem Team des Instituts für Oberflächen- und Schichtanalytik sowie Sandra Wolff und ihrem Team des Nanostrukturzentrums waren sehr stimulierend. Wir sind sehr dankbar, Mitglied des Landesforschungszentrums für Optik und Materialwissenschaften (OPTIMAS) zu sein.

Wir möchten außerdem unseren Geldgebern danken: der Deutschen Forschungsgemeinschaft (DFG), dem Bundesministerium für Bildung und Forschung (BMBF), dem Deutschen Akademischen Austauschdienst (DAAD), der Europäischen Union (ERC, EFRE, INTAS, INTERREG), der Carl Zeiss-Stiftung, dem Land Rheinland-Pfalz und der Technischen Universität Kaiserslautern. In Bezug auf unsere Projekte in der angewandten Forschung möchten wir unsere Dankbarkeit gegenüber der Sensitec GmbH, unserem starken Partner in R&D von spintronischen Sensoren, zum Ausdruck bringen.

Unserer besonderer Dank geht an Halyna Musiienko-Shmarova, Sascha Keller, Morteza Mohseni, Dieter Weller und Sibylle Müller für ihre Hilfe beim Erstellen dieses Berichtes und an das Team von Photo-Repro-Druck, TU Kaiserslautern.

Es ist eine besondere Freude, hiermit auch allen ehemaligen Gruppenmitgliedern einen Gruß zu senden. Möge dieser Bericht uns helfen, im Kontakt zu bleiben. Wenn Sie an unserer Arbeit interessiert sind, würde ich mich freuen, von Ihnen zu hören.

Mit den besten Wünschen für ein frohes Weihnachtsfest und ein gutes Neues Jahr,

Kaiserslautern, im November 2017

Ihr Burkard Hillebrands

Chapter 2: Personnel

2.1 Members of the group

Group leader:

Prof. Dr. Burkard Hillebrands

Senior scientists:

Dr. Thomas Brächer	since 06/17
Jun. Prof. Dr. habil. Andrii Chumak	
Dr. Andrés Conca Parra	
Jun. Prof. Dr. Evangelos Papaioannou	
Dr. Philipp Pirro	
Dr. habil. Alexander Serga	
Dr. Vitaliy Vasyuchka	

Postdocs and long-term guest scientists:

Dr. Dmytro Bozhko	since 03/17
Dr. Thomas Langner	since 03/17
Dr. Spyridon Pappas	since 02/17

Ph.D. students:

M.Sc.	Dmytro Bozhko	until 02/17
Dipl.-Phys.	Tobias Fischer	
Dipl.-Phys.	Pascal Frey	
Dipl.-Phys.	Moritz Geilen	since 02/17
Dipl.-Phys.	Björn Heinz	since 02/17
Dipl.-Phys.	Frank Heussner	
Dipl.-Phys.	Sascha Keller	
Dipl.-Phys.	Martin Kewenig	since 11/16
Dipl.-Phys.	Alexander Kreil	since 02/17
Dipl.-Phys.	Thomas Langner	until 02/17
Dipl.-Phys.	Viktor Lauer	
Dipl.-Phys.	Thomas Meyer	until 10/17
M.Sc.	Morteza Mohseni	since 01/17
Dipl.-Phys.	Timo Noack	
Dipl.-Phys.	Laura Mihalceanu	
Dipl.-Phys.	Michael Schneider	since 02/17
M.Sc.	Halyna Musiienko-Shmarova	
M.Sc.	Qi Wang	

Diploma Students:

Moritz Geilen	until 01/17
Jochen Greser	until 06/17
Björn Heinz	until 01/17
Martin Kewenig	until 11/16
Alexander Kreil	until 06/17
Philipp Lang	since 04/17
Laura Scheuer	since 04/17
Timo Noack	until 05/16
Michael Schneider	until 11/16
Matthias Schweizer	since 05/17
Ellen Wiedemann	until 10/17

Master Students:

Tobias Jost	since 05/17

Bachelor Students:

Milan Ender	since 01/17
Matthias Nabinger	since 01/17
Ulaş Ören	since 09/17

Student Assistants:

Anna Maria Friedel	
David Breitbach	
Hauke Georg Schäfer	
Matthias Schweizer	
Steffen Steinert	since 01/16
Rostyslav Serha	since 05/16

Engineers and Technicians

B.Sc. Sven Rebsamen	since 02/17
Dipl.-Ing. (FH) Dieter Weller	

Administration:

Dr. Isabel Sattler	until 02/17
Marjorie Lägel	since 02/17
Sibylle Müller	

2.2 Visiting scientists, postdoctoral fellows and exchange students

(sorted by date of first arrival in our group)

Dr. Spyridon Pappas, Department of Physics, Uppsala University, Uppsala, Sweden — 27.11. - 29.11.2016

During his visit, Dr. Pappas and the group members discussed about the perspective about magneto-plasmonic interaction and their application in novel magneto optical systems.

Vivian Maria Campos Soares de Andrade, IFIMUP-IN, Departamento de Fisica, Faculdade de Ciencias Univesidade do Porto, Porto, Portugal — 05.12. - 18.12.2016

Vivian, who is a PhD student in group of Prof. Glib Kakazei at the University of Porto, visited us for studies of magnetic structures in the frame of our joint DAAD-FCT project "Linear and nonlinear spin-wave dynamics in magnonic-crystal-based micro-sized magnon conduits."

Dr. Carsten Dubs, Oleksii Surzhenko, INNOVENT e.V. Technologieentwicklung, Jena, Germany — 15.01. - 16.01.2017

During his visit, our guests presented their last progress on LPE growth of thin YIG films.

Prof. Dr. Andrei Slavin, Oakland University, Rochester, Michigan, USA — 25.01. - 29.01.2017, 29.04. - 04.05.2017

Prof. Andrei Slavin visited our group as a Visiting MAINZ Professor. He participated in the PhD defence of Dmytro Bozhko and - worked with us on the theory of the wavelength-dependent transformation of dipolar-exchange magnon modes in obliquely magnetized YIG films.

Prof. Dr. Yury. M. Bunkov, Institut Neel, CNRS, Grenoble, France — 06.03. - 11.03.2017

Prof. Yury Bunkov visited us this year in order to discuss his latest findings in the field of Bose-Einstein magnon condensates. Yury presented an invited talk with the title: "Bose-Einstein magnon condensation in out-of-plane magnetized YIG films."

Dr. Oleksandr Dobrovolskiy, Physikalisches Institut, Goethe-Universität Frankfurt am Main, Frankfurt am Main, Germany — 01.04. - 30.06.2017

During this visit, a collaboration and discussion regarding fluxon-reconfigurable magnonic crystals took place.

Dr. Damien Louis, IPCMS, Strasbourg, France — 03.04. - 14.04.2017

The visit took place in the framework of the MagMatch project. During this visit experimental investigations of spin-wave non-reciprocity in magnetic bilayer systems were discussed.

Dr. Sergiy Bunyaev, IFIMUP-IN, Departamento de Fisica, Faculdade de Ciencias, Univesidade do Porto, Porto, Portugal — 10.04. - 10.05.2017

Dr. Sergiy Bunyaev from the group of Prof. Glib Kakazei at the Department of Physics and Astronomy, University of Porto visited us for joint experimental work on FMR studies of microstructured spin-wave conduits. He presented a talk on "Microwave whispering gallery resonators and their applications."

Alistair Inglis, Department of Physics, University of Oxford, Oxford, UK — 01.05. - 15.05.2017

During his visit, Alistair discussed with us possible mechanisms of magnon excitations via phonons.

Prof. Dr. Glib Kakazei, IFIMUP-IN, Departamento de Fisica, Faculdade de Ciencias, Univesidade do Porto, Porto, Portugal — 26.06. - 29.06.2017

Prof. Glib Kakazei visited us in the frame of our joint DAAD-FCT project "Linear and nonlinear spin-wave dynamics in magnonic-crystal-based micro-sized magnon conduits" to discuss the spin-wave dynamics in 1D magnonic crystals. He presented a talk on "Artificial room temperature magnetic skyrmions."

Dr. Jochiam Gräfe, Max-Planck-Institut für Intelligente Systeme, Stuttgart, Germany — 21.07. - 21.07.2017

Valuable discussions on high-resolution spin-wave spectroscopy took place during this visit.

Dr. Matthieu Bailleul, Dr. Yves Henry, Dr. Damien Louis, IPCMS, Strasbourg, France — 13.09. - 13.09.2017

During this visit, non-reciprocal phenomena in magnetic bilayer systems were discussed in the framework of the joint MagMatch project.

Keita Mastumoto, Laboratory for Optical Condensed Matter Physics, Kyushu University, Fukuoka, Fukuoka Prefecture, Japan — 14.09. - 28.09.2017

Mr. Matsumoto visited us to perform BLS measurements on the rare earth compound $Gd_{4/3}Yb_{2/3}BiFe_5O_{12}$, a material that exhibits a large spin orbit coupling and hosts a large inverse Faraday effect. In a 140 μm thick film, we observed the fundamental thickness mode and the backscattering spin-wave mode. The FMR position was compared to electrical measurements of the ferromagnetic resonance.

Dr. Florin Ciubotaro, IMEC, Leuven, Belgium — 22.09. - 02.10.2017

During this visit, Dr. Ciubotaro discussed novel spin wave excitation mechanisms and he performed BLS measurements of spin-wave devices for spin-wave logic.

2.3 Guest seminars

Dr. Timo Kuschel 14.11.2016	University of Groningen, Groningen, The Netherlands *Electrically and thermally generated nonlocal magnon spin transport in YIG* Group seminar
Dr. Oleksandr Dobrovolskiy 21.11.2016	Physikalisches Institut, Goethe-Universität Frankfurt am Main, Frankfurt am Main, Germany *Microwave spectroscopy of fluxonic metamaterials: theory, applications and perspectives for spin-wave dynamics* Group seminar
Dr. Spyridon Pappas 28.11.2016	Uppsala University, Uppsala, Sweden *Spin dynamics in ferromagnetic thin films and microstructures* Group seminar
Prof. Dr. Yuri M. Bunkov 10.03.2017	Institut Néel, CNRS, Grenoble, France *Bose-Einstein magnon condensation in out-of-plane magnetized YIG films* Special OPTIMAS seminar
Dr. Oleksandr Dobrovolskiy 01.05.2017	Physikalisches Institut, Goethe-Universität Frankfurt am Main, Frankfurt am Main, Germany *Fluxon-reconfigurable magnonic crystal* Spin+X seminar
Dr. Sergiy Bunyaev 08.05.2017	Universidade do Porto, Porto, Portugal *Microwave whispering gallery resonators and their applications* Group seminar
Benjamin Zingsem 30.05.2017	AG Farle, University of Duisburg-Essen and Forschungszentruim Jülich, Duisburg, Germany *Standing waves that would not stand still, magneto-dynamic properties of chiral magnets* Group seminar
Prof. Dr. Glib Kakazei 26.06.2017	Universidade do Porto, Porto, Portugal *Artificial room temperature magnetic skyrmions* Group seminar
Prof. Dr. Eiji Saitoh 28.07.2017	Tohoku University, Sendai, Japan *Spin current physics and applications* IEEE Magnetics Society Distinguished Lecture, Special OPTIMAS seminar

2.4 Visits of group members at other laboratories

Alexander A. Serga	Group of Prof. Dr. G. Kakazei, Universidade do Porto, Porto, Portugal 06.09.2016-20.09.2016 Host: Prof. Dr. Glib Kakazei
Alexander A. Serga	Group of Prof. G.A. Melkov, Faculty of Radiophysics, Electronics and Computer Systems, National Taras Shevchenko University of Kyiv, Kyiv, Ukraine 14.09.2016-21.10.2016 Host: Prof. G. A. Melkov
Andrii Chumak, Vitaliy Vasyuchka, Qi Wang	Group of Prof. Dr. G. Kakazei, Universidade do Porto, Porto, Portugal 11.12.2016-18.12.2016 Host: Prof. Dr. Glib Kakazei
Laura Mihalceanu, Sascha Keller, Jochen Greser, Evangelos Papaioannou	Group of Assoc. Prof. Georgios Vourlias, Aristotle University, Thessaloniki, Greece 09.12.2016-12.12.2016 Host: Assoc. Prof. Georgios Vourlias
Moritz Geilen	Group of Prof. Dr. Mark Freeman, University of Alberta, Edmonton, Canada 27.02.2017-24.03.2017 Host: Prof. Mark Freeman
Qi Wang	Group of Prof. Zhiyong Zhong, University of electronic science and technology of China, Chengdu, Sichuan, China 02.05.2017-14.05.2017 Host: Prof. Zhiyong Zhong
Anna Maria Friedel	Group of Prof. Tim Mewes, MINT Center, University of Alabama, Tuscaloosa, Alabama, USA 01.06.2017-21.07.2017 Host: Prof. Tim Mewes
Martin Kewenig	Group of Prof. Atsufumi Hirohata, University of York, York, Great Britain 12.08.2017-18.10.2017 Host: Prof. Atsufumi Hirohata

2.5 Group member photo gallery

Dmytro Bozhko
PostDoc

Dr. Thomas Brächer
Senior scientist

David Breitbach
Student assistant

JProf. Dr. habil. Andrii Chumak
Senior scientist

Dr. Andrés Conca Parra
Senior scientist

Milan Ender
Bachelor student

Tobias Fischer
Ph.D. student

Pascal Frey
Ph.D. student

Moritz Geilen
Ph.D. student

Björn Heinz
Ph.D. student

Frank Heussner
Ph.D. student

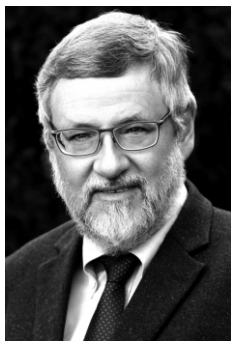

Prof. Dr. Burkard Hillebrands
Group leader

Tobias Jost
Master student

Sascha Keller
Ph.D. student

Martin Kewenig
Ph.D. student

Alexander Kreil
Ph.D. student

Thomas Langner
PostDoc

Marjorie Lägel
Administration

Philipp Lang
Diploma student

Viktor Lauer
Ph.D. student

Anna Maria Friedel
Student assistant

Morteza Mohseni
Ph.D. student

Thomas Meyer
PostDoc

Laura Mihalceanu
Ph.D. student

Halyna Musiienko-Shmarova
Ph.D. student

Sibylle Müller
Secretary

Matthias Nabinger
Bachelor student

Timo Noack
Ph.D. student

JProf. Dr. Evangelos Papaioannou
Senior scientist

Spyridon Pappas
PostDoc

Dr. Philipp Pirro
Senior scientist

Sven Rebsamen
Engineer

Laura Scheuer
Diploma student

Hauke Georg Schäfer
Student assistant

Michael Schneider
Ph.D. student

Matthias Schweizer
Student assistant

Qi Wang
Ph.D. student

Dieter Weller
Mechanical engineer

Dr. Alexander Serga
Senior scientist

Rostyslav Serha
Student assistant

Steffen Steinert
Student assistant

Ulaş Ören
Bachelor student

Dr. Vitaliy Vasyuchka
Senior scientist

Chapter 3: Methods

3.1 Brillouin light scattering spectroscopy (BLS)

Brillouin light scattering spectroscopy (BLS) is the primary key technique in our laboratory to investigate the dynamic properties of magnetic materials and devices. It is based on the interaction of photons with the fundamental excitations of a solid such as magnons, the quanta of magnetic excitations. The interaction can be understood as an inelastic scattering process of the incident photons with magnons, taking into account energy and momentum conservation as indicated in Fig. 1. This technique is sensitive for incoherent, thermal magnons as well as for externally excited, coherent excitations.

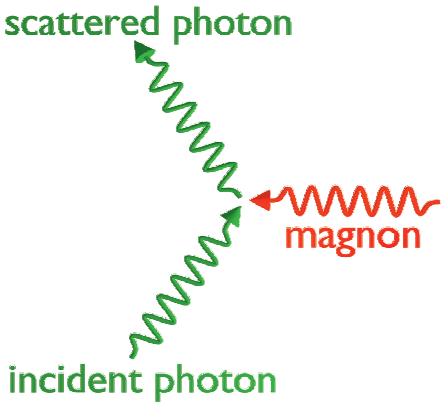

Fig. 1: Scheme of inelastic scattering of an incident photon by a magnon. Here, the annihilation process where the frequency of the scattered photon is increased by the frequency of the annihilated magnon is shown.

The detection of the inelastically scattered photons, i.e. the separation from the elastically scattered photons and the determination of the transferred energy, requires an interferometric technique with extremely high contrast and sensitivity. In our laboratory we implemented the (3+3) Tandem-Fabry-Pérot-Interferometer, designed by John R. Sandercock and schematically shown in Fig. 2. It consists of two Fabry-Pérot interferometers (FPI), each one passed three times by the inelastically scattered light. This approach results in a contrast better than 10^{10} for the separation of the elastically and inelastically scattered photons in a frequency range from 500 MHz up to 1 THz.

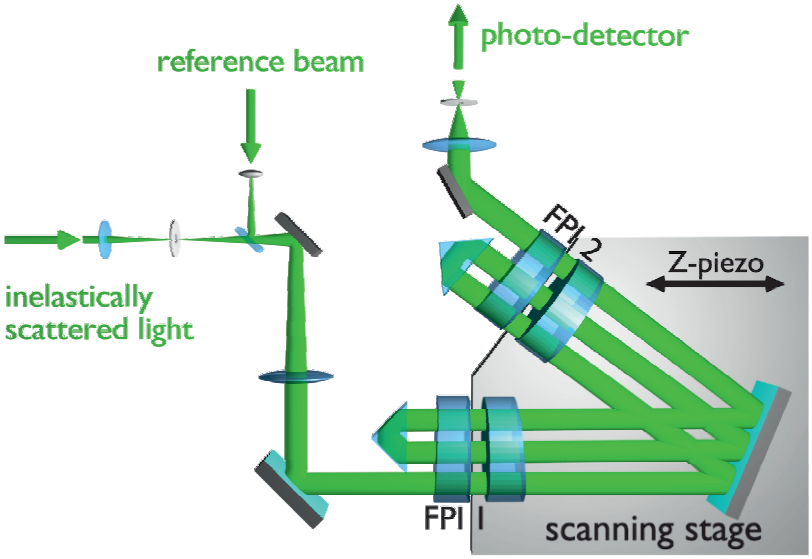

Fig. 2: Scheme of a (3+3) tandem Fabry-Pérot interferometer, designed and build by John R. Sandercock (JRS Scientific Instruments, Mettmenstetten, Switzerland)

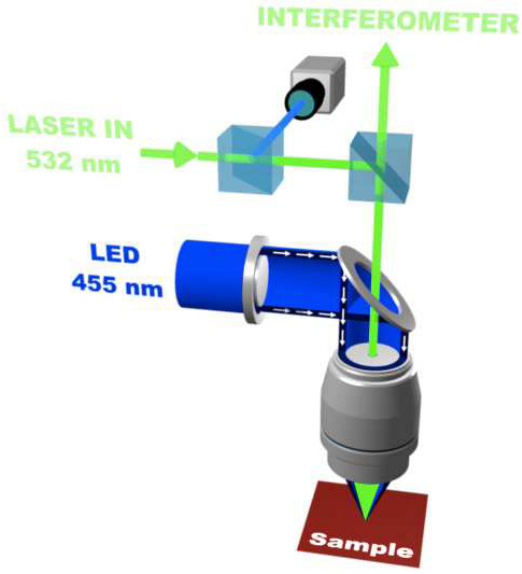

Fig. 3: Schematic setup of a BLS-microscope. The laser light is focused on the sample using a high resolution objective which is also collecting the scattered photons. The LED light is used to monitor the position of the laser focus on the sample by a CCD camera and to apply active position control to the sample stage.

In the last decades we made significant progress in the improvement of BLS spectroscopy. The spatial resolution was pushed to near the fundamental limit of classical optics by constructing a BLS microscope (Fig. 3) with sophisticated active stabilization methods. In this way, spin-wave transport phenomena can be investigated in micro-structures including time- and phase resolved measurements. However, in the BLS microscope, the wavevector resolution is lost since the angle of light incidence is not well defined anymore. Thus, wavevector resolved measurements like the direct determination of the dispersion relation are conducted with conventional BLS which has a typical spatial resolution of about 20 µm.

During the past two years, wavevector resolution in conventional BLS geometry was significantly improved and pushed to its limits by utilization of novel scattering geometry (Fig. 4). It provides the possibility to achieve wave-vector resolution $\delta k \approx 0.2\,\mathrm{rad/\mu m}$ with the maximal wavevector limited only by the wave number of the used probing laser light (for 532 nm laser $k_{\mathrm{max}} = 4\pi/\lambda_{\mathrm{laser}} = 23\,\mathrm{rad/\mu m}$). Moreover, the described setup enables for an easy change in the magnetization angle of the sample from in-plane to completely out-of-plane geometries as well as the full control of the bias magnetic field due to the utilization of a conventional high-field electromagnet. Another significant improvement here is the utilization of a dielectric mirror to enhance the reflectivity of the sample surface. It provides a significant increase in sensitivity without disturbing the magnetic boundary conditions of the sample. Also this technique provides a constant BLS sensitivity and wavevector resolution regardless of the used excitation geometry.

In a further development, our BLS equipment has been upgraded towards the investigation of new

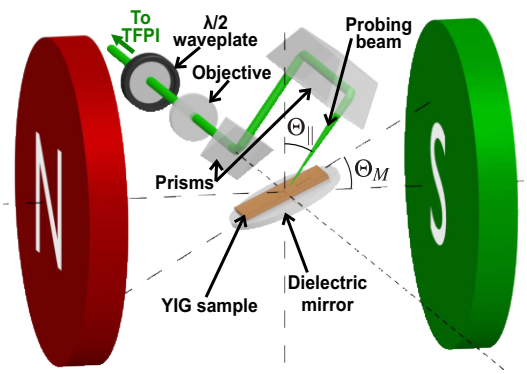

Fig. 4: Schematic setup of a novel wavevector resolved setup. The laser light is steered using a combination of two prisms mounted on a rotary stage (not shown) allowing for a change of the incident angle from 0 to 90°. A $\lambda/2$ waveplate is used to keep the direction of the probing beam polarization constant at the sample.

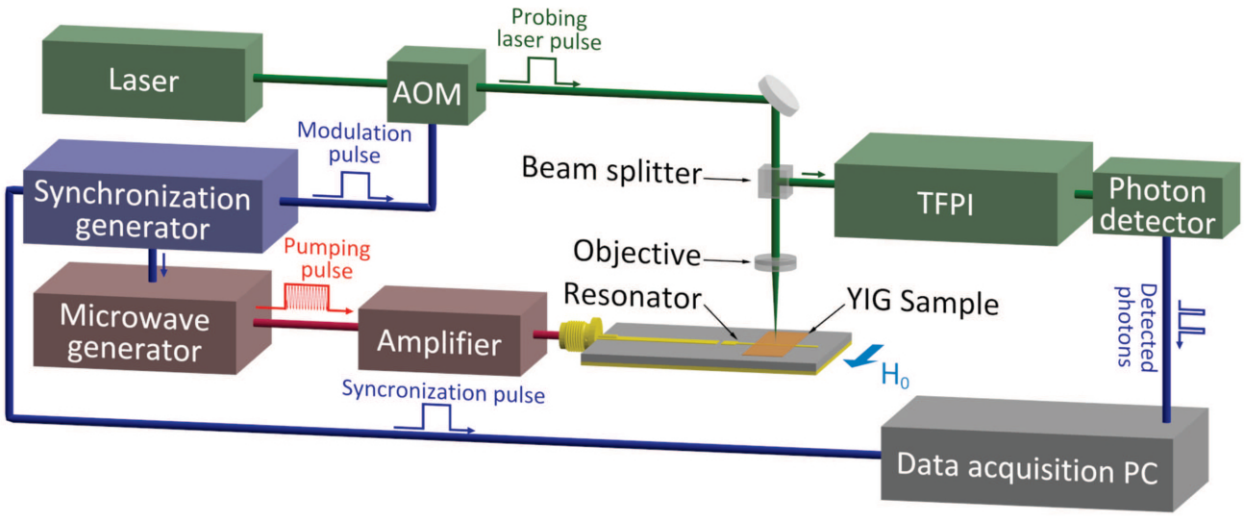

Fig. 5: Schematic illustration of the BLS setup combined with a pulsed probe laser beam technique. The microwave circuit consisting of a microwave source, switch and amplifier is shown. This circuit drives a microstrip resonator, which is placed below a YIG film. The laser beam is sent to an acousto-optic modulator. The modulated sample beam is guided to the objective which focuses the laser beam onto the sample in a spot of about 20 µm in diameter. The scattered light is guided to the Tandem Fabry-Pérot interferometer.

material systems. Integrating a blue laser with a wavelength of 491 nm into our micro-focus BLS setups opened up access to the dynamics of thin YIG films (with thicknesses of 100 nm and below) by largely increasing the sensitivity since the effective scattering cross section is much higher at this wavelength.

A further advancement regarding our standard BLS techniques is the pulsed probe laser beam technique allowing for the detection of various evolution processes such as, e.g., the temperature evolution inside a sample. The special feature of this technique is that the focused laser beam combines the role of the magnon probe with the role of a local sample heater. The heating time is adjusted using amplitude modulation of the probing laser beam by an acousto-optic modulator (AOM). The scheme of the corresponding experimental setup, which consists of a YIG film sample, a microwave circuit, and a BLS laser system, is shown in Fig. 5.

The following list gives an overview of the different BLS setups available in our group. In addition to the optical elements, all setups are equipped with various microwave components to excite and amplify spin waves.

BLS1: High-field electromagnet (1.2 T), conventional BLS spectroscopy (spacial resolution 10 µm, wave-vector resolution $\delta k \approx 0.2\,\mathrm{rad/\mu m}$ with maximal wavevector $k_{\mathrm{max}} \approx 23\,\mathrm{rad/\mu m}$). Time- and option for phase resolution.

BLS2: BLS spectroscopy with microscope (250 nm spatial resolution, $k_{\mathrm{max}} \approx 17\,\mathrm{rad/\mu m}$) and positioning stage. Option for time- and phase resolution.

BLS3: High-field electromagnet (1.2 T) and conventional BLS spectroscopy (wave-vector resolution $\delta k \approx 0.2\,\mathrm{rad/\mu m}$ with maximal wavevector $k_{\mathrm{max}} \approx 23\,\mathrm{rad/\mu m}$). Microscope stage with 250 nm spatial resolution ($k_{\mathrm{max}} \approx 17\,\mathrm{rad/\mu m}$) and electromagnet (0.1 T) for in-plane fields. Option for time- and phase resolution as well as for an out-of-plane electromagnet.

BLS4: Electromagnet (0.1 T), BLS spectroscopy with microscope (250 nm spatial resolution) with

green ($\lambda = 532\,\mathrm{nm}$) and blue laser ($\lambda = 491\,\mathrm{nm}$). Option for time- and phase resolution.

BLS5: High-field electromagnet (2.2 T), conventional BLS spectroscopy (spacial resolution 10 µm, wave-vector resolution $\delta k \approx 0.2\,\mathrm{rad/\mu m}$ with maximal wavevector $k_{\mathrm{max}} \approx 23\,\mathrm{rad/\mu m}$). Time- and option for phase resolution.

BLSA: Electromagnet (0.7 T), BLS spectroscopy with microscope (250 nm spatial resolution) with blue laser ($\lambda = 457\,\mathrm{nm}$). Objective with a correction collar for measurements through transparent substrates and special sample holder with the possibility of connecting picoprobes in upside-down configuration. Time- and option for phase resolution.

3.2 Microwave techniques

Brillouin light scattering (BLS) spectroscopy, as described in the previous section, is a powerful tool for the detection of spin waves and measurement of their characteristics. Nevertheless, it does not allow for spin-wave excitation. Thus, in many of our experiments BLS spectroscopy is combined with microwave techniques which ensure high-efficient generation of spin waves in magnetic structures. Spin waves are emitted by nano- and micro-sized microstrip antennas placed on the surfaces of magnetic thin films and is driven by a microwave signal in the GHz frequency range. Microwave sources in our laboratories generate signals with frequencies of up to 70 GHz providing access to spin waves in a very wide range of frequencies and wavenumbers. Furthermore, large powers provided by the microwave amplifiers allow for the study of strongly nonlinear spin-wave dynamics as well as for quantum effects in parametrically-driven magnon gases and condensates. With the latest upgrades we are able to apply parametric pumping pulses up to 1500 W in peak power. The microwave technique allows for the excitation of both continuous spin waves and short spin-wave packets. Among other advantages, the pulsed technique enables the realization of time resolved (resolution down to 250 ps) BLS spectroscopy shown in Fig. 1. The continuous microwave excitation, by-turn, allows the realization of phase-resolved BLS spectroscopy.

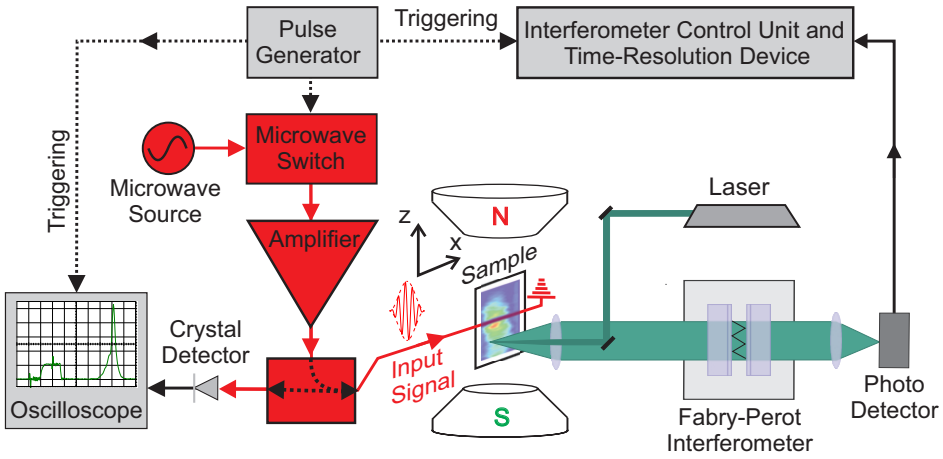

Fig. 1: Scheme of the microwave-assisted time- and space-resolved BLS setup

Besides the excitation of spin waves, the microwave technique is intensively used for high-sensitive (10^{-13} W) detection. Using the same antennas the magnetization precession is converted into microwave currents. These currents are amplified by low-noise amplifiers and analyzed using wide-

band oscilloscopes, vector network analyzers or spectrum analyzers. A vector network analyzer is also used for the ferromagnetic resonance (FMR) measurements allowing determination of such characteristics of the magnetic thin films as the magnetization saturation, the exchange constant, and damping.

Furthermore, we operate a microwave setup for broadband microwave analysis. This setup consists of the following complementary devices: vector network analyzer, spectrum analyzer, microwave signal generator, high-power microwave amplifiers, and a magnet. It has a wide frequency bandwidth of up to 70 GHz which allows for the excitation of spin waves with wavelengths down to 30 nm. This helps us to perform measurements in the frame of modern nanometer-scale magnonics. The broadband microwave analysis can be conducted in both the CW and pulsed regime. The possibility to switch between CW and time-resolved measurements of the vector network analyzer gives us a unique opportunity to discriminate spin-wave signals from much larger electromagnetic leakages.

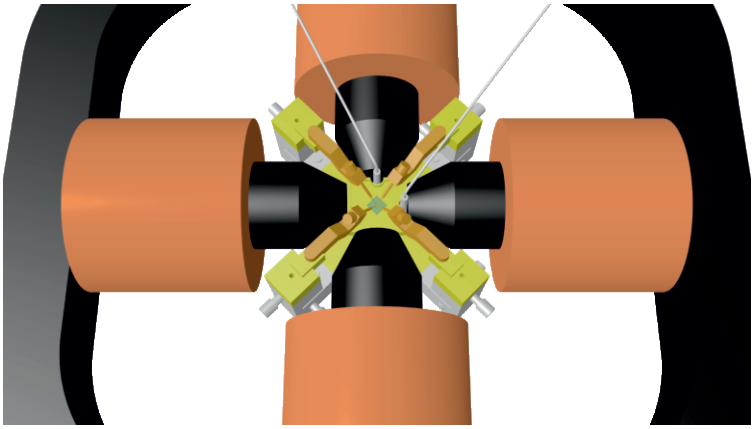

Fig. 2: Schematic illustration of an angle-resolved spin pumping setup

Our microwave techniques are amended by electrical detection of spin waves using the recently installed angle-resolved spin pumping setup schematically shown in Fig. 2. It is developed for separation of the inverse spin Hall effect from spin rectification effects using their angular dependence in an in-plane magnetized ferromagnet / normal-metal bilayer system. The spin pumping setup performs fully automated scans in frequency, microwave power, external magnetic field value and angle. The obtained data can be evaluated using a program with automated fits for extracting angular dependent parameters.

3.3 Magneto-optic Kerr effect magnetometry and microscopy (MOKE)

The magneto-optical Kerr effect (MOKE) is a well established technique to study magnetization properties. The effect is based on the fact, that the plane of polarization of light is rotated when the light is reflected from a magnetic material. The physical origin of MOKE is the magnetic circular dichroism effect: exchange and spin-orbit coupling in a magnetic material lead to different absorption spectra for left- and right-circularly polarized light. Measuring the change of the polarization of the reflected beam (often referred to as Kerr angle Θ_{Kerr}) provides access to the magnetization state of the sample.

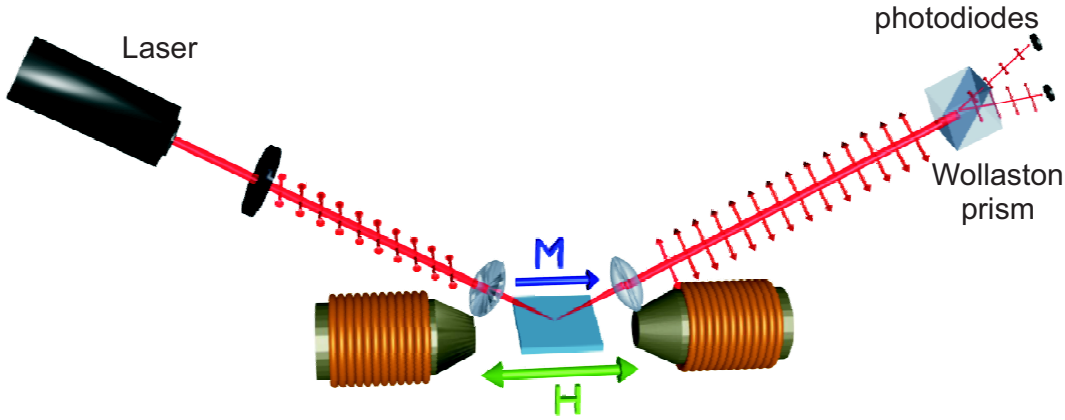

Fig. 1: Schematic setup of a longitudinal Kerr magnetometer.

With MOKE it is possible to study quasi-static magnetization reversal properties and magnetic anisotropies. When using a pulsed laser system it is also possible to study the time dependence of the magnetization under the influence of, e.g., a pulsed magnetic field or a microwave field. Since it is an optical technique it is non invasive, and the spatial resolution is only limited by the optical resolution. Thus, we are able to study the static and dynamic properties of magnetic thin films and magnetic structures with lateral dimension down to 1 µm.

Our group uses three different MOKE setups, all of them using the same principle. The light of a laser source is s-polarized through a thin-film polarizer. The beam is focused onto the sample. The polarization of the reflected light is analyzed by a detector unit that was developed and is built in our laboratory. A Wollaston prism divides the beam into two orthogonally polarized beams, which are monitored by a pair of photodiodes. The detector works as an opto-electrical bridge circuit to increase the signal-to-noise ratio. The obtained normalized differential signal $(I_1 - I_2)/(I_1 + I_2)$ is directly proportional to the Kerr angle Θ_{Kerr}.

Three experimental setups are available to investigate different scientific aspects:

Longitudinal Kerr magnetometer: Longitudinal MOKE geometry to probe quasi-static properties of magnetic thin films. Optical resolution $\sim 100\,\mu\mathrm{m}$, magnetic field up to 0.2 T, automated sample positioning and rotation. Recently, the setup has been expanded to allow spectroscopic measurements. For this, a superK EXTREME supercontinous laser source has been added allowing for light with a wavelength between 550 and 900 nm.

Microfocus Kerr microscope with rotation unit: Longitudinal MOKE geometry to probe quasi-static properties of micro-structured magnetic elements. Optical resolution $< 1\,\mu\mathrm{m}$, magnetic field up to 60 mT, automated sample positioning, rotation and stabilization.

Time resolved scanning Kerr microscope: Longitudinal or polar MOKE geometry to study dynamic magnetization reversal properties of micro-structured elements. Optical resolution $<$ 500 nm, time resolution $\sim 60\,\mathrm{ps}$, magnetic field up to 150 mT, automated sample positioning and stabilization.

3.4 Molecular beam epitaxy (MBE)

The Molecular Beam Epitaxy (MBE) technique involves highly controlled evaporation of materials in an ultra-high vacuum chamber (pressure in the low 10^{-11} mbar region). This deposition

from the vapor phase can lead to single crystal film growth. For this reason MBE possesses a dominant role in the world of nanotechnology regarding fabrication of materials for high performance applications.

Our group operates two Molecular Beam Epitaxy (MBE) growth clusters. Both systems are equipped with tools for cleaning the substrates, for controlling the evaporation from the sources and the film deposition, for *in-situ* structural and chemical characterization, as well as sample storage.

The first cluster is called MDA (Multidepositionsanlage). The MDA has been heavily loaded this year with the growth of magnetic structures. The growth chamber contains two Knudsen cells, and one electron gun with 5 crucibles that are used to heat and evaporate the materials. The growth procedure is controlled *in-situ* by a quartz crystal. Additionally *in-situ* Low-Energy Electron Diffraction (LEED) and Auger analytics can be performed. Furthermore, the linear construction of the sample holder reduces the total time for sample preparation largely.

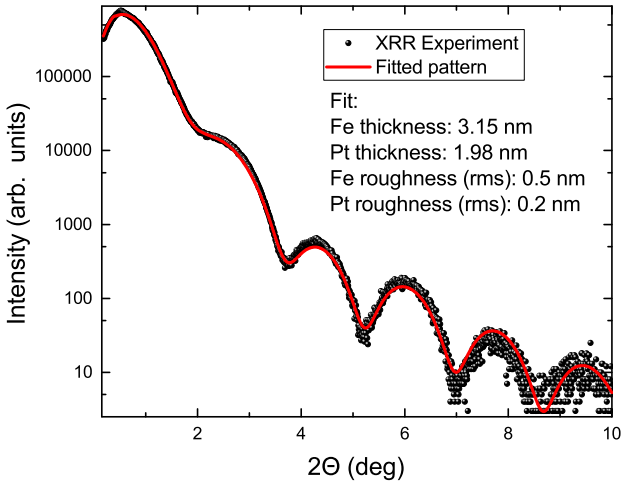

Fig. 1: X-rays Reflectivity pattern (XRR) for an Fe/Pt bilayer (data points) grown on an MgO substrate. The continuous line represents the fitted curved using the GENX code. The fitting parameters are shown in the inset. The XRR measurements were performed by Jörg Lösch at the Institut für Oberflächen und Schichtanalytik (IFOS), Kaiserslautern.

Our second cluster, called MBE, contains two Knudsen cells, and one electron gun with 5 crucibles. The growth procedure is also controlled *in-situ* by a quartz crystal. One of the great advantages of our MBE system is the capability to control the *in-situ* growth by means of Reflection of High-Energy Electron Diffraction (RHEED). The characteristics of the RHEED technique is not to interfere with the deposition. This renders it as a unique tool for real-time structural characterization of the sample during the growth process and enables the control of the growth procedure at the atomic level. Using the MBE, there is also an option for Low-Energy Electron Diffraction (LEED) and Auger spectroscopy.

In addition to the aforementioned techniques and linked to the MBE, an scanning tunneling microscope (STM) set-up is used for *in-situ* atomic probing. This further increases the capabilities of our MBE chamber. STM is a unique tool for surface investigation of the evaporated samples. Also, the cluster includes a load chamber for inserting samples into the vacuum and into the preparation chamber. The latter is used for cleaning the samples since there is the possibility to heat

the samples up to 800 °C. Furthermore, there is an option for optical coatings. The ionization chamber is equipped with a fine-focus noble gas keV ion source. A transfer chamber connects all the parts of the growth cluster while a repository chamber is also available. The MBE chamber has another unique feature: that of *in-situ* magnetic characterization with Brillouin light scattering (BLS) spectroscopy and Kerr effect magnetometry. The applied magnetic field can reach 1.2 T. There is an option for the implementation of a cryostat.

The MBE evaporation technique offers unique advantages for the fabrication of patterned samples. The good control of the film growth and the directionality of the beam renders MBE suitable to grow materials on patterned masks. Patterned samples of very high quality can be produced either with pre- or post treatment techniques.

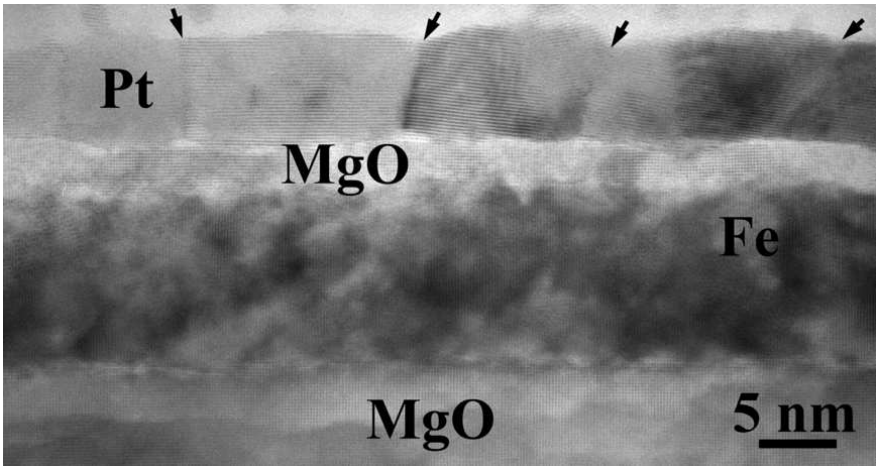

Fig. 2: Cross-sectional high resolution transmission electron microscopy image of a Fe/MgO/Pt trilayer grown on a MgO substrate with the MBE technique (Mihalceanu et al. Appl. Phys. Lett. 110, 252406 (2017)), (Photo courtesy: Thomas Kehagias).

2017 was a very successful year regarding both of our growth chambers. We have focused on the growth of very thin Fe/Pt bilayers (see Fig. 1) with different Fe and Pt thicknesses for spin dynamics studies in the GHz and the THz regime. We have also prepared Fe/MgO/Pt (see Fig. 2) trilayers for spin pumping experiments. In addition, we have used YIG substrates to evaporate Au patterned structures on top for studies in the magneto-plasmonic research field. Furthermore, an upgrade of the thickness control system took place including both hardware and software parts. Finally, the calibration for wedge and checkerboard samples grown on single substrates was performed and now the procedure for such samples is well established.

Chapter 4: Reports on Experimental Results

A. Magnon Gases, Condensates and Supercurrents

In ferromagnetic materials atoms having unpaired electrons act as individual magnets. Their magnetism is mostly caused by the magnetic moments of the uncompensated electron spins. Since these atomic magnets tend to be oriented in the same direction due to quantum-mechanical exchange interaction, a macroscopic magnetic moment appears. As the atoms strongly interact, a reversal of a single atomic magnetic moment is not spatially localized but spreads through the solid as a wave of discrete magnetic momentum transfer. This wave is known as a spin wave, and in frame of second quantization it is associated with a quasi-particle named magnon. Weakly interacting magnons can be considered as a gas of magnetic bosonic quasi-particles and, therefore, this is referred to as a magnon gas.

Nowadays magnon gases are recognized as an excellent model environment for the experimental investigation of collective classical and quantum macroscopic properties of bosonic systems. Its potential is due to the wide controllability of the magnon density as well as of the spectral properties influencing the magnon-magnon interaction. For example, the dispersion branch of a magnon gas can be frequency shifted or otherwise modified by a change in the strength or orientation of a bias magnetic field. The magnon population density can be effectively controlled by means of electromagnetic parametric pumping. In the simplest case one photon of the pumping electromagnetic field excites two magnons with half the energy/frequency that propagate in opposite directions. Such a mechanism creates a huge quantity of phase correlated magnons, which are called a condensate of photon-coupled magnon pairs. The behavior of parametrically created magnon condensates, of gaseous magnon phases, and of Bose-Einstein condensates (BEC), which can be formed at the lowest energy state of a magnon gas, constitutes a hot research topic. A major goal of our work is to study the phase transition processes resulting in the formation of quantum macroscopic states of a magnon gas and to understand the role of magnon-magnon and magnon-phonon interactions in the properties of these correlated states of matter in comparison with the dynamics of ultra-cold quantum gases and quantum spin systems. We investigate the dynamics of the magnon system in a low-damping magnetic insulator (yttrium iron garnet, YIG) using wavevector- and time-resolved Brillouin light scattering (BLS) spectroscopy.

The magnon BEC is described by a unique wavefunction, and thus it can be considered as a macroscopic quantum state. In such a state transport of energy and momentum is possible via a supercurrent mechanism, analogous to charge supercurrents in superconductivity or mass supercurrents in superfluidity. Recently we have succeeded to create magnon supercurrents at room temperature by introducing a time-dependent spatial phase gradient into the BEC's wave function by local laser heating of a YIG film. It has been found that such a heating in the focal point of a probing laser beam leads to an excessive decay of the BEC, which can be associated with the outflow of condensed magnons. The occurrence of the supercurrent opens door to studies in the general field of magnonic macroscopic quantum transport phenomena at room temperature as a novel approach in the field of information processing.

Several very interesting findings in this area are presented this year.

In report 4.1 "Long-distance supercurrent transport in a room-temperature Bose-Einstein magnon condensate" we present the results of non-local probing of a magnon supercurrent, which provide direct evidence of the condensate propagation driven by a phase gradient. By utilizing a separate blue laser for heating purposes, we are able to control the thermal gradient, while a low-power

green laser is used for probing of the condensate area. The propagation of a supercurrent pulse is detected on an undisturbed background of the slowly decaying magnon BEC.

In report 4.2 “From kinetic instability to Bose-Einstein condensation and magnon supercurrents” we demonstrate experimentally and theoretically the ability for the efficient formation of a magnon BEC at the pumping conditions when the multistage chain-like thermalization process is accompanied by a strong direct transfer of parametrically injected magnons to low energy states of a magnon gas. The coherency of the formed BEC phase is evidenced by observations of thermally driven magnon supercurrents.

In report 4.3 “Electrical detection of internally pumped magnons” we investigate the impact of parametrically pumped, thermalized, and condensed magnons on the electrical detection of spin currents in YIG/Pt bilayers. A visible enhancement of the Inverse Spin Hall voltage is observed after the external pumping pulse is switched off. This effect is associate with the efficient excitation of secondary magnons at the YIG/Pt interface in the process of nonlinear thermalization of freely evolving parametric magnons.

In report 4.4 “Control of temperature-induced magnon supercurrent by magnon population” we realized the control of a thermally driven magnon supercurrent by variation of the pumping power leading to the consequent change in the density of a magnon gas. The ability to turn-on and turn-off the supercurrent outflow from the heated sample area is shown. The effect is related to the spontaneous emergence of magnon coherency at the lowest energy state if the magnon gas density exceeds a critical value.

In report 4.5 “Wavelength-dependent transformation of dipole-exchange magnon modes in obliquely magnetized YIG film” we present the first direct observation of an energy-momentum thermal spectrum of dipolar-exchange magnons in a YIG film, experimentally demonstrate radical modifications of the observed spectra in obliquely magnetized films, and theoretically explain these modifications by a strong wavenumber-dependent transformation of the thickness profiles of the magnon modes. Moreover, we predict that such a transformation is related to the arising of a strong permanent spin current across the thickness of obliquely magnetized magnetic films.

In report 4.6 “Temperature dependent relaxation of dipole-exchange magnons in YIG film” we investigate the relaxation of parametrically excited magnons in the temperature range from 20 K to 340 K. It has been found that the magnon lifetime strongly decreases at cryogenic temperatures in a wide range of magnon wavenumbers from zero to $5 \cdot 10^5\,\mathrm{rad\,cm^{-1}}$. Such relaxation behavior is related to the interaction of the YIG spin system with rare-earth impurities and coupling with the paramagnetic gallium gadolinium garnet substrate. These results are significant for further studies of mechanisms underlying the formation and decay of a magnon BEC as well as for quantum information processing.

A. Magnonengase und -kondensate

In ferromagnetischen Materialien treten Atome, die ungepaarte Elektronen haben, als einzelne elementare Magnete auf. Ihr Magnetismus wird in der Regel durch die magnetischen Momente des nicht kompensierten Elektronenspins verursacht. Diese atomaren Magnete richten sich häufig aufgrund der quantenmechanischen Austauschwechselwirkung in einem Ferromagneten parallel zueinander aus. Daher beobachtet man ein makroskopisches magnetisches Moment. Da die Atome stark miteinander wechselwirken, wird das Umklappen eines einzelnen atomaren magnetischen Moments nicht räumlich lokalisiert sein, sondern breitet sich als Welle mit einem diskreten magnetischen Moment über den gesamten Festkörper aus. Diese Welle wird als Spinwelle bezeichnet und ist im Rahmen der zweiten Quantisierung mit einem Quasiteilchen, dem so genannten Magnon, verbunden. Schwach miteinander wechselwirkende Magnonen können als Gas von magnetischen bosonischen Quasiteilchen angesehen werden und werden daher auch als Magnonengas bezeichnet.

Magnonengase sind unlängst als hervorragendes Modellsystem erkannt worden und dienen zur Untersuchung von korrelierten bosonischen Systemen mit sowohl klassischen Eigenschaften als auch makroskopischen Quanteneigenschaften. Ihr Potenzial liegt dabei in der guten Kontrollierbarkeit der Magnonendichte und den Eigenschaften des Spektrums, welches die Magnon-Magnon-Wechselwirkung beeinflusst. Zum Beispiel kann durch die Änderung der Richtung oder der Stärke eines externen Magnetfelds das Spektrum des Magnonengases in der Frequenz verschoben oder auch stark verändert werden. Der wirkungsvollste Mechanismus, die Dichte eines Magnonengases zu erhöhen, ist parametrisches Pumpen mittels Mikrowellen. Im einfachsten Fall erzeugt ein Photon des elektromagnetischen Pumpfeldes zwei Magnonen mit je der Hälfte der Energie/Frequenz des Photons, die sich in entgegengesetzte Richtungen ausbreiten. Dieser Mechanismus erzeugt eine große Anzahl von phasenkorrelierten Magnonen, ein sogenanntes Kondensat von photonengekoppelten Magnonenpaaren. Die Verhaltensweisen parametrisch erzeugter Magnonenkondensate, gasförmiger Magnonenzustände, und von magnonischen Bose-Einstein-Kondensaten (BEC), welche im Zustand niedrigster Energie des Magnonengases erzeugt werden können, bilden ein aktuelles Forschungsthema. Das Hauptziel unserer Forschung ist die Untersuchung der Phasenübergänge, die zu der Bildung von Zuständen mit makroskopischen Quanteneigenschaften in Magnonengasen führen, und das Verständnis der Funktion der Viel-Magnonen-Wechselwirkungen in diesen korrelierten Zuständen der Materie im Vergleich mit der Dynamik von ultrakalten Quantengasen und Quanten-Spinsystemen. Wir untersuchen die Dynamik des Magnonensystems in einem magnetischen Isolator mit niedriger Dämpfung (Yttrium Eisen Granat, YIG) mit Hilfe von wellenvektor- und zeitaufgelöster Brillouin-Lichtstreuspektroskopie.

Magnonische BECs werden durch eine wohldefinierte Wellenfunktion beschrieben. Daher kann man sie als einen makroskopischen Quantenzustand auffassen. In solch einem Zustand kann Transport von Energie oder Drehimpuls durch einen Suprastrom-Mechanismus stattfinden, analog zu einem Ladungs-Suprastrom in der Supraleitung oder zu einem Teilchen-Suprastrom in der Suprafluidität. Vor kurzem hatten wir Erfolg in der Realisierung von Magnonen-Superströmen. Dies ist gelungen durch die Erzeugung eines örtlich ausgedehnten zeitabhängigen Phasengradienten innerhalb des BECs, welcher durch lokale Erhitzung des YIGs mit einem Laser erzeugt wurde. Dabei wurde herausgefunden, dass das Erhitzen des YIGs in dem Fokuspunkt eines Detektionslasers zu einem exzessiven Zerfall des BECs führt. Dieser wird verursacht durch ein Herausfließen der kondensierten Magnonen, angetrieben von dem erzeugten Phasengradienten. Das Auftreten des Superstroms öffnet ein neues Forschungsfeld der magnonischen makroskopischen Quanten-

transportphänomene bei Raumtemperatur zur Anwendung in der Informationsverarbeitung.

Dieses Jahr werden einige sehr interessante Ergebnisse vorgestellt.

Im Bericht 4.1 “Long-distance supercurrent transport in a room-temperature Bose-Einstein magnon condensate” werden die neusten Ergebnisse zur nichtlokalen Messung von Superströmen gezeigt, welche den direkten Einfluss eines Phasengradienten auf die zeitliche Entwicklung eines magnonischen BECs zeigen. Durch die Nutzung eines separaten blauen Lasers zum Heizen ist es möglich einen thermischen Gradienten in der Probe zu erzeugen, während mit einem zweiten grünen Laser geringer Intensität das Kondensat vermessen wird. Die Ausbreitung des Suprastromspeaks wird dabei auf dem ungestörten Hintergrund eines langsam zufallenden magnonischen BECs beobachtet.

Im Bericht 4.2 “From kinetic instability to Bose-Einstein condensation and magnon supercurrents” wird experimentell und theoretisch eine effiziente Möglichkeit gezeigt, um ein magnonisches BEC zu erzeugen. Dabei wurden die äußeren Bedingungen so angepasst, dass neben dem gewöhnlichen Prozess der Thermalisierung über viele Zwischenzustände eine starke direkte Streuung der parametrisch erzeugten Magnonen zum Boden des Spektrums entsteht. Die Kohärenz des BEC wurde dabei durch die thermische Erzeugung von Supraströme nachgewiesen.

Im Bericht 4.3 “Electrical detection of internally pumped magnons” wird der Einfluss von parametrisch gepumpten, thermalisierten und kondensierten Magnonen auf die elektrische Detektion von Strömen in YIG/Pt-Doppelschichten untersucht. Dabei wurde ein sichtbarer Anstieg der inversen Spin-Hall Spannung nach dem Ausschalten des externen Pumppulses beobachtet. Dieser Effekt beruht auf der effizienten Anregung von sekundären Magnonen an der YIG/Pt-Schnittstelle, hervorgerufen durch nichtlineare Thermalisierung von frei entwickelnden parametrischen Magnonen.

Im Bericht 4.4 “Control of temperature-induced magnon supercurrent by magnon population” wird die gezielte Manipulation thermisch erzeugter Supraströme durch Variation der Pumpleistung vorgestellt, denn diese hat einen direkten Einfluss auf die Dichte des Magnonengases. Dabei wurde beobachtet, dass in Abhängigkeit von der Dichte die Supraströme, welche Magnonen aus den geheizten Gebieten abfließen lassen, ein- und ausgeschaltet werden können. Dies zeigt die spontane Entstehung von Kohärenz im untersten Energiezustand bei Überschreitung einer kritischen Magonendichte.

Im Bericht 4.5 “Wavelength-dependent transformation of dipole-exchange magnon modes in obliquely magnetized YIG film” zeigen wir die erste direkte Beobachtung von thermischen Magnonen spektren im Dipolregime. Dabei zeigte sich, dass der Winkel der Magnetisierung der YIG-Filme einen starken Einfluss auf das Spektrum hat. Diesen Effekt kann man auf eine Wellenzahl-abhängige Veränderung der Dickenprofile der Magnonenmoden zurückführen. Wir prognostizieren dass durch diese Veränderung ein starker permanenter Spinstrom senkrecht zur Oberfläche des schräg magnetisierten Films entsteht.

Im Bericht 4.6 “Temperature dependent relaxation of dipole-exchange magnons in YIG film” Untersuchen wir die Relaxation von parametrisch angeregten Magnonen in einem Temperaturbereich von 20 K bis 340 K. Dabei wurde herausgefunden das die Lebenszeit eines Magnons sich in dem Wellenzahlenbereich von 0 bis $5 \cdot 10^5\,\mathrm{rad\,cm^{-1}}$ für tiefe Temperaturen stark verringert. Solch ein Relaxationsverhalten ist auf die Wechselwirkung des YIG-Spinsystems mit den Verunreinigungen durch Seltenen Erden und der Wechselwirkung mit dem paramagnetischen Gallium-Gadolinium-Granat zurückzuführen. Diese Resultate sind wichtig für weiterführende Studien zur Untersuchung der Entstehung und des Zerfalls eines magnonischen BECs sowie auch für die Quanteninformationstechnologie.

4.1 Long-distance supercurrent transport in a room-temperature Bose-Einstein magnon condensate

D.A. Bozhko, A.J.E. Kreil, H.Yu. Musiienko-Shmarova, A.A. Serga, and B. Hillebrands

In collaboration with V.S. L'vov and A. Pomyalov, Department of Chemical Physics, Weizmann Institute of Science, Rehovot 76100, Israel

Magnons are bosons, and thus they are able to form spontaneously a coherent ground state, a Bose-Einstein condensate (BEC) [1, 2], which can be established even at room temperature. Recently we have succeeded to create a magnon supercurrent by introducing a time-dependent spatial phase gradient into the wave function of this spatially extended macroscopic quantum state. [3]. In order to observe the long-time evolution of the magnon BEC, the experiment was performed in a low-damping single-crystal film of yttrium iron garnet ($Y_3Fe_5O_{12}$, YIG). The temporal evolution of the magnon BEC formed in the parametrically populated magnon gas was studied by means of time- and wavevector-resolved Brillouin light scattering (BLS) spectroscopy (description of the method see in 3.1 section of this Annual Report). It has been found that local heating in the focal point of a probing laser beam leads to a excessive decay of the BEC, which is associated with the outflow of condensed magnons driven by a thermal gradient. The occurrence of the supercurrent directly confirms the phase coherency of the magnon condensate and opens door to studies in the general field of magnonic macroscopic quantum transport phenomena at room temperature as a novel approach in the field of information processing.

Here we demonstrate novel results of non-local probing of a magnon BEC, which provide direct evidence for the motion of the condensate caused by a phase gradient induced by a local temperature gradient. Moreover, we show that this propagation of the happens with a constant velocity for a large distance outside of a heated area.

A sketch of the experimental setup is shown in Fig. 1. It consists of microwave and optical parts. The microwave part includes a microwave generator, which is used as a source of pumping pulses (pulse duration 2 µs, repetition time 1 ms, carrier frequency 13.6 GHz) followed by a power amplifier, which drives a microstrip resonator circuit with a peak power of 12.6 W. The 50 µm wide half-wavelength microstrip resonator fabricated on top of an alumina substrate is used for further increase in the amplitude of a pumping microwave magnetic field. The YIG sample of lateral dimensions 1 by 5 mm is positioned on top of the middle part of the resonator, in the area of maximal microwave magnetic field. The optical part comprises as the main parts the probing green laser (single-mode, 532 nm wavelength), an acousto-optic modulator, heating blue laser (multi-mode, 409 nm wavelength), and a tandem Fabry-Pérot interferometer. As we have shown in our previous work [3], an excessive heating of the sample by the probing laser can lead to the formation of a magnon supercurrent. In order to minimize the influence of the probing beam on the magnon dynamics we utilize an acousto-optic modulator, which is used for chopping the probing beam into pulses to reduce a parasitic heating of the sample. The pulsed probing beam (pulse duration 6 µs, peak power 9 mW) is then focused onto the sample surface into a focal spot of 20 µm in diameter. The scattered light is directed to a tandem Fabry-Pérot interferometer for frequency- and time-domain analysis. In order to locally heat the sample in a spatial point separated from the probing spot an additional 405 nm wavelength laser is used. The wavelength of this laser was chosen for a couple of reasons. Firstly, absorption of the light in the YIG layer is inverse proportional to the

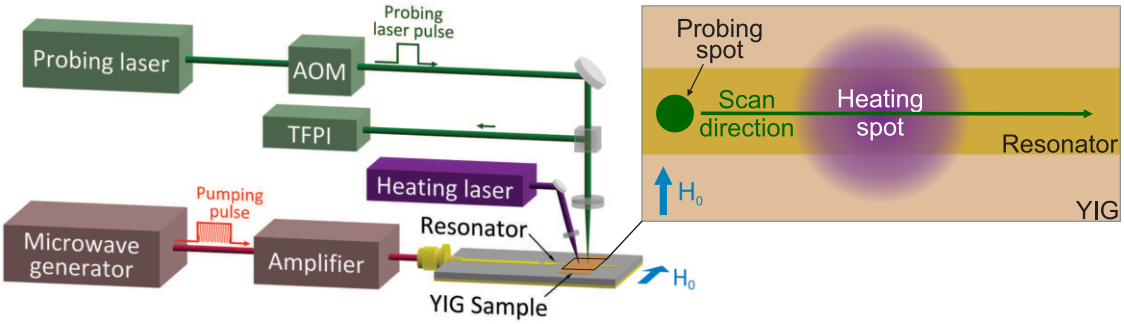

Fig. 1: (a) Experimental setup. A probing laser beam of 532 nm wavelength is focused onto a sample, which is fixed on top of a pumping microstrip resonator. A blue laser of 405 nm wavelength is used for local heating of the sample and is focused into a 80 µm spot. The inset shows a magnified view of a scan area.

wavelength of the light, allowing for an efficient heating of the thin YIG film. Secondly, the chosen wavelength is well separated from the probing laser wavelength, thus it can be rather easily filtered out to exclude any possible influence on the detection system. The heating beam focused into a focal spot of 80 µm in diameter provides a local increase in the temperature of the sample of 40 K at maximal laser power of 116 mW. Spatial-resolved probing of the magnon dynamics is performed by a controlled displacement of the sample using a precise linear positioning stage. Because the heating laser is located on the same stage, the position of the heating spot is fixed in relation to the sample and the excitation circuit (and, thus, in relation to the created magnon BEC). The described setup allows for non-local space-resolved measurements of the magnon dynamics across the heated and cold areas of the sample as it is shown in Fig. 1. The spatial resolution (scanning step) is set to 10 µm, which corresponds to the half of the probing focal spot size.

In order to achieve Bose-Einstein condensation [1, 2], magnons are injected into the YIG spin system via parallel parametric pumping [4], which currently is considered to be the most efficient technique for magnon excitation over a large wavevector range. The process can be described by a splitting of a photon of a pumping electromagnetic wave with nearly zero wavevector and the pumping frequency ω_p into two magnons with opposite wavevectors $\pm\boldsymbol{q}$ and frequency $\omega_p/2$ (see, for example, Figure 1 in Report 4.2). The strength of the bias magnetic field $H_0 = 1690$ Oe is chosen to allow for magnon injection slightly above the ferromagnetic resonance frequency ω_{FMR}, where the parallel pumping process has its highest efficiency [5, 6]. Then, the injected quasiparticles thermalize via four-magnon scattering processes conserving both their number and the total energy [7, 8]. Finally, when the total number of magnons reaches a threshold value a magnon BEC forms [1, 2]. Due to the spatially confined microwave excitation, the BEC is formed above the pumping resonator, which extends for 50 µm across and for 1 mm along the bias magnetic field directions respectively. Because of the large anisotropy of the magnon spectrum, for the given film thickness, the effective mass of magnons with wavevectors oriented accross the bias magnetic field is approximately 21 times smaller in comparison with magnons having wavevectors along the field. Thus, a magnon supercurrent is expected to be approximately 21 times stronger across the biasing magnetic field and thus along the large extent of the condensate [3]. The BLS observation of the magnon dynamics needs to ensure a good reflectivity from the sample substrate. In our case this is realized only at the surface of the resonator. Because of all these reasons, this time, we restrict ourselves to scanning in only one dimension: along the pumping resonator.

The results of non-local measurements of the evolution of the magnon density at the bottom of the spin-wave spectrum for different heating conditions are shown in Fig. 2. To understand the

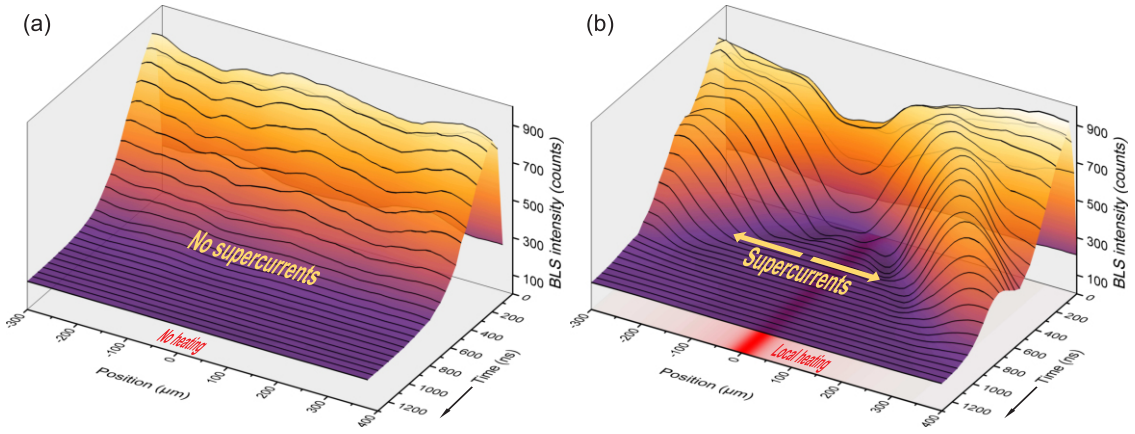

Fig. 2: Time-space diagrams of the magnon Bose-Einstein condensate (BEC) population after termination of the pumping pulse. (a) Without external heating after formation, the BEC decays uniformly in space and time; (b) with external continous heating by a 116 mW blue laser: the magnon BEC is pushed out by a phase gradient created by the non-uniform temperature distribution (the simulated temperature profile is shown in the plane below).

dynamics of the magnon BEC, one first needs to determine how it behaves in the case of a spatially uniform room-temperature profile. The reference measurement performed for the case of absence of heating shows, that the spatial distribution of the magnon condensate along the microstrip resonator is uniform (see Fig. 2a). Similar to the results presented by us in Ref. [2], the BLS signal rises sharply after the microwave pumping pulse is switched off due to a supercooling of the magnon gas and consequent intensification of the BEC formation process. Because of the intrinsic magnon relaxation to the phonon bath the magnon BEC density exponentially decreases and we observe a spatially uniform decay of the BLS signal, which is proportional to the magnon density, after its formation.

Now we focus on the temperature-gradient dependent behavior of the magnon condensate. The outcome of the experiment is strongly changed when an additional local heating by the blue laser is applied (see Fig. 2b). Note that the heating is applied continuously, thus the condensate forms already in the non-uniform part of the temperature profile. In contrast to the temperature-uniform reference measurement, already during the formation of the condensate the magnon density distribution becomes spatially-inhomogeneous: a pronounced dip in the magnon population is formed in the heated region of the sample. The decrease of the condensate population as well as the increased relaxation rate in the hot spot was already reported and is associated with the formation of a magnon supercurrent flowing outside of the high temperature region [3]. Moreover, after some time we start to observe the formation of two propagating peaks, traveling outwards from the hot spot. It is necessary to emphasize, that their propagation occurs outside of the hot spot: as it is shown in Fig. 2b, the heating by the blue laser is rather local, and does not extend beyond $\pm 100\,\mu$m from the center of the focal spot. At the same time the peak propagation length reaches $\pm 400\,\mu$m.

By tracking the position of the magnon density peaks, we can determine their group velocity. Figure 3 shows the positions of the peak maxima as a function of time. One can see that for different heating laser powers these dependencies show a linear behavior. The slopes of the fitting lines correspond to the group velocities, which appear to be close to $360\,\mathrm{m/s}$ for all the cases. The independence of the peak's group velocities on the heating laser power and their propagation outside of the temperature gradient cannot be understood in terms of the supercurrent model developed in [3].

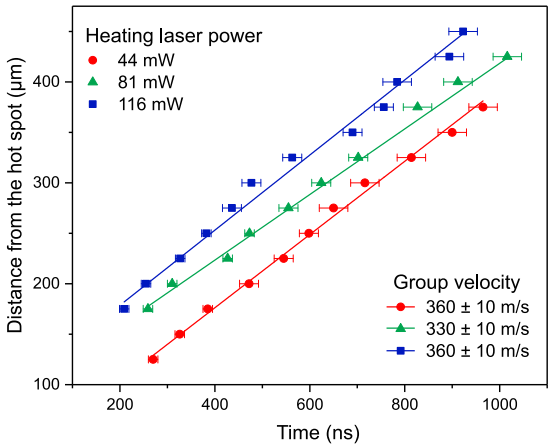

Fig. 3: Estimation of the group velocity of the magnon supercurrent at different heating laser powers.

The possible scenario of such a propagation is the following. It starts from the initial formation of a dip in the magnon population the in hot spot due to the temperature gradient-driven supercurrent. Then, magnons pushed out from the hot spot form peaks at the sides of the dip. These peaks start propagating through the condensate in a form of wave packets, which are secondary eigen excitations of the magnon condensate and could be related to the second sound and shock wave phenomena.

In conclusion, the results presented in this report addressing non-local probing of a magnon BEC provide direct evidence of supercurrent-related motion of the condensate outwards from the heated spot. The occurrence of the magnon propagation outside of the temperature gradient can be associated with the excitation of second sound wave packets in the magnon condensate.

The work is supported by the ERC within the ERC AdG "Supercurrents of Magnon Condensates for Advanced Magnonics" and the DFG within the SFB/TR49.

References

[1] S.O. Demokritov, V.E. Demidov, O. Dzyapko, G.A. Melkov, A.A. Serga, B. Hillebrands, A.N. Slavin, *Bose-Einstein condensation of quasi-equilibrium magnons at room temperature under pumping*, Nature **443**, 430 (2006).

[2] A.A. Serga, V.S. Tiberkevich, C.W. Sandweg, V.I. Vasyuchka, D.A. Bozhko, A.V. Chumak, T. Neumann, B. Obry, G.A. Melkov, A.N. Slavin, B. Hillebrands, *Bose-Einstein condensation in an ultra-hot gas of pumped magnons*, Nat. Commun. **5**, 4452 (2014).

[3] D.A. Bozhko, A.A. Serga, P. Clausen, V.I. Vasyuchka, F. Heussner, G.A. Melkov, A. Pomyalov, V.S. L'vov, B. Hillebrands, *Supercurrent in a room-temperature Bose-Einstein magnon condensate*, Nature Physics **12**, 1057 (2016).

[4] A.G. Gurevich, G.A. Melkov, *Magnetization Oscillations and Waves* (CRC Press, New York, 1996).

[5] A.A. Serga, C.W. Sandweg, V.I. Vasyuchka, M.B. Jungfleisch, B. Hillebrands, A. Kreisel, P. Kopietz, M.P. Kostylev, *Brillouin light scattering spectroscopy of parametrically excited dipole-exchange magnons*, Phys. Rev. B **86**, 134403 (2012).

[6] T. Neumann, A.A. Serga, V.I. Vasyuchka, B. Hillebrands, *Field-induced transition from parallel to perpendicular parametric pumping for a microstrip transducer*, Appl. Phys. Lett. **94**, 192502 (2009).

[7] P. Clausen, D.A. Bozhko, V.I. Vasyuchka, G.A. Melkov, B. Hillebrands, A.A. Serga, *Stimulated thermalization of a parametrically driven magnon gas as a prerequisite for Bose-Einstein magnon condensation*, Phys. Rev. B **91**, 220402(R) (2015).

[8] D.A. Bozhko, P. Clausen, A.V. Chumak, Yu.V. Kobljanskyj, B. Hillebrands, A.A. Serga, *Formation of Bose-Einstein magnon condensate via dipolar and exchange thermalization channels*, Low Temp. Phys. **41**, 1024 (2015).

4.2 From kinetic instability to Bose-Einstein condensation and magnon supercurrent

D.A. Bozhko, A.J.E. Kreil, H.Yu. Musiienko-Shmarova, B. Hillebrands, and A.A. Serga

In collaboration with V.S. L'vov and A. Pomyalov, Department of Chemical Physics, Weizmann Institute of Science, 76100 Rehovot, Israel

By means of electromagnetic parametric pumping an ensemble of magnons, the quanta of spin waves, can be prepared as an overpopulated Bose gas of weakly interacting quasiparticles. The evolution of this gas via magnon-magnon scattering processes, which conserve the number of particles, can lead to the formation of a Bose-Einstein condensate (BEC) at the bottom of a spin-wave spectrum $\omega_{\min}(\boldsymbol{q}_{\min})$ [1]. Furthermore, if a phase gradient is imposed on the condensate wavefunction by, e.g., a temperature gradient, a magnon supercurrent appears [2] (see also report 4.1). Here, we study these macroscopic quantum phenomena by Brillouin light scattering (BLS) spectroscopy in a single-crystal yttrium iron garnet (YIG, $Y_3Fe_5O_{12}$) magnetic film in a wide range of external magnetic fields. This allows us to compare features of the condensation process in the cases when one of the two physical mechanisms of the magnon transfer from a pumped high-frequency spectral area to the BEC state prevails: a step-by-step Kolmogorov-Zakharov [3] cascade of weak wave turbulence process (similar to the Richardson-Kolmogorov cascade in hydrodynamic turbulence [4]) or a kinetic-instability (KI) channel [5, 6], which directly transfers magnons from the pumping area to the BEC point.

In our experiments, the time evolution of the total number $N_{\text{tot}}(t)$ of magnons near the bottom of their frequency spectrum, $(\omega_{\min}, \pm\boldsymbol{q}_{\min})$, was studied at room temperature in an in-plane magnetized YIG film by frequency-, time- and wavevector-resolved BLS spectroscopy (see Fig. 1). Following the conventional approach, which was established in previous experiments on a magnon BEC [1, 2, 7], magnons were injected into the YIG film via parallel parametric pumping [8, 9]. Next, non-linear magnon scattering processes transfer the injected magnons to the area near $\omega_{\min}$ and cause the local thermalization of low-energy magnons in phase and energy space. This thermalization leads to an increase in the chemical potential of the low-energy part of the magnon gas,

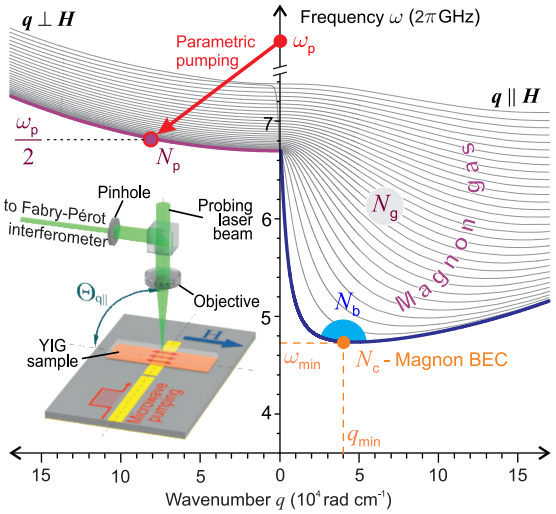

Fig. 1: Magnon spectrum of a 5.6 µm thick YIG film magnetized by a bias magnetic field $H = 1700$ Oe shown for the wavevector $\boldsymbol{q}$ perpendicular (left part) and parallel (right part) to the applied field. The red arrow illustrates the process of parametric pumping. N_p – total number of parametrically excited magnons at $\omega_p/2$; N_c – number of BEC magnons at $\omega_c = \omega_{\min}$; N_b – number of gaseous magnons near $(\omega_{\min}, q_{\min})$; N_g – number of magnons in the parametrically overpopulated gas of magnons below $\omega_p/2$. The inset shows a sketch of the experimental setup. By using a microstrip resonator the conditions of parallel parametric pumping were realized. The light inelastically scattered by magnons is analyzed by a Fabry-Pérot interferometer. Wavenumber-selective probing of magnons with wavevectors $\mathbf{q} \parallel \mathbf{H}$ is realized by varying the incidence angle $\Theta_{q_\parallel}$ between the field $\mathbf{H}$ and the probing laser beam.

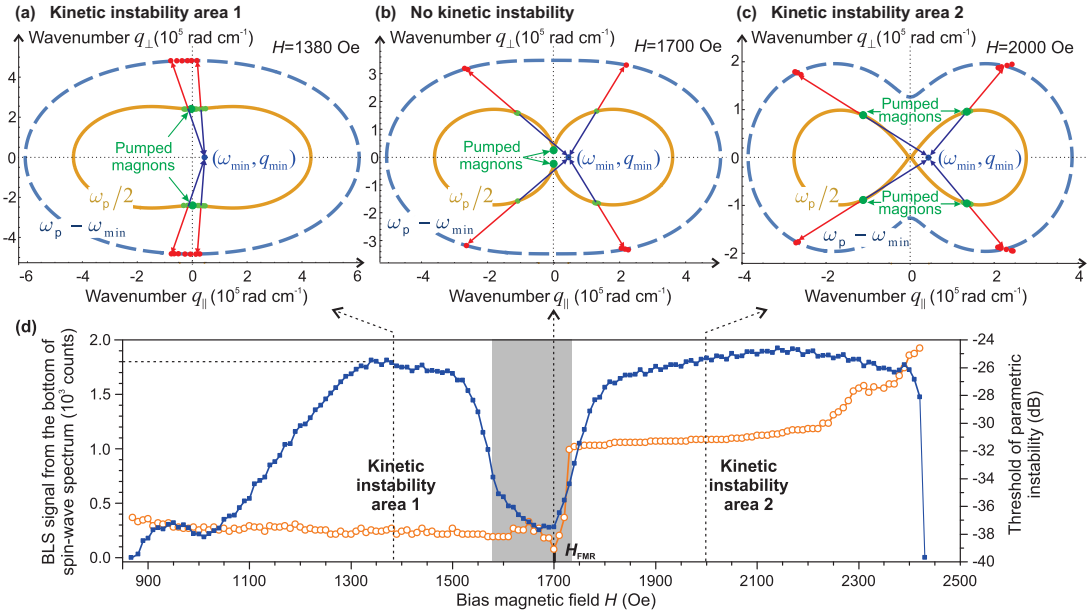

Fig. 2: Panels a, b and c: Diagrams describing the kinetic instability processes. Parallel parametric pumping injects pairs of magnons with opposite wavevectors $\pm\boldsymbol{q}_\mathrm{p}$ at $\omega_\mathrm{p}/2$. The isofrequency curve $\omega(H,q_\parallel,q_\perp)=\omega_\mathrm{p}/2$ is shownin each panel a by solid line while the isofrequency curve $\omega(H,q_\parallel,q_\perp)=\omega_\mathrm{p}-\omega_\mathrm{min}$ is shown by a dashed line. The BEC's spectral position at $(\omega_\mathrm{min},\boldsymbol{q}_\mathrm{min})$ is indicated by the blue dots. The dots on the isofrequency curve $\omega_\mathrm{p}/2$ show the positions of two magnons with $\boldsymbol{q}_1\approx\boldsymbol{q}_2$, which can potentially participate in the kinetic instability processes. The kinetic instability processes develop when these spectral positions are sufficiently populated by parametrically pumped magnons. The dots on the isofrequency curve $\omega_\mathrm{p}-\omega_\mathrm{min}$ show the wavevectors $\boldsymbol{q}_\mathrm{hf}$ of high-frequency magnons created by the kinetic instability process. Four pairs of arrows toward the dashed line and the spectral minimum point indicate the momentum conservation law $2\boldsymbol{q}_{1,2}=\boldsymbol{q}_\mathrm{min}+\boldsymbol{q}_\mathrm{hf}$. Panel d: The intensity of the light scattered by bottom magnons (curve with squares) is presented in comparison with the threshold curve of the parametric pumping process (curve with circles). The lowest threshold values around H_FMR indicate the highest efficiencies of the magnon pumping process but correspond to rather small magnon densities at the lowest energy states. The development of the processes of kinetic instability in the magnetic field regions marked as "Kinetic instability areas 1 and 2" ensures much higher densities of the bottom magnons.

and when it becomes equal to the minimal energy $\hbar\omega_\mathrm{min}$ a magnon BEC forms at this spectral point.

In order to understand the processes of magnon transfer to the bottom of the spectrum we plotted in Fig. 2 the magnon scattering diagrams, which presents the kinetic instability process, in comparison with the intensity of the BLS signal from the bottom spectral area. The scattering diagrams are calculated for three different bias magnetic fields $H=1380\,\mathrm{Oe}$ (Fig. 2a), $1700\,\mathrm{Oe}$ (Fig. 2b) and $2000\,\mathrm{Oe}$ (Fig. 2c). The four pairs of contra-directional arrows illustrate the direct scattering of two magnons with near the same wavevectors from the frequency band around half of the pumping frequency $\omega_\mathrm{p}/2\pm2\pi\cdot50\,\mathrm{MHz}$ to one of the two spectral global minima $(\omega_\mathrm{min},\pm q_\mathrm{min})$ and to upper energy states at the $\omega_\mathrm{p}-\omega_\mathrm{min}$ isofrequency curve. In Fig. 2d the BLS signal proportional to the total number of gaseous and condensed magnons $N_\mathrm{tot}=N_\mathrm{b}+N_\mathrm{c}$ is measured at ω_min for a fixed value of the pumping power ($40\,\mathrm{W}$) as a function of the bias magnetic field H (see the line with squares).

One can see that in two regions of the magnetic field, where kinetic instability of parametrically pumped magnons is allowed, the population of the bottom magnons is one order of magnitude larger than in the shaded area, where the parametric magnons are well separated from the spectral areas of kinetic instability and, thus, can be transferred to the lowest energy states only via chain-like scattering processes.

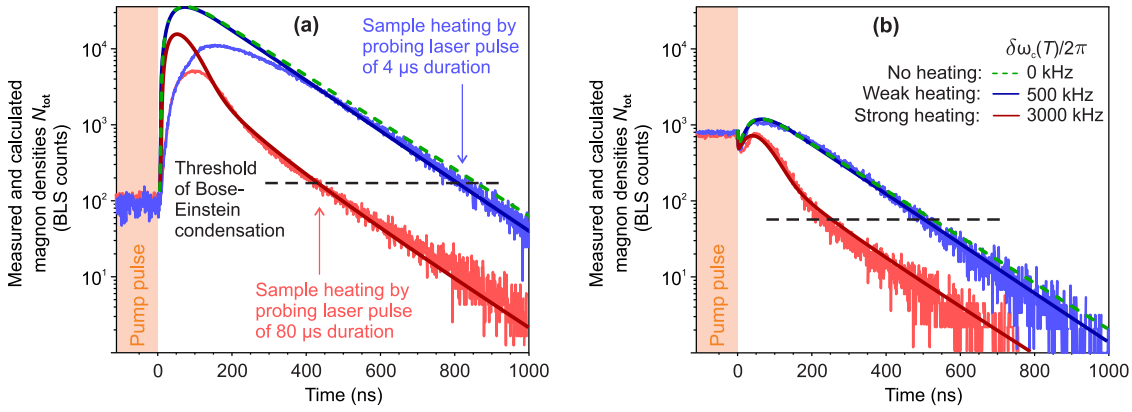

Fig. 3: Panels a and b: Temporal dynamics of the magnon BEC under local laser heating are measured by wave-vector and time-resolved BLS spectroscopy from the global minimum of a SW spectrum in the first area of kinetic instability for different durations of probing laser pulse. Theoretical dependencies (solid and dashed lines) of the magnon densities are calculated taking into account different temperature-dependent shifts $\delta\omega_c(T)$ of the BEC frequency using the model from Ref. [2] with initial conditions conformed to the case of kinetic instability. The BLS data are collected in 150 MHz frequency band near the bottom of the magnon spectrum.

Another important question is how the magnon transfer by the kinetic instability process influences the process of Bose-Einstein condensation and the appearance of a magnon supercurrent. To answer this question, following Ref. [2], we compare the free evolution of the magnon BEC observed after the termination of the parametric pumping pulse both in the weakly and strongly heated focal spots. Figure 3a presents the magnon decay dynamics for $H = 1700$ Oe, when kinetic instability is absent or not essential, while Fig. 3b represents this dynamics for $H = 1380$ Oe in the first area of kinetic instability (see Fig. 2a). There are some differences between the initial stages of the evolutions of the BLS signals in Fig. 3a and Fig. 3b. The main one is a difference in the total number of bottom magnons observed just before the termination of the pumping pulse: $N_{\text{tot}} \simeq 100$ BLS counts for the case without kinetic instability in Fig. 3a and $N_{\text{tot}} \simeq 1000$ BLS counts in the case with kinetic instability in Fig. 3b. It is a result of the much higher efficiency of a direct one-step magnon transfer (kinetic instability process) from the pumping area to the bottom of the magnon spectrum in comparison with a step-by-step Kolmogorov-Zakharov [3] cascade.

In the case of the prohibited kinetic instability, the thermalized magnons are rather uniformly redistributed in a relatively wide region near the bottom of the magnon spectrum and overall in the magnon gas. After the termination of the pumped pulse these magnons move to the energy minimum state by means of non-linear four-magnon scattering process and form there a pronounced peak of the magnon gas density, which is clearly visible in Fig. 3a. In contrast, the kinetic instability process creates a strongly non-uniform population of a magnon gas by transfer of many magnons to the higher energy states near the $\omega_p - \omega_{\text{min}}$ frequency. These high-energy magnons must pass a much larger number of scattering stages before they reach the bottom of the magnon spectrum. Thus, their contribution to the formation of the density peak may be assumed to be rather small. As a result, the after-pumping density peak is only weakly visible in Fig. 3b.

Nevertheless, in both cases shown in Fig. 3a and Fig. 3b the heating of the probing point by a long probing laser pulse leads to the same effect of the enhanced signal decay at the high magnon densities $N_{\text{tot}}(t)$. This phenomenon, which is associated with the supercurrent-related outflow of condensed magnons from the heated probing spot [2], serves as a signature of the spontaneously established coherent magnon phase, i.e. the Bose-Einstein magnon condensate, both in the presence and in the absence of the kinetic instability processes.

To study in more details the decay of the BEC in both these cases, we adopt the phenomenological model developed in Ref. [2] for the evolution of three groups of magnons: the magnon BEC $N_c(t)$, marked in Fig. 1 with a dot at $(\omega_{min},\ q_{min})$, the nearby "bottom" magnons $N_b(t)$ and the "gaseous magnons" $N_g(t)$ occupying the rest of the $(\omega,\boldsymbol{q})$-plane. This model involves a identical relaxation rate Γ for the gaseous, bottom and BEC magnons, the phenomenological parameter N_{cr} representing the threshold of Bose-Einstein condensation, and a supercurrent term describing the outflow of coherent magnons from the hot spot to the cold part of the film. It is assumed that the supercurrent is driven by a phase difference in the BEC wavefunction. This difference arises in the course of time due to a thermally induced change of the saturation magnetization leading to a frequency shift $\delta\omega_c$ between different parts of the magnon condensate. The presence of the kinetic instability process is accounted by the tenfold increase in the initial density of the "bottom" magnons $N_b(t)$ in accordance with the experimental BLS data shown in Fig. 3.

The numerical solutions of the phenomenological equations, shown in Fig. 3 by solid lines, demonstrate a good quantitative agreement with the corresponding experimental data. The solutions, which account for the supercurrent, nicely reproduce two clearly distinguished stages of decay of $N_{tot}(t)$ in the hot spot: first a fast and then a more slow decay.

In conclusion, both by experimental observation and by theoretical modeling of a supercurrent-related transitional dynamics of a freely evolving magnon gas we demonstrate the formation of a coherent condensed magnon state even in the presence of the kinetic instability processes leading to a strongly unbalanced non-equilibrium population of the low-energy part of the magnon spectrum.

Financial support from the European Research Council within the ERC Advanced Grant "Super-Magnonics" is gratefully acknowledged.

References

[1] S.O. Demokritov, V.E. Demidov, O. Dzyapko, G.A. Melkov, A.A. Serga, B. Hillebrands, A.N. Slavin, *Bose-Einstein condensation of quasi-equilibrium magnons at room temperature under pumping*, Nature (London) **443**, 430 (2006).

[2] D.A. Bozhko, A.A. Serga, P. Clausen, V.I. Vasyuchka, F. Heussner, G.A. Melkov, A. Pomyalov, V.S. L'vov, B. Hillebrands, *Supercurrent in a room temperature Bose-Einstein magnon condensate*, Nat. Phys. **12**, 1057 (2016).

[3] V.E. Zakharov, V.S. L'vov, G.E. Falkovich, *Kolmogorov spectra of turbulence (Wave Turbulence)* (Springer, 1992).

[4] U. Frisch, *Turbulence: The Legacy of A.N. Kolmogorov* (Cambridge University Press, 1995).

[5] A.V. Lavrinenko, V.S. L'vov, G.A. Melkov, V.B. Cherepanov, *"Kinetic" instability of a strongly nonequilibrium system of spin waves and tunable radiation of a ferrite*, Sov. Phys. JETP. **54**, 542–549 (1981).

[6] G.A. Melkov, S.V. Sholom, *Kinetic instability of spin waves in thin ferrite films*, Sov. Phys. JETP **72**, 341–346 (1991).

[7] A.A. Serga, V.S. Tiberkevich, C.W. Sandweg, V.I. Vasyuchka, D.A. Bozhko, A.V. Chumak, T. Neumann, B. Obry, G.A. Melkov, A.N. Slavin, B. Hillebrands, *Bose-Einstein condensation in an ultra-hot gas of pumped magnons*, Nat. Commun. **5**, 3452 (2014).

[8] V.S. L'vov, *Wave turbulence under parametric excitations (Applications to Magnetics)* (Springer, 1994).

[9] A.G. Gurevich, G.A. Melkov, *Magnetization Oscillations and Waves* (CRC Press, 1996).

[10] O. Büttner, M. Bauer, S. Demokritov, B. Hillebrands, Y. Kivshar, V. Grimalsky, Y. Rapoport, A.N. Slavin, *Linear and nonlinear diffraction of dipolar spin waves in yttrium iron garnet films observed by space- and time-resolved Brillouin light scattering*, Phys. Rev. B **61**, 11576 (2000).

[11] C.W. Sandweg, M.B. Jungfleisch, V.I. Vasyuchka, A.A. Serga, P. Clausen, H. Schultheiss, B. Hillebrands, A. Kreisel, P. Kopietz, *Wide-range wavevector selectivity of magnon gases in Brillouin light scattering spectroscopy*, Rev. Sci. Instrum. **81**, 073902 (2010).

4.3 Electrical detection of internally pumped magnons

T. Noack, D.A. Bozhko, B. Heinz, A.A. Serga, B. Hillebrands, and V.I. Vasyuchka

The prominent phenomena of Bose-Einstein condensation (BEC) of magnons in magnetic systems [1] attracted a lot of interest from the magnonics community during the last years. As a result, many novel ideas and experiments connected with the magnon condensation appeared, e.g. magnon supercurrents [2–4], vortices in magnon condensates [5], thermally excited coherent auto-oscillations [6], the magnon Josephson effect [3], etc. A prominent feature of the BEC of magnons is the possibility to observe a macroscopic magnon quantum state at room temperature. For this one must increase the chemical potential of a quasiequilibrium magnon gas to the energy of the lowest magnon state by increasing the number of magnons. The most convenient way for magnon injection into a ferromagnet is a process of microwave parametric pumping, which enables reaching a pumped magnon density of up to $10^{20}\,\mathrm{cm}^{-3}$ [1]. During this process, a strong alternating pumping field couples with the precessing magnetization of a ferromagnet and passes energy into its spin system. Usually, the pulsed regime of parametric pumping is used in order to avoid the thermal overheating of the ferromagnet and to investigate freely evolving magnon gases and condensates [7]. However, a dense group of externally generated parametric magnons does not solely serve as a quasiparticle source for the magnon BEC. Due to the inherent induction of a strong microwave magnetic field at pumping frequency, this group can significantly affect the behavior of the whole magnon system in course of pumping [8] and even after the external pumping pulse is switched off. Previously, we have shown that new magnon groups in the spin-wave spectra are effectively generated by this internal pumping field [8, 9]. Such a process influences the thermalization of the magnon gas and, consequently, can modify the formation of the condensed phase. This influence is expected to be especially visible in a ferrimagnet/normal-metal bilayer, where new magnon groups can be electrically detected in an extremely wide range of frequencies and wavevectors [10].

In this report, we investigate the impact of parametrically pumped, thermalized, and condensed magnons on the electrical detection of spin currents in yttrium iron garnet/platinum (YIG/Pt) bilayers. An enhancement in the amplitude of the inverse spin Hall voltage is observed after the external pumping pulse is switched off. This effect is associated with the efficient excitation of secondary magnons at the YIG/Pt interface in the process of nonlinear thermalization of freely evolving parametric magnons.

The measurements presented here are performed for a YIG/Pt bilayer with a YIG-thickness of 6.7 µm and a Pt-thickness of 10 nm. The YIG film is grown by liquid phase epitaxy on a gadolinium gallium garnet (GGG) substrate. The sample is magnetized by a bias magnetic field H oriented in the plane of the YIG film. For the generation of a large group of magnons in the YIG layer the parallel parametric pumping process is utilized when the microwave pumping Oersted field is orientated parallel to the bias magnetic field. To supply the strong pumping field to the YIG/Pt bilayer, the latter was placed inside an open dielectric resonator tuned for the pumping frequency of 13.86 GHz. The Pt layer is wired to an oscilloscope for the detection of generated voltages. The detailed description of the used experimental setup is presented in report 4.15.

When microwave pulses with a pumping frequency and high power are applied to the dielectric resonator, parametric magnons are generated in the YIG layer. This leads to the spin pumping (SP) effect which drives a spin current from the ferrimagnetic layer into the adjacent normal metal. The

transfer of the spin current across the interface is achieved by a coupling of the magnons in the ferrimagnetic layer to the free electrons in the metallic layer. In the normal metal layer the pure spin current carried by the electrons gets converted into a charge current by the inverse spin Hall effect (ISHE). The generated voltage is proportional to the number of parametric magnons absorbed at the YIG/Pt interface. Simultaneously with the generation of parametric magnons, applied microwave pumping pulses heat the Pt layer by eddy currents. This results in a strong thermal gradient through the YIG/Pt interface, which generates a spin current due to the longitudinal spin Seebeck effect (LSSE). This spin current flows in the opposite direction from Pt to YIG that results in the opposite polarity of the generated voltage.

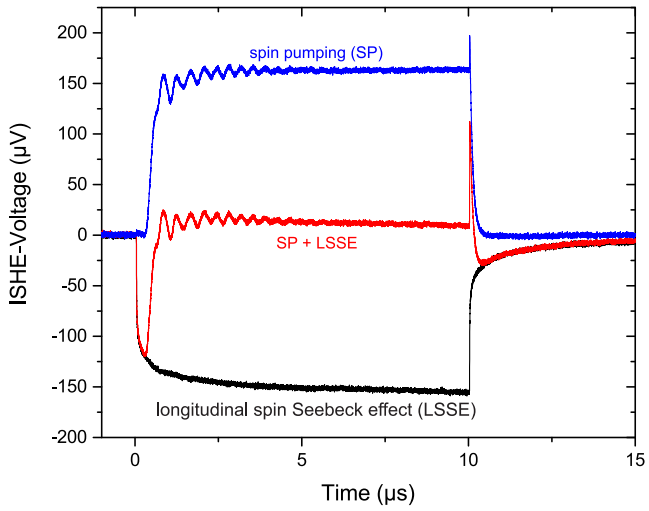

Fig. 1: The temporal evolution of detected voltages measured for different magnetic fields. The negative voltage pulse is measured at $H = 3\,\mathrm{kOe}$, where only the longitudinal spin Seebeck effect contributes to the detected signal. The sign-changing voltage waveform is measured at $H = 1.7\,\mathrm{kOe}$, where the interplay between spin pumping by parametric magnons and the LSSE takes place. The positive voltage pulse is the result of subtraction between these two waveforms and displays the pure contribution of spin pumping by parametric magnons at $H = 1.7\,\mathrm{kOe}$.

In our experiments, we observe the resulting voltage generated due to the simultaneous contribution of both phenomena: the spin pumping by parametric magnons and the longitudinal spin Seebeck effect. A typical example of the temporal evolution of the measured voltages on the application of a 10 µs-long pumping pulse is shown in Fig. 1. It presents voltage waveforms measured for different magnetic fields. To achieve the strongest parametric pumping we chose the magnetic field of 1.7 kOe. This condition corresponds to the generation of long-wavelength parametric magnons with frequencies close to the ferromagnetic resonance. Here both the SP and the LSSE effects form the resulting voltage profile (the middle, sign-changing curve in Fig. 1). The detected signal shows a wide negative peak of a few hundred nanoseconds in duration at the beginning of the pumping pulse. After the pumping pulse is switched off, a strong positive sharp voltage peak appears. It features a fast decay which is followed by a voltage sign change and subsequent slow relaxation.

Such a temporal evolution of the detected signal can be understood by comparing it with a voltage measurement at 3 kOe (the negative voltage curve in Fig. 1). For this high magnetic field the magnon spectrum is shifted to higher frequencies so that parametric pumping is prohibited and only the LSSE takes place. It is clearly visible that both curves show an identical evolution at the beginning of the pumping pulse as well as the same slow decay at the end. Therefore, we can conclude that the LSSE voltage is independent on the magnetic field and can be subtracted. Consequently, the result of subtraction (the upper positive voltage curve in Fig. 1) shows the pure contribution of spin pumping by parametric magnons at 1.7 kOe. This assertion can be confirmed by a short delay in appearance of the SP voltage, which is typical for the threshold behavior of the parametric pumping process, and the clearly visible auto-oscillations, which develop in a system

of parametrically pumped magnons at strong pumping powers.

Surprisingly, at the end of the SP voltage pulse a positive voltage spike is formed. No change in the electrical detection is expected with time. Thus, only the sharp change in the magnon population after the pumping is switched off can be the origin of the peak appearance. In order to reveal the properties of the observed effect, a sweep of the external magnetic field from 20 Oe to 2500 Oe was performed to vary the pumping conditions. It was found that the spike exists in the whole range of applied magnetic fields and the ratio between the saturation level (voltage shortly before the end of the pumping pulse) and the spike amplitude is constant. Only for small fields this ratio deviates due to the demagnetization of the YIG film.

In addition, the dependence of the detected SP signal on the applied pumping power was investigated. In Fig. 2 temporal profiles of SP pulses for different pumping powers are shown on the logarithmic scale. The microwave power was precisely controlled with an attenuator.

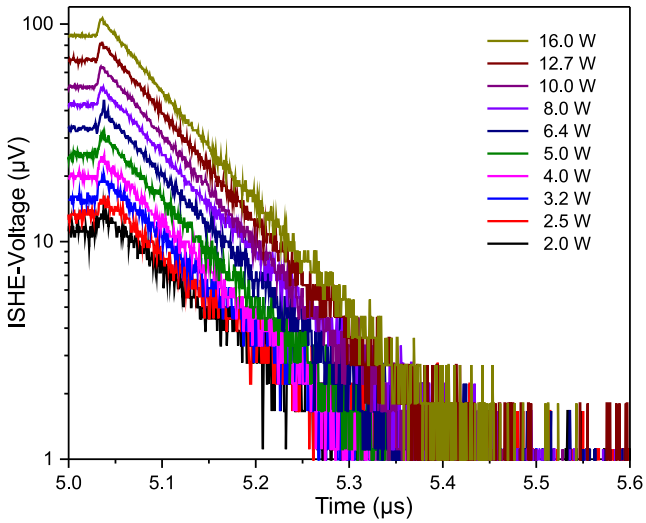

Fig. 2: Temporal profiles of the SP spikes for different levels of applied pumping power. The evolution of the voltage at the end of the pumping pulse in the logarithmic scale is shown.

One can see in Fig. 2 that the spike is formed for all applied pumping powers. Its rise time of around 5 ns remains practically unchanged in the whole range of powers. Moreover, the decay of the signal is perfectly exponential for all curves with only weak changes in the exponential decay time from 170 ns to 230 ns. This is an additional proof that the LSSE contribution was completely removed during the subtraction while the LSSE signal demonstrates a significantly non-exponential decay after the pumping pulse is switched off.

Recently, the formation of the magnon density peak at the bottom of the magnon spectrum when the pumping is switched off was observed using Brillouin light scattering spectroscopy [2, 7]. This effect was attributed to the formation of a magnon Bose-Einstein condensate (BEC) in the presence of a nonlinear “evaporative supercooling” mechanism. However, the results presented in this report demonstrate distinctive features in comparison to the magnon BEC peak. For example, a much smaller rise time of the voltage spike and its presence in a much wider range of magnetic fields.

The observed effect can be understood as an enhancement of the spin pumping process due to the generation of the secondary magnons at the YIG/Pt interface. The precession of the longitudinal component of magnetization, which is caused by the externally injected parametric magnons, leads to the formation of the strong internal alternating magnetic field. Due to the phase mechanism of

limitation of the external parametric pumping, the internal field, oscillating at the pumping frequency, partially compensates the external one. Thus, the net pumping field acting on the spin system during the microwave pulse can be much smaller than external or internal fields [11]. The fast switching off of the external pumping leads to a transient increase of the resulting field. Therefore, a much stronger internal pumping can generate much more secondary magnons during the short time after the pumping pulse is switched off. These magnons at the YIG/Pt interface will lead to the enhancement of the detected electric signal. A similar phenomenon was already observed in electromagnetic radiation measurements using a microstrip antenna [9]. Since the antenna has limitations to the detected wavelengths, only a small region near the ferromagnetic resonance was accessible in these experiments. In our present experiment, the external pumping pulse is switched off during approximately 5 ns that perfectly fits to the observed rise time of the spike. The pure exponential decay of the electric signal correlates with the relaxation of the injected parametric magnons and the respective decay of the internal pumping field.

In summary, we investigated the spin pumping effect in YIG/Pt bilayers by the electric detection of magnons. We observed a distinct enhancement of the spin pumping by magnons after switching off the external pumping pulse. This effect was observed for different pumping powers and in a wide regime of magnetic fields. The nature of this spike can be understood as the result of enhancement of the spin-pumping process due to the excitation of internally pumped secondary magnons close to the YIG/Pt interface.

Financial support from the Deutsche Forschungsgemeinschaft in the frame of SFB/TR 49 is gratefully acknowledged.

References

[1] S.O. Demokritov, V.E. Demidov, O. Dzyapko, G.A. Melkov, A.A. Serga, B. Hillebrands, A.N. Slavin, *Bose-Einstein condensation of quasi-equilibrium magnons at room temperature under pumping*, Nature **443**, 430 (2006).

[2] D.A. Bozhko, A.A. Serga, P. Clausen, V.I. Vasyuchka, F. Heussner, G.A. Melkov, A. Pomyalov, V.S. L'vov, B. Hillebrands, *Supercurrent in a room-temperature Bose-Einstein magnon condensate*, Nat. Phys. **12**, 1057 (2016).

[3] K. Nakata, K.A. van Hoogdalem, P. Simon, D. Loss, *Josephson and persistent spin currents in Bose-Einstein condensates of magnons*, Phys. Rev. B **90**, 144419 (2014).

[4] B. Flebus, S.A. Bender, Y. Tserkovnyak, R.A. Duine, *Two-fluid theory for spin superfluidity in magnetic insulators*, Phys. Rev. Lett. **116**, 117201 (2016).

[5] P. Nowik-Boltyk, O. Dzyapko, V.E. Demidov, N.G. Berloff, S.O. Demokritov, *Spatially non-uniform ground state and quantized vortices in a two-component Bose-Einstein condensate of magnons*, Sci. Rep. **2**, 482 (2012).

[6] C. Safranski, I. Barsukov, H.K. Lee, T. Schneider, A.A. Jara, A. Smith, H. Chang, K. Lenz, J. Lindner, Y. Tserkovnyak, M. Wu, I.N. Krivorotov, *Spin caloritronic nano-oscillator*, Nat. Commun. **8**, 117 (2017).

[7] A.A. Serga, V.S. Tiberkevich, C.W. Sandweg, V.I. Vasyuchka, D.A. Bozhko, A.V. Chumak, T. Neumann, B. Obry, G.A. Melkov, A.N. Slavin, B. Hillebrands, *Bose-Einstein condensation in an ultra-hot gas of pumped magnons*, Nat. Commun. **5**, 3452 (2014).

[8] P. Clausen, D.A. Bozhko, V.I. Vasyuchka, B. Hillebrands, G.A. Melkov, A.A. Serga, *Stimulated thermalization of a parametrically driven magnon gas as a prerequisite for Bose-Einstein magnon condensation*, Phys. Rev. B **91**, 220402(R) (2015).

[9] V.I. Vasyuchka, A.A. Serga, C.W. Sandweg, D.V. Slobodianiuk, G.A. Melkov, B. Hillebrands, *Explosive electromagnetic radiation by the relaxation of a multimode magnon system*, Phys. Rev. Lett. **111**, 187206 (2013).

[10] C.W. Sandweg, Y. Kajiwara, A.V. Chumak, A.A. Serga, V.I. Vasyuchka, M.B. Jungfleisch, E. Saitoh, B. Hillebrands, *Spin pumping by parametrically excited exchange magnons*, Phys. Rev. Lett. **106**, 216601 (2011).

[11] V.S. Zhitnyuk, G.A. Melkov, *Relaxation of longitudinal microwave magnetization in parametric excitation of spin waves in ferrites*, Sov. Phys. JETP **48**, 5 (1978).

4.4 Control of temperature-induced magnon supercurrent by magnon population

A.J.E. Kreil, H.Yu. Musiienko-Shmarova, D.A. Bozhko, B. Hillebrands, and A.A. Serga

Probably the most known transport effect related to the Bose-Einstein condensation phenomenon is the phenomenon of a supercurrent. The supercurrent is a macroscopic effect and describes the phase-induced collective motion of a quantum condensate. Recently, we reported on the discovery of a room-temperature magnon supercurrent driven by a thermally induced phase shift in the condensate's wave function [1]. The phenomenon was evidenced by analysis of the decay of the magnon density measured by means of pulsed Brillouin light scattering (BLS) spectroscopy in the case when a focused laser beam acted both as a probe of the magnon density and as a heating source, which induces a thermal gradient across the probing light spot. The temperature in the spot, and thus the value of the thermal gradient, was controlled by duration of a probing laser pulse. The magnon BEC was created by parametric injection of magnons into the spin system of an yttrium iron garnet (YIG) film [1, 2]. The thermal gradient locally changes the saturation magnetization and induces a frequency shift between different parts of the magnon condensate. Consequently a phase gradient in the BEC wavefunction arises in course of time and a magnon supercurrent flowing out of the hot region of the focal spot is excited. Such a process reduces the number of magnons in the heated area and results in the disappearance of the condensate and, thus, in the disappearance of the supercurrent after some time. The conventional relaxation dynamics of the magnons then recovers.

Here, we demonstrate a way to control such a supercurrent by varying the density of the magnon gas.

Figure 1 provides a sketch of the experimental setup. The setup is placed between the poles of an electromagnet, which creates a homogeneous magnetizing field $\mathbf{H}_0$ lying in the plane of YIG film. In order to reach a high enough density of the magnon gas to form a BEC phase, a rather strong microwave pulse with the peak power $P_{\max} = 41\,\mathrm{dBm}$ is applied to the half-wave microstrip resonator at a carrier frequency $f_{\mathrm{pump}} = 13.6\,\mathrm{GHz}$. The resonator creates an Oersted field $\mathbf{h}(t) \parallel \mathbf{H}_0$ in the YIG film to excite magnons by means of parallel parametric pumping [3]. Additionally, a

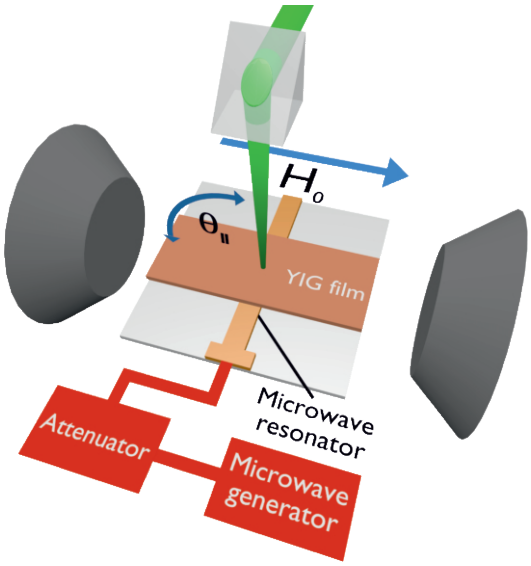

Fig. 1: Sketch of the experimental setup. The 5.6 µm thick YIG film is placed on top of a 50 µm wide copper microstrip resonator produced on an alumina substrate. The 500 µm thick gadolinium gallium garnet (GGG, $Gd_3Ga_5O_{12}$) substrate isn't shown above the YIG film. The external magnetic field is $H_0 = 1400\,\mathrm{Oe}$. The BLS probing beam is focused on the YIG sample and can be rotated around it up to the maximum angle $\theta_{\parallel} = \pm 90°$.

variable attenuator is implemented in the microwave circuit to allow to reduce the power of the amplified microwave pulse to a lower value $P_{\mathrm{pump}} \leq P_{\mathrm{max}}$. The microwave pulse duration is kept constant at $\tau_{\mathrm{p}} = 2\,\mu\mathrm{s}$ with a repetition rate of $f_{\mathrm{rep}} = 1\,\mathrm{kHz}$ to ensure that microwave heating effects are negligible.

The temporal magnon dynamics were investigated by means of time- and wavevector-resolved pulsed BLS spectroscopy (see Methods 3.1 section of this report) with a time resolution of 1 ns. Both the detection of the magnons and the heating of the YIG film were done by using the probing laser beam with the power of 30 mW. The beam is chopped by an acusto-optic modulator (AOM) to control the heating of the YIG sample. A duration of the laser pulse of $\tau_{\mathrm{L}} = 80\,\mu\mathrm{s}$ is used to heat, while the pulse duration $\tau_{\mathrm{L}} = 6\,\mu\mathrm{s}$ is used to reduce the heating of the sample. The probing laser pulse is synchronized with the microwave pumping and has the same repetition rate f_{rep}. The laser pulses of both durations are switched on before the application of the microwave pulse and are switched off 3 µs after its end. In order to selectively detect the magnons condensed in the lowest energy state of the magnonic system at the non-zero wave vector $q_{\parallel} \approx 4.5\,\mathrm{rad\,\mu m^{-1}}$ ($\mathbf{q}_{\parallel} \parallel \mathbf{H}_0$), the probing laser beam angle $\theta_{\parallel}$ (see Fig. 1) was set to 12 ° and only the signal within a small frequency range of 100 MHz around the bottom of the magnons spectrum $f_{\mathrm{min}} = 4\,\mathrm{GHz}$ was registered.

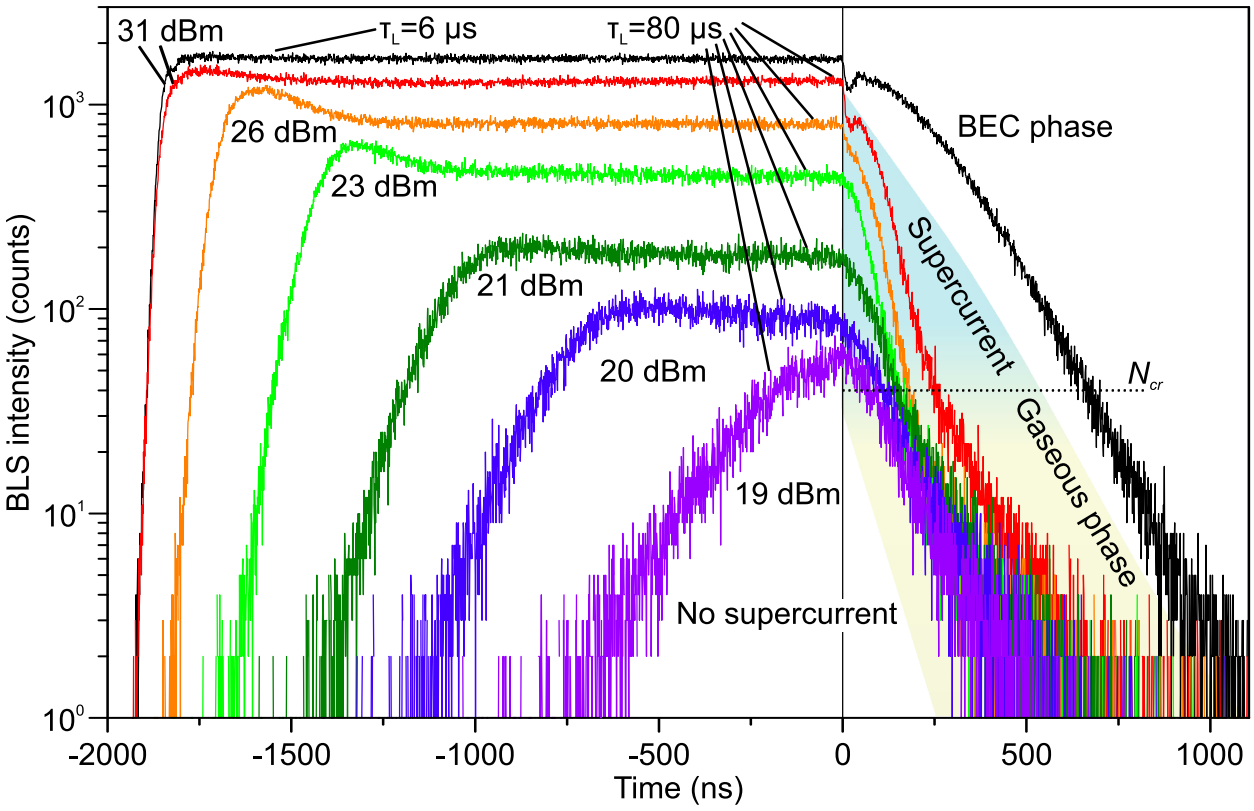

Fig. 2: Measured BLS intensity for different pumping powers P_{pump} and probing laser pulse durations τ_{L} as indicated. The top BLS waveform measured for $\tau_{\mathrm{L}} = 6\,\mu\mathrm{s}$ and $P_{\mathrm{pump}} = 31\,\mathrm{dBm}$ corresponds to the case of the weakly heated YIG sample and, therefore, is not affected by a supercurrent magnon outflow. This also means, that a distinction between the BEC and gaseous phases isn't possible. In all other cases the non-uniform heating of the YIG sample ($\tau_{\mathrm{L}} = 80\,\mu\mathrm{s}$) creates a magnon supercurrent and, therefore, a higher decay rate of the magnons in the BEC phase is observed. This effective decay rate falls with the pumping power. Below a critical magnon density N_{cr}, which characterizes the transition from the coherent BEC phase to the incoherent gaseous magnon phase, the decay rate is the same for all cases.

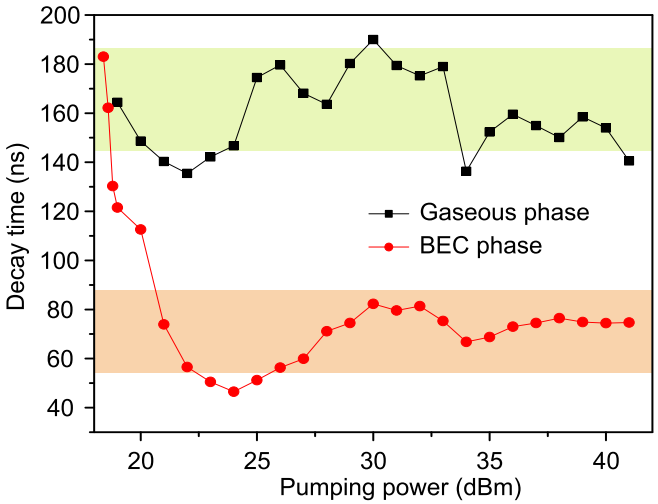

Fig. 3: The decay time τ_{dec} during the BEC phase and gaseous phase plotted over the pumping power P_{pump}. If a supercurrent occurs due to a thermal gradient during the BEC phase (circles), one can observe a fall in the decay time with rising pumping power. The decay time of the gaseous phase (squares) shows no such tendency. In contrary, it remains in the same range for all different pumping powers.

Figure 2 exemplarily presents the measured BLS intensity as a function of time for selected pumping powers P_{pump} and two probing laser pulse durations τ_L. The pumping pulse acts during the time interval from $-2000\,\text{ns}$ to $0\,\text{ns}$. It is clearly visible that a decrease in the pumping power from $P_{pump} = 31\,\text{dBm}$ to $P_{pump} = 19\,\text{dBm}$ and a consequent reduction in the number of parametric magnons, which are injected at half of the pumping frequency, leads to a reduction of magnon-magnon scattering processes and, thus, to the increasing delay in the appearance of these magnons in the spectral energy minimum. The densities of the bottom magnons, which are proportional to the intensity of the measured BLS signal, are reduced as well.

After the pumping pulse is switched off (after $0\,\text{ns}$) the magnons condense in the energetic minimum of the spectrum. In case of strong heating ($\tau_L = 80\,\mu\text{s}$), this process results in the appearance of a magnon supercurrent, which only involves the condensed and therefore coherent magnons. This outflow of magnons (shaded area in Fig. 2 named supercurrent) results in a higher decay rate of the magnon gas in the laser focal point. As one can see, this effective decay rate, which is influenced by the inherent damping of both coherent and incoherent magnons to the phonon bath and by the supercurrent-related leakage of the magnon BEC, is strongly depending on the pumping power. This originates from the fact, that a lower pumping power leads to a reduced density of the magnon gas and therefore to a smaller condensed fraction. Below a certain threshold density N_{cr} (shaded area in Fig. 2 named gaseous phase), when the majority of condensed magnons are flown out of the measured region of the BEC, the observed decay rate approaches the same value for all different pumping powers. This is due to the fact that we are now only measuring the inherent decay rate of an overpopulated incoherent magnon gas.

It is worth to note that the same dynamics of the magnon BEC and the incoherent magnon phase has been reported in Ref. [4], there it was interpreted as a result of the sensitivity of the BLS technique to the coherence degree of the scattering magnons. However, such an interpretation contradicts with our measurements performed at shorter heating times $\tau_L = 6\,\mu\text{s}$. For example, the black top waveform in Fig. 2 shows the dynamics of a well formed magnon BEC ($P_{pump} = 31\,\text{dBm}$) in the situation when heating of the YIG sample can be neglected ($\tau_L = 6\,\mu\text{s}$). It is not possible to distinguish between the BEC and the gaseous phases via the decay rate measurements in this case.

In Fig. 3 we present the inverse decay rates (decay times τ_{dec}) measured as functions of the pumping power. These values are obtained by fitting exponential decays to the measurement data above and below N_{cr}. A fit to the first region (above N_{cr}) for the measurements with $\tau_L = 80\,\mu\text{s}$ provides the decay times for the BEC phase where a supercurrent is observable (circles). The earlier

described rise of the effective decay rate with increasing pumping power is therefore represented by a fall of the decay times τ_{dec}. A fit to the second region (below N_{cr}) provides the decay time for the gaseous phase, when the magnon population is below the threshold for the BEC formation (squares). Note that a simple exponential fit to the first region doesn't describe the physical behavior correctly and is only made to quantify the observed dynamics of the magnon population in the focal laser point.

Looking now at Fig. 3 one can see, as mentioned before, that in the presence of a thermal gradient the rising pumping power and the associated rise in the magnon density is clearly connected to a fall in the effective decay time of the partly coherent magnon gas, whereas the decay time for the gaseous phase remains unaffected in a certain range of experimental error. The decay times for the BEC and the gaseous phase coincide at around $\tau_{dec} = 160\,\text{ns}$, which corresponds in our case to a pumping power of $P_{pump} = 19\,\text{dBm}$. From this point we conclude, that the threshold for the formation of a magnon BEC is reached and, thus, no supercurrent can exist. We are therefore able to control the flow of magnons out of the heated area by varying the magnon density in the system.

In conclusion, we have presented experimental studies on the quantum dynamics of magnon gases and the temporal development of magnon condensates. We have shown the influence of the magnon density on the occurrence of a magnon supercurrent by lowering the pumping power which drives the magnons into the system. By using a smaller pumping field the magnon density can be reduced to a point, where it arrives below the threshold value for the formation of a BEC and the magnon supercurrents vanishes. The results shown here provide evidence for the previously proposed concept of a thermally driven magnon supercurrent and propose the method to control the supercurrent by the magnon population.

Financial support from the European Research Council (ERC) within the ERC Advanced Grant "Supercurrents of Magnon Condensates for Advanced Magnonics" is gratefully acknowledged.

References

[1] D.A. Bozhko, A.A. Serga, P. Clausen, V.I. Vasyuchka, F. Heussner, G.A. Melkov, A. Pomyalov, V.S. L'vov, B. Hillebrands, *Supercurrent in a room-temperature Bose-Einstein magnon condensate*, Nat. Phys. **12**, 1057 (2016).

[2] A.A. Serga, V.S. Tiberkevich, C.W. Sandweg, V.I. Vasyuchka, D.A. Bozhko, A.V. Chumak, T. Neumann, B. Obry, G.A. Melkov, A.N. Slavin, B. Hillebrands, *Bose-Einstein condensation in an ultra-hot gas of pumped magnons*, Nat. Commun. **5**, 3452 (2014).

[3] A.G. Gurevich, G.A. Melkov, *Magnetization oscillations and waves*, CRC press, New York (1996).

[4] V.E. Demidov, O. Dzyapko, S.O. Demokritov, G.A. Melkov, A.N. Slavin, *Observation of spontaneous coherence in Bose-Einstein condensate of magnons*, Phys. Rev. Lett. **100**, 47205 (2008).

4.5 Wavelength-dependent transformation of dipole-exchange magnon modes in obliquely magnetized YIG films

D.A. Bozhko, H.Yu. Musiienko-Shmarova, B. Hillebrands, and A.A. Serga

In collaboration with V.S. Tiberkevich, A.N. Slavin*, and I.I. Syvorotka*[†]

**Department of Physics, Oakland University, Rochester, Michigan 48309, USA*
[†]*Department of Crystal Physics and Technology, Scientific Research Company Carat, 79031 Lviv, Ukraine*

We report on results of experimental and theoretical investigation of dipole-exchange magnon spectra and mode profiles in an obliquely magnetized thin YIG film. We succeeded to directly observe the energy-momentum spectra of low-energy dipole-exchange magnons and transversal phonons in a wide range of wavenumbers from close to zero to $2 \cdot 10^5\,\mathrm{rad\,cm^{-1}}$. Analysis of the obtained data revealed an effect of wavelength-dependent mode transformation: the mode profiles over the thickness of the film drastically change as a function of the in-plane magnon wavenumber. This phenomenon has a strong influence on the visibility of these magnon modes in our Brillouin light scattering experiments owing to the sensitivity of the detection method to the degree of uniformity i.e. the integrated oscillating dipolar magnetic moment of the mode profiles. In the case of an in-plane magnetized film, the thickness profiles of the magnon modes are usual standing waves formed by two partial waves having contradirectional wave vectors along the film thickness. In contrast, in the case of an oblique (out of plane) magnetization the thickness profiles turn out to be those of *quasi-traveling* waves, which, similarly to the standing waves, do not transfer energy, but create a flow of spin angular momentum (or spin current) along the film thickness.

The thermal spectra of magnons and phonons were studied at room temperature in yttrium iron garnet (YIG, $Y_3Fe_5O_{12}$) film by means of frequency- and wavevector-resolved Brillouin light scattering (BLS) spectroscopy (see Methods 3.1 section of this report). The YIG film of $L = 5.6\,\mu\mathrm{m}$ thickness was grown in the (111) crystallographic plane on a gadolinium gallium garnet (GGG) substrate by liquid-phase epitaxy. The bias magnetic field H is set to 250 mT, which is sufficient for complete out-of-plane magnetization of the YIG film with the saturation magnetization $4\pi M_S = 1750\,\mathrm{G}$. By change the external magnetization angle Θ_H between the magnetic field H and the film plane the internal magnetization angle Θ_M between the film plane and the direction of magnetization $\mathbf{M}_S$ can be set to the values from 0° (in-plane magnetization) to 90° (out-of-plane magnetization).

The measured dipole-exchange magnon dispersions are presented in Figure 1. The first column (Figs. 1a, d, g, j) presents the experimentally measured dependence of the BLS signal intensity maps of the room-temperature population of magnon and phonon spectra as a function of Θ_H. For the in-plane magnetization ($\Theta_H = \Theta_M = 0^\circ$, Fig. 1a), the observed spin-wave spectrum represents the well-known dispersion curve of the fundamental dipole-exchange backward volume mode ($\mathbf{q} \parallel \mathbf{M}_S$). The steep linear branches correspond to the transversal acoustic phonons.

A change of the magnetization angle leads to the modification of the spin-wave dispersion (see Figs 1d, g and j). Note, that with increase in the external magnetization angle Θ_H the magnitude of the internal biasing field, as well as its direction, change because of the demagnetization field created by $\mu_0 M_S$. The internal angle of magnetization Θ_M and the value of the internal magnetic

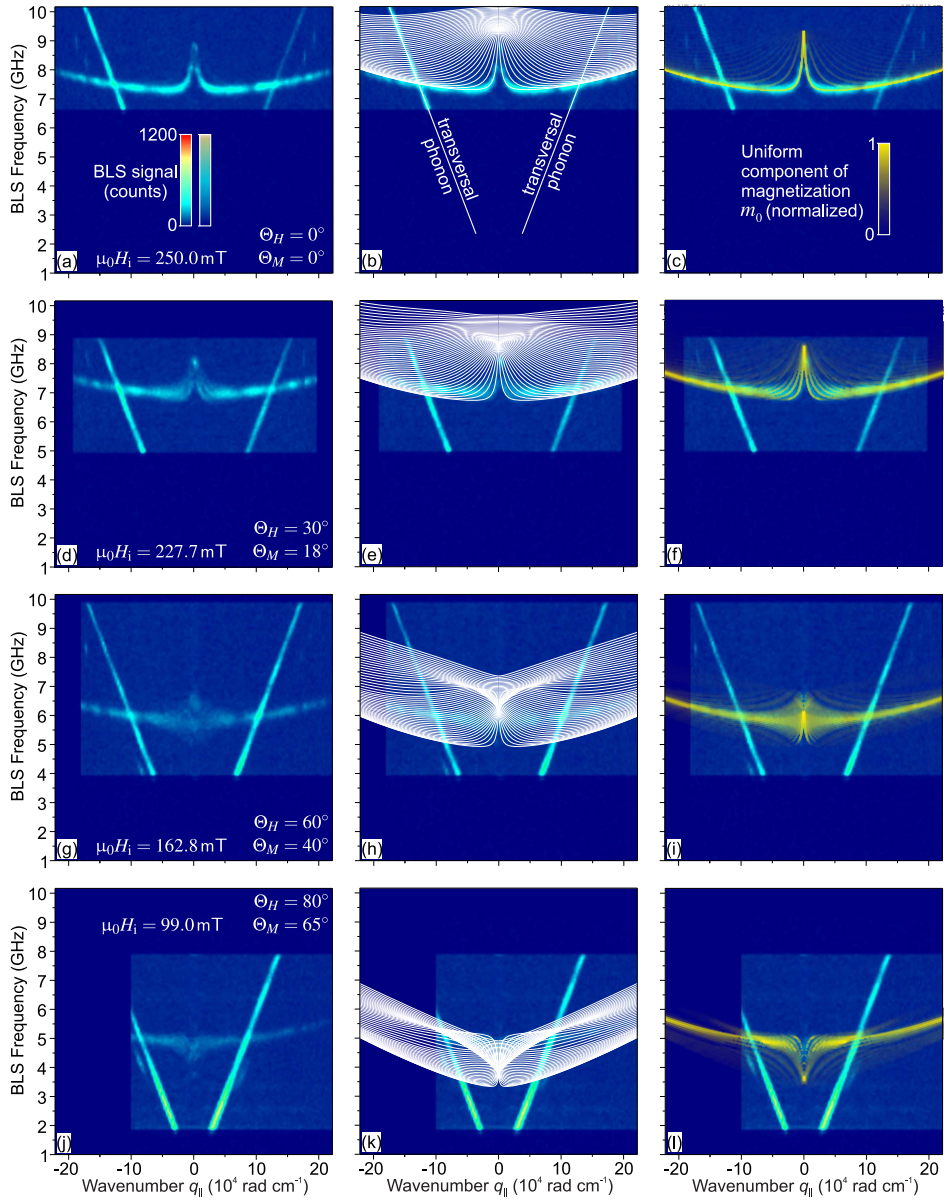

Fig. 1: Thermal spectra of spin waves in a 5.6 μm thick YIG sample measured using the wavevector-resolved BLS setup at different magnetization angles Θ_M. Only the Stokes component of the spectrum is shown. (a-c) $\Theta_H = 0°$; (d-f) $\Theta_H = 30°$; (g-i) $\Theta_H = 60°$; (j-l) $\Theta_H = 80°$. In the first column raw measured spectra are presented. In the second column the same data are presented in comparison with theoretically calculated dispersion branches shown by thin white curves. In the third column, the intensity plots representing the calculated uniformity of thickness profiles of magnon modes are shown in comparison with the corresponding experimental data.

field H_i can be found by solving the static case ($\partial M/\partial t = 0$) of the Landau-Lifshitz equation [1]. The corresponding values are indicated in Figs. 1a, d, j and i.

For $\Theta_H = 30°$ shown in Fig. 1d one can see that the magnon branch splits into several plexiform curves in the dipolar area ($|q_\parallel| < 10^4\,\mathrm{rad\,cm^{-1}}$). With further increase of Θ_H the splitting increases and simultaneously it becomes harder to distinguish between the different curves. Furthermore, the spin-wave spectrum in the dipolar region drastically reshapes: it contains branches with negative and positive dispersions, which could be associated with backward and forward spin waves.

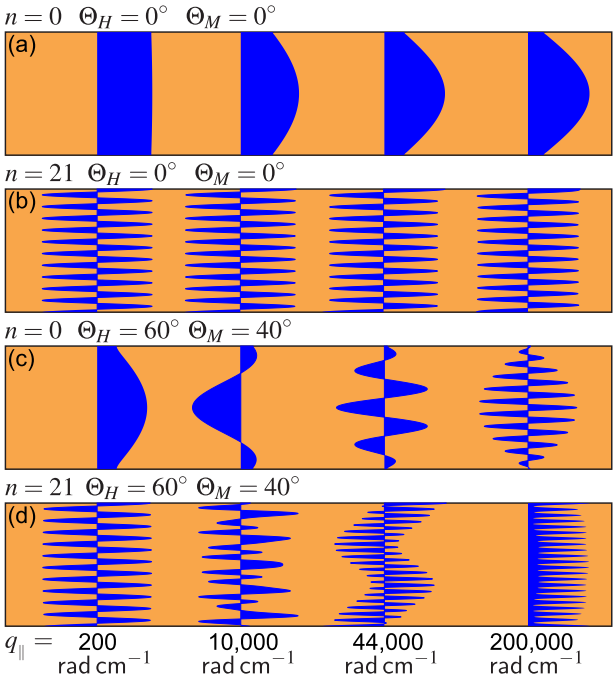

Fig. 2: Wavevector-dependent calculated spin-wave mode profiles of the 5.6 μm thick YIG film magnetized to saturation by the external field of 250 mT for different magnetization angles Θ_M: (a) In-plane magnetization $\Theta_H = 0^\circ$, fundamental mode; (b) $\Theta_H = 0^\circ$, 21st mode; (c) $\Theta_H = 60^\circ$, fundamental mode; (d) $\Theta_H = 60^\circ$, 21st mode.

However, for all Θ_H in Fig. 1 the fuzzy dipolar branches merge into a single exchange branch for the high wavenumber region ($q_\parallel > 10^4$ rad cm^{-1}). Finally, at $\Theta_H = 80^\circ$ the smearing of the dipolar magnon branches starts to vanish, and the magnon spectrum looks similar to the forward volume waves [2]. Unfortunately, the Brillouin light scattering cross section becomes smaller with increase in the magnetization angle and approaches zero when the magnetization is oriented perpendicularly to the film plane [3]. Thus, the intensity of the inelastically scattered light becomes smaller and for $\Theta_M = 90^\circ$ completely vanishes, making the BLS measurements of magnon spectrum impossible.

In Figs. 1b, e, h, and k the obtained experimental data are compared with theoretical magnon spectra, calculated using the approach developed in Ref. [4]. One can see very good agreement of the calculations and the experimental data for the fundamental spin wave mode in the case of in-plane magnetization (see Fig 1b). As it is expected, the higher thickness modes are not visible in the experiment: The BLS cross section is proportional to the total average oscillating part of the magnetic moment of a spin wave, thus modes with non-uniform distributions along the film thickness do not contribute to the BLS signal. However, at magnetization angles $\Theta_M > 0^\circ$ not all the modes (including the fundamental one) fit the experiment. Moreover, with increase of Θ_M the fundamental mode vanishes at large wavenumbers. Such a mismatch between the experimental and theoretical data suggests to us that the BLS visibility of magnon spectra can be influenced by a strong transformation of thickness mode profiles in obliquely magnetized magnetic films.

In order to understand the behavior of the mode profiles in the case of oblique magnetization, we calculated them as a function of in-plane wavenumber. These profiles are shown in Fig. 2. As in the experiment, we begin from the in-plane magnetization configuration and evaluate the mode profiles for the fundamental $n = 0$ and for the higher thickness mode $n = 21$. As one can see in Fig. 2a, the fundamental mode possesses a practically uniform distribution at relatively small wavenumbers, and thus it is perfectly visible in the experiment. With decrease in the in-plane magnon wavelength the effective dipolar pinning, which appears at the film's surfaces, transforms the mode profile to a sine-like form, and thus slightly decrease its BLS visibility at large wavenumbers. Such a pinning can be understood as follows: with increase in magnon wavenumber the stray fields induced by precessing magnetic moments act to an increasing degree against their nearest neighbors, which,

in fact, is not an energetically favorable situation. Thus, the amplitude of precession decreases near the sample surfaces. The profile of the higher order mode ($n = 21$) is completely non-uniform in the entire range of in-plane wavenumbers and cannot be detected in our experiment.

The situation largely changes in the case of oblique magnetization. The case of $\Theta_H = 60°$, is exemplarily presented in Fig. 2c-d. Similar to the in-plane magnetization case, at small wavenumber $q_{\parallel} = 200\,\mathrm{rad\,cm^{-1}}$ the fundamental mode possesses uniform distribution. As a result, it is clearly visible in the experiment. However, for larger magnon wavenumbers, the mode profile acquires more and more variations across the thickness of the film. This effect perfectly correlates with the decrease in visibility of this mode in our experiment. The opposite situation occurs for the mode with $n = 21$ (see Figure 2d). The initially non-uniform distribution of dynamic magnetization at $q_{\parallel} = 200\,\mathrm{rad\,cm^{-1}}$ surprisingly transforms into a quasi-uniform distribution at $q_{\parallel} = 200,000\,\mathrm{rad\,cm^{-1}}$.

Such a behavior can be understood as follows. In a first approximation, a mode profile across the thickness of a magnetic film can be imagined as a standing wave, formed by two partial waves having the same frequency and propagating transversally to the film surfaces. In the case of in-plane magnetization, these partial waves have equal absolute value, but are contrapropagating (see Fig. 2a and b). In the case of oblique magnetization, the wavenumbers of these partial waves are different. In the latter case, the corresponding mode profile has a form of a beating pattern between two co-propagating waves. If one of these partial waves will have zero transversal wavenumber, a mode profile will acquire an uniform component (see Figure 2d for $q_{\parallel} = 200,000\,\mathrm{rad\,cm^{-1}}$).

A Fourier expansion of the calculated mode profiles provides the possibility to extract their uniform component m_0 and to predict the visibility of the spectrum in a BLS experiment. In the third column in Fig. 1c, f, i, l the calculated spectra are plotted taking into account the amplitude of the uniform component m_0 of the mode magnetization distribution across the film thickness: The visibility of the calculated dispersion curves is a function of normalized m_0. As one can see, the calculated spectrum in this case perfectly fits the experiment for all magnetization angles.

In conclusion, using our novel wavevector resolved BLS setup, we measured the energy-momentum spectra of low-energy dipole-exchange magnons and transversal phonons in a wide range of wavenumbers. By taking into account the calculated spin-wave mode thickness profiles we can perfectly fit the experimentally observed dispersion relations. We showed that the mode profiles in the case of oblique magnetization are not forming a standing wave pattern and, thus, intrinsically transfer angular momentum across the thickness of the film.

Support by the Deutsche Forschungsgemeinschaft within the SFB/TR 49 as well as financial support by the European Research Council (ERC) within the ERC Advanced Grant "Supercurrents of Magnon Condensates for Advanced Magnonics" is gratefully acknowledged.

References

[1] A.G. Gurevich, G.A. Melkov, *Magnetization Oscillations and Waves* (CRC Press, 1996).
[2] D.D. Stancil, A. Prabhakar, *Spin Waves, Theory and Applications*, Springer (2009).
[3] B. Hillebrands, *Brillouin light scattering from layered magnetic structure*, in *Light Scattering In Solids VII*, Ed. by M. Cardona and G. Güntherodt, Springer-Verlag Berlin Heidelberg (2000).
[4] B.A. Kalinikos, A.N. Slavin, *Theory of dipole-exchange spin wave spectrum for ferromagnetic films with mixed exchange boundary conditions*, J. Phys. C **19**, 7013 (1986).

4.6 Temperature dependent relaxation of dipole-exchange magnons in YIG film

L. Mihalceanu, V.I. Vasyuchka, D.A. Bozhko, T. Langner, B. Hillebrands, and A.A. Serga

In collaboration with O.Yu. Nechiporuk (a.k.a. A.Yu. Nechiporuk) and V.F. Romanyuk from the Faculty of Radiophysics, Electronics and Computer Systems, Taras Shevchenko National University of Kyiv, 01601 Kyiv, Ukraine

Low energy consumption due to chargeless information transport, which is free from ohmic heating, and the ability to process phase-encoded data by nanometer-sized interference devices at GHz and THz frequencies are just a few benefits of spin-wave-based technologies. Simultaneously, novel magnetic phenomena – and as, e.g., room-temperature Bose-Einstein magnon condensates, magnon vortices and supercurrents – open a whole new range of research areas both for basic and applied spin physics. Furthermore, when approaching cryogenic temperatures, quantum phenomena occur paving the path towards quantum information processing. All of this in connection with arising demands on miniaturization of magnonic devices motivates our studies of the damping behavior in YIG films towards cryogenic temperatures in a wide range of spin-wave wavelengths.

Parametric pumping technique allows for the efficient excitation and probing of dipolar-exchange magnons with wavenumbers up to $q \leq 10^6\,\mathrm{rad\,cm^{-1}}$ [1]. Using this method we investigated temperature dependent relaxation of parametrically excited magnons in an in-plane magnetized 53 µm YIG film epitaxially grown on a GGG substrate. Afterwards, the GGG substrate was polished away down to a 30 µm YIG thickness in order to reveal a possible contribution of the interaction between the ferrimagnetic YIG and paramagnetic GGG spin systems to the magnon damping.

Figure 1a shows the experimental microwave setup allocated inside of a closed cycle refrigerator system. The microwave Oersted field $\mathbf{h}_\mathrm{p}$ induced by a 50 µm-wide microstrip resonator at the pumping frequency $\omega_\mathrm{p} = 2\pi \cdot 14\,\mathrm{GHz}$ drives the spin system of the YIG film. When the certain threshold field condition $h_\mathrm{p} = h_\mathrm{thr}$ is fulfilled, the action of the pumping compensates the spin-wave damping and gives rise to the parametric instability process, where a selected magnon mode, which has the lowest damping and the strongest coupling to the pumping, grows exponentially in time. The arising mode increasingly absorbs the microwave energy and, thus, changes the level of the microwave signal reflected from the resonator. As a result, a kink appearing at the end of the reflected pump pulse indicates the threshold power $P_\mathrm{p} = P_\mathrm{thr}$ required for the parametric excitation process. P_thr can be determined for magnon modes over the wide q-spectral range by changing the bias magnetic field H. This change leads to a vertical shift of the dispersion curve (Fig. 1b) along frequency axis and results in the characteristic threshold curve shown in Fig. 1c. At the critical field H_c spin waves with $q \to 0$ are excited near the frequency of the ferromagnetic resonance ω_FMR (minima of the threshold curves $P_\mathrm{thr}(H)$ in Fig. 1c). The threshold power at $H \leq H_\mathrm{c}$ is dominated by parametric excitation of the lowest thickness mode belonging to the transversal magnon dispersion branch as it is shown in Fig. 1b. Above H_c magnons propagating at angles $\theta_q < 90^\circ$ relative to the field $\mathbf{H}$ are excited. These magnons escape the narrow pumping area above the microstripe resonator (Fig. 1a) and the related energy leakage results in the sharp increase in the threshold power just above H_c [2].

For determining the magnon relaxation behavior the pumping regime $H \leq H_\mathrm{c}$ is of main interest in this Report as the wavenumbers of the parametrically excited magnons can be unambiguously calculated in this case. Figure 1c presents the dependencies $P_\mathrm{thr}(H)$ for the 53 µm thick film for

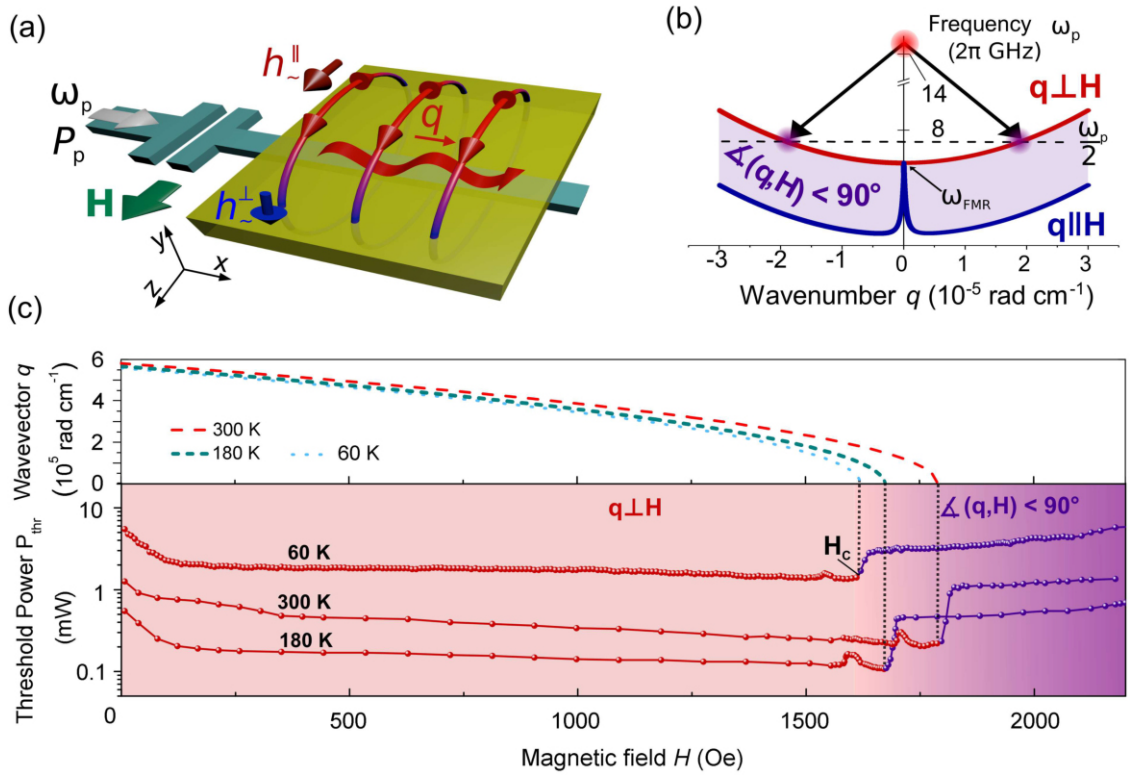

Fig. 1: (a) Experimental setup. (b) Scheme of the parametric pumping process. (c) Wavenumber (top) and threshold curves (bottom) examplified for a 53 µm thick YIG film on GGG at 60 K, 180 K and 300 K.

three different temperatures. $P_{\mathrm{thr}}(H_{\mathrm{c}})$ is minimal at 180 K, while the experimentally determined H_{c} value monotonically decreases towards lower temperatures. This decrease relates to an upward frequency shift of the magnon spectrum caused by a temperature dependent increase in the saturation magnetization $4\pi M_{\mathrm{s}}$ as well as by changes of the cubic $H_{\mathrm{a}}^{\mathrm{c}}$ and uniaxial $H_{\mathrm{a}}^{\mathrm{u}}$ anisotropy fields of the YIG film, which can be accounted for the perpendicular magnon branch as $4\pi M_{\mathrm{s}} - H_{\mathrm{a}}^{\mathrm{c}} - H_{\mathrm{a}}^{\mathrm{u}}$. The calculated dependencies of magnon wavenumbers $q = q(H)$ for different temperatures are shown in Fig. 1c. The vertical dashed lines correlate the threshold curves with the corresponding wavenumber at H_{c}. As is shown, in our experiment spin waves are probed in the wavenumber range from zero to $5 \cdot 10^5\,\mathrm{rad\,cm^{-1}}$.

The variation of $4\pi M_{\mathrm{s}}$ directly affects the coupling between the microwave pumping field $\mathbf{h}_{\mathrm{p}}$ and the longitudinal component $\mathbf{m}_z$ of the precessing magnetic moment $\mathbf{M}$. As a result, the threshold field h_{thr} is influenced by two temperature dependent physical quantities: the spin-wave relaxation rate and the parametric coupling strength. These influences can be estimated from Ref. [1] as

$$h_{\mathrm{thr}} = \min\left\{ \left(\omega_{\mathrm{p}} \Delta H_q\right) / \left(\gamma 4\pi M_{\mathrm{s}} \sin^2 \theta_q\right) \right\}, \tag{1}$$

with the gyromagnetic ratio $\gamma = 2.8\,\mathrm{MHz/Oe}$. For the parametric excitation near and above the FMR frequency the angle $\theta_q = 90°$. ΔH_q is the linewidth of the parametrically excited magnon mode with the wavenumber q. It is defined as $\Delta H_q = \Gamma_q/\gamma$, where Γ_q is the spin-wave relaxation rate. The saturation magnetization $4\pi M_{\mathrm{s}}$ for bulk YIG crystals demonstrates a rather non-linear change with temperature [7], which can be calculated by the two-sublattice model [5] as illustrated by the solid line in Fig. 3a. By turn, the temperature behavior of the cubic anisotropy field can be

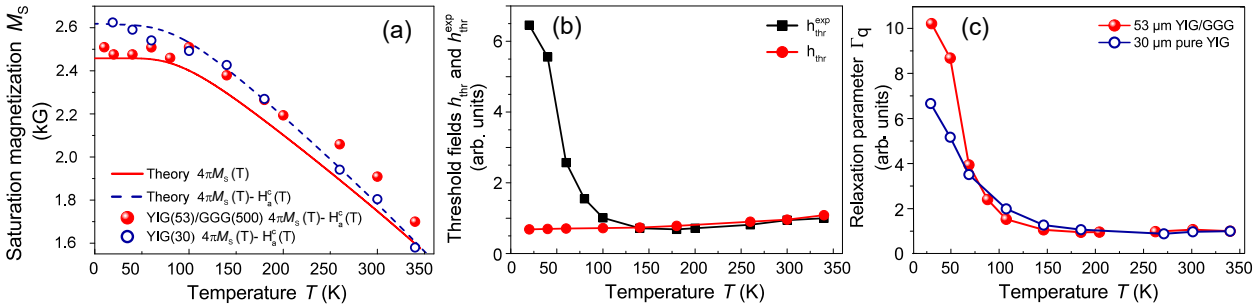

Fig. 2: (a) The saturation magnetization $4\pi M_s$ vs. temperature (experiment and theoretical calculation). (b) Threshold pumping field against temperature: Squares – h_{thr}^{exp} determined by the measured threshold powers P_{thr}. Circles – h_{thr} calculated over Eq. 1 for the 53 μm thick sample. (d) Relaxation parameter of 53 μm thick YIG on GGG compared to 30 μm thick pure YIG after polishing off GGG.

approximated [4] as

$$H_a^c = H_a^c(0) + \alpha T^{\frac{3}{2}}, \tag{2}$$

with $H_a^c(0) = -147\,\mathrm{Oe}$ and $\alpha = 2.175 \cdot 10^{-2}\,\mathrm{Oe\,K^{-1.5}}$.

However, due to the unknown contribution of the uniaxial anisotropy H_a^u [3], which is caused by a temperature dependent mismatch between the YIG and GGG crystal lattices, the calculated temperature dependencies for both $4\pi M_s$ and for $4\pi M_s - H_a^c$ (dashed line in Fig. 3a) significantly diverge from the experimentally determined difference $4\pi M_s - H_a^c - H_a^u$ shown by solid circles in Fig. 3a. At the same time, the substrate-free YIG sample of 30 μm thickness demonstrates a good agreement between experimentally measured (open circles) and theoretically calculated values of $4\pi M_s - H_a^c$ (dashed line in Fig. 3a). This agreement evidences the applicability of the bulk two-sublattice model [5] for our YIG films and allows us to use the theoretical magnetization values for the calculation of the temperature dependent parametric coupling strength. By assuming initially the value of ΔH_q in Eq. 1 to be constant over the entire temperature range and taking into account the theoretical values of $4\pi M_s(T)$ we calculated the normalized (with respect to 340 K) temperature dependence of the threshold field, which is solely determined by the change in the parametric coupling strength. This dependence is shown by the circles in Fig. 3b.

The experimental threshold field h_{thr}^{exp} can be calculated from the measured threshold powers using the relation $h_{thr}^{exp} = C\sqrt{P_{thr}}$. The parameter C depends on the pumping frequency ω_p, the geometry and the quality factor of the pumping resonator. As the resonance frequency and the quality factor of our microstrip resonator do almost not change with temperature we assume C to be constant.

The experimental values of the dimensionless threshold field normalized to the reference value at the temperature of 340 K are plotted in Fig. 3b (squares) for magnons excited near the FMR frequency ($H = H_c$). Its behavior is visibly non-monotonic: down to 180 K the threshold field h_{thr}^{exp} slightly decreases, while below 180 K it increases up to 5 times compared to the reference value.

The comparison of the calculated ($h_{thr}(T)$, circles) and experimental ($h_{thr}^{exp}(T)$, squares) threshold dependencies clearly evidences that at high temperatures ($T \geq 180$ K) the experimental dependencies are mostly determined by the variation in the parametric coupling strength, while the increase of h_{thr}^{exp} in the low-temperature range ($T < 180$ K) is caused by the spin-wave relaxation.

Figure 3c shows the normalized relaxation rate Γ_q calculated at H_c with help of Eq. 1 using $h_{thr}^{exp}(T)$ and theoretically calculated $4\pi M_s(T)$. For the temperature decrease from 180 K to 20 K the relaxation rate Γ_q increases up to about 9.5 times for the 53 μm thick YIG film and 6.5 for the 30 μm pure

YIG. The same relaxation behavior is observed over the whole range of probed magnon wavenumbers up to $5 \cdot 10^5\,\mathrm{rad\,cm^{-1}}$. The strong increase of Γ_q is considered to be atypical for *pure* YIG, for which a monotonic decrease of Γ_q is expected with decreasing temperature [6].

The relaxation behavior at low temperatures can be related either to the contribution of fast-relaxing rare-earth ions contaminating the chemical composition of YIG or to the magnetic losses caused by the dipolar coupling of magnons with the spin-system of the paramagnetic GGG substrate [8]. The comparison of the relaxation rate for the 53 µm thick YIG sample to the 30 µm substrate-free YIG film after polishing the GGG side down is shown in Fig. 3c. Both samples demonstrate a strong increase in Γ_q for decreasing temperatures, starting from $\sim$150 K. This fortifies the assumption of the prevailing contribution of fast-relaxing rare-earth ion impurities in epitaxial YIG films at low temperatures [7]. Below $\sim$80 K the relaxation rate of the substrate-free YIG sample increases slowly in comparison with the one of the YIG/GGG sample. This difference can be attributed to coupling of YIG's ferrimagnetic spin system with the electron spins of Gd^{3+} ions of paramagnetic GGG. The coupling is supposed to be proportional to $1/T$ [8] and leads to additional low-temperature energy losses for YIG on GGG.

Our results show that both, the fast-relaxing rare-earth ions in YIG and the magnetic losses caused by the dipolar coupling with the spin-system of the GGG substrate lead to a strong growing of the relaxation rate at low temperatures. We conclude that in order to sustain a long magnon lifetime low-temperature magnetic experiments in YIG must be performed in chemically-pure and substrate-free samples.

Financial support from the Deutsche Forschungsgemeinschaft (project INST 161/544-3 within SFB/TR 49, projects VA 735/1-2 and SE 1771/4-2 within SPP 1538 "Spin Caloric Transport", and project INST 248/178-1) is gratefully acknowledged.

References

[1] A.G. Gurevich, A.N. Anisimov, *Intrinsic spin wave relaxation processes in yttrium iron garnets*, Sov. Phys. JETP **41**, 336 (1975).
[2] T. Neumann, A.A. Serga, V.I. Vasyuchka, B. Hillebrands, *Field-induced transition from parallel to perpendicular parametric pumping for a microstrip transducer*, Appl. Phys. Lett. **94**, 192502 (2009).
[3] M. Kaack, S. Jun, S.A. Nikitov, J. Pelzl, *Magnetostatic spin wave modes excitation in yttrium-iron-garnet film under various temperatures*, J. Magn. Magn. Mater. **204**, 90 (1999).
[4] V.V. Danilov, D.L. Lyfar', Yu.V. Lyubon'ko, A.Yu. Nechiporuk, and S.M. Ryabchenko *Low-temperature ferromagnetic resonance in epitaxial garnet films on paramagnetic substrates*, Sov. Phys. J. **32**, 276 (1989).
[5] P. Hansen, P. Röschmann, W. Tolksdorf, *Saturation magnetization of gallium-substituted yttrium iron garnet*, J. Appl. Phys. **45**, 2728 (1974).
[6] M. Sparks, *Theory of three-magnon ferromagnetic relaxation frequency for low temperatures and small wave vectors*, Phys. Rev. **160**, 2 (1967).
[7] L. Mihalceanu, V.I. Vasyuchka, D.A. Bozhko, T. Langner, A.Yu. Nechiporuk, B. Hillebrands, A.A. Serga, *Temperature dependent relaxation of dipole-exchange magnons in yttrium iron garnet films*, arXiv:1711.07517, (2017).
[8] M.G. Balinskii, V.V. Danilov, A.Yu. Nechiporuk, V.M. Talalaevskii, *Damping of magnetostatic spinwaves in substrates*, Radiofizika **29**, 1253 (1986).

B. Nano- and Micro-Magnonics

Spin waves and their quanta, magnons, typically feature frequencies in the GHz to THz range and wavelengths in the micrometer to nanometer range. They are envisioned for the design of faster and smaller next generational information processing devices where information is carried by magnons instead of electrons. The field of science that refers to information transport and processing by spin waves is known as magnonics. A set of recent groundbreaking physical discoveries and the revolutionary progress in the fabrication of magnetic micro- and nano-structures opened a way to the practical development of magnonic data processing systems. In this Section we present a set of reports that are mainly devoted to the question of guiding of information in form of spin waves. For example, we will answer the questions which physical phenomena should be taken into account while decreasing the sizes of spin-wave waveguides from microns to nanometers and how to guide information in two dimensions without any structuring using spin-wave caustics or thermal gradients, how to ensure robust reflection-less spin-wave propagation. In addition, we study spin-wave dispersions in magnetic bi-layers, and, finally, we demonstrate how to realize a frequency-division multiplexing operation based on the investigated phenomena.

The first report (report 4.7) is devoted to the investigations of the spin-pinning conditions in nano-scale Yttrium Iron Garnet (YIG) waveguides. The recent advances in the growth of high-quality films of the ferrimagnetic insulator YIG with thicknesses in the range of tens of nanometers have boosted research on spin waves greatly. The creation of micro- and even nanostructures from this material which is the workhorse of 'conventional' research on spin waves due to its record low damping allows for the realization of prototype spin-wave devices on microscopic scales. As the lateral sizes of an investigated spin-wave waveguide get closer to the exchange length, the influence of exchange on the profile of the waveguide modes, i.e., the laterally quantized waves propagating along the waveguide, can no longer be neglected. In particular, for waveguides with a width comparable to their thickness, where also the demagnetization tensor of the waveguide differs drastically from a thin film, large differences for the mode profiles are expected. In this report, we analyze the change of the mode profile in such nanometric waveguides by means of micromagnetic simulations. It is shown that the pinning changes from pinned states in micron wide waveguides to fully unpinned states in nano-scale wide waveguides.

Since the discovery of surface spin waves by Damon and Eshbach there is a large interest in coupling of such modes in a bilayer system consisting of two different ferromagnetic layers with different magnetization and exchange constants. Report 4.8 is devoted to the investigation of the spin-wave dispersion in nickel-permalloy bilayers. This material system is a possible candidate for the realization of magneto-elastic spin-wave devices since permalloy provides good properties for the propagation of spin waves and the magnetization of nickel can be manipulated with mechanical stress due to it magnetostrictive property. The dispersion relation of a Ni/Py bilayer system is studied experimentally using Brillouin Light Scattering (BLS) spectroscopy and the experimental findings are explained using micromagnetic simulations. It is shown that this bi-layer system shows a strong frequency shift between counter-propagating spin waves up to several GHz and that a sign change of the frequency shift only occurs when exchange interaction is taken into account.

Spin-wave losses are among the most important parameters that are necessary to be taken into account for designing magnonic conduits and data processing units. Besides the intrinsic losses, the spin waves experience also extrinsic losses which are induced from external effects, e.g. fabrication-induced disorders, film non-uniformities and magnetic inhomogeneities that are unpreventable and finally lead to scattering of the spin-wave energy and low efficiency of the system.

Therefore, pursuing novel ways to prevent (or at least to reduce) the spin-wave backward reflections or their scattering into other spin-wave modes are highly desired. We show in report 4.9 that back-scattering immune spin wave modes exist and that in an in-plane magnetized YIG film with relatively small thickness propagating waves can be robust even against large inhomogeneities and disorders. This is a consequence of the interplay between exchange and dipole interactions in thin magnetic films that leads to a frequency-gap between the fundamental mode and the thickness mode, and creates a one-way traveling route for the excited waves at a given surface.

The following report 4.10 presents space-resolved BLS spectroscopy studies of the excitation and propagation of spin-wave beams in two-dimensional magnetic films. One of the advantages of magnonics with respect to electronics is thea possibility to guide information coded into spin waves in two dimensions without fabrication of magnonic conduits. Spin waves can be guided in the form of spin-wave caustics (discussed in the last report of this section) or in the form of monochromatic spin-wave beams presented in this report. In order to excite the beams a type of antenna recently proposed theoretically by Gruszecki *et al* is used. It was shown that it is possible to restrict the spin-wave excitation to specific areas and, with that, to create propagating spin-wave beams. Lifetimes and propagation lengths of spin waves in these beams are investigated experimentally and theoretically.

The dispersions of dipolar spin waves in in-plane magnetized films are strongly anisotropic. Dipolar spin waves propagating along the static magnetization are known as backward volume magnetostatic spin waves (BVMSWs) and waves propagating perpendicularly are magnetostatic surface spin waves (MSSWs). Hence, a change of the propagation direction with respect to the magnetization requires mode conversion between MSSWs and BVMSWs. This is a challenge since these spin-wave modes exist in different frequency ranges. In report 4.11 we propose and study experimentally the usage of reconfigurable laser-induced magnetization gradients to realize the mode conversion. The changes in the magnetization shift the dispersion relations locally and allow for operating with BVMSW and MSSW spin-wave modes of the same frequency. Spin-wave momentum is first transformed via refraction at the edge of the magnetization gradient region and then continuously modified inside it. An adiabatic continuous transformation of the spin-wave momentum leads to a highly-efficient mode conversion over a wide frequency range.

Finally, in report 4.12 we use micromagnetic simulations to present an approach for the realization of Frequency-Division Multiplexing (FDM) in magnonic networks by utilizing caustic-like spin-wave beams. FDM networks are of interest for application since the signals at different frequencies are used to simultaneously transfer information through the same conduits in separated frequency channels. Caustic beams originate from the anisotropic spin-wave propagation in in-plane magnetized two-dimensional magnetic media and the direction of propagation of the caustic beams strongly depends on spin-wave frequency. This makes the caustics beams an ideal candidate for the realization of FDM networks that is presented and characterized in this report.

B. Nano- und Mikromagnonik

Spinwellen und ihre Quanten, Magnonen, weisen typischerweise Frequenzen im Bereich von GHz bis THz und Wellenlängen im Mikrometer- bis Nanometerbereich auf. Sie werden als interessante Kandidaten für die Realisierung von schnelleren und kleineren Informationsverarbeitungsgeräten der nächsten Generation gehandelt, bei denen Informationen von Magnonen anstatt von Elektronen übertragen werden. Das Gebiet der Wissenschaft, das sich auf den Informationstransport und

deren Verarbeitung durch Spinwellen bezieht, wird als Magnonik bezeichnet. Eine Reihe neuer bahnbrechender physikalischer Entdeckungen und der revolutionäre Fortschritt bei der Herstellung von magnetischen Mikro- und Nanostrukturen hat einen Weg zur praktischen Entwicklung von magnonischen Datenverarbeitungssystemen eröffnet. In diesem Abschnitt stellen wir eine Reihe von Berichten vor, die sich hauptsächlich der Frage der Führung des Informationsflusses in Form von Spinwellen widmen. Zum Beispiel werden wir die Fragen beantworten, welche physikalischen Phänomene berücksichtigt werden sollten, während die Größen von Spinwellen-Wellenleitern von Mikrometern zu Nanometern verringert werden, wie Informationen in zwei Dimensionen ohne jegliche Strukturierung unter Verwendung von Spinwellenkaustiken- oder Wärmegradienten geführt werden können, und wie eine robuste reflexionsfreie Spinwellenausbreitung realisierbar ist. Darüber hinaus untersuchen wir die Spinwellendispersion in magnetischen Bilagen und zeigen schließlich, wie ein spinwellen Frequenzmultiplexverfahren realisiert werden kann.

Der erste Bericht 4.7 ist einer Untersuchung der Spin-Pinning-Bedingungen in nanometrischen Yttrium-Eisen-Granat (YIG) Wellenleitern gewidmet. Die jügsten Verbesserungen des Wachstums qualitativ hochwertiger Schichten des ferrimagnetischen Isolators YIG mit Dicken im Bereich einiger zehn Nanometer haben die Spinwellenforschung sehr vorangebracht. Die Herstellung von Mikro- und Nanostrukturen aus diesem Material, welches auf Grund seiner unerreicht kleinen Spinwellendämpfung das Arbeitspferd der Magnonik darstellt, ermöglicht die Realisierung von Spinwellenbauteilen auf mikrokopischen Skalen. Mit Abnahme der Wellenleiterbreite bis in den Bereich der Austauschlänge kann der Einfluss der Austauschwechselwirkung auf das Profil der Wellenleitermoden, also der sich im Wellenleiter ausbreitenden quantisierten Moden, nicht mehr vernachlässigt werden. Insbesondere für Wellenleiter, deren Breite vergleichbar zu ihrer Dicke ist, in denen sich der Entmagnetisierungstensor also drastisch von einem Dünnfilm unterscheidet, sind große Abweichungen der Profile zu erwarten. In diesem Bericht analysieren wir die Änderung der Modenprofile in nanometrischen Wellenleitern durch den Einsatz mikromagnetischer Simulationen. Es wird gezeigt, dass das Pinning sich vom vollständigen Pinning für Mikrometer-breite Wellenleiter zu ungepinnten Moden in nanometrischen Wellenleitern modifiziert.

Seit der Entdeckung von Oberflächenspinwellen durch Damon und Eshbach gibt es ein großes Interesse an der Kopplung dieser Moden in Bilagen welche aus zwei ferromagnetischen Materialien mit verschiedenen magnetischen Parametern bestehen. Der Bericht 4.8 befasst sich mit einer Untersuchung der Spinwellendispersion in Nickel-Permalloy-Bilagen. Dieses Materialsystem ist ein interessanter Kandidat für die Realisierung magnetoelastischer Spinwellenbauteile, da Permalloy gute Spinwelleneigenschaften aufweist und die Magnetisierung von Nickel auf Grund seiner magnetostriktiven Eigenschaften durch mechanischen Stress manipuliert werden kann. Die Dispersion in den Bilagen wird experimentell mittels der Brillouin-Lichtstreuspektroskopie untersucht und zu ihrem Verständnis werden mikromagnetische Simulationen zu Rate gezogen. Es wird aufgezeigt, dass in solchen Bilagen eine große Frequenzverschiebung von mehreren GHz zwischen den Moden, die in entgegengesetzter Richtung propagieren, auftritt. Ferner wird auf einen Vorzeichenwechsel dieser Frequenzverschiebung als Konsequenz der Austauschwechselwirkung hingewiesen.

Die Dämpfung von Spinwellen ist einer der wichtigsten Aspekte der beim Entwurf magnonischer Bauteile berücksichtigt werden muss. Neben intrinsischen Verlusten erfahren Spinwellen auch extrinsische Verluste, die z.B. von strukturellen Defekten aus der Fabrikation oder Inhomogenitäten der Wellenleiter herrühren. Solche Defekte treten häufig auf und führen unter anderem zur Rückstreuung von Spinwellen und dem Verlust von Information. Aus diesem Grund ist es wichtig, Wege aufzuzeigen, wie der Einfluss von Defekten minimiert werden kann. Im Bericht 4.9 un-

tersuchen wir insbesondere diese häufig auftretende Rückstreuung und zeigen Wege auf, sie zu minimieren. Wir zeigen dass in magnetischen Dünnfilmen Moden existieren, die immun gegen Rückstreuung sind. Dies ist eine Folge aus dem Wechselspiel der Austausch- und der dipolaren Wechselwirkung und der damit verbundenen Bandlücke im Spektrum der über die Schichtdicke quantisierten Spinwellenmoden

Der anschließende Bericht 4.10 diskutiert eine ortsaufgelöste Studie der Anregung und Ausbreitung von Spinwellen in zweidimensionalen magnetischen Filmen mittels BLS. Ein Vorteil der Magnonik gegenüber der Elektronik ist die Möglichkeit, Informationen, die in einem Spinwellenstrahl kodiert sind, in zweidimensionalen Systemen ohne die Herstellung von Wellenleitern zu übertragen. Spinwellen können sich dabei in der Form von Spinwellenkaustiken (s. dazu den letzten Bericht in diesem Kapitel) oder als monochromatische Spinwellenstrahlen, so wie in diesem Bericht, ausbreiten. Um solche Strahlen anzuregen untersuchen wir ein Antennenkonzept welches kürzlich von Gruszecki *et al* theoretisch vorgestellt wurde. Es wird gezeigt, dass eine solche Antenne es ermöglicht, die Spinwellenanregung auf gewünschte Areale einzugrenzen und dass auf diese Weise propagierende Spinwellenstrahlen erzeugt werden können. Darüber hinaus analysieren wir die Lebenszeit und die Abklinglänge der gemessenen Spinwellenstrahlen.

Die Dispersion dipolarer Spinwellen in der Schichtebene magnetisierter Filme ist stark anisotrop. Dipolare Spinwellen, die sich entlang der statischen Magnetisierung ausbreiten werden als Rückwärtsvolumenspinwellen (Englisch: backward volume spin waves (BVMSWs)) bezeichnet. Wellen die sich senkrecht zu ihr ausbreiten als magnetostatische Oberflc̈henspinwellen (Englisch: magnetostatic surface spin waves (MSSWs)). Eine Änderung der Propagationsrichtung erfordert somit die Konversion zwischen MSSWs und BVMSWs. Da beide Moden in verschiedenen Frequenzbereichen liegen, stellt dies eine Herausforderung dar. Im Bericht 4.11 schlagen wir einen neuen Mechanismus zur Konversion vor und untersuchen ihn experimentell. Durch das Erzeugen eines laserinduzierten Magnetisierungsgradienten ist eine solche Modenkonversion möglich, da er eine lokale Verschiebung der Dispersionsrelationen erlaubt und es so ermöglicht, dass MSSWs und BVSMWs bei gleichen Frequenzen existieren. Der Impuls der Spinwellen wird dabei zunächst bei Brechung an der Kante des Magnetisierungsgradients und danach beim Durchgang durch den Gradienten kontinuierlich angepasst. Eine solche adiabatische Transformation des Spinwellenimpulses ermöglicht eine hocheffiziente Modenkonversion in einem weiten Frequenzbereich.

Zum Schluss wird im Bericht 4.12 in mikromagnetischen Simulationen ein Ansatz zur Realisierung eines Frequenzmultiplexverfahrens (Englisch: Frequency-Division Multiplexing (FDM)) mittels Kaustiken in magnonischen Netzwerken untersucht. Solche FDM-Netzwerke sind hochinteressant für Anwendungen, da in ihnen Signale bei verschiedenen Frequenzen gleichzeitig Informationen durch den selben Wellenleiter in verschiedenen Frequenzkanälen übertragen. Kaustikartige Strahlen gehen dabei aus der anisotropen Spinwellendispersion in in der Schichtebene magnetisierten zweidimensionalen Medien hervor und die Ausbreitungsrichtung dieser Strahlen hängt, unter anderem, stark von ihrer Frequenz ab. Dadurch sind Kaustikstrahlen ein idealer Kandidat für die Realisierung von FDM-Netzwerken und dieser Aspekt wird in diesem Bericht beleuchtet.

4.7 Spin-pinning conditions in nano-scale YIG waveguides

Q. Wang, M. Kewenig, B. Heinz, P. Pirro, T. Meyer, T. Brächer, and A.V. Chumak

In collaboration with Roman Verba, Institute of Magnetism, Kyiv 03680, Ukraine and Carsten Dubs, INNOVENT e.V., Technologieentwicklung, Prüssingstr. 27B, 07745 Jena, Germany

Spin waves and their quanta, magnons, typically feature frequencies in the GHz to THz range and wavelengths in the micrometer to nanometer range. They are envisioned for the design of faster and smaller next generational information processing devices where information is carried by magnons instead of electrons [1, 2]. The recent advances in the growth of high-quality films of the ferrimagnetic insulator Yttrium Iron Garnet (YIG) with thicknesses in the range of only a few tens of nanometers [3, 4] have boosted research on spin waves greatly. The creation of micro- and even nanostructures from this material, which is the workhorse of 'conventional' research on spin waves due to its record low damping [2, 5], allows for the realization of prototype spin-wave devices on microscopic scales [6]. As the lateral sizes of spin-wave waveguides in such devices get closer to the exchange length (16.9 nm in YIG), the influence of exchange on the profile of the waveguide modes, i.e., the laterally quantized waves propagating along the waveguide, can no longer be neglected. In particular, for waveguides with a width comparable to their thickness, where also the demagnetization tensor of the waveguide differs drastically from a thin film, large differences for the mode profiles are expected compared to the case of a planar waveguide. In this report, we analyze the change of the mode profile in such nanometric waveguides by means of micromagnetic modeling [7]. We discuss the presence of exchange-mediated depinning which opposes dipolar pinning [8, 9] and its influence onto the spin-wave dispersion. We present in this report also results of analytical theory developed by R. Verba in collaboration with our group. Experimental studies of the discussed phenomena, obtained using YIG samples provided by C. Dubs, support our theoretical finding but are not presented in this report.

The structure under investigation is schematically shown in Fig. 1a. Waveguides of 30 µm length, of width w in the range from 100 nm to 5000 nm, and with a fixed thickness of 100 nm are studied. The following parameters of a nanometer-thick YIG film were used [6]: saturation magnetization $M_s = 1.4 \times 10^5$ A/m, exchange constant $A = 3.5$ pJ/m, and Gilbert damping $\alpha = 2 \times 10^{-4}$. The Gilbert damping α at the ends of the waveguide exponentially increases to 0.5 to prevent spin-wave reflection. The static magnetic field $B_{ext} = 40$ mT is applied along the long axis of the waveguide (x-direction), a geometry referred to as the backward volume geometry. The cell size used in the simulations is $10 \times 10 \times 100\,\text{nm}^3$. In this single layer approximation, the dynamic magnetization distribution is homogeneous along the waveguide thickness h (z-direction), which is a reasonable

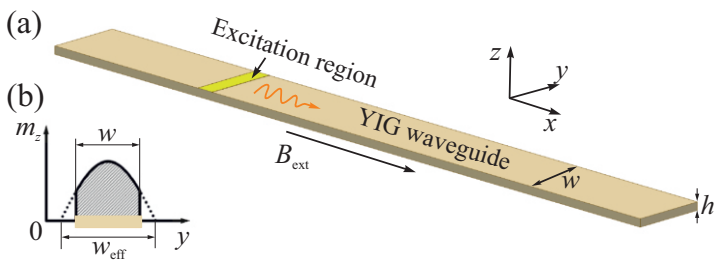

Fig. 1: (a) Coordinate system and sketch of a rectangular waveguide with thickness h and width w. (b) Sketch of the cross section of the waveguide showing the geometric width of the waveguide w and the effective width w_{eff}.

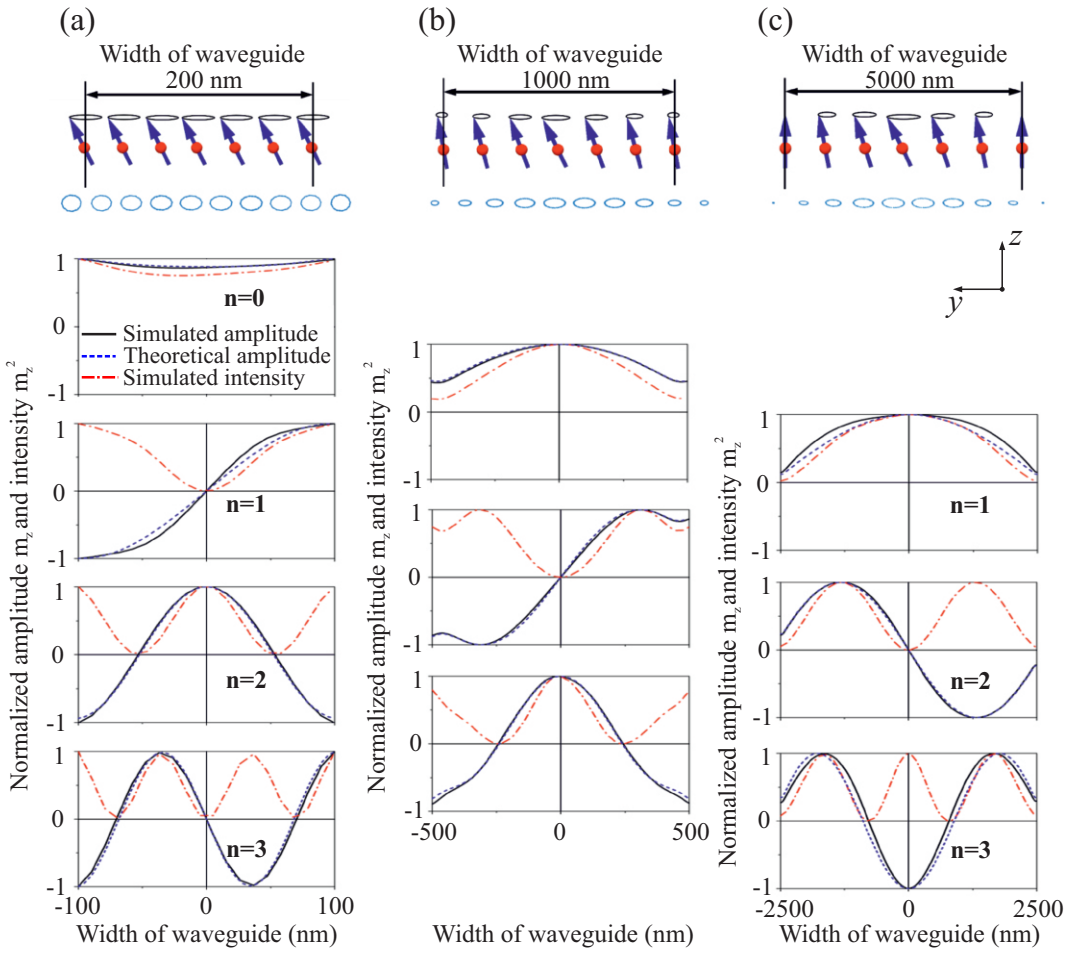

Fig. 2: Schematic representation of the precessing spins (top panel), simulated precession trajectories in y-z plane (ellipses in the second panel) of the lowest width mode, and the spin-wave profile expressed by the z-component m_z of the dynamic magnetization **m** for a few lowest width modes obtained by micromagnetic modeling (solid lines) and by analytic theory (dashed lines) for a (a) 200 nm, (b) 1000 nm and (c) 5000 nm wide waveguide. The dash-dotted lines show the normalized intensity of the spin-wave modes obtained from micromagnetic modeling. The thicknesses of waveguides are fixed to 100 nm.

approximation for thicknesses below 150 nm. This critical thickness has been obtained by comparing the spin-wave profile of single-layer and multilayer simulations, which are beyond the scope of this report. In order to excite a single frequency spin wave, a sinusoidal field $b_y = b_0 \sin(2\pi f t)$ is applied in a 30 nm wide area (marked in Fig. 1a), with an amplitude of $b_0 = 1$ mT and excitation frequency f. Then, the spatial distribution of the excited spin waves were obtained by performing a two-dimensional Fast Fourier Transformation (FFT) of the time- and position-dependent data. The spin-wave width profiles were extracted along the width of the waveguides.

The main panel of Fig. 2 shows the spin-wave mode profiles (z-component m_z of the dynamic magnetization **m** as function of the coordinate y across the waveguide) of the three (four) lowest width modes which have been obtained this way (solid lines). The dashed lines indicate the profiles expected from theory, which we developed jointly with R. Verba. The dash-dotted lines in the Figure show the normalized intensity distribution of the spin-wave modes obtained from the simulations (this quantity is often measured experimentally using Brillouin Ligtht Scattering (BLS) spectroscopy). Three exemplary waveguide widths of 200 nm, 1000 nm and 5000 nm are

considered. One can see that the profiles of the lowest modes for the 200 nm and 5000 nm wide waveguides are strikingly different. The spins at the edges of the narrow waveguide are unpinned (see also schematic sketches in the top panels of Fig. 2), and the amplitude of the dynamic magnetization m_z of the lowest spin-wave mode $n = 0$ is almost constant across the width of the waveguide. In contrast, for the 5000 nm wide waveguide, the spins are nearly fully pinned and the amplitude of m_z at the edges of the waveguide is close to zero. This results in the cos-like profile of the lowest width mode $n = 1$ that is well known from the experimental BLS investigations on the micron scale [6]. For the intermediate case of a 1000 nm wide waveguide, the spins are partially pinned and the mode profile shows some intermediate profile. The two top panels of Fig. 2 show a schematic representation of the precessing spins and the simulated precession trajectories in the y-z plane of the lowest width modes. The simulated results show that in micron wide waveguides the precession trajectory is highly elliptic in the center of the waveguide due to the strong demagnetizing field along the z-direction ($\varepsilon = 1 - |m_z|^2/|m_x|^2 = 0.714$ for 1000 nm and $\varepsilon = 0.7525$ for 5000 nm). The elliptic precession trajectory gradually becomes circular towards the edges of the waveguides due to the influence of the y-component of the demagnetizing field at the edges. In line with this, the ellipticity of precession is much weaker ($\varepsilon = 0.4672$) for the 200 nm wide waveguide with a small aspect ratio (width/thickness).

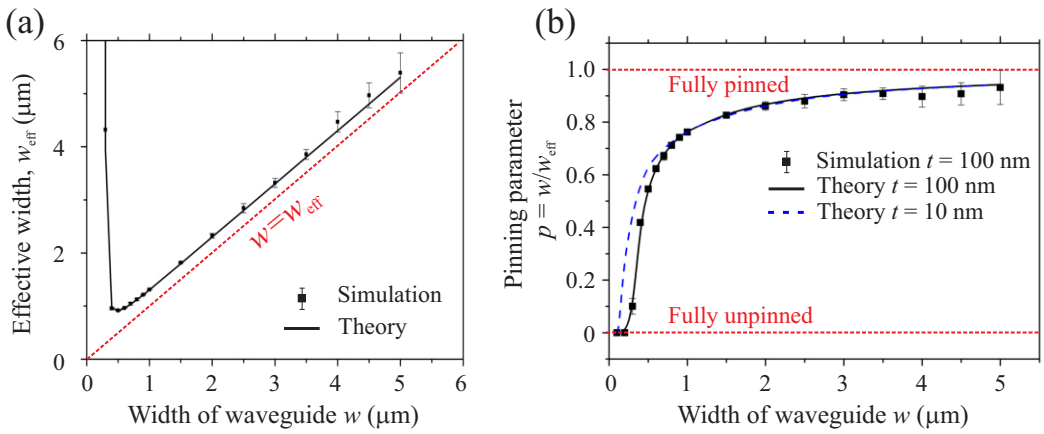

Fig. 3: Dependence of (a) effective width and (b) pinning parameter on the width (w) of waveguide. Black dots are the result of micromagnetic simulations, solid lines are calculated from analytical theory (not presented in this report).

For a quantitative description of the spin pinning conditions, we use the approach of an effective width w_{eff} of the spin-wave waveguide which was introduced in Refs. [7, 8]. For brevity, we restrain our discussion to the lowest width mode, which is the most interesting mode for magnonic applications. The higher width modes exhibit similar features.The cos-like profile has two virtual intersections (zero amplitude) with the y-axis shown in Fig. 1b. The effective width is the distance between these two intersections. In general, in the backward volume geometry, the effective width is larger than the geometric width of waveguide. The effective width w_{eff} is determined by both, the geometric waveguide width w and the spin pinning conditions. Figure 3a shows how a decrease in the geometric width results in a reduction of the effective width when the width is larger than 500 nm. In this region, the effective width is similar to the geometric width (the diagonal dashed line shows the limitation if the geometric width is assumed to be equal to the effective width), since exchange effects do not play a decisive role here. A further reduction of the geometric width

results in a large increase of the effective width since the exchange interaction counteracts the dipolar pinning at the edges of the waveguides. In order to quantify the influence of exchange-dipolar pinning, the pinning parameter p is defined by the ratio w/w_{eff}. Figure 3b shows the dependence of the pinning parameter p on the width of waveguide w. The pinning parameter decreases from one (fully pinned) for large widths of the waveguide to zero (fully unpinned) for the 100 nm wide waveguide. The decrease of the pinning parameter is mediated by the fact that the geometric width approaches the exchange length. In addition, theoretical lines in the Figure show that for small waveguide widths the pinning parameter depends on the thickness of the film. This is due to a demagnetisation tensor which is responsible for the dipolar pinning. Therefore, the spins in the samples with the aspect ratio width to thickness close to 1 are getting unpinned easier in comparison to the waveguides with the width much larger than the thickness.

In conclusion, micromagnetic simulations and analytic theory are employed to study the spin pinning conditions of propagating spin waves in nano-scale waveguides. These two methods give very similar results. The effective width w_{eff} and pinning parameter p are studied as functions of the width of the spin-wave waveguide. The pinning parameter increases from one (fully pinned) in micron wide waveguides to zero (fully unpinned) in nano-scale wide waveguides. The changes of the spin pinning conditions on the nano-scale are important for applications in nano-magnonics in which spin waves propagate in waveguides with small width.

The project was financially supported partially by the European Union via the ERC Starting Grant 678309 MagnonCircuits.

References

[1] V.V. Kruglyak, S.O. Demokritov, D. Grundler, *Magnonics*, J. Phys. D: Appl. Phys. **43**, 246001 (2010).
[2] A.V. Chumak, V.I. Vasyuchka, A.A. Serga, B. Hillebrands, *Magnon spintronics*, Nat. Phys. **11**, 453 (2015).
[3] C. Dubs, O. Surzhenko, R. Linke, A. Danilewsky, U. Brückner, J. Dellith, *Sub-micrometer yttrium iron garnet LPE films with low ferromagnetic resonance losses*, J. Phys. D: Appl. Phys. **50**, 204005 (2017).
[4] Haiming Yu, O.d'Allivy Kelly, V. Cros, R. Bernard, P. Bortolotti, A. Anane, F. Brandl, R. Huber, I. Stasinopoulos, D. Grundler, *Magnetic thin-film insulator with ultra-low spin wave damping for coherent nanomagnonics*, Sci. Rep. **4**, 6848 (2014).
[5] D.A. Bozhko, A.A. Serga, P. Plausen, V.I. Vasyuchka, F. Heussner, G.A. Melkov, A. Pomyalov, V.S. L'vov, B. Hillebrands, *Supercurrent in a room-temperature Bose-Einstein magnon condensate*, Nat. Phys. **12**, 1057 (2016).
[6] P. Pirro, T. Brächer, A.V. Chumak, B. Lägel, C. Dubs, O. Surzhenko, P. Gornert, B. Leven, B. Hillebrands, *Spin-wave excitation and propagation in microstructured waveguides of yttrium iron garnet/Pt bilayers*, Appl. Phys. Lett. **104**, 012402 (2014).
[7] A. Vansteenkiste, J. Leliaert, M. Dvornik, M. Helsen, F. Garcia-Sanchez, B. Van Waeyenberge, *The design and verification of MuMax3*, AIP Adv. **4**, 107133 (2014).
[8] K.Yu. Guslienko, S.O. Demokritov, B. Hillebrands, A.N. Slavin, *Effective dipolar boundary conditions for dynamic magnetization in thin magnetic stripes*, Phys. Rev. B. **66**, 132402 (2002).
[9] K.Yu. Guslienko, A.N. Slavin, *Boundary conditions for magnetization in magnetic nanoelements*, Phys. Rev. B. **72**, 014463 (2005).

4.8 Magnon dispersion in a magnetic bi-layer system

M. Geilen, M. Mohseni, T. Brächer, B. Hillebrands, and P. Pirro

In collaboration with F. Ciubotaru and C. Adelmann, IMEC, Leuven, Belgium
Y. Henry, D. Louis, M. Bailleul, IPCMS, Strasbourg, France

Since the discovery of surface spin waves by Damon and Eshbach there has been a large interest in coupling phenomena of such modes in ferromagnetic multilayer systems. The most simple multilayer system is a bilayer system consisting of two different ferromagnetic layers with different saturation magnetization and exchange constants. An interesting bilayer is the combination of nickel (Ni) and permalloy (Py), since this material system is a possible candidate for magneto-elastic spin-wave devices. While permalloy provides good properties for the propagation of spin waves, the magnetization of nickel can be manipulated with mechanical stress due to its magnetostictive behaviour. In this report we present our latest results on the dispersion relation of a Ni/Py bilayer system. First we will show the experimental results based on Brillouin light scattering spectroscopy (BLS). Next we compare the experimental results with micromagnetic simulations.

Surface spin waves are often considered as the most relevant spin waves for magnonic applications due to their high group velocity in thin films. If the exchange interaction is neglected they also have an imaginary wave-vector component $k_\perp$ across the film thickness, which is proportional to the in-plane wave-vector component $k_\parallel$, which is perpendicular to the magnetization and leads to a localization of this mode to one surface of the film and the highly non-reciprocal propagation behavior. For thin films the role of the exchange interaction becomes more dominant and the mode can not be described that easily [1]. But as long as the both surfaces of the film are equal and the film itself has homogeneous material parameters across its thickness the frequency of spin waves with wave vectors $+k_\parallel$ and $-k_\parallel$ are degenerate. This symmetry can be broken in many ways by changing the properties of one surface (metallization, surface anisotropy or interfacial Dzyaloshinskii-Moriya

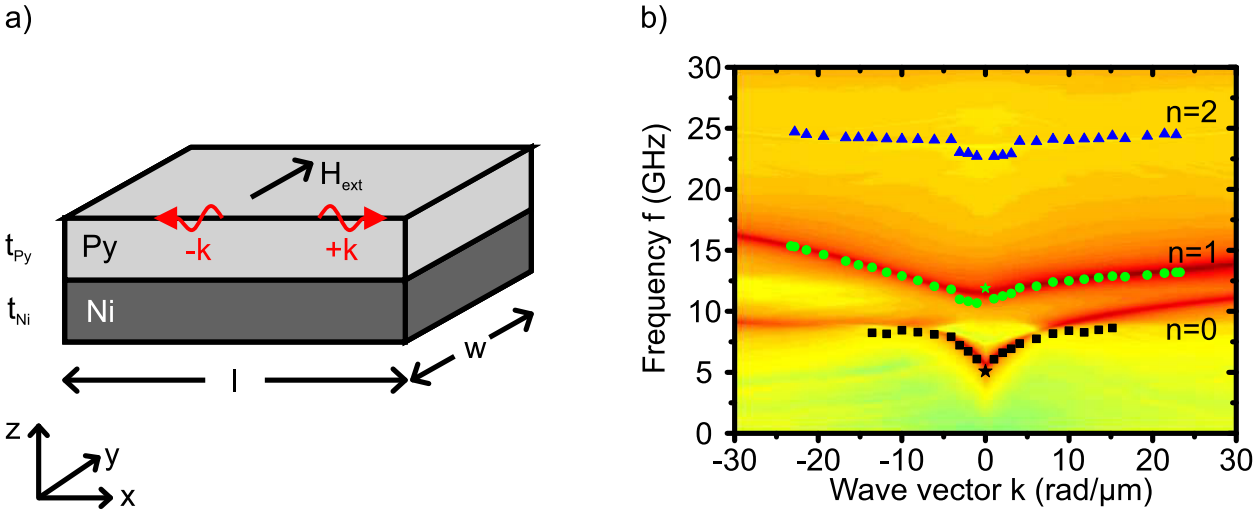

Fig. 1: a) Sketch of the investigated bilayer system consisting of a Py film on top of a Ni film with the same thickness $t_{Ni} = t_{Py}$ =25 nm. b) The dispersion relations for the first three modes obtained from the micromagnetic simulations and measured with BLS (dots).

interaction). In this report the symmetry is broken by a second magnetic layer, which is attached to one surface of the film and coupled via dipole-dipole or exchange interaction to the first layer (compare Fig. 1a). In comparison to the previously mentioned ways this is a promising approach for magnonic applications since the second layer will not degrade the propagation properties of the magnetic layer in comparison to the single layer case. To show the non-reciprocal behavior of the investigated Ni/Py bilayer a sample with a thickness of Ni t_{Ni} =25 nm and of Py t_{Py} =25 nm has been produced by sputter deposition at IMEC in Leuven, Belgium.

To get a first impression about the magnetic properties of the materials, stripline FMR measurements have been performed. From the measurements two different modes could be identified, which are shown in Fig. 2. The mode with the mode number $n = 0$ can be described by the Kittel formula. The second mode ($n = 1$), however, has a significant exchange or anisotropy contribution, what leads to a non-zero frequency for vanishing external field. The dashed lines indicate the FMR frequency for an external field of $\mu_0 H_{\mathrm{ext}}$ =50 mT, which was used in the following BLS measurements.

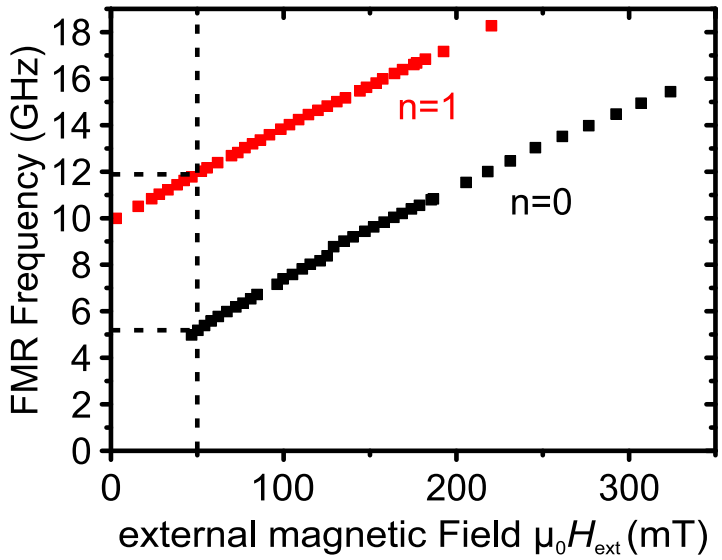

Fig. 2: The FMR spectroscopy shows two different modes. The dashed lines indicate the FMR values for $\mu_0 H_{\mathrm{ext}}$ =50 mT.

Subsequently, the dispersion relation of the surface spin waves was measured with conventional BLS technique. Therefore the in-plane wave-vector perpendicular to the applied field was probed up to $k_{\parallel}$ =23.3 rad/µm. The frequencies for (positive) negative wave-vectors were extracted from the (anti-)Stokes peaks of the BLS spectra. The dots in Fig. 1b show the obtained dispersion relation for the first three spin-wave modes with the mode numbers up to $n = 2$ from thermally excited spin waves at an external field of $\mu_0 H_{\mathrm{ext}}$ =50 mT. In addition, the frequencies for k =0 rad/µm, indicated by stars, were obtained by stripline FMR spectroscopy. For the first two modes a highly non-reciprocal dispersion relation is observed. For example, for the mode with $n = 1$ the dispersion relation increases strongly for negative wave-vectors, while it becomes flat and the group velocity of the spin waves decreases almost to zero for positive wave-vectors. Therefore, spin waves will effectively propagate only in one direction. The third mode can be identified as a standing spin wave mode over the film thickness. Due to its flat and reciprocal behavior it will not be further considered.
Figure 3 shows the frequency difference $\Delta f = f(+k) - f(-k)$ between counter-propagating spin

waves. For small wave-vectors the difference of the mode $n = 0$ is negative but changes sign around $k = 10\,\mathrm{rad/\mu m}$ before it further increases. For $n = 1$ it is vice versa and the frequency difference decreases down to $\Delta f(k = 23.3\,\mathrm{rad/\mu m}) = -2.12\,\mathrm{GHz}$. In addition, the frequency difference for two magnetic films with the same material parameters, but without exchange interaction has been calculated from the dispersion relation published by Grünberg [3]. In this case the frequency is a monotonously growing or decreasing function of the in-plane wave-vector without a sign change. This indicates that the sign change is a feature that only occurs if exchange interaction at the interface is present. In Ref. [4] a link between the frequency difference and the asymmetry of the imaginary part of the out-of plane dynamic magnetization has been shown. Thus, this feature might offer a new way to determine the strength of the interlayer exchange between to magnetic films.

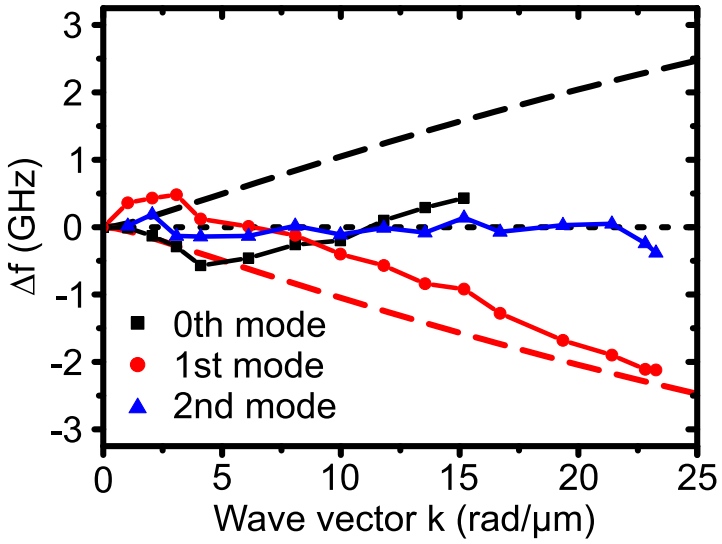

Fig. 3: The frequency difference $\Delta f = f(+k) - f(-k)$ for the zeroth (black) and the first mode (grey) show a sign change for the BLS measurements (dots), while for the purely dipole coupled bilayer system after Grünberg [3] (dashed line) no sign change can be observed.

To understand the experimental findings, micromagnetic simulations using *Mumax3* [2] have been performed. The simulated magnetic volume is shown in Fig. 1a. It has a length of $l = 15\,\mu\mathrm{m}$, a width of $w = 1\,\mu\mathrm{m}$ and periodic boundary conditions were used in the y-direction. The thickness of the two layers are, like in the experiment, chosen to be $t_{\mathrm{Ni}} = t_{\mathrm{Py}} = 25\,\mathrm{nm}$. Each layer has been divided into $5000 \times 10 \times 4$ cells. Furthermore for the simulations the following material parameter have been used for Nickel and Permalloy: saturation magnetization $M_{\mathrm{Ni}} = 400\,\mathrm{kA/m}$ and $M_{\mathrm{Py}} = 721\,\mathrm{kA/m}$, exchange constant $A_{\mathrm{Ni}} = 6\,\mathrm{pJ/m}$ and $A_{\mathrm{Py}} = 11.5\,\mathrm{pJ/m}$, Gilbert damping $\alpha_{\mathrm{Ni}} = 0.01$ and $\alpha_{\mathrm{Py}} = 0.005$. For the exchange interaction at the interface between neighbouring cells with different materials the parameter A/M is a crucial value, which in this case was determined by the harmonic mean of the material parameter. The external field was $\mu_0 H_{\mathrm{ext}} = 50\,\mathrm{mT}$. The excitation of the spin waves was modeled by a Gaussian shaped point source, which is homogenous over the thickness. The obtained dispersion relation is shown in Fig. 1b as the gray-scale figure. It can be seen that the simulation confirms the dispersion relations measured by BLS spectroscopy.

Besides the frequencies also the mode profile of the spin waves across the film thickness can be extracted from the simulations. They lead to one approach to explain the non-reciprocal behavior of the surface spin waves in a bilayer system. Figure 2 shows the normalized amplitude of the Fourier-transformed dynamic magnetization component M_z across the film for different negative wave-vectors. For the $n = 0$ mode, the amplitude is nearly constant over the thickness for $k_{\parallel} = 0\,\mathrm{rad/\mu m}$ and becomes more localized to the Ni surface with increasing wave-vector. There-

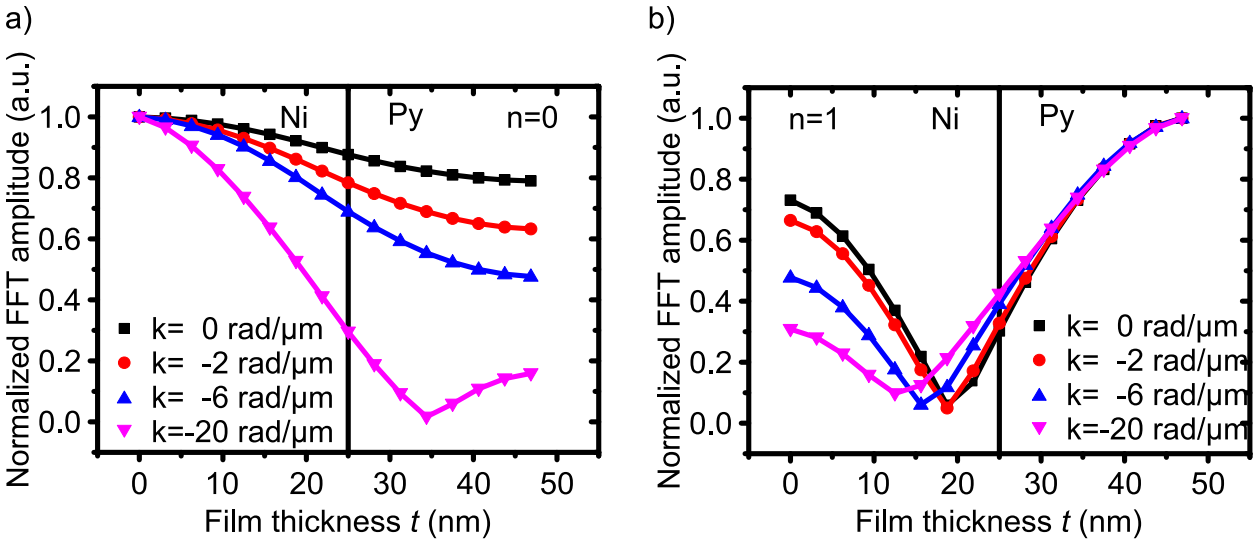

Fig. 4: The normalized FFT amplitude over the film thickness for positive wave vectors. The $n = 0$ mode (a) becomes more localized to the Ni surface with increasing wave vector, whereas the $n = 1$ mode (b) is more localized in the Py.

fore, the dispersion of this mode is dominated by the Ni layer and will tend to follow the dispersion of a pure 50 nm thick Ni film. The $n = 2$ mode becomes more localized to the Py surface with increasing wave-vector. However, its mode profile shows a node around the interface similar to a PSSW mode.

We have investigated in this report the dispersion relation for surface spin waves in a Ni/Py bilayer system. It can be concluded that this system shows a strong frequency shift between counter-propagating spin waves up to several Gigahertz. It has also been shown that a sign change of the frequency shift only occurs when exchange interaction is taken into account.

Financial support from DFG within project B01 of SFB/TRR 173, Spin+X - Spin in its collective environment, is gratefully acknowledged.

References

[1] M. Kostylev, *Non-reciprocity of dipole-exchange spin waves in thin ferromagnetic films*, J. Appl. Phys. **113**, 053907 (2013).
[2] A. Vansteenkiste, J. Leliaert, M. Dvornik, M. Helsen, F. Garcia-Sanchez, B. Van Waeyenberge, *The design and verification of MuMax3*, AIP Adv. **4**, 107133 (2014).
[3] P. Grünberg, *Magnetostatic spin-wave modes of a heterogeneous ferromagnetic double layer* J. Appl. Phys. **52**, 11 (1981).
[4] Y. Henry, O. Gladii, M. Bailleul, *Propagating spin-wave normal modes: A dynamic matrix approach using plane-wave demagnetizating tensors*, arXiv:1611.06153 (2016).

4.9 Identification of backscattering-immune spin-wave modes

M. Mohseni, Q. Wang, B. Hillebrands, and P. Pirro

Spin-waves have recently gained a great interest as a suitable candidate for information technology systems [1]. They are considered as an alternative to electrons and photons for carrying information in wave-based computing systems. Functionality of different spin-wave devices for this aim has been realized up to now, namely majority gates [2] and magnonic crystals [3, 4]. Among the most important parameters that are necessary to be taken into account for designing such systems, propagation properties hold an important role. Indeed, controlling such properties can promise high efficient devices. Overcoming losses which are effective on the propagation of the spin-waves in magnetic materials, is considered as one of the biggest challenges in this field. Considering this fact, external losses which are induced from external effects, e.g. fabrication-induced disorders, film non-uniformities and magnetic inhomogeneities are unpreventable and finally lead to scattering of the spin-wave energy and low efficiency of the system. Therefore, pursuing novel ways to prevail these challenges or at least reduce their contributions to the functionality of the elements, are highly desired.

Here, we have realized that back-scattering immune spin-wave modes exist. We show that in an in-plane magnetized YIG film with relatively small thickness, propagating waves can be robust against even large inhomogeneities and disorders. Such robust waves, open the possibility for designing highly efficient magnonic elements. They can also provide new insights into the mechanisms of spin-wave propagation in magnetic thin films.

We begin the discussion by considering LLG equation and referring to the possible underlying mechanisms. One can immediately find from the LLG equation that precession of the magnons are allowed only in one direction, which essentially means that time-reversal symmetry for them is broken. Considering the traveling waves, this effect leads to non-reciprocal propagation if the in-plane magnetization and wave vector are orthogonal to each other [5]. In this particular configuration, a spatial chirality for the traveling magnons appears. We show that such waves which are known as Magneto Static Surface Waves (MSSW) have scattering-immunity from perturbation in thin films, although in thick films and due to a different spin-wave band structure, the immunity trend becomes weakened.

Figure 1a shows a schematic picture of the system under study (a YIG slab) if only dipole-dipole interaction is taken into account. It illustrates the spin-wave non-reciprocity for the excited waves (excited with a spin-wave source in the middle) that are propagating perpendicular to the magnetization. d represents the thickness, and the excited spin-waves propagate in the direction of k_y. This demonstrates that propagating MSSW are localized at the surfaces of the film in the as-known Damon-Eshbach geometry [5]. The localization at the surfaces of the film takes place due to the broken time-reversal symmetry in the system with respect to the inversion of the direction propagation ($M \perp k$), caused by the dynamic dipole-dipole interaction of the magnons, as the only way for them to convey their energy and conduct through their traveling path. Indeed, magnon localization in this configuration depends on the field H_0 and traveling direction k_y, which essentially means that localization is possible only at one of the surfaces (rotational symmetry) [5, 6].

Figure 1b-d shows the micromagnetically simulated magnon band structure of Backward Vol-

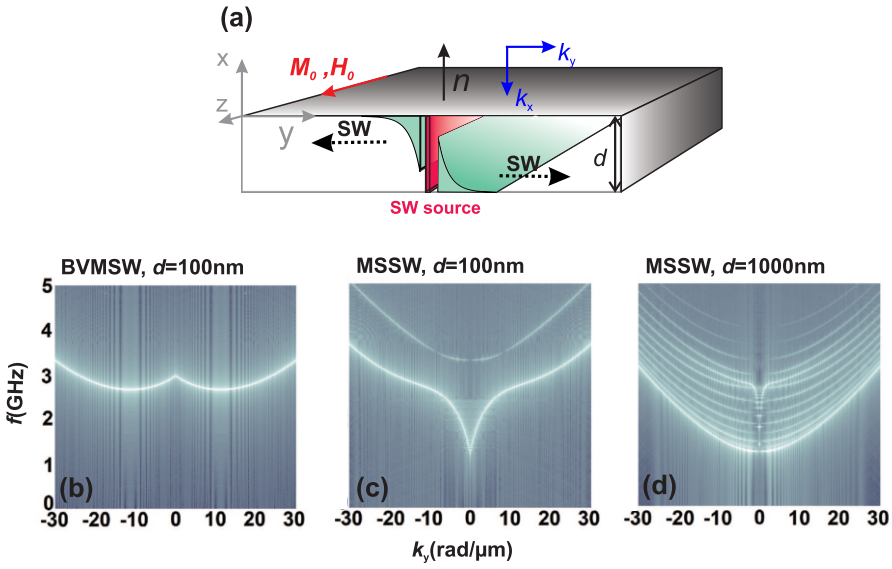

Fig. 1: a) Sketch of the spin-wave non-reciprocity, direction of the field and wavevector. b-d) Magnon band structures calculated numerically for BVMSW in a film with $d = 100\,\text{nm}$, MSSW in a film with $d = 100\,\text{nm}$ and $d = 1000\,\text{nm}$ respectively.

ume Magneto Static Waves (BVMSW) and MSSW for films with thicknesses of $d = 100\,\text{nm}$ and $d = 1000\,\text{nm}$ respectively. When the film thickness is at the nm-scale ($d = 100\,\text{nm}$ in our case), the fundamental mode (MSSW mode) has the lowest frequency (Fig. 1c), separated by a distinguishable gap from other modes of the system in the frequency domain, which results in the prevention of any hybridization among the modes. In this case, the magnon amplitude decays exponentially over the thickness, caused by the acting dipole-dipole interaction [6]. Increasing the thickness in this geometry brings an interplay among dipole-dipole and exchange interaction of the magnons over the thickness into the play (especially when the thickness is much larger than the exchange length of the system) by establishing interference and hybridization between MSSW and thickness modes (Fig. 1d, also known as perpendicularly standing spin wave or PSSW modes). Please note that the localization of the fundamental mode (MSSW mode) at the two surfaces is supposed to be swapped due to this fact in comparison to thin films [7].

The thickness modes provide alternative channels for magnon transport (k_y) from the source region, reflecting that the localization will not necessarily decay homogenously over the thickness, considering possible hybridization and interference of the fundamental mode and thickness modes over the whole magnon band structure. On the other hand, it is worth to mention that thickness modes have reciprocal propagation [7]. Changing the configuration of H_0 and k_y from $M \perp k$ (MSSW) to $M \parallel k$ (BVMSW) (Fig. 1b), not only changes the magnon dispersion relation considering its anisotropic nature [6], but also results in the disappearance of the localization at the surfaces.

Now, let us to study the scattering of the different spin-wave modes. Figure 2a-c addresses time traces of the propagating spin-waves excited with a spin-wave source at the middle including MSSW for the films of thickness d = 100nm and $d = 1000\,\text{nm}$ and BVMSW for $d = 100\,\text{nm}$, respectively. A topographical defect (2 µm long), with a height equal to 20 percent of the film thickness (d), acting as a film non-uniformity is placed at the surface of the films (the surface

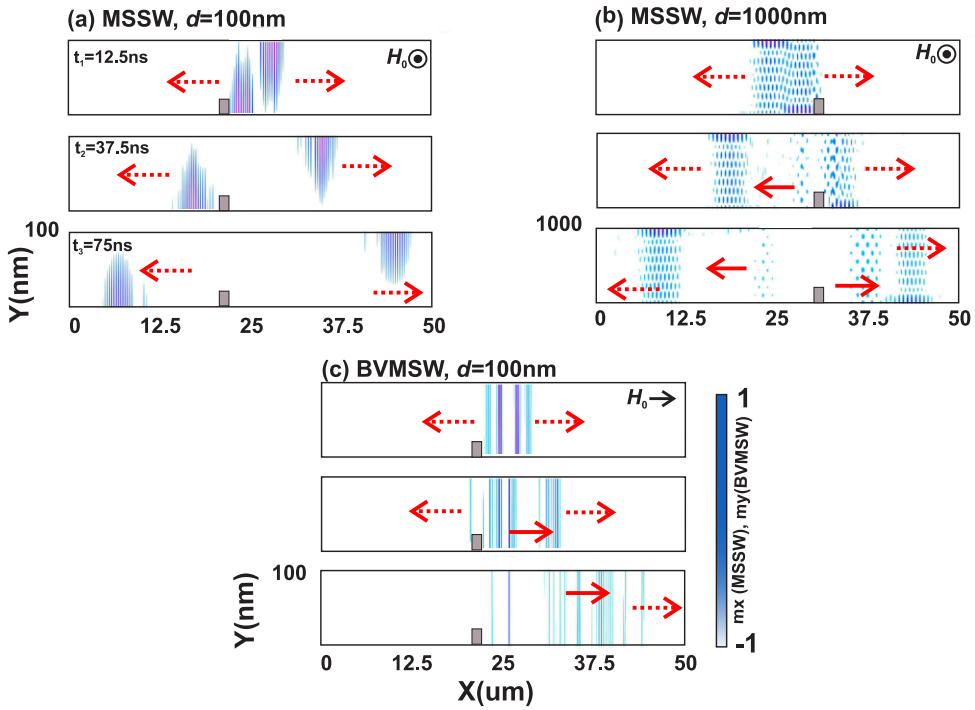

Fig. 2: Snap shots of the spin-wave propagation of a) MSSW in $d = 100\,\text{nm}$ film, (b) MSSW in a $d = 1000\,\text{nm}$ film, and (c) BVMSW in a $d = 100\,\text{nm}$ film, all in the presence of the defects. Propagating and reflected waves are marked with dotted and continues arrows, respectively.

where the MSSW are localized) to study spin-wave reflections from this defects.

For the case of MSSW, the spin-waves are excited with an identical frequency of $f = 3\,\text{GHz}$. Localization of the spin-waves at the surfaces are evidenced by the snapshots presented in Fig. 2a-b. For the case of $d = 100\,\text{nm}$, propagating spin-waves cross over the defect without any back reflections (Fig. 2a). This confirms lack of backscattering channels, since the broken time-reversal symmetry provides a one-way propagating route at the surfaces (only positive or negative group velocities) for the magnons, which means that they are allowed to propagate only at a given surface (k_y) with respect to the applied field (H_0). Nevertheless, increasing the thickness challenges the backscattering-immune trend. For the case of $d = 1000\,\text{nm}$, backscattering takes place when spin-waves face the defect (Fig. 2b). Although the geometry is the same, due to the presence of thickness modes caused by the exchange contribution over the thickness, magnons find a way to go backward when they face a non-uniformity, since hybridization among different modes is unpreventable. Propagating and scattered waves are marked with dotted and continues arrows in Fig. 2.

By changing the field configuration from MSSW to BVMSW and exciting spin-waves with $f = 2.8\,\text{GHz}$, one can see from Fig. 2c that not only the localization does not take place, but indeed a strong back-reflection occurs when spin-waves confront the defect. This indicates that BVMSW magnons undergo strong scattering, even if the thickness is small to prevent hybridization with thickness modes.

In order to give a better insight into the scattering physics in these systems, an averaged spatial FFT amplitude of the excited waves in the discussed configurations in Fig. 2 are presented in Fig. 3. Figure 3a-b addresses the MSSW for $d = 100\,\text{nm}$ and $d = 1000\,\text{nm}$ and Fig. 3c shows the BVMSW for $d = 100\,\text{nm}$, respectively. As explained before, the presence of a defect almost does not lead

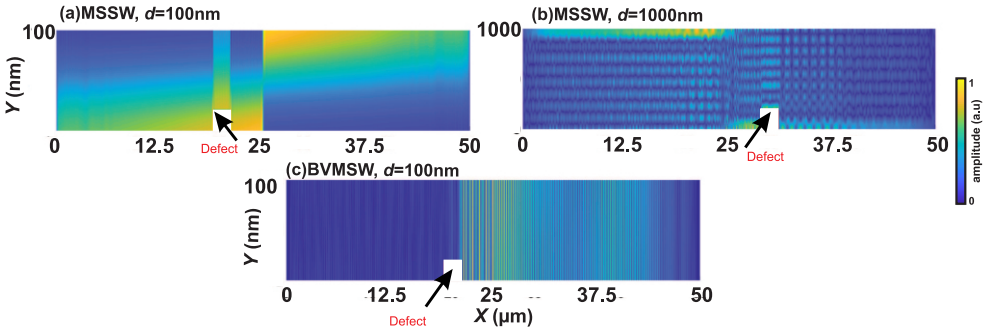

Fig. 3: FFT amplitude of the excited spin-waves for a) MSSW in $d = 100\,\text{nm}$ film, (b) MSSW in a $d = 1000\,\text{nm}$ film, and (c) BVMSW in a $d = 100\,\text{nm}$ film, all in the presence of the defects.

to any spin-wave reflections for MSSW, providing the same decay length like the reference film, which is equal to 63 µm and a transmission rate of 99%.

However in the case of $d = 1000\,\text{nm}$ the defect is strongly affecting the propagation by dropping the transmission down to 80%. For the case of BVMSW, the back scattering is strong enough to nearly suppress the transmission completely and it reduces the transmission to near 7.6 %.

In summary, our findings predict the existence of back-scattering immune spin-wave modes in thin magnetic YIG films. The interplay between exchange and dipole interactions in thin YIG films leads to a frequency-gap between the fundamental mode and the thickness mode, which creates a one-way travelling route for the excited waves at a given surface. Our results provide novel insight in spin-wave propagation in magnetic thin films and might convey the way for novel magnonic and spintronic devices employing MSSWs.

Financial support from DFG within project B01 of SFB/TRR 173, Spin+X - *Spin in its collective environment*, is gratefully acknowledged.

References

[1] A. V. Chumak, V. I. Vasyuchka, A.A. Serga, B. Hillebrands, *Magnon spintronics*, Nat. Phy. **11**, 453 (2015).
[2] T. Fischer, M. Kewenig, D.A. Bozhko, A.A. Serga, I.I. Syvorotka, F. Ciubotaru, C. Adelmann, B. Hillebrands, A.V. Chumak, *Experimental prototype of a spin-wave majority gate*, App. Phys. Let **110**, 152401 (2017).
[3] A.V. Chumak, A.A. Serga, B. Hillebrands, M.P. Kostylev, *Scattering of backward spin waves in a one-dimensional magnonic crystal*, App. Phys. Let **93**, 022508 (2008).
[4] M. Vogel, A.V. Chumak, E.H. Waller, T. Langner, V. I. Vasyuchka, B. Hillebrands, G. Freymann, *Optically reconfigurable magnetic materials* , Nat. Phy. **11**, 487 (2015).
[5] R. W. Damon, J. R. Eschbach, *Magnetostatic modes of a ferromagnet slab*, J. Phys. Chem. Solids **19**, 308 (1961).
[6] M.J. Hurben, C.E. Patton, *Theory of magnetostatic waves for in-plane magnetized isotropic films*, J. Magn. Magn. Mater. **163**, 39 (1996).
[7] M. Kostylev, *Non-reciprocity of dipole-exchange spin waves in thin ferromagnetic films*, J. App. Phys. **113**, 053907 (2013).

4.10 Excitation and investigation of spin-wave beams

D. Breitbach, T. Fischer, B. Heinz, B. Hillebrands, and T. Brächer*

In collaboration with B. Lägel, Nano Structuring Center TU Kaiserslautern, Erwin-Schrödinger-Straße 13, 67663 Kaiserslautern, Germany

**Graduate School Materials Science in Mainz, Staudingerweg 9, 55128 Mainz, Germany*

A deep understanding of mechanisms for the excitation and manipulation of spin waves on the route towards the realization of magnon-based information processing devices [1] is crucial. In many investigations, narrow stripes patterned from thin films of a ferromagnetic material act as waveguides for spin waves [2], whose excitation is realized by microwave currents in metal antennas on top of these waveguides [3].
In this work, we aim at a different concept to spatially localize the excitation and propagation of spin waves in a thin layer of magnetic material and, hence, to enable a tunable and variable data transport by two-dimensional spin-wave beams adapted to specific experimental needs.
Current-conducting coplanar waveguides (CPWs) offer largely enhanced possibilities to tailor the excitation to specific needs depending on their geometric properties. With this, even structuring the underlying magnetic material into waveguides can be made obsolete since the geometry of the excitation structures can be adjusted such that excitation is restricted to specific regions. The basis of this has been investigated by numerical simulations in the work of Gruszecki *et al.* [4]. An experimental realization has also been observed using time-resolved Kerr microscopy [5] whereas in this work Brillouin light scattering spectroscopy (BLS) has been utilized which also gives insight into the lifetime of the spin waves.
A fundamental aspect in this context is the fact that the spatial distribution of the magnetic field generated by the currents in the CPW determines the efficiency with which spin waves of a certain wavevector are excited. More specifically, the excitation efficiency is directly proportional to the Fourier transform of the field distribution [6]. For micro- and nanoscopic CPWs, the generated field can be obtained in a straightforward approach from Biot and Savart's law [7].
Initially, thin films of Permalloy (Py, $Ni_{81}Fe_{19}$) with a nominal thickness of $d = 40\,\mathrm{nm}$ were sputtered onto thermally oxidized Si substrates. To prevent the material from oxidation, a double layer of MgO(5 nm)|Pt(5 nm) has been deposited onto the films. Characterization of these films has been performed employing ferromagnetic resonance spectroscopy which revealed an effective magnetization of $M_{\mathrm{eff}} = (701 \pm 2)\,\mathrm{kAm^{-1}}$ and a Gilbert damping parameter of $\alpha = 8.7 \times 10^{-3}$. These values are in reasonable agreement with the ones reported elsewhere [8]. Subsequently, the Py films have been structured into pads utilizing Ar^+ ion beam etching in order to prevent an unnecessary absorption of microwave power in the input leads of the CPWs. For the same purpose and to prevent short circuits, a 25 nm thick layer of hydrogen silsesquioxane was used to coat the magnetic structures. Following the production of the magnetic structures, the CPWs for spin-wave excitation were fabricated using a conventional lift-off process and electron beam evaporation. They consisted of a 115 nm thick Au layer on top of a 20 nm Cr layer. In order to enable a localized excitation of spin waves of certain wave vectors, the spatial dimensions of the CPWs were modulated. Fig. 1 shows an SEM image taken of one of the structures. The modified geometry is visible in the center of the image. A smooth and defect-free transition between the areas of

All values in nm (±30 nm)	*Type A*		*Type B*	
Length of excitation area l_b	3550		2296	
Geometry	Wide	Narrow	Wide	Narrow
Outer width w_a	2455	1553	1748	1130
Spacing s	535	550	240	310
Inner width w_i	1275	355	1008	335

Table 1: Spatial dimensions of the CPW structures produced. All values are given in nanometers. For the respective parameters, cf. Fig. 1.

the CPW has been obtained. Two different types of CPWs were fabricated whose dimensions are listed in Table 1.

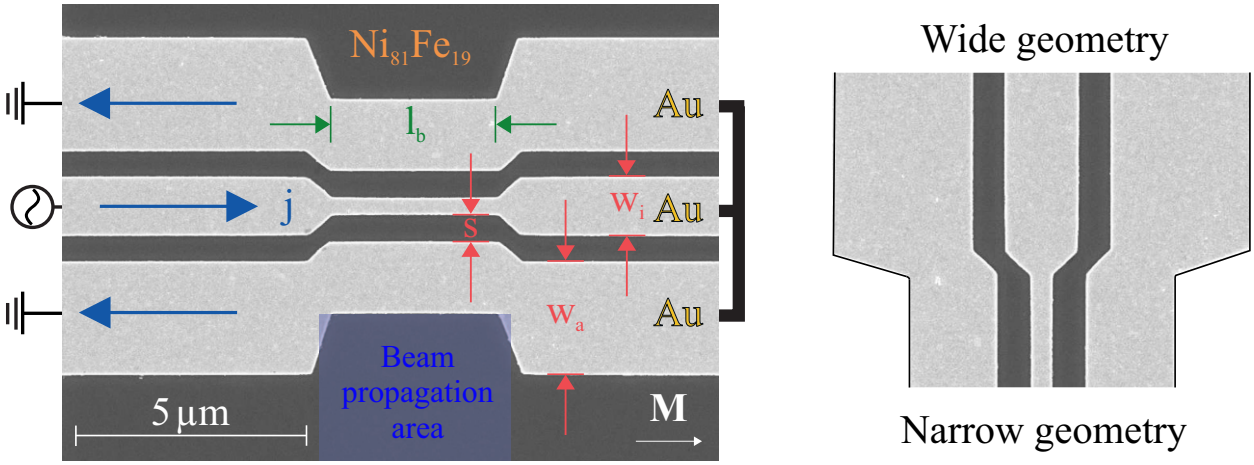

Fig. 1: SEM images of a CPW structure investigated in this work. The geometry of the structure is locally modified within a region of length l_b. Due to the different excitation efficiency (cf. Fig. 2), a proper selection of the frequency of the microwave current restricts the excitation of spin waves to the region of narrow geometry and their propagation to the beam propagation area (marked only on one side of the CPW structure).

For the investigation of the excitation characteristics, a static magnetic field of $\mu_0 H_{\text{ext}} = 300\,\text{mT}$ was applied parallel to the CPWs fed by a microwave current of varying frequency. For the different microwave frequencies, the BLS intensity was recorded in the center of the region of narrow geometry at a distance of 3 µm from the edge of the outer lead of the CPW as well as outside of the beam propagation area. Clearly, the results show the differing excitation spectra of both CPW geometries. The measured spin-wave intensity was compared to the calculated intensities which was obtained by a conversion from the momentum space into the frequency space taking into account the spin-wave dispersion relation and, hence, the parameters influencing it such as the saturation magnetization. Furthermore, the decreasing efficiency of the BLS detection needs to be considered.

The solid curves in Fig. 2 have been calculated for a (effective) film thickness of 30 nm and a saturation magnetization of $695\,\text{kAm}^{-1}$.
Based on the measured spin-wave spectra, we select an excitation frequency of $f_{\text{SW}} = 8.3\,\text{GHz}$ for

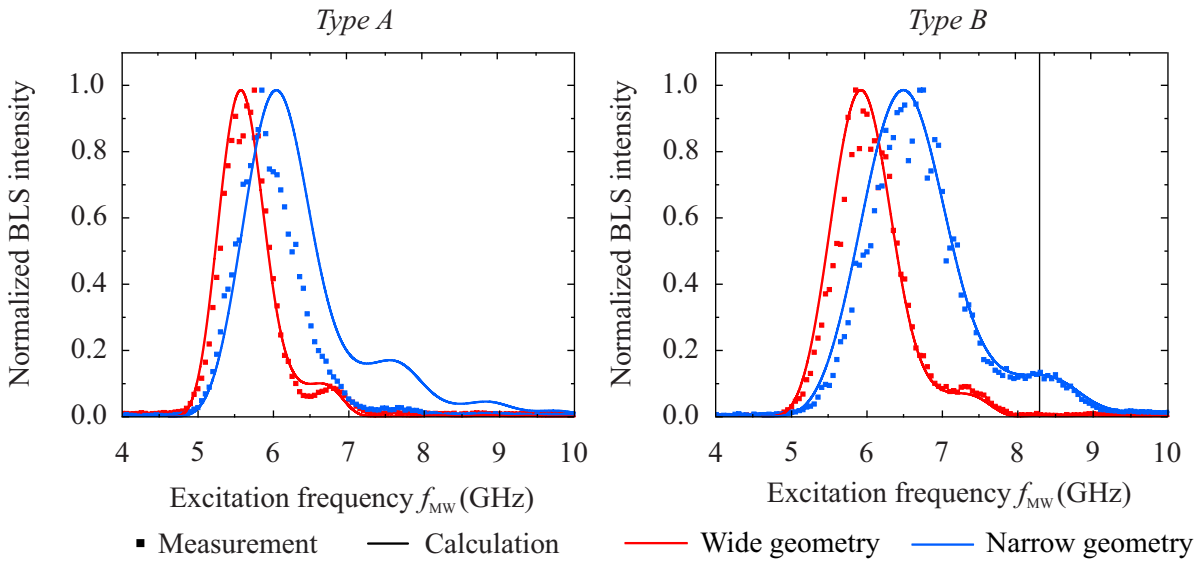

Fig. 2: Calculated (solid lines) and measured (squares) excitation efficiency of the CPW structures for the narrow and wide geometry, i.e., inside and outside the designated excitation area, respectively. Left: CPW of Type A, Right: CPW of Type B (cf. Table 1). The vertical line marks the excitation frequency for the measurements as discussed in the following.

a CPW of *Type B* (cf. Table 1) and apply a microwave power of $-10\,\mathrm{dBm}$. For this frequency, a pronounced restriction of the excitation to the area of narrow geometry is expected (cf. Fig. 2). A two-dimensional scan in the area of spin-wave propagation originating from the excitation zone reveals the profile of the spin-wave beam. As depicted in Fig. 3, a highly localized excitation and propagation of spin waves is clearly visible. These results underline the successful restriction of the excitation to specific areas and, with that, the creation of propagating spin-wave beams for further investigations of spin-wave manipulation techniques.

Using waveguides may come along with an increase in spin-wave damping, i.e., a decrease of lifetime, due to defects induced by the structuring process [9]. Especially with regards to advances in the field of nanomagnonics employing waveguides with widths in the range of 100 nm this influence requires clarification. Hence, the investigation of propagating spin waves in films can give a deeper insight into the origin of the lifetime reduction. The lifetime τ can be found from the exponential decay of the spin waves according to the following procedure: From a twodimensional BLS scan of the propagating spin waves the integrated intensity is extracted across the spin-wave beam. Fitting an exponential decay to the obtained curve leads to the amplitude decay length δ which is twice the value of the intensity decay length. From that, together with the group velocity v_g which is calculated from the dispersion relation, the lifetime of the propagating surface modes can be determined according to the relation $\tau = \frac{\delta}{v_\mathrm{g}}$. These are found to be practically independent on the frequency. From the FMR measurements, the lifetime can be estimated according to the relation [10]

$$\frac{1}{\tau_\alpha} = \alpha \left(\omega_0 + \frac{\omega_\mathrm{M}}{2} \right) \tag{1}$$

leading to $\tau_\alpha = (1.346 \pm 0.019)\,\mathrm{ns}$ (with $\omega_0 = \gamma\mu_0 H$ and $\omega_0 = \gamma\mu_0 M_\mathrm{S}$). For an excitation frequency of 8.3 GHz, a spin-wave lifetime of $\tau_\mathrm{SW} = (1.165 \pm 0.169)\,\mathrm{ns}$ is found which is in reasonable

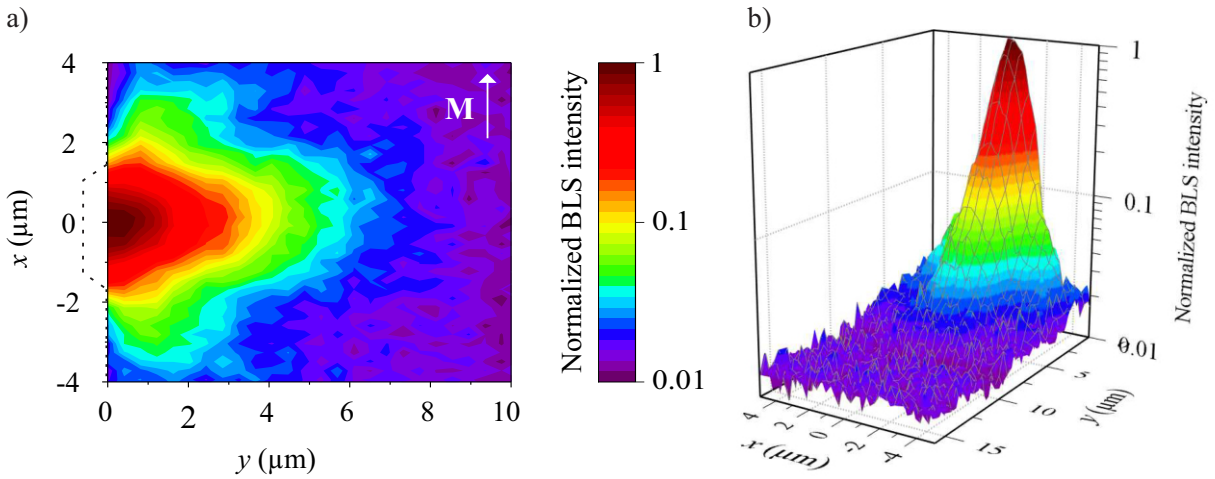

Fig. 3: Visualization of the spin-wave intensity for an excitation frequency of 8.3 GHz measured at a CPW of *Type B*. a) Intensity map of the spin-wave beam. The dashed line shows the edge of the CPW structure. b) Profile of the spin-wave beam clearly underlining its exponential decay.

agreement with the lifetime obtained from the FMR spectroscopy. A good accordance between these lifetimes is also found for other excitation frequencies. This leads to the conclusion that an intrinsic effect can be excluded as a reason for the lifetime reduction. Hence, defects induced during the structuring process might play a significant role for the damping of spin waves possibly impeding the development of devices based on nano-sized magnonic structures.

Financial support within SFB/TRR 173 *Spin+X* is gratefully acknowledged.

References

[1] V.V. Kruglyak, S.O. Demokritov, D. Grundler, *Magnonics*, Journal of Physics D: Applied Physics **43**, 264001 (2010).
[2] K. Vogt, H. Schultheiss, S.J. Hermsdoerfer, P. Pirro, A.A. Serga, B. Hillebrands, *All-optical detection of phase fronts of propagating spin waves in a $Ni_{81}Fe_{19}$ microstripe*, Applied Physics Letters **95**, 182508 (2009)
[3] B.A. Kalinikos, *Excitation of propagating spin waves in ferromagnetic films*, IEE Proceedings H: Microwaves, Optics and Antennas **1**, 4 (1980)
[4] P. Gruszecki, M. Kasprzak, A.E. Serebryannikov, M. Krawczyk, W. Smigaj, *Microwave excitation of spin wave beams in thin ferromagnetic films*, Scientific Reports **6**, 22367 (2016)
[5] H.S. Körner, J. Stigloher; C.H. Back, *Excitation and tailoring of diffractive spin-wave beams in NiFe using nonuniform microwave antennas*, Physical Review B, **10** 100401(R) (2017).
[6] V.E. Demidov, M.P. Kostylev, K. Rott, P. Krzysteczko, G. Reiss, S. O. Demokritov, *Excitation of microwaveguide modes by a stripe antenna*, Applied Physics Letters, **11**, 112509 (2009).
[7] D. Chumakov, *High Frequency Behaviour of Magnetic Thin Film Elements for Microelectronics*, PhD Thesis, TU Dresden (2006).
[8] S.S. Kalarickal, P. Krivosik, M. Wu, C.E. Patton, M.L. Schneider, P. Kabos, T.J. Silva; J.P. Nibarger, *Ferromagnetic resonance linewidth in metallic thin films*, Journal of Applied Physics, **9**, 93909 (2006).
[9] T. Fischer, *Herstellung, Charakterisierung und Spinwelleneigenschaften mikrostrukturierter $Co_{40}Fe_{40}B_{20}$-Spinwellen-Wellenleiter*, Diploma Thesis, TU Kaiserslautern (2015)
[10] D.D. Stancil, A. Prabhakar, *Spin Waves. Theory and Applications*, Springer, New York (2009)

4.11 Spin-wave mode conversion in a thermal gradient

A.V. Chumak, P. Pirro, and B. Hillebrands

In collaboration with M. Vogel, R. Aßmann, and G. von Freymann, Arbeitsgruppe "Optische Technologien und Photonik", Fachbereich Physik and Landesforschungszentrum OPTIMAS, Technische Universität Kaiserslautern, 67663 Kaiserslautern, Germany

Spin waves, and their quanta magnons, are considered to be the information carriers for novel data-processing devices [2]. However, the dispersion relations of spin waves in in-plane magnetized films are strongly anisotropic. This anisotropy has to be taken into account for efficient data transfer between the building blocks in future magnonics circuits. For dipolar spin waves in in-plane magnetized films two modes can be distinguished: backward volume magnetostatic spin waves (BVMSWs) propagating along the static magnetization and magnetostatic surface spin waves (MSSWs) propagating perpendicularly, respectively [3, 4]. For a fixed saturation magnetization and a fixed external magnetic field, the frequencies of MSSWs lie above the ferromagnetic resonance (FMR) frequency whereas the frequencies of BVMSWs lie below. Hence, a change of the propagation direction with respect to the magnetization requires mode conversion between MSSWs and BVMSWs, which energy conservation obviously prohibits in homogeneous films. Thus, non-linear or non-stationary mechanisms need to be employed.

Here, we propose to use reconfigurable laser-induced magnetization gradients [5] to break the system's translational symmetry [1]. The resulting changes in the magnetization shift the dispersion relations locally and allow for operating with different spin-wave modes at the same frequency. Spin-wave momentum is first transformed via refraction at the edge of the magnetization gradient region and then continuously modified inside the region. An adiabatic continuous transformation of the spin-wave momentum in the magnetization gradient region leads to a highly-efficient mode conversion over a wide frequency range as opposite to previous realisations of the mode conversion [6–9].

Let us first discuss the mechanism behind the two-dimensional magnon guiding for the case of converting a pure BVMSW into a pure MSSW, propagating perpendicularly to the BVMSWs mode. Fig. 1a depicts this configuration. The pure initial and final modes propagate in regions of the magnetic waveguide with saturation magnetization M_{S1} (blue region online) and M_{S2} (red region online), respectively. To obey energy conservation, the dispersion relations of the two modes have to overlap, requiring $M_{S2} < M_{S1}$ (see solid blue line and dashed red line in Fig. 1b, overlap is found in the grey marked conversion area). To additionally fulfil momentum conservation, the wavevectors have to adiabatically be transformed into each other. This adiabatic transformation is enabled by a gradient of the saturation magnetization perpendicular to the initial propagation direction (grey area in Fig. 1a) and spatially represents the area in which the dispersion relations overlap. To illustrate the flow of spin-wave energy during the conversion process, the local spin-wave group velocities $\mathbf{v}_{gr}$ are depicted in Fig. 1a by black arrows. This process is initiated by refraction of the spin wave [10] at the edge of the magnetization gradient (orange line in Fig. 1a, modified wavelength but no change in the direction of $\mathbf{k}$ for our simple example but important for other heating patterns) and continues with quasi-adiabatic transformation of the spin-wave wave vector [11] (highlighted with coloured arrows at certain positions).

This work has been published recently on arXiv [1].

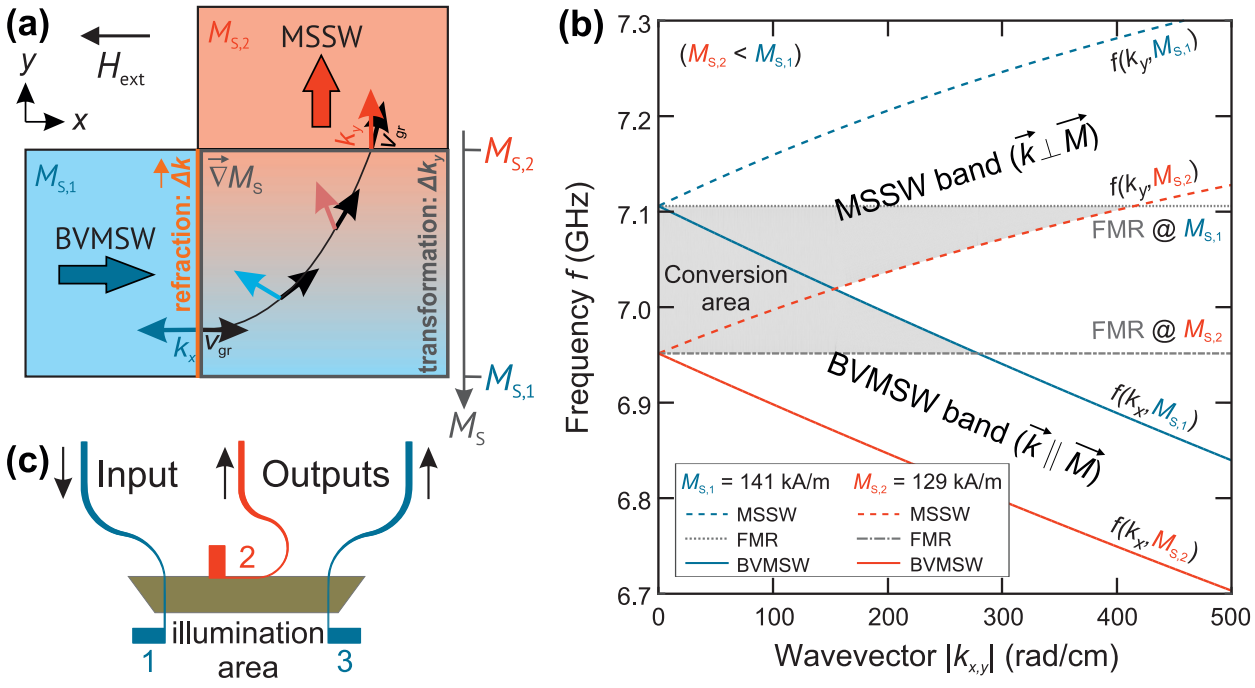

Fig. 1: a) The mode conversion process transforms BVMSW (blue) to MSSW (red) modes. Both types of spin waves propagate in the sketched areas at different values of the saturation magnetization M_S. b) The dispersion relations of MSSW (propagating in the y direction) and BVMSW modes (propagating in the x direction) are shown versus the wavevector $\mathbf{k}$ projections. Due to the saturation magnetization gradient, a wide band for both modes is realised. The intersection of these bands forms the conversion area (grey), where the mode conversion is allowed. The conversion area is limited by the ferromagnetic resonance frequencies (FMR) for M_{S1} and M_{S2}, respectively. c) The experimental set-up is shown schematically. A light pattern which creates a magnetization gradient is formed close to the center in x-direction of the waveguide at antenna 2 (illumination area). With respect to the externally applied magnetic field H_{ext}, antennas 1 and 3 can excite and detect BVMSWs. Antenna 2 is used for the detection of MSSWs.

We perform experimental studies on a 6.6 μm thick ferrimagnetic Yttrium Iron Garnet (YIG) film acting as spin-wave waveguide. The dependency of its saturation magnetization M_S on the temperature T is well known: $M_S(T)$ decreases for increasing T [5, 12]. To heat the magnon waveguide arbitrary intensity distributions are realized via computer-generated holograms. Green laser light from a continuous wave laser (532 nm) illuminates a phase-only spatial light modulator resulting in a controlled intensity distribution on the spin-wave waveguide. The optical set-up is similar to the one developed earlier in [5]. An infrared camera records the resulting temperature distribution over the sample. The corresponding local saturation magnetization is calculated using the given spatial temperature distribution. To excite and detect spin waves, a vector network analyser is connected to the three-microstrip-antenna configuration shown in Fig. 1c to determine the scattering parameters S_{31} and S_{21}.

Fig. 2a depicts transmission spectra for spin-wave transmission from antenna 1 to 3 (parameter S_{31}). Without any intensity distribution, S_{31} follows a typical BVMSW transmission spectrum [13] with a maximum of about -24 dB. This value is defined by the excitation/detection efficiency of the antennas and by the damping of spin waves propagating over 10 mm distance. The grey shaded area (7.10 – 7.15 GHz) marks the spectral region above the ferromagnetic resonance frequency for an unheated sample. In this frequency range, only higher width-modes (pronounced peak) can be excited by antenna 1. However, spin-wave modes with frequencies above 7.1 GHz are

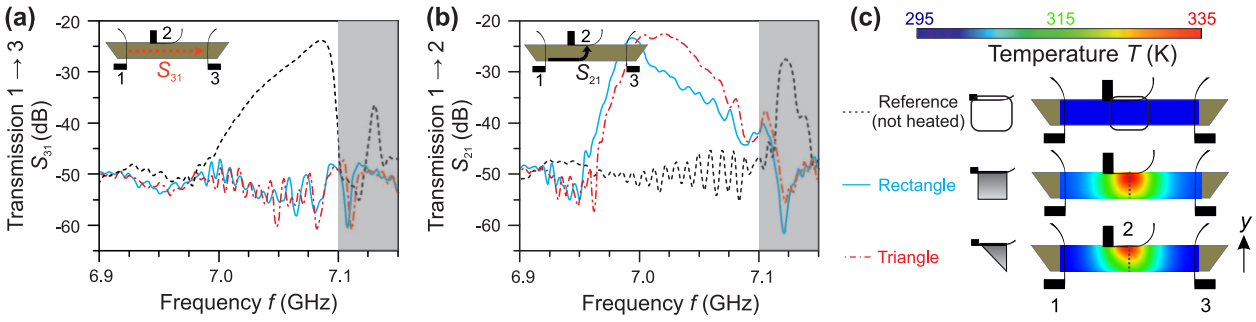

Fig. 2: Transmission characteristics for different light intensity distributions and the corresponding local saturation magnetization. A rectangular and triangular graded intensity distribution is applied in the center between antenna 1 and 3 - at the position of antenna 2 (illumination area in Fig. 1c) - and the corresponding spin-wave transmission S_{31} (a) and S_{21} (b) is measured.

not of interest in this work. The picture dramatically changes, if we shine either one of the two exemplary intensity distributions onto the sample: for a rectangular (solid blue curve) as well as for a triangular distribution (dash-dotted red curve) the transmission from antenna 1 to antenna 3 vanishes completely.

In Fig. 2b, we observe the opposite behaviour. Transmission from antenna 1 to 2 (parameter S_{21}) for the reference measurement (black dashed line) shows practically no signal: The constant background around $-50\,\mathrm{dB}$ over a wide frequency range up to 7.1 GHz is due to the electromagnetic leakage between the antennas. The absence of the S_{21} transmission shows that no excitation of waves with $\mathbf{k} \perp \mathbf{H}$ occur and, consequently, no BVMSW-to-MSSW mode conversion is possible, as expected. For the rectangular and triangular pattern, a strong transmission signal is observed, comparable in strength to the one measured for the BVMSW in the reference measurement (Fig. 2a). This behaviour is consistent with mode-conversion from BVMSW to MSSW mode. To explain this further, let us discuss the resulting saturation magnetization gradient in more detail. Both intensity patterns form a gradient reaching from the maximum intensity (upper waveguide edge at antenna 2) down to 20 % of this value (lower waveguide edge, see bottom part of Fig. 2c). Due to the intrinsic thermal conductivity of YIG a temperature gradient ∇T and, thus, a magnetization gradient $\nabla M_\mathrm{S}(T)$ evolves inside the sample. We keep the saturation magnetization $M_{\mathrm{S}2}(T)$ at antenna 2 approximately constant by adjusting the laser power appropriately. This is done to allow a quantitative comparison of the two cases. Antenna 1 and antenna 3 are kept far away from the heated area, thus $M_{\mathrm{S}1}$ and $M_{\mathrm{S}3}$ are almost equal and correspond approximately to the value at room temperature. By non-uniformly heating the sample, the S_{21}-parameter maximum increases up to $-23\,\mathrm{dB}$ for the rectangular pattern. Compared to the maximum of the BVMSW spectrum S_{31} ($-24\,\mathrm{dB}$), the mode conversion in magnetization gradients is very efficient. Furthermore, the bandwidth of the converted spectrum at $-30\,\mathrm{dB}$ is around 38 MHz. In contrast to the unheated sample, now the S_{31}-parameter shows practically no transmission since the spin waves are converted and partially reflected in the heated region.

In order to obtain deeper insight into the conversion mechanism, we performed numerical micromagnetic calculations and an isofrequencies-based analysis in [1]. In general, two mechanisms changing the direction of the spin-wave propagation are indentified. First, the refraction at the interface or at the shape of the magnetization gradient takes place [10]. Afterwards, mode conversion occurs in the case of a rectangular magnetization pattern: the spin-wave wavevector and, respectively, its wavelength change differently in different positions over the waveguide's width re-

sulting in a bending of the phase fronts and in an adjustment of the group velocity's direction (like it is shown in Fig. 1a). The spin waves propagate into regions with decreased M_S adiabatically. A similar behaviour is observed in the triangular case. The spin wave is converted adiabatically while propagating towards the region of lower saturation magnetization. However, for the triangle, an additional refraction [10] due to the shape of the $\nabla M_S(T)$ area that changes the orientation of the spin-wave wave vector (as opposite to the rectangular case) occurs. The wave propagates towards the interface under an angle of 45° and, thus, k_x and k_y are modified. And afterwards, the magnetizaton gradient $\nabla M_S(T)$ leads only to an increase in k_y. It is shown in [1] that a direct conversion from BVMSWs to MSSWs due to the geometrical shape is possible. By combining both conversion principles, the efficiency of the mode conversion is improved. This is in direct agreement with our experimental findings.

To conclude, we proposed and demonstrated experimentally mode conversion between backward volume and magnetostatic surface spin-wave modes using gradients of the saturation magnetization M_S. The gradients perpendicular to the spin-wave propagation direction allow for the 90 degree rotation of the spin-wave wavevector via breaking the translational symmetry of the waveguide. As opposite to the spin-wave momentum, the energy of spin waves is conserved in this process due to the intersection of frequency bands of both spin-wave modes allowed in a non-uniform media. Since the proposed conversion is an adiabatic process (the characteristic sizes of the gradients are much larger than the spin-wave wavelength) it allows for the minimization of undesirable reflections and ensures high efficiency of the conversion in a wide range of spin-wave frequencies.

Financial support by DFG within project SFB/TRR 173, Spin+X - Spin in its collective environment, is gratefully acknowledged.

References

[1] M. Vogel, R. Aßmann, P. Pirro, A.V. Chumak, B. Hillebrands, G. von Freymann, *Adiabatic control of spin-wave propagation using magnetisation gradients*, arXiv:1711.00508 (2017).
[2] A.V. Chumak, V.I. Vasyuchka, A.A. Serga, B. Hillebrands, *Magnon spintronics*, Nature Physics **11**, 453 (2015).
[3] R.W. Damon, J.R. Eshbach, *Magnetostatic modes of a ferromagnet slab*, Phys. Chem. Solids **19**, 308 (1961).
[4] B.A. Kalinikos, A.N. Slavin, *Theory of dipole-exchange spin-wave spectrum for ferromagnetic films with mixed exchange boundary conditions*, J. Phys. C **19**, 7013 (1986).
[5] M. Vogel, A.V. Chumak, E.H. Waller, T. Langner, V.I. Vasyuchka, B. Hillebrands, G. von Freymann, *Optically-reconfigurable magnetic materials*, Nature Physics **11**, 487 (2015).
[6] K. Vogt, H. Schultheiss, S. Jain, J.E. Pearson, A. Hoffmann, S.D. Bader, B. Hillebrands, *Spin waves turning a corner*, Appl. Phys. Lett. **101**, 042410 (2012).
[7] T. Brächer, P. Pirro, J. Westermann, T. Sebastian, B. Lägel, B. Van de Wiele, A. Vansteenkiste, B. Hillebrands, *Generation of propagating backward volume spin waves by phase-sensitive mode conversion in two-dimensional microstructures*, Appl. Phys. Lett. **102**, 132411 (2013).
[8] A.V. Sadovnikov, C.S. Davies, S.V. Grishin, V.V. Kruglyak, D.V. Romanenko, Yu.P. Sharaevskii, S.A. Nikitov, *Magnonic beam splitter: the building block of magnonic circuitry*, Appl. Phys. Lett. **106**, 192406 (2015).
[9] C.S. Davies, V.V. Kruglyak, *Graded-index magnonics*, Low Temperature Physics **41**, 760 (2015).
[10] J. Stigloher, M. Decker, H.S. Körner, K. Tanabe, T. Moriyama, T. Taniguchi, H. Hata, M. Madami, G. Gubbiotti, K. Kobayashi, T. Ono, C.H. Back, *Snell's law for spin waves*, Phys. Rev. Lett., **117**, 037204 (2016).
[11] O. Dzyapko, I.V. Borisenko, V.E. Demidov, W. Pernice, S.O. Demokritov, *Reconfigurable heat-induced spin wave lenses*, Appl. Phys. Lett. **109**, 232407 (2016).
[12] P. Hansen, P. Röschmann, W. Tolksdorf, *Saturation magnetization of gallium-substituted yttrium iron garnet*, J. Appl. Phys. **45**, 2728 (1974).
[13] A.A.Serga, A.V. Chumak, B. Hillebrands, *YIG magnonics*, J. Phys. D: Appl. Phys. **43**, 264002 (2010).

4.12 Frequency-division multiplexing in magnonic logic networks based on caustic-like spin-wave beams

F. Heussner, T. Fischer, T. Brächer, A.A. Serga, B. Hillebrands, and P. Pirro

Frequency-division multiplexing (FDM) constitutes the basis for parallel data processing in a single device and for efficient information transport through logic circuits. In such networks, signals at different frequencies are used to simultaneously transfer information through the same conduits in separated frequency channels. In this work, we present an approach for the realization of FDM in magnonic networks [1, 2] by utilizing caustic-like spin-wave beams, which originate from the anisotropic spin-wave propagation in in-plane magnetized 2D magnetic media [3–5].
Anisotropic spin-wave propagation has two consequences. On the one hand, for a fixed spin-wave frequency, a change in the direction of the spin-wave wavevector is accompanied by a change of its absolute value. On the other hand, in general, the group-velocity vector and the wavevector of the spin waves are not parallel. Hence, even changing the wavevector direction, and, consequently, also its absolute value, can leave the direction of the group velocity nearly unchanged. Is this the case, a focusing of spin-wave energy into designated directions of the magnetic film resulting in the creation of so called caustic-like spin-wave beams will occur even if spin waves are excited in a broad wavevector range by, e.g., point-like spin-wave sources.

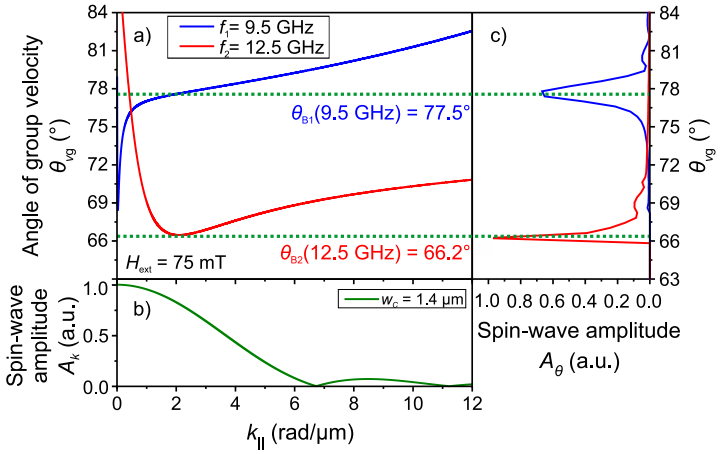

Fig. 1: Calculation of the propagation angle θ_B of caustic-like spin-wave beams. a) Angle of the group-velocity vector relative to the local magnetization as a function of the wavevector component parallel to the magnetization (material parameters of CMFS). b) Wavevector spectrum of an input waveguide connected to a 2D magnetic film area acting as a spin-wave source. c) Resulting spin-wave amplitudes depending on the angle of the group-velocity vector.

To calculate the direction of these beams, the following approach was refined based on the discussions in [6]. For a given material system in combination with the applied bias magnetic field H_{ext} and the excitation frequency f, the possible angles θ_{vg} of the spin-wave group-velocity vector relative to the local magnetization can be calculated from the spin-wave dispersion [7]. Its dependence on the wavevector component $k_{||}$, which is the projection of $\mathbf{k}$ onto the magnetization, is shown in Fig. 1a. In this case, an excitation of spin waves at two fixed frequencies $f_1 = 9.5\,\text{GHz}$ and $f_2 = 12.5\,\text{GHz}$ taking place in a 30 nm thick $Co_2Mn_{0.6}Fe_{0.4}Si$ (CMFS [8]) film, which is in-plane magnetized by a field of $\mu_0 H_{\text{ext}} = 75\,\text{mT}$, is assumed. For a precise estimation of the beam directions, the specific excitation scheme of the spin waves in the magnetic film needs to be considered as well since it determines the excited wavevector spectrum. In our case, the first transversal spin-wave mode propagating in a narrow waveguide acts as an effective point-like spin-wave source if this input waveguide is connected to an unstructured magnetic film [3, 4]. The resulting wavevector spectrum in the 2D film area, i.e. the wavevector dependent spin-wave amplitude $A_k(k_{||})$,

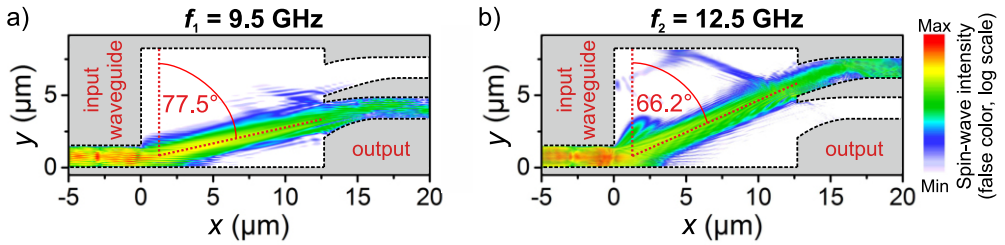

Fig. 2: Design of a spin-wave demultiplexer based on caustic-like spin-wave beams. Spin-wave signals at a) $f_1 = 9.5\,\mathrm{GHz}$ and b) $f_1 = 12.5\,\mathrm{GHz}$ become spatially separated and channeled into different output waveguides due to their different angles of propagation.

calculated by Fourier transforming the transversal mode profile, is shown in Fig. 1b. In this calculation, the input spin-wave waveguide of a width of $w_c = 1.4\,\mu\mathrm{m}$ is considered to be magnetized along its short axis. The final step to determine the beam direction θ_B is to calculate the spin-wave amplitude A_θ in dependence on the angle θ_{vg} of the group-velocity vector. This can be done by assigning the $k_{||}-$dependent amplitudes A_k of Fig. 1b to the corresponding angles θ_{vg} of Fig. 1a. Figure 1c shows the result for the previously discussed parameters.

For both frequencies, a strong focusing of the spin-wave amplitude around the group-velocity angles θ_B takes place, despite the broad wavevector spectrum A_k. This can be attributed to the very small variation of the group-velocity angle θ_{vg} over big ranges of the wavevector $k_{||}$. Aiming at an approach to realize FDM in a magnonic logic circuit, the strong frequency dependency of the spin-wave beam directions has to be highlighted which becomes obvious when comparing the beam angle $\theta_{B1} = 77.5^\circ$ for spin waves at the frequency of $f_1 = 9.5\,\mathrm{GHz}$ and the beam angle $\theta_{B2} = 66.2^\circ$ at $f_2 = 12.5\,\mathrm{GHz}$. Hence, a frequency variation of $\Delta f = 3\,\mathrm{GHz}$ results in a pronounced change of the beam angle of $\Delta\theta_B = 11.3^\circ$ which is much larger than the maximal beam divergence angle of around 3°. The strong beam angle variation demonstrates the applicability of the caustic effect to separate and combine spin-wave signals of different frequencies.

By the utilization of micromagnetic simulations [9] using the open-source simulation tool MuMax3 [10], a device design has been developed which enables the implementation of the FDM concept into magnonic logic circuits. The results are presented in the form of time-averaged, frequency-dependent spin-wave intensity maps which have been obtained by Fourier-transforming the raw data in time [11]. In all cases, the material parameters of CMFS have been used and the 30 nm thick structures are in-plane magnetized along the y-direction by an external magnetic field of $\mu_0 H_{ext} = 75\,\mathrm{mT}$.

As a first step, it will be demonstrated how spin-wave signals of different frequencies can be spatially separated by utilizing a specially designed magnetic structure which, hence, acts as a spin-wave demultiplexer (DEMUX). Simultaneously, the calculation of the beam angles and, by association, the presented theoretical approach is verified. The magnetic structure of the DEMUX design is indicated by the surrounding black, dashed lines in Fig. 2. It consists of a 1.5 µm wide input waveguide [12], a broadened magnetic area and two 1.5 µm wide output waveguides. Spin waves, which represent the input signal inside a magnonic network, are excited in the input waveguide by a microwave magnetic field oriented along the z-axis. The sharp transition to the broad magnetic area ($x = 0\,\mu\mathrm{m}$) acts as a point-like source for secondary spin waves exhibiting a broad wavevector spectrum, which leads to the creation of caustic-like spin-wave beams as discussed above. Already up to this point, the first important result can be seen in Fig. 2. In case the spin waves are excited at a frequency of $f_1 = 9.5\,\mathrm{GHz}$ (Fig. 2a), the resulting spin-wave beam occurs at

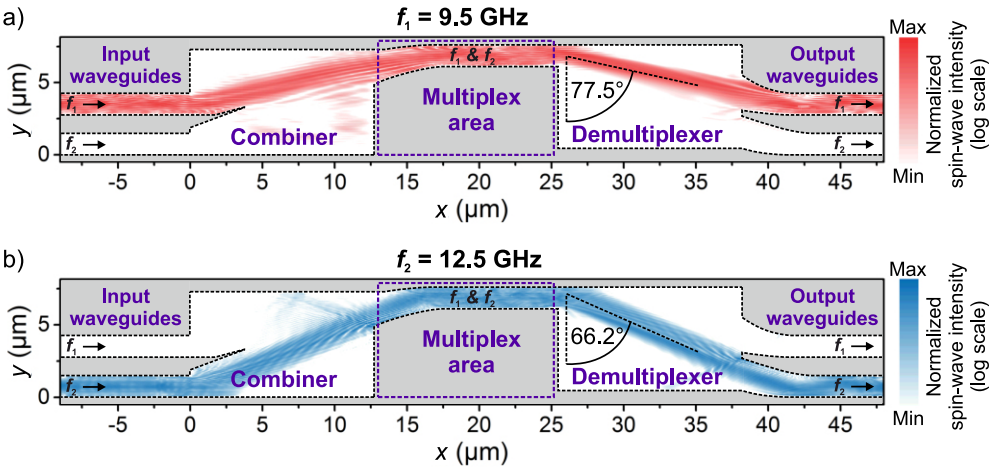

Fig. 3: FDM circuit for magnonic logic networks based on caustic-like spin-wave beams [15]. Spin-wave signals of different frequencies enter the circuit through different input waveguides. Due to different beam angles, they are combined into the shared multiplex area and afterwards separated again into different output waveguides. The procedure is shown separately for spin-wave signals at a) $f_1 = 9.5\,\mathrm{GHz}$ and b) $f_2 = 12.5\,\mathrm{GHz}$.

an angle of $\theta_{B1} = 77.5\,^\circ$, whereas the beam direction is changed to $\theta_{B2} = 66.2\,^\circ$ for $f_2 = 12.5\,\mathrm{GHz}$ (Fig. 2b). The occurring beam angles are in perfect agreement with the calculations and, hence, the simulation confirms the theoretical approach.

To exploit the frequency dependence of the beam angles, two output waveguides are added. The transition zones are specially tailored and the positions are adjusted to ensure an efficient channeling of spin-wave energy into the output [13] according to the occurring beam directions. The results shown in Fig. 2 proof the targeted functionality. Spin-wave signals entering the device are channeled into different output waveguides and, hence, are separated depending on their frequency. It should be stressed that this device is based on intrinsic effects of the creation of caustic-like spin-wave beams and no external control, as, e.g., utilized in Ref. [14] to realize a time-division multiplexer, is required.

Finally, the design of a whole FDM circuit is demonstrated. The results are shown in Fig. 3 [15] and the magnetic structure is again depicted by the surrounding dashed lines. By employing the same approach as for the DEMUX, a combiner (MUX) for two spin-wave signals at two different frequencies can be designed. This is the first part of the structure. In this case, two input waveguides assigned to two different input frequencies are connected to the wide film area. The spike-shaped structure between the two inputs ensures that no spin-wave energy of the upper input spreads into the negative y-direction during the beam formation. At the end of the 2D combiner area, only one output is added so that the energy of both inputs can be collected if their corresponding spin-wave beams occur under the proper angles. This center waveguide constitutes the shared transmission line for the combined signals and, thus, is referred to as the multiplex area. After the pass-through of the spin waves, it also acts as the input for the DEMUX component.

Exemplarily, the passage of a spin-wave signal of frequency $f_1 = 9.5\,\mathrm{GHz}$ through the circuit will be discussed (Fig. 3a). The spin waves enter the device in the upper input waveguide. In the combiner region, caustic-like spin-wave beams are created and they reach the multiplex area due to their propagation angle of $\theta_{B1}(9.5\ \mathrm{GHz}) = 77.5\,^\circ$. According to Ref. [13], the caustic-like beams are transferred back to a waveguide mode. After passing this center waveguide, the signal enters the DEMUX and is channeled back to the upper output waveguide. Following the same princi-

ple, spin waves of the frequency $f_2 = 12.5\,\mathrm{GHz}$ entering the lower input are channeled into the same mulitplex area and finally guided into the lower output waveguide again (Fig. 3b). Hence, this design of a FDM circuit makes it possible to combine two spin-wave signals of two different frequencies into a shared transmission line and to separate them again afterwards. The working principle of the FDM circuit has been shown individually for every frequency in Fig. 3. However, in the linear regime due to the superposition principle, both signals can pass the device simultaneously without disturbing each other as has been proven in further simulations (not shown here).
The presented circuit is a passive network element without any additional power consumption. It enables simultaneous signal transport. In addition, by inserting proper logic elements in the multiplex area, simultaneous data processing in a single device can be realized resulting in a large efficiency boost of the logic circuits. Hence, the presented device can be a pivotal element for multi-frequency magnonic logic networks.

Financial support by DFG within project SFB/TRR 173 Spin+X is gratefully acknowledged.

References

[1] A. Khitun, *Multi-frequency magnonic logic circuits for parallel data processing*, J. Appl. Phys. **111**, 054307 (2012).
[2] A.V. Chumak, V.I. Vasyuchka, A.A. Serga, B. Hillebrands, *Magnon spintronics*, Nat. Phys. **11**, 453 (2015).
[3] V.E. Demidov, S.O. Demokritov, D. Birt, B. O'Gorman, M. Tsoi, X. Li, *Radiation of spin waves from the open end of a microscopic magnetic-film waveguide*, Phys. Rev. B **80**, 014429 (2009).
[4] T. Schneider, A.A. Serga, A.V. Chumak, C.W. Sandweg, S. Trudel, S. Wolff, M.P. Kostylev, V.S. Tiberkevich, A.N. Slavin, B. Hillebrands, *Nondiffractive subwavelength wave beams in a medium with externally controlled anisotropy*, PRL **104**, 197203 (2010).
[5] T. Sebastian, T. Brächer, P. Pirro, A.A. Serga, B. Hillebrands, T. Kubota, H. Naganuma, M. Oogane, Y. Ando, *Nonlinear emission of spin-wave caustics from an edge mode of a microstructured $Co_2Mn_{0.6}Fe_{0.4}Si$ waveguide*, PRL **110**, 067201 (2013).
[6] T. Schneider, *Phasenaufgelöste Untersuchung der Propagation von Spinwellenpaketen und der Entstehung von Spinwellen-Kaustiken* (PhD Thesis, Department of Physics, Technische Universität Kaiserslautern, 2009).
[7] B.A. Kalinikos, A.N. Slavin, *Theory of dipole-exchange spin wave spectrum for ferromagnetic films with mixed exchange boundary conditions*, J. Phys. C: Solid State Phys. **19**, 7013 (1986).
[8] CMFS: Saturation magnetization $M_S = 1151\,\mathrm{kA/m}$, exchange const. $A_{ex} = 22\,\mathrm{pJ/m}$, damping const. $\alpha = 0.0021$
[9] All magnetic structures are discretized into cells of $15\,\mathrm{nm} \times 15\,\mathrm{nm} \times 30\,\mathrm{nm}$ ensuring that in-plane wavevectors up to at least $100\,\mathrm{rad/\mu m}$ can be resolved. At the vertical boundaries of the structures, the damping is incrementally increased in 25 steps over a distance of $0.5\,\mu\mathrm{m}$ to $\alpha = 0.5$ to suppress reflections of spin-wave energy.
[10] A. Vansteenkiste, J. Leliaert, M. Dvornik, M. Helsen, F. Garcia-Sanchez, B. Van Waeyenberge, *The design and verification of MuMax3*, AIP Advances **4**, 107133 (2014).
[11] After calculating the ground state, the spin waves are excited during the whole simulation time of $t_s = 7.5\,\mathrm{ns}$ (DEMUX, Fig.2) or $t_s = 10\,\mathrm{ns}$ (FDM circuit, Fig.3), respectively. The resulting raw data of the simulation is the spatially resolved magnetization distribution which is saved every 25ps. The shown spin-wave intensity maps are calculated by a temporal Fourier-transformation and an integration of the resulting frequency-dependent spin-wave amplitude over an interval of $[f_i - 0.25\,\mathrm{GHz}, f_i + 0.25\,\mathrm{GHz}]$.
[12] Due to demagnetizing fields, an effective width of $w_c = 1.4\,\mu\mathrm{m}$ can be assumed as it was used in the theoretical calculations of the beam angles θ_B.
[13] F. Heussner, A.A. Serga, T. Brächer, B. Hillebrands, P. Pirro, *A switchable spin-wave signal splitter for magnonic networks*, Appl. Phys. Lett. **111**, 122401 (2017).
[14] K. Vogt, F.Y. Fradin, J.E. Pearson, T. Sebastian, S.D. Bader, B. Hillebrands, A. Hoffmann, H. Schultheiss, *Realization of a spin-wave multiplexer*, Nat. Commun. **5**, 3727 (2014).
[15] The normalized intensity shown here is calculated by normalizing the spin-wave intenstiy along the y-direction to its maximum. By this, the spin-wave damping is compensated to illustrate the working principle of the device.

C. Magnon Spintronics

The utilization of Spin Hall and Inverse Spin Hall effects to create and detect spin currents and magnetization dynamics has push the field of *magnon spintronics* into new directions. *Magnon spintronics* aims for the magnon to charge current conversion and for magnon-based data processing devices. A magnon, i.e. the quantum of a spin wave, carries an angular momentum or spin as well and can be used for storage, processing and transport of spin information, building on its outstanding properties such as long lifetime and potential for dissipationless transport.

In this section we focus on Spin Hall related effects such as the spin-pumping (SP) and the Inverse Spin Hall Effect (ISHE) by addressing systems like Fe/Pt, CoFeB/Pt-W, and YIG/Pt bilayers. We extend the field of magnon spintronics to the THz regime by presenting efficient metallic THz emitters, and we address the role of Dzyaloshinskii-Moriya interaction (DMI) on the future development of unidirectional spin wave emitters. We reveal important factors that could lead to more efficient spin-to-charge conversion in YIG/Pt and Fe/Pt bilayers. Furthermore, we probe the spin pumping mechanism through interfacial magnetite nanoparticles.

Report 4.13 presents recent results of the Terahertz radiation generation with epitaxial spintronic Fe/Pt bilayer emitters with a time domain spectroscopy system. We show, that epitaxial spintronic emitters have an increased signal amplitude compared to polycrystalline emitters. The usage of a collimating hyper-hemispherical Si lens increased the signal strength by a factor of almost 30. The THz pulse length and bandwidth is, in principle, only limited by the relaxation time of hot electrons in the Pt material. The Fe and Pt layer thicknesses were individually optimized in terms of the THz-E-field amplitude. We present a quantitative model that takes the optical absorption, the spin polarization of Fe, the impedance, the spin accumulation in Pt and the THz absorption in Fe into account.

In report 4.14 we demonstrate a large Spin Hall angle of $(7 \pm 1)\,\%$ of a Pt layer epitaxially grown on Fe by combining vector network analyzer ferromagnetic resonance spectroscopy (VNA-FMR) and angle-resolved spin pumping measurements. We determine the real part of the spin mixing conductance and show a very small spin diffusion length of the epitaxial Pt film of (1.13 ± 0.12) nm thickness. By examining a microstructured Fe/Pt sample having the saturated spin mixing conductance value and by making use of the different angular dependencies of the effects, we distinguish between spin rectification effects and the Inverse Spin Hall Effect. The large obtained value of the Spin Hall angle points to the direction that an epitaxially grown non-magnetic material could be more efficient in the spin-to-charge current conversion.

In report 4.15 we present our studies on the efficiency of spin pumping by both long-wavelength dipolar and short-wavelength exchange magnons parametrically excited in in-plane magnetized Pt-covered YIG films. In the field-dependent measurements of the Inverse Spin Hall voltage, a clearly visible sharp voltage peak is detected. The peak position does not depend on the film thickness and well relates to the confluence of two magnons, which are parametrically excited at half of the pumping frequency, into one magnon with the double frequency and wavevector.

In report 4.16 we address the role of Dzyaloshinskii-Moriya interaction (DMI) into causing frequency splitting on the spin wave dispersion of ultrathin CoFeB/Pt and CoFeB/W bilayers. The DMI constant was obtained with the help of wave-vector resolved Brillouin light scattering (BLS) spectroscopy that allowed us to determine the shift between positive and negative spin-wave wavevectors resulting in a value for the DMI constant. The DMI value was found to be significantly larger for the samples with an adjacent Pt interface in comparison to a W layer.

In report 4.17 we probe the spin pumping mechanism at the Fe/Pt interface by inserting insulating Fe_3O_4 nanoparticles. The presence of magnetite nanoparticles increases significantly the magnetic anisotropy of the system compared to a Fe/Al reference sample. In ferromagnetic resonance experiments the line width ΔH is almost 10 times larger for the sample with the interfacial nanoparticles. The spin pumping reveals a pronounced symmetric contribution together with a strongly increased line width of the measured DC voltage. The results hint to a strong interaction of nanoparticles with the surrounding spin system.

C. Magnon-Spintronik

Die Verwendung des Spin-Hall- und des inversen Spin-Hall-Effekts zur Erzeugung und Detektion von Spinströmen und Magnetisierungsdynamik hat das Forschungsfeld der *Magnon-Spintronik* in neue Bahnen gelenkt. Die *Magnon-Spintronik* zielt auf die Magnon- zu Ladungsstrom-Konversion und auf die technische Realisierung Magnonen-basierter Informationsverarbeitung ab. Ein Magnon, d.h. das Quant einer Spinwelle, trägt einen Drehimpuls oder Spin und kann für die Speicherung, Verarbeitung oder Transport von Spin-Informationen basierend auf seinen bemerkenswerten Eigenschaften wie der langen Lebenszeit und dem Potential für verlustfreien Transport benutzt werden.

In diesem Abschnitt fokussieren wir auf Spin-Hall-zugehörige Effekte wie dem Spin Pumping (SP) und dem inversen Spin-Hall Effekt (ISHE) durch das Addressieren von Systemen wie Fe/Pt, CoFeB/Pt-W Doppelschichten und YIG/Pt Doppelschichten. Wir erweitern das Feld der *Magnon-Spintronik* in den THz-Bereich durch das Vorstellen effizienter, metallischer THz-Emitter und wir zeigen die Rolle der Dzyaloshinskii-Moriya-Wechselwirkung (DMI) auf die zukünftige Entwicklung von unidirektionalen Spinwellen-Emittern auf. Wir decken wichtige Faktoren auf, die zu einer effizienteren Spin- zu Ladungsstrom-Konversion in YIG/Pt und Fe/Pt Doppelschichten führen könnte. Weiterhin untersuchen wir den Spin-Pump-Mechanismus durch Magnetite-Nanopartikel die sich an der Grenzfläche des Fe/Pt Systems befinden.

Der Bericht 4.13 präsentiert kürzliche Resultate für die Terahertz-Strahlungserzeugung durch epitaktische, spintronische Fe/Pt-Emitter mit Hilfe der Zeitdomänen-Spektroskopie. Wir zeigen, dass epitaktische, spintronische Emitter eine erhöhte Signalamplitude gegenüber polykristallinen Emittern haben. Die Verwendung einer hyper-hemisphärischen Si-Linse erhöht die Signalstärke um einen Faktor von nahezu 30. Die THz-Pulslänge und -Bandweite ist im Prinzip nur durch die Relaxationszeit der heißen Elektronen im Pt limitiert. Die Fe- und Pt-Schichtdicken wurden individuellt im Bezug auf die THz-E-Feld-Amplitude optimier. Wir beschreiben ein quantitatives Modell, dass die optische Absorption des Fe, die Impedanz, die Spin-Akkumulation im Pt und die THz-Absorption des Fe berücksichtigt.

Im Bericht 4.14 wird ein großer Spin-Hall-Winkel von $(7 \pm 1)\,\%$ für eine auf Fe epitaktisch gewachsene Pt-Schicht durch die Kombination von Vektor-Netzwerkanalysator-Ferromagnetische-Resonanzspektroskopie (VNA-FMR) und winkelaufgelösten Spin Pumping-Messungen demonstriert. Wir bestimmen den Realteil der Spin Mixing Conductance und belegen eine sehr kurze Spin-Diffusionslänge des epitaktischen Pt von (1.13 ± 0.12) nm. Durch die Untersuchung einer mikrostrukturierten Fe/Pt-Probe und durch die Ausnutzung der verschiedenen Winkelabhängigkeiten der Effekte können wir zwischen den Spin-Gleichrichtungseffekten und dem inversen Spin-Hall-Effekt unterscheiden. Der erhaltene große Wert des Spin-Hall-Winkels zeigt, dass ein epitaktisches, nicht-magnetisches Material mehr effizient sein könnte als polykristalline in Materialien.

In Bericht 4.15 zeigen wir unsere Studie über die Effizienz des Spinpump von sowohl langwelligen

dipolaren als auch kurzwelligen Austausch-Magnonen, die parametrisch in in-Film-magnetisierten, Pt-beschichteten YIG-Filmen angeregt wurden. In den Feld-abhängigen Messungen der inversen Spin-Hall-Effekt-Spannung wurde eine klar deutliche, scharfe Spannungsspitze entdeckt. Die Position der Spitze hängt nicht von der Schichtdicke ab und bezieht sich klar auf die Konfluenz zweier Magnonen, die parametrisch bei der halben Pumpfrequenz erzeugt wurden, zu einem Magnon mit doppelter Frequenz und Wellenvektor.

Bericht 4.16 addressiert die Rolle der Dzyaloshinskii-Moriya-Wechselwirkung (DMI) auf die Verursachung der Frequenzaufsplittung der Spinwellendispersion in ultra-dünnen CoFeB/Pt und CoFeB/W Doppelschichten. Die DMI-Konstante konnte mit Hilfe von Wellenvektor-aufgelöster Brillouin-Lichtstreuungsspektroskopie, gemessen werden die uns erlaubte die Verschiebung zwischen dem positiven und negativen Spinwellenvektor zu bestimmen. Die DMI-Konstante erwies sich als signifikant größer für Proben mit angrenzender Pt-Grenzschicht im Vergleich zu einer W-Grenzschicht.

In Bericht 4.17 untersuchen wir den Spin Pump-Mechanismus einer Fe/Pt Grenzschicht durch das Einfügen von Fe_3O_4-Nanopartikeln. Die Anwesenheit der Magnetit-Nanopartikel erhöht die magnetische Anisotropie des Systems signifikant im Vergleich zu einer Fe/Al-Referenzprobe. In ferromagnetischen Resonanzexperimenten ist die Linienbreite ΔH um ein fast Zehnfaches größer für die Probe mit den Grenzschicht-Nanopartikeln. Das Spin Pumping zeigt einen ausgesprochen symmetrischen Anteil zusammen mit einer stark erhöhten Linienbreite der gemessenen Gleichspannung. Die Ergebnisse deuten auf eine starke Wechselwirkung der Nanopartikel mit dem umgebenen Spin-System hin.

4.13 Optimized spintronic terahertz emitters based on epitaxially grown Fe/Pt layer structures

S. Keller, L. Scheuer, and E.Th. Papaioannou

In collaboration with G. Torosyan, Photonic Center Kaiserslautern, Kaiserslautern, 67663, Germany;
R. Beigang, Department of Physics, University of Kaiserslautern, Kaiserslautern, 67663, Germany

The use of Spin Hall Effects to generate and manipulate spin currents has provided a large thrust in the research field of spintronics the last decade. The Spin Hall effect and its reciprocal, the Inverse Spin Hall Effect (ISHE), provide the means for conversion between spin and charge currents [1]. In spin pumping experiments the generation of a spin current from a precessing magnetization in a magnetic layer (FM) and the electrical detection by an attached nonmagnetic metallic layer (NM) with a large spin-orbit coupling (e.g. Pt) are investigated. Recently, the decisive role of the ISHE on extending the field of spintronics into the terahertz (THz) regime was revealed [2,3]. THz spintronics has the potential of application in ultra-fast current and computer technologies [4]. In the particular case of THz emission induced by the ISHE in FM/NM layers, a femtosecond (fs) laser pulse pumps a FM/NM heterostructure and generates non-equilibrium spin polarized electrons in the FM layer. Subsequently, these electrons are diffusing in the non-magnetic layer through a super-diffusive process [5,6]. The spin current is then converted into a transient transverse charge current due to the ISHE in the NM layer. This transient current generates a short terahertz pulse polarized in the direction of the charge current that propagates perpendicular to the electrical current. The experimental demonstration of THz emission from FM/NM heterostructures due to ISHE has been shown recently [2,3]. Seifert et al. have shown that the THz signal exhibits a maximum for a specific total thickness of the metallic bilayer. In this work, we present the influence of the thickness of the individual layers on the THz emission amplitude and we discuss the role of the substrate. We demonstrate that for both Fe- and Pt-thickness dependencies the THz signal exhibits a maximum and a fast decrease after that. We quantify this behavior by using a model that takes into account generation of spin polarization starting at a minimum layer thickness of the magnetic material, spin diffusion, spin accumulation, and the electrical as well as optical properties of the spintronic emitters [7].

A standard THz time-domain spectroscopy (THz-TDS) system [8], has been used for generation and measurements of THz waveforms from different spintronic emitters (see Fig. 1a). The system is driven by a femtosecond Ti:Sa laser delivering sub-100 fs optical pulses at a repetition rate of 75 MHz. The laser beam is split into a pump and probe beam by a 90:10 beam-splitter. The stronger part is led through a mechanical computer-controlled delay line to pump the THz emitter, and the weaker part is used to gate the detector photoconductive antenna (PCA) with a 20 μm dipole antenna. The spintronic (ST) Fe/Pt emitter is placed in a weak (20 mT) magnetic field perpendicular to the direction of the pump beam and in the direction of the easy axis of Fe. The direction of the magnetic field determines the polarization of the THz field which is perpendicular to the direction of the magnetic field. Easily rotating the magnetic field into the opposite direction changes the phase of the detected THz waveforms by 180° (Fig. 1 b). In our configuration a hyperhemispherical Si-lens is being attached to the substrate of the emitter (shown in Fig. 2). With the lens attached an enhancement factor of up to 30 in electric field amplitude has been observed.

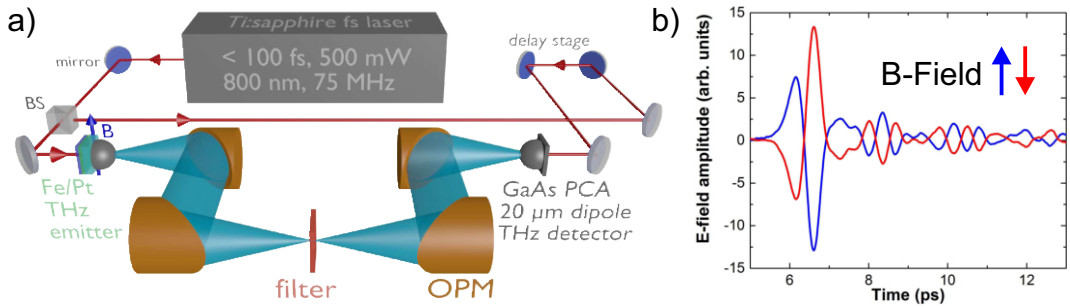

Fig. 1: a) Experimental set-up for THz generation. b) THz pulses for two opposite directions of the magnetic field.

The epitaxial Fe/Pt thin films were grown epitaxially on 0.5 mm-thick MgO (100) and Al_2O_3 (0001) substrates by molecular beam epitaxy (MBE) technique in an ultrahigh vacuum (UHV) chamber with a base pressure of 3×10^{-10} mbar. The thickness of the individual layers has been varied for Fe (1-12 nm) and for Pt (0.25-18 nm). The growth of Fe on sapphire (0001) is not perfect epitaxial because of a large lattice mismatch influencing the THz generation.

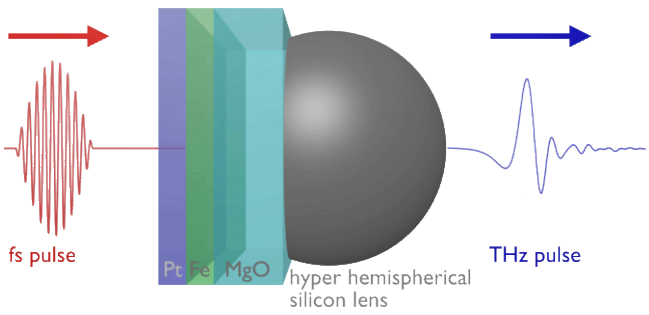

Fig. 2: Geometrical arrangement of the sample for the generation of THz radiation. In order to collimate the strongly divergent THz beam, a hyperhemispherical silicon lens is attached directly to the substrate without damaging the delicate Pt surface.

The pulse length and bandwidth of the THz pulse strongly depend on the rise and fall time of the transient electrical current in the NM layer induced via the ISHE. Whereas the rise time is mainly determined by the pump pulse length and the diffusion properties of the spin current, the fall time is limited by the relaxation time of the hot electrons in the conducting material. For the relaxation time we have considered a superdiffusive transport process resulting in a relaxation time in the order of 5 fs in Pt [9]. Such a relaxation time supports bandwidths up to several tens of THz and does not limit the bandwidth we have observed in our experiments. In addition, THz absorption in the layer structures and the substrate influences both pulse length and bandwidth. A typical pulse and the corresponding spectral amplitude extending to approximately 8 THz are shown in Fig. 3 for a 2 nm / 3nm Fe/Pt layer structure on MgO and Al_2O_3, respectively. The two spectra are shown as measured and are not corrected for the detector response. Above 3 THz the strong THz absorption of MgO is visible for the emitter on MgO. The maximal dynamic range is well above 60 dB, comparable with spectra obtained from PCA emitters. The maximum frequency measured in these experiments was finally determined by the frequency response of the PCA detector. The absorption around 8 THz in GaAs which is used as the semiconductor material for the detector limits the bandwidth. Epitaxial Fe/Pt emitters on MgO provide a higher dynamic range below 3 THz compared to the one grown on Al_2O_3. This finding is supported by results of experiments with polycrystalline emitters resulting in considerably weaker THz signals (not shown here). Together with a different detector (e.g. using electro-optical sampling in GaP) a much broader bandwidth

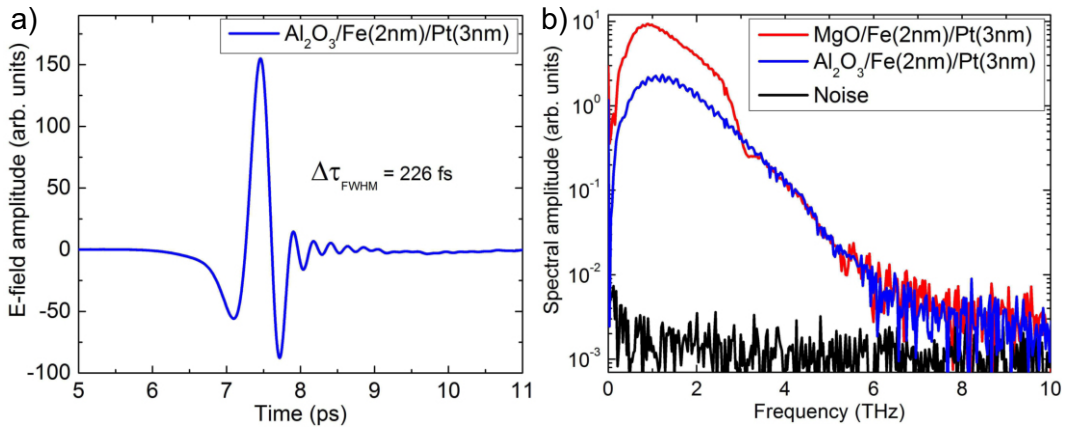

Fig. 3: a) Typical THz pulse obtained from a 2nm / 3 nm Fe/Pt sample. b) Spectra of the generated THz pulses for samples with two different substrates, MgO (red) and Al_2O_3 (blue).

can be obtained. In order to optimize our THz emitter we have performed a systematic study of the dependence of the THz amplitude on the thickness of the Pt and Fe layers for samples epitaxially grown on 0.5 mm thick MgO substrates. In Fig. 4a the results of the Fe (12 nm) / Pt (x nm) and Fig. 4b the Fe (x nm) / Pt (3 nm) series are shown. As a measure of the strength of the THz signal, the peak to peak amplitude of the first two oscillations of the THz pulse was determined. The variation in pump beam absorption with changing thicknesses has been taken into account for the comparison. The theoretical fitting curves in Fig. 4 are based on the following expression:

$$E_{\mathrm{THz}} \propto \frac{P_{\mathrm{abs}}}{d_{\mathrm{Fe}}+d_{\mathrm{Pt}}} \cdot \tanh\left(\frac{d_{\mathrm{Fe}}-d_0}{2\lambda_{\mathrm{pol}}}\right) \cdot \frac{1}{n_{\mathrm{air}}+n_{\mathrm{MgO}}+Z_0\cdot(\sigma_{\mathrm{Fe}}d_{\mathrm{Fe}}+\sigma_{\mathrm{Pt}}d_{\mathrm{Pt}})} \cdot \tanh\left(\frac{d_{\mathrm{Pt}}}{2\lambda_{\mathrm{Pt}}}\right) \cdot e^{-d_{\mathrm{Fe}}/s_{\mathrm{THz}}} \quad , \tag{1}$$

where n_{air}, n_{MgO} and Z_0 are the index of refraction of air and MgO at THz frequencies and the impedance of vacuum, respectively. In detail, the first factor accounts for the absorption of the fs-laser pulse in the metal layers. As only spin polarized electrons within a certain distance from the boundary between Fe and Pt will reach the Pt layer only a fraction of the measured total absorbed power contributes to the generated THz signal. This fraction scales with $1/(d_{Fe} + d_{Pt})$. The second term describes the loss of ferromagnetic ordering of Fe below a certain thickness d_0. Above this critical thickness the in-plane spin polarization saturates fast with λ_{pol}. The third term refers to the total impedance of the emitter and the fourth term refers to the spin accumulation in Pt (spin diffusion length λ_{Pt}). σ_{Fe} and σ_{Pt} are the electrical conductivities of the two materials, respectively. Although the electrical conductivity depends on layer thickness for very thin layers we have used a constant value for all layer thicknesses which are considerably smaller than the bulk valuesThe last term describes the attenuation of the THz radiation during propagation through the Fe layer itself. For the calculations we have assumed a spin current diffusion length in Pt of λ_{Pt} = 1.40 nm. This is in good agreement with direct measurements of the diffusion length using microwave techniques. The other parameters used for this fit are n_{air} = 1, n_{MgO} = 3, Z_0 = 377 Ω, $\sigma_{Fe} = 3.2\cdot10^6$ $\Omega^{-1}m^{-1}$, $\sigma_{Pt} = 4.5\cdot10^6$ $\Omega^{-1}m^{-1}$, d_0 = 0.9 nm, λ_{pol} = 0,3 nm, and s_{THz} = 8 nm.

We have shown that Fe/Pt epitaxial bilayer systems can be considered as a competitive THz radiation source. They have a number of advantages compared to other optical and electro-optical THz emitters, like simplified alignment, easy attachment of a collimating Si lens enhancing the signal

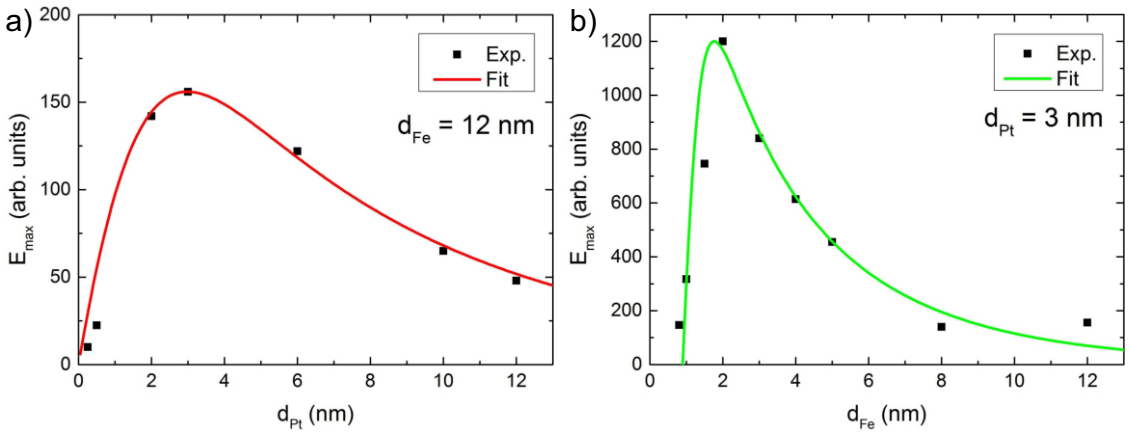

Fig. 4: a) Pt thickness dependence of the THz field amplitude for a constant Fe thickness of 12 nm. b) Fe thickness dependence of the THz field amplitude for a constant Pt thickness of 3 nm.

and pump fluence robustness. Furthermore, no electrical connections are required for the operation of the emitter and the polarization of the generated THz radiation can easily be rotated by a weak magnetic field. The THz pulse length and bandwidth is, in principle, only limited by the relaxation time of hot electrons in the Pt material. The best THz emitter made with the parameters 2 nm Fe and 3 nm Pt revealed to be the optimum thicknesses for THz generation. We have successfully developed a quantitative model that takes into account the optical absorption, the spin polarization of Fe, the impedance, the spin accumulation in Pt and the THz absorption in Fe.

We thank Burkard Hillebrands for his scientific support. We acknowledge support from the Deutsche Forschungsgemeinschaft (DFG) through SFB TRR 173: SPIN+X Project B07 and the Carl Zeiss Foundation. We thank Marco Battiato and Hans Christian Schneider for helpful discussions.

References

[1] A. Hoffmann, *Spin Hall Effects in metals*, IEEE Transactions on Magnetics **49**, 5172 (2013).
[2] T. Seifert, S. Jaiswal, U. Martens, J. Hannegan, L. Braun, P. Maldonado, F. Freimuth, A. Kronenberg, J. Henrizi, I. Radu, E. Beaurepaire, Y. Mokrousov, P.M. Oppeneer, M. Jourdan, G. Jakob, D. Turchinovich, L.M. Hayden, M. Wolf, M. Münzenberg, M. Kläui, T. Kampfrath, *Efficient metallic spintronic emitters of ultrabroadband terahertz radiation*, Nat. Photon. **10**, 483 (2016).
[3] T. Kampfrath, M. Battiato, P. Maldonado, G. Eilers, J. Nötzold, S. Mæhrlein, V. Zbarsky, F. Freimuth, Y. Mokrousov, S. Blügel, M. Wolf, I. Radu, P.M. Oppeneer M. Münzenberg, *Terahertz spin current pulses controlled by magnetic heterostructures*, Nat. Nano. **8**, 256 (2013).
[4] J. Walowski, M. Münzenberg, *Perspective: Ultrafast magnetism and THz spintronics*, J. Appl. Phys. **120**, 140901 (2016).
[5] M. Battiato, K. Carva, P.M. Oppeneer, *Superdiffusive spin transport as a mechanism of ultrafast demagnetization*, Phys. Rev. Lett. **105**, 027203 (2010).
[6] A. Melnikov, I. Razdolski, T.O. Wehling, E.Th. Papaioannou, V. Roddatis, P. Fumagalli, O. Aktsipetrov, A.I. Lichtenstein, U. Bovensiepen, *Ultrafast transport of laser-excited spin-polarized carriers in* Au/Fe/MgO(001), Phys. Rev. Lett. **107**, 076601 (2011).
[7] G. Torosyan, S. Keller, L. Scheuer, R. Beigang, E.Th. Papaioannou, *Optimized spintronic terahertz emitters based on epitaxial grown Fe/Pt layer structures*, arXiv:1707.08894v2 (2017).
[8] C. Fattinger, D. Grischkowsky, *Terahertz beams*, Appl. Phys. Lett. **54**, 490 (1989).
[9] M. Battiato, K. Carva, P.M. Oppeneer, *Theory of laser-induced ultrafast superdiffusive spin transport in layered heterostructures*, Phys. Rev. B **86**, 218 (2012).

4.14 Large spin Hall angle of single-crystalline Pt obtained from spin pumping experiments

S. Keller, L. Mihalceanu, M. R. Schweizer, J. Greser, P. Lang, B. Heinz, M. Geilen, T. Brächer, P. Pirro, T. Meyer, A. Conca, B. Hillebrands, and E.Th. Papaioannou

In spintronics bilayers composed of a ferromagnetic (FM) and a nonmagnetic (NM) layer with large spin orbit interaction are used to investigate spin-to-charge current conversion. At ferromagnetic resonance (FMR) the spin pumping (SP) effect results in the injection of a pure spin current into the NM layer [1] and the Inverse Spin Hall Effect (ISHE) in the NM generates a charge current by spin-dependent deflection [2]. For magnon spintronics the spin-to-charge current conversion may play a dominant role for its success since it can provide the interface to common CMOS technology. Many works have been published on this topic: ferromagnetic metals [4] and insulators [5] as well as many non-magnetic layers [6] have been investigated. Most of the studies on metallic systems are devoted to sputtered polycrystalline samples, thus the influence of the crystal structure of those materials onto spin pumping experiments is neglected. Recently, studies on epitaxial bilayer systems are arising in literature [3, 4, 7, 8]. A parameter, which typically describes the efficiency of the spin-to-charge current conversion, is the spin Hall angle Θ_{SH}. It is defined as the ratio of the measured charge current deflected by ISHE in the NM material and the spin current injected into the NM material. For the often-used NM material Pt, which exhibits a rather large Θ_{SH}, the literature quotes a wide span in its value, namely from 1 up to 11 % [9]. Another parameter, strongly correlated to the spin Hall angle, the spin diffusion length λ_{SD} describes the typical length scale in which the spin current is attenuated by its deflection through ISHE after its injection from the FM into the NM material. Both parameters normally show a reciprocal behavior: A large Θ_{SH} is typically related to a small λ_{SD} and vice versa. The spin diffusion length is crucial to calculate the spin Hall angle for spin pumping experiments. With the usage of metallic ferromagnets, the signal from spin rectification (SR) effects, in particular caused by the anisotropic magnetoresistance (AMR) and the Anomalous Hall Effect (AHE), is overlapping with the Inverse Spin Hall Effect signal [8, 10]. By making use of the different angular dependencies of the effects, we distinguish between spin rectification effects and Inverse Spin Hall Effect. In this report we address the efficient ISHE in epitaxial grown and highly pure Fe/Pt bilayers with angle-resolved spin pumping measurements through microwave excitation by a microstructured coplanar waveguide-like antenna. Epitaxial Fe/Pt bilayers with a constant Fe thickness of 12 nm and a varying Pt thickness have been grown by molecular beam epitaxy (MBE) on MgO (100) substrates in an ultra-high vacuum system with a base pressure of $1 \cdot 10^{-9}$ mBar. The epitaxial growth of the samples was confirmed by high resolution transmission electron microscopy (HRTEM) and X-ray diffraction (XRD) measurements (not shown here). The TEM measurements show, that the layers have grown stress-free by inducing an atomic roughness of 2 monolayers in the Fe/Pt interface. Subsequently, the Fe/Pt(6nm) sample was microstructured into narrow stripes (Fig. 1) for the angle-resolved spin pumping measurements.

Using a vector network analyzer, ferromagnetic resonance spectroscopy (VNA-FMR) measurements of the unstructured Fe/Pt samples have been made to determine the saturation value of the real part of the spin mixing conductance $g^{\uparrow\downarrow} = (4.4 \pm 0.2) 10^{19}$ m^{-2} of the Fe/Pt interface and the spin diffusion length of the epitaxial Pt $\lambda_{SD} = (1.1 \pm 0.1)$ nm. $g^{\uparrow\downarrow}$ has the same order of magnitude as other metallic systems, like Py/Pt and CoFeB/Pt [12] In general, $g^{\uparrow\downarrow}$ can vary between different experiments and material systems, but stays in the same order of magnitude. The spin diffusion

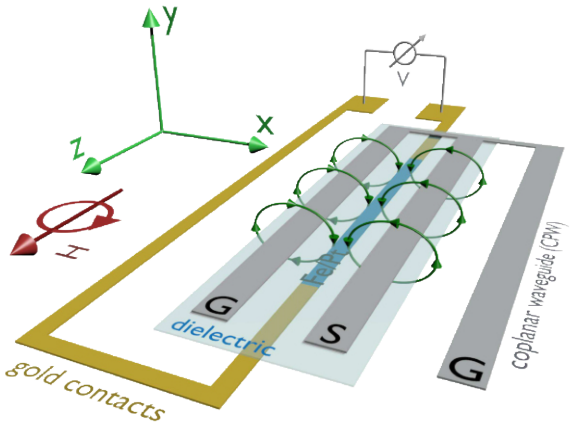

Fig. 1: Scheme of the microstructured Fe/Pt samples with 200×10 µm stripes along the Fe (100) axis structured by electron beam lithography for angular dependent spin pumping measurements with excitation and DC measurements by picoprobes. Cr/Au/Cr contacts for the Fe/Pt stripes and a coplanar waveguide Ti/Au/Ti antenna structure have been fabricated by e-beam evaporation and electron-beam lithography. The microstructuring allows for a distinct excitation by an out-of-plane exciting microwave field which allows us to disentangle ISHE from SR.

length of the epitaxial Pt layer is rather small, but the value is comparable to the one determined in Terahertz-spintronic measurements with the epitaxial Fe/Pt bilayers shown in report 4.13.

To investigate the ISHE in the microstructured sample an angle resolved spin pumping setup [8] was used, where the external magnetic field is rotated in-plane. For each individual external field angle, the field is swept and the DC-voltage is measured by a lock-in amplification technique. The so measured curves are then fitted by Eq. 1 involving symmetric and antisymmetric Lorentzians [12]:

$$V_{\mathrm{DC}}^{z}(H) \;=\; V_{\mathrm{sym}}^{z}\frac{(\Delta H)^2}{(H-H_{\mathrm{r}})^2+(\Delta H)^2} \;+\; V_{\mathrm{asym}}^{z}\frac{-\Delta H(H-H_{\mathrm{r}})}{(H-H_{\mathrm{r}})^2+(\Delta H)^2} \quad , \tag{1}$$

where ΔH denotes the linewidth, H_{r} is the magnetic resonance field, V_{sym} is the symmetric and V_{asym} is the antisymmetric voltage amplitude. To be able to interpret the angular dependence of the fit parameters, especially the voltage amplitudes, one needs to consider the microwave dynamic fields (in- and out-of-plane) and the induced microwave currents in the Fe as well as the the contact geometry. Since the Fe/Pt stripe is located between one ground line and the signal line (see Fig. 1) the out-of-plane dynamic magnetic microwave field h_y is about one order of magnitude larger than the in-plane field h_x. The other field component h_z is expected to be negligibly small. With the DC contacts along the z-direction, the angular dependence of the voltage amplitudes are then given by [8, 10]:

$$\begin{aligned} V_{\mathrm{sym}}^{z} \;=\;& V_{\mathrm{ISHE,AMR}}^{h_x}\sin(2\Theta_{\mathrm{M}})\cos(\Theta_{\mathrm{M}}) + V_{\mathrm{AMR}}^{h_y}\sin(2\Theta_{\mathrm{M}}) + \\ & V_{\mathrm{ISHE}}^{h_y}\sin(\Theta_{\mathrm{M}}) + V_{\mathrm{AHE}}^{h_x}\cos(\Theta_{\mathrm{M}}) \;+\; V_{\mathrm{AHE}}^{h_y} \\ V_{\mathrm{asym}}^{z} \;=\;& V_{\mathrm{AMR}}^{h_x}\sin(2\Theta_{\mathrm{M}})\cos(\Theta_{\mathrm{M}}) \;+\; V_{\mathrm{AMR}}^{h_y}\sin(2\Theta_{\mathrm{M}}) + \\ & V_{\mathrm{AHE}}^{h_x}\cos(\Theta_{\mathrm{M}}) + V_{\mathrm{AHE}}^{h_y} \quad . \end{aligned} \tag{2}$$

Since the SR effects and ISHE are dependent on the alignment between the magnetization and the z-axis (Θ_{M}), which differs from the alignment between the external magnetic field and the z-axis (Θ_{H}) resulting from the anisotropy fields, the measured data sets need to be readjusted. Therefore, the cubic anisotropy K_1 (arising from the Fe lattice) and uniaxial anisotropy K_{u} (arising from shape anisotropy of the Fe/Pt stripe) are extracted from the change in resonance field H_{r} according to:

$$f_\mathrm{r} = \frac{\gamma}{2\pi}\sqrt{\left(H_\mathrm{r}\cos\left(\Theta_\mathrm{H}-\Theta_\mathrm{M}\right)\left(N_x+N_x^e\right)M_\mathrm{S}\right)\left(H_\mathrm{r}\cos\left(\Theta_\mathrm{H}-\Theta_\mathrm{M}\right)\left(N_y+N_y^e\right)M_\mathrm{S}\right)} \quad , \tag{3}$$

with the demagnetization factor for a thin magnetic film $N_x = 0$, $N_y = 1$ and $N_z = 0$, using the effective demagnetization factors N_x^e and N_y^e to take into account the cubic and uniaxial anisotropy for the resonance condition [13, 14], $M_\mathrm{S} = 1712\,\mathrm{kA/m}$, $K_1 = 44290\,\mathrm{J/m^3}$ and $K_\mathrm{u} = 3600\,\mathrm{J/m^3}$. Equation 3 is then used to numerically relocate the data points in the angle axis with the results shown in Fig. 2.

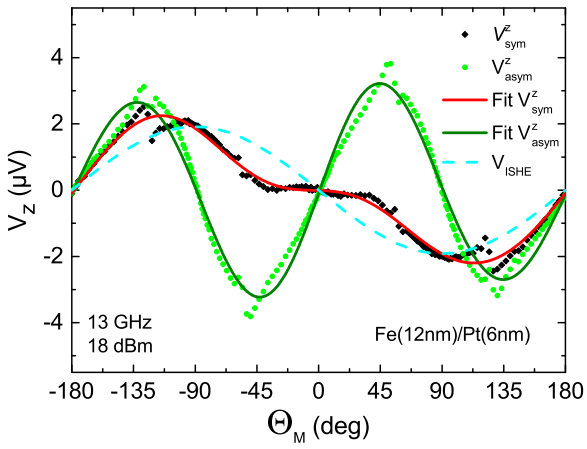

Fig. 2: Symmetric and antisymmetric voltage amplitudes of the Fe/Pt microstructure dependent on the angle of magnetization. The out-of-plane excited ISHE, which is a component of the symmetric voltage, is shown as dashed blue line with amplitude extracted from the fit to Eq. 2.

In Fig. 2, V^z_asym has almost no deviation from the expected $\sin(2\Theta_\mathrm{M})\cos(\Theta_\mathrm{M})$ shape for out-of-plane excited AMR (green dots) indicating low AHE and low in-plane fields. The shape of V^z_sym (black squares) can be described by the overlapping of out-of-plane AMR and out-of-plane excited ISHE $\propto \sin(\Theta_\mathrm{H})$. The ISHE component excited by the out-of-plane dynamic magnetic field ($1.92\,\mu\mathrm{V}$, component of V^z_sym according to Eq. 2) is plotted as a dashed blue line. The ISHE voltage is of similar magnitude as the AMR voltage indicating a high efficiency of SP and ISHE compared to other polycrystalline samples. To further quantify the efficiency of the spin current to charge current conversion in epitaxial Fe/Pt, we determine the spin Hall angle Θ_SH via Eq. 4 [6, 10]:

$$V^z_\mathrm{ISHE} = -\frac{l}{M_\mathrm{S}^2}\sin(\Theta_\mathrm{M})A_{xy}A_{yy}h_y^2\frac{\Theta_\mathrm{SH}\lambda_\mathrm{SD}g^{\uparrow\downarrow}}{\sigma_\mathrm{film}t_\mathrm{film}}\left(\frac{e\omega}{2\pi}\right)\tanh\left(\frac{t_\mathrm{Pt}}{2\lambda_{SD}}\right) \quad , \tag{4}$$

with $l = 200\,\mu\mathrm{m}$ denoting the Fe/Pt stripe length, $A_{xy} = 188.4$ and $A_{yy} = 31.4$ the calculated Polder tensor components, σ_film the measured film conductivity, $t_\mathrm{film} = 18\,\mathrm{nm}$ the Fe/Pt film thickness, $\omega = 2\pi\cdot 13\,\mathrm{GHz}$ the angular frequency of the microwave and $t_\mathrm{Pt} = 6\,\mathrm{nm}$ the Pt layer thickness. The out-of-plane exciting microwave field $h_y = 266.3\,\mathrm{A/m}$ was determined by using COMSOL Multiphysics to simulate the microwave fields and currents inside and around the Fe/Pt stripe. By measuring the AMR ratio externally and comparing the AMR component of the signal in Fig. 2 with the simulated microwave fields and currents we verified the actual microwave power applied to the CPW antenna. Using Eq. 4 the spin Hall angle is then calculated as $\Theta_\mathrm{SH} = (7\pm1)\,\%$. Therefore, the value of epitaxial Pt film lies within the range of 1% up to 10% reported for mostly polycrystalline RF-sputtered Pt [9] and is comparable to epitaxial Pt reported by other authors [7]. Nevertheless, since many authors reported significantly lower values with polycrystalline metallic bilayers, we believe epitaxial ordering greatly enhances the spin-to-charge current conversion. Because of the small λ_SD, we assume, that the atomically rough interface (about 2 monolayers)

has an important extrinsic contribution to the relatively large Θ_{SH} at room temperature. We propose the ISHE in epitaxial Pt is very sensitive to the interface morphology and, in our case, the atomic interface roughness might support ISHE by surface-assisted skew-scattering [3, 15].

In this work, the real part of the spin mixing conductance $(4.38 \pm 0.19) 10^{19}\,\mathrm{m}^{-2}$ and the spin diffusion length of the epitaxial Pt (1.1 ± 0.1) nm were determined by VNA-FMR measurements with large area Fe/Pt sample series with Pt thicknesses ranging from 0 to 18 nm. With angle-resolved spin pumping measurements on a microstructured Fe/Pt stripe and with a COMSOL simulation of the microwave excitation, we calculated the spin Hall angle. Its value of $(7 \pm 1)\,\%$ is very large for highly pure, epitaxial Pt. We explain this behavior with an increased extrinsic skew scattering near the atomically rough Fe/Pt interface indicated by the small spin diffusion length.

The Carl Zeiss Stiftung is gratefully acknowledged for financial support. We thank Tobias Fischer for the support with the design of the nanostructures and thank the team of the Nanostructuring Center of the TU Kaiserslautern for the use of their facilities.

References

[1] Y. Tserkovnyak, A. Brataas, G.E.W. Bauer, *Enhanced Gilbert damping in thin ferromagnetic films*, Phys. Rev. Lett. **88**, 117601 (2002).
[2] E. Saitoh, M. Ueda, H. Miyajima, G. Tatara, *Conversion of spin current into charge current at room temperature: Inverse spin-Hall effect*, Appl. Phys. Lett. **88**, 182509 (2006).
[3] E.Th. Papaioannou, P. Fuhrmann, M.B. Jungfleisch, T. Brächer, P. Pirro, V. Lauer, J. Lösch, B. Hillebrands, *Optimizing the spin-pumping induced inverse spin Hall voltage by crystal growth in Fe/Pt bilayers*, Appl. Phys. Lett. **103**, 162401 (2013).
[4] A. Conca, S. Keller, L. Mihalceanu, T. Kehagias, G.P. Dimitrakopulos, B. Hillebrands, E.Th. Papaioannou, *Study of fully epitaxial Fe/Pt bilayers for spin pumping by FMR spectroscopy*, Phys. Rev. B **93**, 134405 (2016).
[5] F.D. Czeschka, L. Dreher, M.S. Brandt, M. Weiler, M. Althammer, I.-M. Imort, G. Reiss, A. Thomas, W. Schoch, W. Limmer, H. Huebl, R. Gross, S.T.B. Goennenwein, *Scaling behavior of the spin pumping effect in ferromagnet/platinum bilayers*, Phys. Rev. Lett. **107**, 046601 (2011).
[6] A. Azevedo, L.H. Vilela-Leão, R.L. Rodríguez-Suárez, A.F. Lacerdo Santos, S.M. Rezende, *Spin pumping and anisotropic magnetoresistance voltages in magnetic bilayers: Theory and experiment*, Phys. Rev. B **83**, 144402 (2011).
[7] Y. Huo, F.L. Zeng, C. Zhou, Y.Z. Wu, *Spin pumping and the Inverse Spin Hall Effect in single crystalline Fe/Pt heterostructure*, AIP Adv. **7**, 056024 (2017).
[8] S. Keller, J. Greser, M.R. Schweizer, A. Conca, V. Lauer, C. Dubs, B. Hillebrands, E.Th. Papaioannou, *Relative weight of the Inverse Spin-Hall and spin-rectification effects for metallic polycrystalline Py/Pt, epitaxial Fe/Pt, and insulating YIG/Pt bilayers: Angular dependent spin pumping measurements*, Phys. Rev. B **96**, 024437 (2017).
[9] A. Hoffmann, *Spin Hall Effects in Metals*, IEEE Trans. Magn. **49**, 10 (2013).
[10] M. Harder, Y. Gui, C.-M. Hu, *Electrical detection of magnetization dynamics via spin rectification effects*, Phys. Rep. **661**, 1 (2016).
[11] Y. Tserkovnyak, A. Brataas, G.E.W. Bauer, B.I. Halperin, *Nonlocal magnetization dynamics in ferromagnetic heterostructures*, Rev. Mod. Phys. **77**, 1375 (2005).
[12] A. Ruiz-Calaforra, T. Brächer, V. Lauer, P. Pirro, B. Heinz, M. Geilen, A.V. Chumak, A. Conca, B. Leven, B. Hillebrands, *The role of the non-magnetic material in spin pumping and magnetization dynamics in NiFe and CoFeB multilayer systems*, J. Appl. Phys. **117**, 163901 (2015).
[13] C. Kittel, *On the theory of ferromagnetic resonance absorption*, Phys. Rev. **73**, 155 (1948).
[14] O. Kohmoto, *Effective demagnetizing factors in ferromagnetic resonance equations*, J. Magn. Magn. Mater. **262**, 280 (2003).
[15] B. Gu, T. Ziman, G.-Y. Guo, N. Nagaosa, S. Maekawa, *Giant spin Hall effect of Au films with Pt impurities: Surface-assisted skew scattering*, J. Appl. Phys. **109**, 07C502 (2011).

4.15 Enhancement of the spin pumping effect by two-magnon confluence process in YIG-Pt bilayers

T. Noack, D.A. Bozhko, B. Heinz, A.A. Serga, B. Hillebrands, and V.I. Vasyuchka

The electrical detection of magnons by means of the spin pumping (SP) and the inverse spin Hall effect (ISHE) is a widely utilized method in the field of magnon spintronics for investigations of magnetization dynamics [1]. Besides its simple realization, one of the main advantages of this approach is the sensitivity to all excited magnons independent from their frequencies and wavevectors [2]. Therefore, it allows the simultaneous detection of different groups of magnons over the whole magnon spectrum. The electrical detection of magnons can be efficiently utilized for studies of magnon-magnon scattering processes, when magnons with different wavevectors are involved. For instance, the increase in the ISHE voltage related to an enhancement of spin-current emission at the magnetic insulator / normal metal interface by both three-magnon splitting [3, 4] and four-magnon scattering processes [4] was reported. In the case of three-magnon splitting, the observed effect was attributed to an angular momentum transfer from the crystal lattice to the spin system of the magnetic insulator.

In this Report we present the experimental investigation of the spin pumping process by both long-wavelength dipolar and short-wavelength exchange magnons parametrically excited in in-plane magnetized yttrium iron garnet / platinum bilayers. In our field-dependent measurements of the ISHE voltage, a clearly visible sharp voltage peak is detected. The peak position does not depend on the film thickness and corresponds with the process of confluence of two magnons, which are parametrically excited at half of the pumping frequency, into one magnon having twice the frequency and the sum of the wavevectors.

A sketch of the experimental setup is shown in Fig. 1. In the experiments, we utilized the method of parallel parametric pumping for the efficient excitation of magnons in a wide range of wavevectors. The pumping microwave pulses with a tunable pulse duration in the range from 1 µs to 10 µs are created by a microwave generator. The repetition rate is set to 1 kHz, which is sufficient to provide the system with enough time to reach its equilibrium state after every pulse. After amplification to the maximal output microwave power of 40 W the incident microwave signal is sent through an attenuator and a circulator to the sample holder consisting of a rectangular waveguide closed by a thin metallic diaphragm at the end. The sample, for which experimental data are presented in this Report, is a 22.8 µm-thick yttrium iron garnet (YIG) film grown by liquid phase epitaxy in

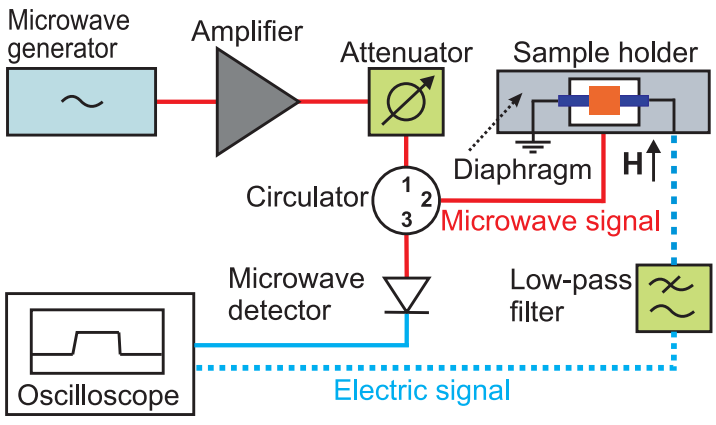

Fig. 1: Sketch of the microwave setup used in the experiments.

the (111) crystallographic plane on a gallium gadolinium garnet (GGG) substrate with the size of 10 mm × 2 mm × 0.5 mm. The film surface is covered by a platinum (Pt) layer with thickness of 10 nm. The GGG/YIG/Pt sample is placed into a hole in an open dielectric resonator (ODR) and both are mounted in an rectangular slot of the diaphragm as it is schematically shown in Fig. 1. In such a geometry the $H_{1\delta 1}$ electromagnetic mode of the ODR is efficiently excited. A microwave magnetic field of this mode, which lies in the YIG film plane perpendicularly to the long side of the YIG/Pt sample, is used for the parametric pumping. Two dielectric resonators of different sizes were utilized in the experiments in order to probe the system at different pumping frequencies f_p. The microwave absorption is monitored by the observation of a pumping pulse reflected from the sample and passed through the circulator to a microwave detector and to an oscilloscope. The Pt layer is wired through a low-pass filter to the oscilloscope allowing for the detection of the generated voltage. A bias magnetic field H is oriented along the microwave magnetic field and transversally to the spin current flowing through the YIG/Pt interface in order to fulfil simultaneously the conditions of the parallel parametric pumping and the ISHE voltage detection. This voltage is measured across the spin current and the bias magnetic field directions.

In the case of magnon excitation, the observed signal consists of two ISHE voltages generated by two different spin currents. The first one is created by the spin pumping from the YIG film to the Pt layer. On the contrary, the other current flows from the Pt layer, which is heated by microwave eddy currents, to the YIG film due to the longitudinal spin Seebeck effect (LSSE). Here, we are interested only in that part of the ISHE voltage which is related to the spin pumping by parametrically excited magnons. Therefore, the contribution of the LSSE voltage measured at a high magnetic field, when the parametric instability is prohibited by the energy conservation law, was subtracted from the total voltage signal.

Since our experiments were performed using pulsed magnon excitation, the resulting ISHE voltage has also a pulsed profile. We have measured the dependence of the ISHE pulse amplitude as a function of the applied bias magnetic field. Obtained results for two parametric pumping frequencies $f_p = 14.45$ GHz (squares) and $f_p = 17.09$ GHz (circles) are shown in Fig. 2.

One can see that the spin pumping induced ISHE voltage is at maximum close to the field of the ferromagnetic resonance (FMR). This result agrees with the previous measurements presented in Ref. [2]. For smaller and higher magnetic fields the measured signal decreases. In contrast to

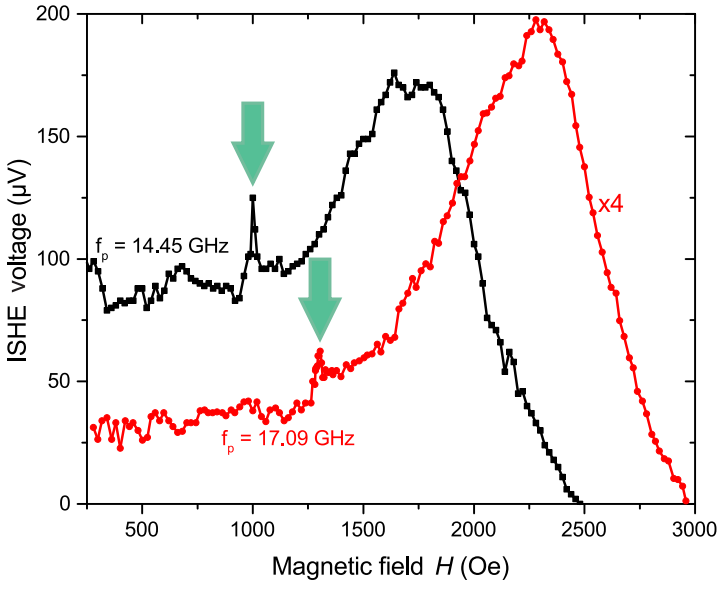

Fig. 2: Spin pumping induced ISHE voltage as a function of the magnetic field for two pumping frequencies $f_p = 14.45$ GHz (squares) and $f_p = 17.09$ GHz (circles). In both cases the measured dependencies have their maxima nearby the fields of the ferromagnetic resonance. The peaks caused by the confluence process are marked by arrows (see main text).

the monotonous voltage reduction for higher magnetic fields, the measured signal demonstrates a sharp peak in the area of low fields. The existence of this peak was already shortly addressed in Ref. [2]. However, the amplitude and the position of the peak were just roughly determined due to the low field resolution. In our experiments with the finer step size in the magnetic field we found that the voltage peak exists in a very narrow field range and its amplitude turned out to be much higher than measured before. Moreover, the increase of the parametric pumping frequency leads to a shift of the peak position towards higher fields with the accompanying reduction of its amplitude (see Fig. 2). At the same time, additional measurements show that the peak position does not depend on the thickness of the used YIG film.

The appearance of the peak can be related to the three-magnon confluence process in an in-plane magnetized YIG film. In this process, two magnons, which are parametrically excited at half of the pumping frequency on the perpendicular magnon branch [5], combine into one magnon with the pumping frequency and twice the wavevector (see Fig. 3a). The magnetic field for which the three-magnon confluence occurs can be estimated using the simplified dispersion relation for the fundamental mode of the transversal magnon branch in exchange approximation: $\omega = \omega_{\mathrm{FMR}} + \eta k^2$, where $\omega_{\mathrm{FMR}} = \gamma\sqrt{H(H+4\pi M_{\mathrm{s}})}$, the gyromagnetic ratio $\gamma = 1.76 \cdot 10^7\,\mathrm{Oe^{-1}s^{-1}}$, the exchange constant $\eta = 9.15 \cdot 10^{-2}\,\mathrm{cm^2/s}$, and the saturation magnetization $4\pi M_{\mathrm{s}} = 1750\,\mathrm{G}$. Then, the wavenumber of the parametrically pumped magnons depends on the pumping frequency as $k_1 = \sqrt{(\omega_{\mathrm{p}}/2 - \omega_{\mathrm{FMR}})/\eta}$. The confluence of two such magnons results in the appearance of the resulting magnon at the pumping frequency ω_{p} with the wavenumber $k_2 = 2k_1$. If the created magnon belongs to the same dispersion curve, we can derive the following relation:

$$\omega_{\mathrm{p}} = \omega_{\mathrm{FMR}} + 4\eta k_1^2 = 2\omega_{\mathrm{p}} - 3\omega_{\mathrm{FMR}} \quad . \tag{1}$$

This leads to the approximation of the condition for the three-magnon confluence process as $\omega_{\mathrm{FMR}} = \omega_{\mathrm{p}}/3$, from which the field of the confluence peak H_{peak} can be roughly estimated. This simple relation describes to which frequency the ferromagnetic resonance of the in-plane magnetized film ω_{FMR} has to be tuned by varying the external magnetic field in order to allow the three-magnon confluence process.

In order to find the peak field H_{peak} more accurately we used the dispersion relation of the excited

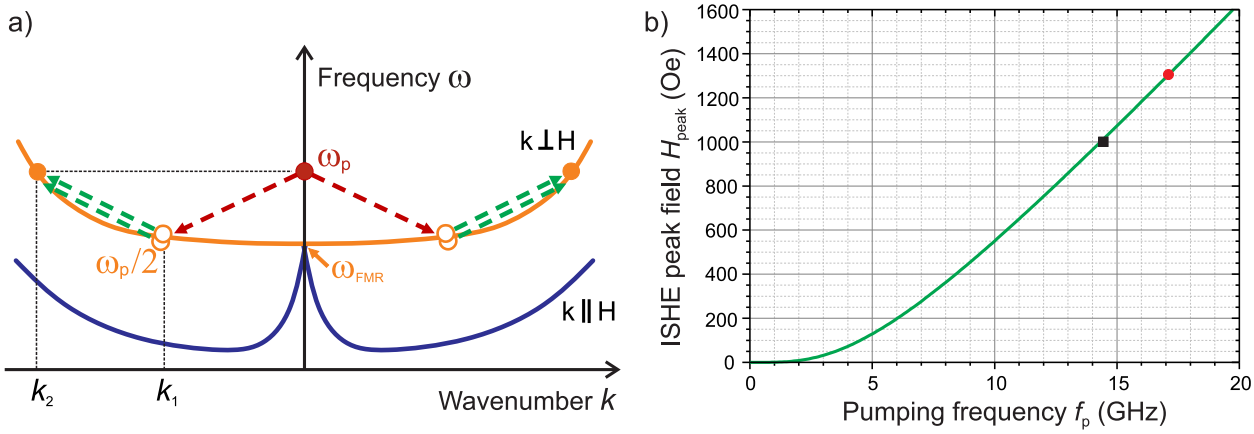

Fig. 3: (a) Schematic illustration of the three-magnon confluence process. (b) Dependence of the three-magnon confluence peak field H_{peak} on the parametric pumping frequency f_{p} calculated numerically (solid line). Experimentally measured ISHE peak fields are shown for parametric pumping frequencies of 14.45 GHz (square) and 17.09 GHz (circle).

magnon mode in the following form: $\omega^2 = (\omega_H + \eta k^2)(\omega_H + \omega_M + \eta k^2)$, where $\omega_H = \gamma H$ and $\omega_M = \gamma 4\pi M_s$. Taking into account the conditions for frequencies and wavevectors of magnons participating in the three-magnon confluence, the peak field as a function of the pumping frequency was calculated numerically. The obtained result is shown in Fig. 3b by a solid line. The experimentally measured ISHE peak fields for two different parametric pumping frequencies of 14.45 GHz (square) and 17.09 GHz (circle) perfectly correspond to the calculations without additional fitting parameters.

Our measurements show that the three-magnon confluence has a strong influence on the spin pumping process in YIG/Pt bilayers. In contrast to the three-magnon splitting, where the enhancement of spin-current emission was observed due to the increase in the magnon number and the related flow of angular momentum from the crystal lattice into the magnetic subsystem [3], unexpectedly, the three-magnon confluence process results also in the increase of the spin pumping signal. The possible nature of the observed phenomenon can be associated with a direct transfer of angular momentum from the magnon subsystem of the YIG film to free electrons in the Pt layer.

In conclusion, we present our studies on the spin pumping by both long-wavelength dipole and short-wavelength exchange magnons parametrically excited in in-plane magnetized Pt-covered YIG films. In time-resolved field-dependent measurements of the ISHE voltage, a clearly visible sharp voltage peak is detected. The peak position can be related to the process of confluence of two parametrically excited magnons into one magnon. This relation has been confirmed by further measurements at different pumping frequencies.

Financial support from the Deutsche Forschungsgemeinschaft in the frame of SFB/TR 49 and the project INST 248/178-1 is gratefully acknowledged.

References

[1] A.V. Chumak, V.I. Vasyuchka, A.A. Serga, B. Hillebrands, *Magnon spintronics*, Nat. Phys. **11**, 453 (2015).
[2] C.W. Sandweg, Y. Kajiwara, A.V. Chumak, A.A. Serga, V.I. Vasyuchka, M.B. Jungfleisch, E. Saitoh, B. Hillebrands, *Spin pumping by parametrically excited exchange magnons*, Phys. Rev. Lett. **106**, 216601 (2011).
[3] H. Kurebayashi, O. Dzyapko, V.E. Demidov, D. Fang, A.J. Ferguson, S.O. Demokritov, *Controlled enhancement of spin-current emission by three-magnon splitting*, Nat. Mater. **10**, 660 (2011).
[4] H. Sakimura, T. Tashiro, K. Ando, *Nonlinear spin-current enhancement enabled by spin-damping tuning*, Nat. Commun. **5**, 5730 (2014).
[5] A.A. Serga, C.W. Sandweg, V.I. Vasyuchka, M.B. Jungfleisch, B. Hillebrands, A. Kreisel, P. Kopietz, M.P. Kostylev, *Brillouin light scattering spectroscopy of parametrically excited dipole-exchange magnons*, Phys. Rev. B **86**, 134403 (2012).

4.16 Dzyaloshinskii-Moriya interaction in CoFeB|Pt and CoFeB|W thin films

T. Fischer, F. Heussner, B. Hillebrands, and P. Pirro*

In collaboration with S. Jaiswal[†,§], G. Jakob[†], and M. Kläui[,†]*

**Graduate School Materials Science in Mainz, Staudingerweg 9, 55128 Mainz, Germany*
[†]Institut für Physik, Staudingerweg 7, Johannes Gutenberg-Universität, 55128 Mainz, Germany
[§]Singulus Technologies AG, Hanauer Landstraße 103, 63796 Kahl am Main, Germany

Conventional CMOS-based devices for information processing are reaching critical power densities and can therefore no longer keep up with Moore's law [1]. The concept of magnonics [2], which aims at the utilization of spin waves as information carriers, promises a significant reduction of Joule heating and Ohmic losses.
As predicted by Dzyaloshinskii and Moriya [3, 4], in low-symmetry systems the exchange interaction exhibits an antisymmetric contribution and as a result, an additional term which is linear in the spin-wave wavevector enters the dispersion relation of spin waves propagating perpendicular to the static magnetization. This effect known as Dzyaloshinskii-Moriya interaction (DMI) causes a frequency splitting which could pave the way towards the development of versatile spin-wave devices and could allow for the development of unidirectional spin-wave emitters [5]. It also has a significant influence on the stabilization of skyrmions which are considered a key actor of a new generation of data storage devices [6].
Considering exchange only, the interaction between magnetic moments can be described by the Heisenberg Hamiltonian

$$\hat{H} = \sum_{i \neq j} J_{ij} \mathbf{S}_i \cdot \mathbf{S}_j - K_{\text{eff}} \sum_i (\mathbf{S}_i \cdot \hat{e})^2 + \sum_{i \neq j} \mathbf{D}_{ij} \cdot \mathbf{S}_i \times \mathbf{S}_j. \tag{1}$$

Here, the first term describes standard Heisenberg exchange and the second term accounts for magnetic anisotropy. The third term which contains the DMI vector $\mathbf{D}_{ij}$ describes the DMI which favors a chiral alignment of spins.
Due to its origin from a broken inversion symmetry and the presence of an interface to a material featuring a large spin-orbit coupling, (ultra-)thin films are of large interest for the investigation of interfacial DMI (iDMI) [8]. Also, since spin waves exhibit a chirality depending on their direction of propagation perpendicular to the magnetization, the DMI leads to an energy shift by favoring one chirality over the other. In consequence, a term linear in the spin-wave wavevector enters the dispersion relation [7]: $f = f_0 + \Delta f_{\text{DMI}}$. Here, f_0 describes the unperturbed dispersion relation and f_{DMI} describes the influence of the DMI with

$$f_0 = f_{\text{FMR}} + Jk^2 \qquad \Delta f_{\text{DMI}} = \frac{\gamma}{\pi M_{\text{S}}} Dk. \tag{2}$$

It should be noted that in this case the unperturbed dispersion relation takes into account exchange only. f_{FMR} describes the ferromagnetic resonance frequency, the spin-wave wavevector is denoted by k and D is the DMI constant. In case the DMI is of purely interfacial origin, the DMI constant D can be related to the film thickness t resulting in an interfacial DMI constant [9] $D_{\text{S}} = Dt$.

The samples under investigation were grown using a *Singulus Rotaris* tool and are composed of CoFeB films with a thickness of 0.6 nm sandwiched between an underlying 5 nm thick Pt (or W, respectively) layer and a capping of MgO(2)|Ta(5). Measurements of the spin-wave frequency were performed using wave-vector resolved Brillouin light scattering (BLS) spectroscopy with the external magnetic field applied perpendicular to the plane of incidence. Hence, magnetostatic surface waves are probed. In order to determine the DMI shift and to exclude a setup-induced shift, we identify the DMI shift from the difference of the Stokes and anti-Stokes peak frequencies, respectively, under a reversal of the sign of the external field which is equivalent to a change of the sign of the spin-wave wave vector. The spin-wave frequency is determined as the center frequency of Lorentzian peaks fitted to the BLS spectra.

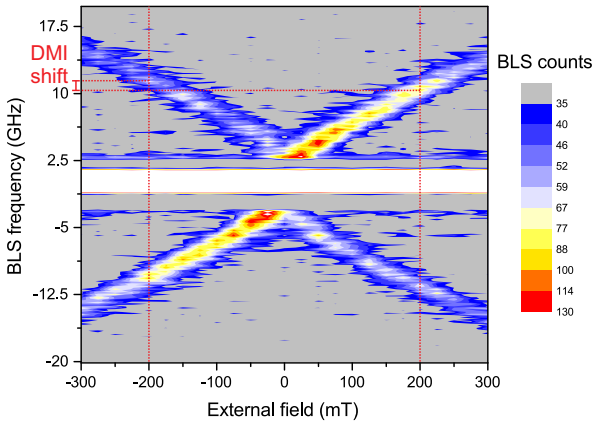

Fig. 1: Field-sweep measurement performed with the CoFeB film with an adjacent Pt layer. The angle of incidence is $\phi = 15^\circ$ and the external field is varied in steps of 25 mT. The dependence of the spin-wave frequency on the applied field is clearly visible. Dotted red lines exemplarily show the DMI shift for the anti-Stokes peak.

The results of a field sweep measurement with the CoFeB|Pt sample at an angle of incidence of 15° (corresponding to a spin-wave wave vector of $6.11\,\mathrm{rad/\mu m}$ for a laser wavelength of 532 nm) are shown in Fig. 1. Here, the external field has been swept from -300 mT to $+300$ mT in steps of 25 mT. The spin-wave frequency increases monotonically with the absolute value of the applied field as expected for a film featuring an in-plane anisotropy. Additionally, the asymmetry of the Stokes and anti-Stokes peak is visible in the intensity plot [10]. Also, this sample shows no sign of a pronounced perpendicular magnetic anisotropy (PMA). We now choose a fixed field value of $\mu_0 H_{\mathrm{ext}} = \pm 200\,\mathrm{mT}$ to perform wave vector-resolved measurements by changing the angle of incidence, i.e., the probed spin-wave wavevector. This allows for determining the shift between positive and negative k resulting in a value for the DMI constant.
The extracted frequency for different spin-wave wavevectors is shown in Fig. 2a. The graph clearly resembles the linear dependence of the DMI-induced frequency shift on the wave vector. From this, by fitting a linear relation to the measured values, the DMI constant can be extracted. For the Stokes peak, this leads to

$$|D| = (1.33 \pm 0.03)\ \mathrm{mJ/m^2} \qquad |D_{\mathrm{S}}| = (0.80 \pm 0.02)\ \mathrm{pJ/m}. \tag{3}$$

The measured signals can also be employed to obtain the dispersion relation which is imaged in Fig. 2b. The exchange character of the probed spin waves (leading to a dispersion relation quadratic in k) is clearly observable in the data superposed by a linear contribution as a trace of DMI. An interesting finding in this context is the fact that in the entire probed wavevector range the group velocity which is the derivative of the dispersion relation, is positive revealing a unidirectional propagation of spin waves dominated by the DMI.
A similar set of measurements has been performed with the CoFeB film featuring an adjacent W

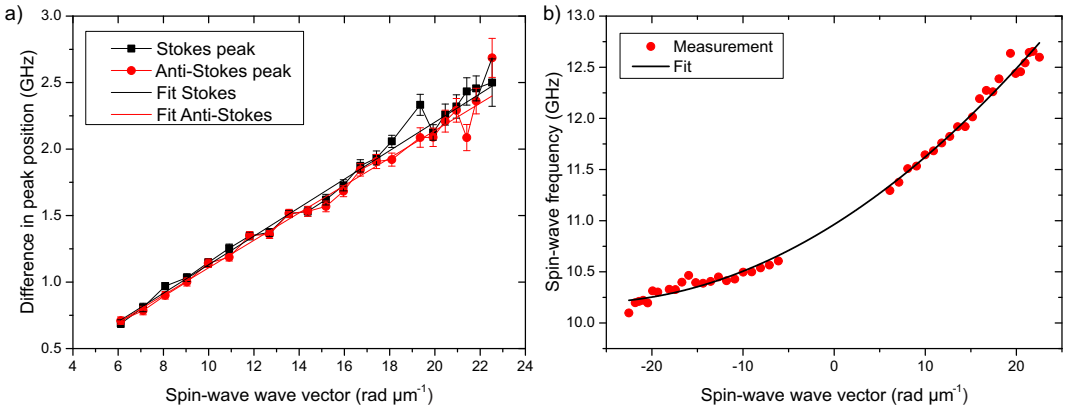

Fig. 2: a) Difference in peak positions under reversal of the external magnetic field ($\mu_0 H_{\mathrm{ext}} = \pm 200\,\mathrm{mT}$) for Stokes and anti-Stokes peaks and linear fit with the DMI constant as proportionality factor. b) Dispersion relation obtained from an analysis of the Stokes peak frequency for negative and positive fields ($\mu_0 H_{\mathrm{ext}} = \pm 200\,\mathrm{mT}$). (Fit: $J = 1.02 \cdot 10^{-3}\,\mathrm{GHz\,\mu m^2}$, cf. Eq. 3; assuming $M_{\mathrm{S}} = 1389\,\mathrm{kA/m}$ leads to $|D| = 1.39 \pm 0.02\,\mathrm{mJ/m^2}$)

layer. The results of the field-sweep measurement are presented in Fig. 3a. The dependence of the signal frequency on the externally applied field is much more complex than for the CoFeB|Pt film. Up to absolute field values of 270 mT, the frequency of the spin-wave signal decreases with increasing field before increasing proportionally to the field for higher field values. In fact, the behavior leads to the conclusion that this film exhibits a PMA strong enough to orient the magnetization out-of-plane in remanence.

Again, also for this film we performed wavevector dependent measurements with the field fixed at $\mu_0 H_{\mathrm{ext}} = \pm 400\,\mathrm{mT}$. This allows for the extraction of the frequency shift under reversal of the spin-wave wavevector which is presented in Fig. 3b. The dependence of this shift again exhibits a linear dependence on the wavevector indicating the presence of DMI in the film. However, the DMI constant which can be obtained from a linear fit to the measured values appears to be significantly smaller than for the sample with an adjacent Pt interface. Specifically, from the shift of the Stokes signal we obtain

$$|D| = (0.09 \pm 0.02)\ \mathrm{mJ/m^2} \qquad |D_{\mathrm{S}}| = (0.05 \pm 0.01)\ \mathrm{pJ/m}. \tag{4}$$

Even though W features a large spin orbit coupling, an adjacent W layer appears to not necessarily come with a large DMI in the CoFeB|W sample.

However, various other effects can affect the spin-wave dispersion relation in thin films, one of which is the surface anisotropy [12]. This mainly influences magnetostatic surface waves which are investigated in the experiments in this work. Due to their surface character, different surface anisotropy constants at the film interfaces can result in a frequency shift which is linear in the spin-wave wave vector and, hence, exhibits a DMI-like behavior but scales quadratically with the film thickness. For the CoFeB|W film, the anisotropy field has been measured employing VSM resulting in $\mu_0 H_{\mathrm{k}} = 489\,\mathrm{mT}$ and $M_{\mathrm{S}} = 1389\,\mathrm{kA/m}$. Assuming this effective anisotropy being a superposition of surface anisotropy and demagnetizing field, with the relation

$$\mu_0 H_{\mathrm{k}} = \mu_0 H_{\mathrm{ani,s}} - \mu_0 H_{\mathrm{demag}} = \frac{2}{M_{\mathrm{S}}} \left(\frac{K_{\mathrm{s}}}{t} - \frac{\mu_0}{2} M_{\mathrm{S}}^2 \right) \tag{5}$$

we can estimate $K_{\mathrm{s}} = 0.94\,\mathrm{mJ/m^2}$. For a spin-wave wavevector of $k_{\mathrm{SW}} = 15\,\mathrm{rad/\mu m}$, the frequency shift amounts to [12] $\Delta f = 2.02$ MHz which is clearly negligible compared to the shift determined

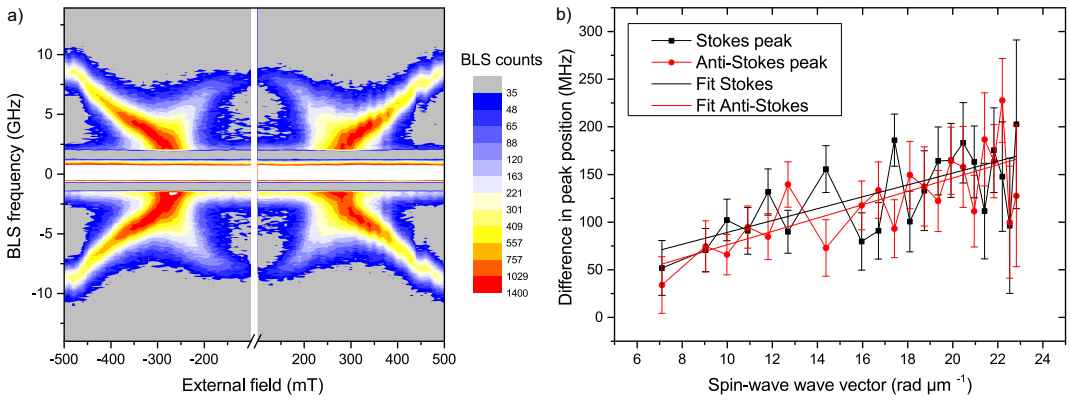

Fig. 3: a) Field-sweep measurement performed with the CoFeB film with an adjacent W layer. The angle of incidence amounts to $\phi = 15^\circ$ and the external field is varied in steps of 10 mT. In contrast to the CoFeB|Pt sample, the signal frequency exhibits a more complex dependence on the externally applied field which is an indicator for the presence of PMA in this film. b) Frequency shift of Stokes and Anti-Stokes peak under sign reversal of the spin-wave wave vector. The values show a linear trend which is an indicator for the presence of a (weak) DMI.

as a consequence of the DMI.

We gratefully acknowledge financial support within SFB/TRR 173 *Spin+X*.

References

[1] M. Mitchell Waldrop, *More Than Moore*, Nature **530**, 144 (2016).
[2] V.V. Kruglyak, S.O. Demokritov, D. Grundler, *Magnonics*, Journal of Physics D: Applied Physics **43**, 264001 (2010).
[3] I.E. Dzyaloshinskii, *A Thermodynamic Theory of Weak Ferromagnetism of Antiferromagnetism*, J. Phys. Chem. Solids **4**, 241 (1958).
[4] T. Moriya, *Anisotropic Superexchange Interaction and Weak Ferromagnetism*, Physical Review **1**, 91 (1960).
[5] T. Brächer, O. Boulle, G. Gaudin, P. Pirro, *Creation of unidirectional spin-wave emitters by utilizing interfacial Dzyaloshinskii-Moriya interaction*, Physical Review B **95**, 064429 (2017).
[6] A. Fert, V. Cros, J. Sampaio, *Skyrmions on the track*, Nature Nanotechnology **3**, 152 (2013).
[7] J.-H. Moon, S.-M. Seo, K.-J. Lee, K.-W. Kim, J. Ryu, H.-W. Lee, R.D. McMichael, M.D. Stiles, *Spin-wave propagation in the presence of interfacial Dzyaloshinskii-Moriya interaction*, Physical Review B **88**, 184404 (2013).
[8] A.A. Stashkevich, M. Belmeguenai, Y. Roussigné, S.M. Cherif, M.P. Kostylev, M. Gabor, D. Lacour, C. Tiusan, M. Hehn, *Experimental study of spin-wave dispersion in Py/Pt film structures in the presence of an interface Dzyaloshinskii-Moriya interaction*, Physical Review B **91** 214409 (2015).
[9] M. Belmeguenai, J.-P. Adam, Y. Roussigné, S. Eimer, T. Devolder, J.-V. Kim, S.M. Cherif, A.A. Stashkevich, A. Thiaville, *Interfacial Dzyaloshinskii-Moriya interaction in perpendicularly magnetized Pt/Co/AlO$_x$ ultrathin films measured by Brillouin light spectroscopy*, Physical Review B **91**, 180405(R) (2015).
[10] R.E. Camley, P. Grünberg, C.M. Mayr, *Stokes - anti-Stokes asymmetry in Brillouin scattering from magnons in thin ferromagnetic films*, Physical Review B **26**, 2609 (1982).
[11] B. Hillebrands, *Spin-wave calculations for multilayered structures*, Physical Review B **41**, 530 (1990).
[12] O. Gladii, M. Haidar, Y. Henry, M. Kostylev, M. Bailleul, *Frequency nonreciprocity of surface spin wave in permalloy thin films*, Physical Review B **93**, 54430 (2016).

4.17 Spin pumping through a Fe_3O_4 nanooxide at the Fe/Pt interface

L. Mihalceanu, S. Keller, A. Conca, B. Hillebrands, and E.Th. Papaioannou,

In collaboration with T. Kehagias, Department of Physics, Aristotle University of Thessaloniki, Thessaloniki 54124, Greece

For spintronics, a field in which the spin-degree of freedom is aimed to be the main information carrier, the spin current generation via spin pumping is one prominent method for the establishment of potential spin-current-generating devices. The spin-pumping effect is based on a spin current injected from a ferromagnetic (FM) layer into an adjacent non-magnetic (NM) layer at their interface. An indirect detection of this effect is provided by measuring the inverse Spin Hall Effect (ISHE) voltage V_{ISHE}. Various experiments have been performed in order to probe the interface properties of such bilayer systems by inserting different insulating interlayers at the FM–NM interface. Some examples are Py/MgO/Pt [1], $Y_5Fe_5O_{12}$/insulating barrier (Sr_2GaTaO_6,$SrTiO_3$, Sr_2CrNbO_6)/Pt structures [2] and Fe/MgO/Pt [3]. In our previous work on Fe/MgO/Pt we have shown the impact of an MgO tunneling barrier on the spin-pumping effect: spin currents are still inducing an ISHE voltage for very thin MgO tunneling barriers. The present article reveals the impact of nanosized Fe_3O_4 particles at the interface of thin epitaxial Fe(12 nm)/Pt(10 nm) layers. The sample quality and composition have been investigated by high resolution transmission electron microscopy (HRTEM). Angular resolved magneto-optical Kerr-effect in the longitudinal alignment (L-MOKE) was used for the characterization of the magnetic anisotropy. Furthermore, ferromagnetic resonance (FMR) together with spin-pumping effect experiments were applied to quantify the ISHE signal. The data are compared to a reference sample of Fe(12 nm)/Al(2.5 nm) grown epitaxially by molecular beam epitaxy under the same fabrication conditions.

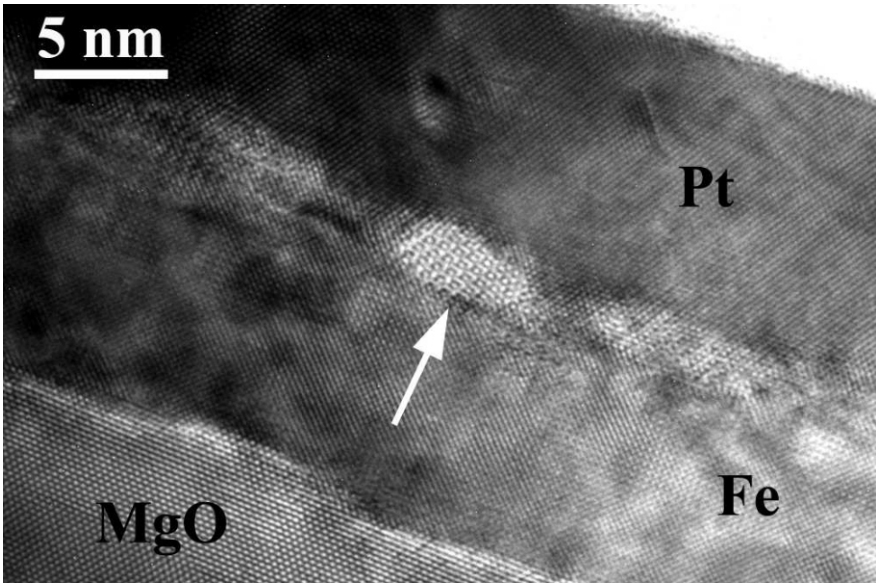

Fig. 1: HRTEM image of the Fe/Pt interface, illustrated along the [011]MgO/[001]Fe/[011]Pt projection. The white arrow indicates a pocket at the Fe/Pt interface filled with magnetite, Fe_3O_4. Unexpectedly, the orientation of the $Fe/Fe_3O_4/Pt$ trilayer confirms epitaxial growth.

Unlike in Fe/Pt, in Fe/Al no ISHE signal is expected and Al functions exclusively as a protection layer against oxidation. Figure 1 shows a HRTEM image from a section of the Fe/Pt interface. The Fe surface is rough and contains surface pits with different diameters. The structure of the pocket

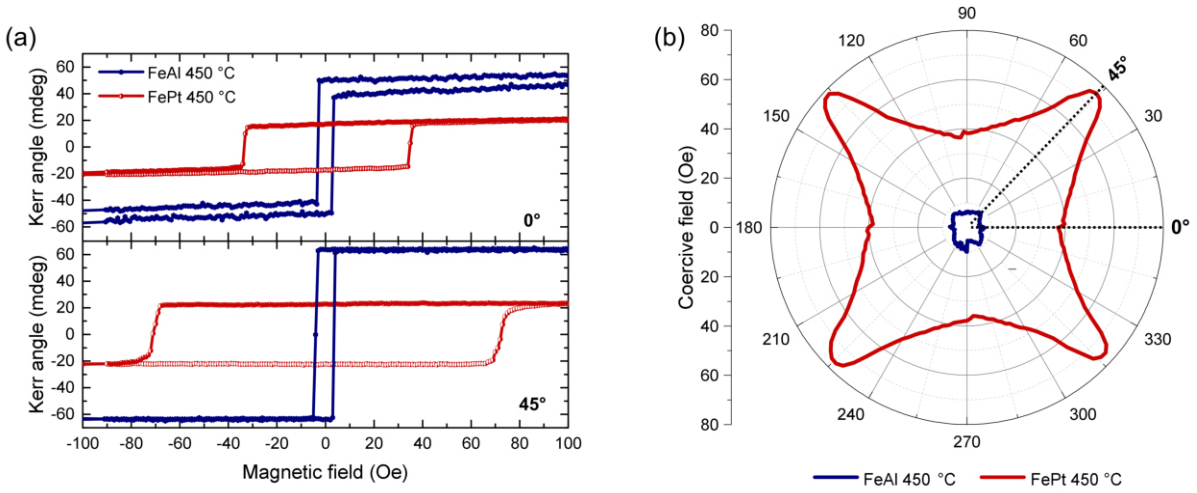

Fig. 2: L-MOKE characterization: (a) Hysteresis curves of Fe/Pt compared to the reference sample Fe/Al for 0° (top) and 45° (bottom) oriented external magnetic field. (b) Angular resolved L-MOKE of Fe/Pt compared to the reference sample Fe/Al, illustrating the strong increase in anisotropy of up to 10 times for Fe/Pt.

denoted with a white arrow exhibits a completely different symmetry that cannot be associated with either Fe or Pt. Electron diffraction analysis using FFT diffractograms have revealed the presence of magnetite Fe_3O_4 pockets with a mean diameter of 5 nm, presenting the Fd-3m diamond symmetry. Remarkably, the orientation of Fe_3O_4 turns out to be epitaxial on Fe. The epitaxial orientation of the multilayers along the [100] growth axis is: (100)MgO/(100)Fe/(100)Fe_3O_4/(100)Pt. The presence of any other Fe–Pt alloy has been excluded.

The magnetic anisotropy is probed by magneto-optical Kerr effect microscopy in the longitudinal alignment (L-MOKE). As shown in Fig. 2, the Fe_3O_4 nanoparticles at the interface and the presence of Pt as opposed to an Al capping have a strong impact on the coercive field (Fig. 2a) and induce a very pronounced cubic anisotropy behaviour (Fig. 2b) in comparison to the reference system Fe/Al. Magnetite is a ferrimagnetic material with a Néel temperature of 850 K. Isolated magnetite nanoparticles are widely studied for magnetic hyperthermia, and are superparamagnetic below $12-15\,\mathrm{nm}$. Given the size of around $5\,\mathrm{nm}$, our Fe_3O_4 nanoparticles are classified as superparamagnetic. No net magnetic field is expected to arise from them, as opposed to thin Fe_3O_4 layers [4, 5], where a strong anisotropy has been observed. However, one possible explanation for our strongly increased anisotropy may originate from the presence of nanoparticles as pockets inside an Fe matrix.

For probing the ferromagnetic resonance (FMR) the sample is placed onto a microwave antenna, which generates a dynamic magnetic Oersted field oriented perpendicularly to an external static magnetic field H. The detection of the FMR signal then occurs over a vector network analyzer. The Gilbert damping parameter α can be extracted by fitting the FMR frequency f_{FMR} dependence on the FMR linewidth ΔH [6]:

$$\Delta H(f_{\mathrm{FMR}}) = \Delta H_0 + \frac{4\pi\alpha f_{\mathrm{FMR}}}{\gamma} \quad , \tag{1}$$

where ΔH_0 is the inhomogeneous broadening and γ is the gyromagnetic ratio. The results are shown in Fig. 3a and Fig. 3b. While for the Fe/Al reference an effective Gilbert damping of

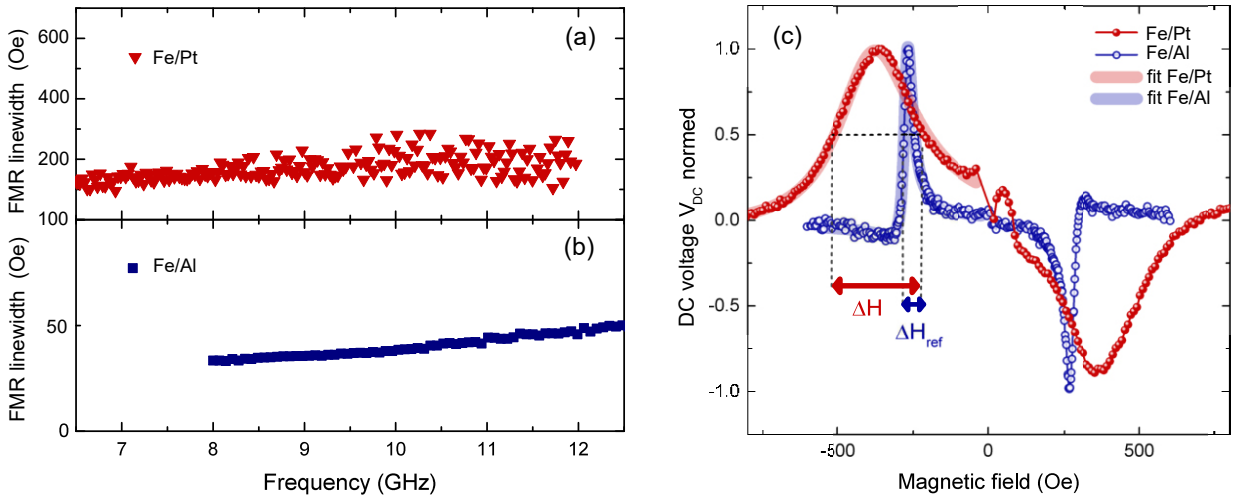

Fig. 3: Full width half maximum (FWHM) of the ferromagnetic resonance peak signal against the FMR frequency for Fe/Pt (a) and for the Fe/Al reference (b). (c) ISHE-voltage against the external magnetic field H compared for Fe/Pt and Fe/Al including fit functions according to Eq. 2.

$\alpha = (6.1 \pm 0.1) \times 10^{-3}$ is found, the Fe/Pt comparably reveals an up to 4 times increased linewidth which strongly varies with increasing frequency. The FMR linewidth of Fe/Pt is dominated by the inhomogeneous broadening, and, as a consequence, an estimation of α is not possible.

For the spin-pumping experiment the sample is placed onto a microwave antenna in the same geometry as previously done in the FMR setup. In addition, perpendicular to the externally applied magnetic field H and the antenna the sample is connected to a lock-in amplifier for voltage detection. When the FMR condition is reached, a spin current gets injected at the FM/NM interface, from the FM into the NM, which then generates a charge current perpendicularly oriented to H via the ISHE. Using the lock-in amplifier this signal together with voltages induced by parasitic effects is detected in form of a DC voltage V_{DC} induced around the ferromagnetic resonance field H_{FMR}. In Fig.3b the normalized V_{DC} is plotted against H.

In order to analyze the V_{DC} voltage composition, the signal is fitted by an expression composed of symmetric and antisymmetric Lorentzian functions [3]:

$$V_{\mathrm{DC}}(H) = V_0 + V_{\mathrm{Sym}} \frac{(\Delta H)^2}{(H - H_{\mathrm{FMR}})^2 + (\Delta H)^2} - V_{\mathrm{Asym}} \frac{\Delta H (H - H_{\mathrm{FMR}})}{(H - H_{\mathrm{FMR}})^2 + (\Delta H)^2} \quad , \tag{2}$$

where V_0 is a constant offset and ΔH is the linewidth of the Lorentzian fit curve. Having a line width of $\Delta H = 156.0 \pm 2.0$ Oe for Fe/Pt the sample with interfacial Fe_3O_4 nanoparticles reveals a significantly increase in linewidth of 9.8 times compared to the Fe/Al reference, which has a linewidth of $\Delta H_{\mathrm{ref}} = 16.0 \pm 0.2$ Oe. These results are in conformity with the previously obtained results in FMR.

In addition, the line shape provides insight into the detected DC voltage around FMR as it is linked to several rectification effects, besides the by spin-pumping generated V_{ISHE} [7]. With disregard of the interfacial nanoparticles, the further symmetric contributions in our Fe/Pt arise from spin pumping, anisotropic magneto-resistance (AMR) and anomalous Hall effect (AHE) [8]. Since rectification effects contribute mainly in an antisymmetric manner, the ratio of $V_{\mathrm{Sym}}/V_{\mathrm{Asym}}$ gives a

first estimate of the V_{DC} composition. For Fe/Pt this ratio is $V_{Sym}/V_{Asym} = 10.00 \pm 0.01$ while for the reference $V_{Sym}/V_{Asym} = 3.36 \pm 0.01$. Together with the strongly increased linewidth we assume that other dynamics as multiresonances induced by the presence of the Fe_3O_4 nanoparticles take place, giving rise to a voltage over a broader H scale around the FMR. Another possible explanation can be given by the nano-oxide particles which could be ferrimagnetic and couple dynamically to the spin system at the Fe/Pt interface. For clarification further investigations are required.

In summary we show that Fe_3O_4 nanoparticles at the Fe/Pt interface significantly increase the fourfold anisotropy compared to the pure Fe/Al reference. In FMR and spin-pumping experiments a very broad linewidth of the FMR peak is revealed. The V_{DC} voltage is steadily generated over a wide external magnetic field range ΔH. These results lead to the presumption that magnetite particles embeded at the Fe/Pt latice interface strongly interact with the surounding spin system.

The Carl Zeiss Stiftung is gratefully acknowledged for financial support.

References

[1] O. Mosendz, J.E. Pearson, F.Y. Fradin, S.D. Bader, A. Hoffmann, *Suppression of spin-pumping by a MgO tunnel-barrier* Appl. Phys. Lett. **96**, 022502 (2010).

[2] C.H. Du, H.L. Wang, Y. Pu, T.L. Meyer, P.M. Woodward, F.Y. Yang, and P.C. Hammel, Phys. Rev. Lett. **111**, 247202 (2013).

[3] L. Mihalceanu, S. Keller, J. Greser, D. Karfaridis, K. Simeonidis, G. Vourlias, T. Kehagias, A. Conca, B. Hillebrands, and E. Th. Papaioannou, Appl. Phys. Lett. **110**, 252406 (2017).)

[4] P Prieto, J. de la Figuera, L. Martín-García, J.E. Prieto, J.F, Marco, *Fourfold in-plane magnetic anisotropy of magnetite thin films grown on TiN buffered*, J. Mater. Chem. C **4**, 7632 (2016).

[5] T. Schemme, A. Krampf, F. Bertram, T. Kuschel, K. Kuepper, and J. Wollschläger, *Modifying magnetic properties of ultra-thin magnetite films by growth on Fe pre- covered MgO(001)*, J. Appl. Phys. **118**, 113904 (2015).

[6] A. Conca, J. Greser, T. Sebastian, S. Klingler, B. Obry, B. Leven, B. Hillebrands, *Low spin-wave damping in amorphous CoFeB thin films*, J. Appl. Phys. **113**, 213909 (2013).

[7] M. Harder, Y. Gui, C.-M. Hu, *Electrical Detection of Magnetization Dynamics via Spin Rectification Effects*, Phys. Rep. **661**, 1-59 (2016).

[8] S. Keller, J. Greser, M.R. Schweizer, A. Conca, V. Lauer, C. Dubs, B. Hillebrands, and E.Th. Papaioannou, *Relative weight of the inverse spin-Hall and spin-rectification effects for metallic polycrystalline Py/Pt, epitaxial Fe/Pt, and insulating YIG/Pt bilayers: Angular dependent spin pumping measurements*, Phys. Rev. B **69** , 024437 (2017).

D. New Materials and Heusler Compounds

Developing new materials as well as modifying already well-known materials in order to generate properties of interest is an important aspect in our research. In our group we focus on the application of these materials in magnon-spintronic devices. The samples are mostly shared thanks to national and international collaborations, involving a strong student exchange. The material class of Heusler compounds contains several promising candidates regarding their utilization in the field of *spintronics* and in particular of *magnon spintronics*. The major reasons for the interest in Heusler compounds are their high Curie temperature, their high spin polarization, and their low magnetic Gilbert damping. In addition, some of them find application in devices requiring perpendicular orientation of magnetization as for instance in spin torque switching devices. The perpendicular magnetization is either a result of the bulk properties of the material, or is achieved due to the contribution of a interface with another layer material. Heusler compounds have the general composition X_2YZ or XYZ, where X and Y are transition metals, and Z is an element of the main groups III-V. One of the most promising classes of Heusler materials is given by the cobalt-based compounds with the composition Co_2YZ. This class shows high spin polarization as well as a low Gilbert damping. The reason for both is the half-metallic character of Heusler compounds. Half metallicity describes the different features in the band structure of minority and majority electrons close to the Fermi energy. For the minority electrons, a band gap can be found at the Fermi energy. In contrast to this, the majority spin channel exhibits a finite density of states at the Fermi level and, thus, metallic character. Among the wide family of the Heusler compounds, the interest has been lately focused on candidates that exhibit a robust perpendicular magnetic anisotropy together with the compatibility with standard tunneling barrier materials such as MgO or $MgAl_2O_4$.

In report 4.18 we investigate the effect of Al doping on the magnetic properties of the CoFeB alloy. Comparative measurements of the saturation magnetization, the Gilbert damping parameter α, and the exchange constant as a function of the annealing temperature for CoFeB and CoFeAlB thin films are presented. The data prove that CoFeAlB fulfills the requirements to be considered as an attractive candidate for spin torque switching purposes and a reduction of the switching current in comparison with CoFeB is expected.

In report 4.19 we reveal the enhancement of the longitudinal magneto-optical effect in the ferromagnetic dielectric bismuth substituted yttrium iron garnet (Bi-YIG), induced by localized surface plasmons in gold nanoparticles. The magnetoplasmonic interactions were studied with the aid of a spectroscopic Magneto-Optical Kerr Effect (MOKE) setup in combination with an optical spectrophotometer. The spectroscopic measurements were performed using a selectively filtered supercontinuum laser source.

In report 4.20 we investigate a series of films with varying thickness of the Heusler alloy Co_2FeAl in order to study the effect of annealing on the interface with a MgO layer and on the bulk magnetic properties. This work is part of the joint HEUMEM research project. The evolution of the strength of the perpendicular magnetic anisotropy with annealing is reported and discussed. We observe that while the perpendicular anisotropy is not present in as-deposited samples, it increases strongly with annealing and it stabilizes a perpendicular orientation for films thinner than 1.7 nm. The evolution of the in-plane bulk anisotropy and the Gilbert damping parameter is also shown.

E. Neue Materialien und Heusler-Legierungen

Sowohl die Entwicklung neuer als auch die Verbesserung bereits bekannter Materialien zur Untersuchung interessanter Materialeigenschaften ist ein wichtiger Aspekt unserer Forschung. In unserer Gruppe legen wir ein spezielles Augenmerk auf die Anwendung der Materialien in magneto-spintronische Devices. Die Proben werden dazu häufig über nationale und internationale Zusammenarbeit hergestellt. Hierzu gibt es einen intensiven Doktorandenaustausch. Die Gruppe der Heusler-Verbindungen enthält zahlreiche erfolgversprechende Kandidaten hinsichtlich der Nutzung im Bereich der Spintronik und insbesondere der Magnon-Spintronik. Die Hauptgründe für das Interesse an Heusler-Verbindungen sind ihre hohe Curie-Temperatur, ihre große Spinpolarisation sowie ihre geringe magnetische Gilbert-Dämpfung. Darüber hinaus finden einige von ihnen Anwendung in Bauteilen, die eine senkrechte Ausrichtung der Magnetisierung erfordern, wie z. B. in Spin-transfer-torque-Systemen. Die senkrechte Magnetisierung ist entweder eine Folge der Volumeneigenschaften des Materials oder wird durch den Beitrag einer Grenzfläche mit einem anderen Schichtmaterial erreicht. Heusler-Verbindungen besitzen die allgemeine Zusammensetzung X_2YZ oder XYZ. Hierbei sind X und Y Übergangsmetalle, während Z ein Element der Hauptgruppen III-V ist. Eine der vielversprechendsten Untergruppen der Heusler-Materialien sind die Kobalt-basierten Verbindungen mit der Zusammensetzung Co_2YZ. Der Grund sowohl für die große Spinpolarisation als auch für die geringe Gilbert-Dämpfung liegt im halbmetallischen Charakter der Heusler-Verbindungen. Dieser halbmetallische Charakter beschreibt die verschiedenen Eigenheiten der Bandstruktur von Minoritäts- und Majoritätselektronen nahe der Fermi-Kante. Für die Minoritätselektronen lässt sich eine Bandlücke an der Fermi-Kante beobachten, wohingegen die Bandstruktur der Majoritätselektronen dort eine endliche Zustandsdichte und somit metallischen Charakter aufweist. Innerhalb der großen Gruppe der Heusler-Verbindungen wurde das Hauptaugenmerk zuletzt auf solche Verbindungen gelegt, die eine starke senkrechte magnetische Anisotropie aufweisen und ebenfalls kompatibel sind mit üblichen Materialien für Tunnelbarrieren wie MgO oder $MgAl_2O_4$.

In Bericht 4.18 untersuchen wir den Einfluss der Al-Dotierung auf die magnetischen Eigenschaften der CoFeB-Legierung. Vergleichsmessungen der Sättigungsmagnetisierung, des Gilbert-Dämpfungsparameters α und der Austauschkonstante als Funktion der Tempertemperatur fürs CoFeB- und CoFeAlB-Dünnschichten werden dargestellt. Die Daten belegen, dass CoFeAlB die Anforderungen als attraktiver Kandidat für Spin-Drehmomentschalten erfüllt und eine Reduzierung des Schaltstroms gegenüber CoFeB erwartet wird.

In Bericht 4.19 wird die Verbesserung des longitudiualen magneto-optischen Effekts im ferromagnetischen, dielektrischen Wismut-substituierten Yttrium-Eisen-Granat (Bi-YIG) gezeigt, der durch lokalisierte Oberflächenplasmonen in Gold-Nanopartikeln induziert wird. Die magneto-plasmonischen Wechselwirkungen wurden mit Hilfe einer spektroskopischen magneto-optischen Kerr-Effekt (MOKE) Apparatur in Kombination mit einem optischen Spektralphotometer untersucht. Die spektroskopischen Messungen wurden mit einer selektiv gefilterten Superkontinuum-Laserquelle durchgeführt.

In Bericht 4.20 wird eine Reihe von Filmen mit unterschiedlicher Dicke der Heusler-Legierung Co_2FeAl gemessen, um den Einfluss des Temperns auf die Grenzfläche mit einer MgO-Schicht und auf die magnetischen Volumen-Eigenschaften zu untersuchen. Diese Arbeit ist Teil des gemeinsamen Forschungsprojekts HEUMEM. Die Erhöhung der senkrechten magnetischen Anisotropie durch das Tempern wird berichtet und diskutiert. Wir stellen fest, dass die senkrechte Anisotropie zwar nicht in ungetemperten Proben vorhanden ist, dass sie jedoch beim Tempern stark zunimmt

und eine senkrechte Orientierung für dünnere Filme unterhalb von $1,7\,\mathrm{nm}$ stabilisiert. Die Entwicklung der Volumen-Anisotropie und des Gilbert-Dämpfungsparameters werden ebenfalls dargestellt.

4.18 Low damping and low magnetization CoFeAlB alloy for spin transfer torque switching

A. Conca, T. Meyer, and B. Hillebrands

In collaboration with T. Nakano and Y. Ando, Department of Applied Physics, Tohoku University, Sendai, Japan.

For the application in magnetic random access memories, the switching of the magnetization of the free layer via the spin transfer torque (STT) effect using spin polarized currents is a key technology. However, the required currents for the switching process are still large and hinder the applicability of this technique. The critical switching current density for an in-plane magnetized system is given by [2]

$$J_{c0} = \frac{2e\alpha\mu_0 M_S t_f (H_K + H_{ext} + M_S/2)}{\hbar\eta} \quad , \tag{1}$$

where e is the electron charge, α is the Gilbert damping parameter, M_S is the saturation magnetization, t_f is the thickness of the free layer, H_{ext} is the external field, H_K is the effective anisotropy field and η is the spin transfer efficiency. From the expression it is clear that, concerning material parameters, J_{c0} is ruled by the product αM_S^2. For out-of-plane oriented layers, the term $M_S/2$ vanishes and J_{c0} is proportional to αM_S. A proper strategy to reduce the critical switching currents is then defined by the reduction of M_S of available materials. A critical point is, however, that this reduction must not be associated with an increase of the Gilbert damping.

Here, we report on results on Al doped CoFeB alloy thin films characterized by ferromagnetic resonance spectroscopy (FMR). The dependence of M_S, α and the exchange constant on the annealing temperature is discussed together with the suitability of the investigated alloy for STT switching.

The samples are grown on Si/SiO_2 substrates using DC (for metals) and RF (for MgO) sputtering techniques. The layer stack of the samples is Si/SiO_2/Ta(5)/MgO(2)/FM(40)/MgO(2)/Ta(5) where FM = $Co_{40}Fe_{40}B_{20}$ (CoFeB) or $Co_{36}Fe_{36}Al_{18}B_{10}$ (CoFeAlB). Here, the values in brackets denote the layer thicknesses in nm. Subsequently, the samples are annealed for 60 min at different temperatures ranging from 200°C to 500°C. The material parameters are studied by measuring the ferromagnetic resonance using a strip-line vector network analyzer (VNA-FMR). A detailed description of the FMR measurement and analysis procedure is shown in previous works [3, 4]. In addition, Brillouin light spectroscopy (BLS) is used for the determination of the exchange constant.

The crystalline bulk properties of the films were studied by X-ray diffractometry (XRD) using the Cu-K_α line. The onset of the CoFe diffraction peaks have proven the start of crystallization at high annealing temperatures $T_{ann} > 400$°C. In the case of lower annealing temperatures or the as-deposited samples, the FM layer is in an amorphous state. The first appearance of the (200) diffraction peak occurs at the same point for both alloys showing a very similar thermal evolution. This simplifies a substitution of CoFeB by the CoFeAlB alloy in tunneling junctions since the same annealing recipes can be applied.

This work has been recently published in [1].

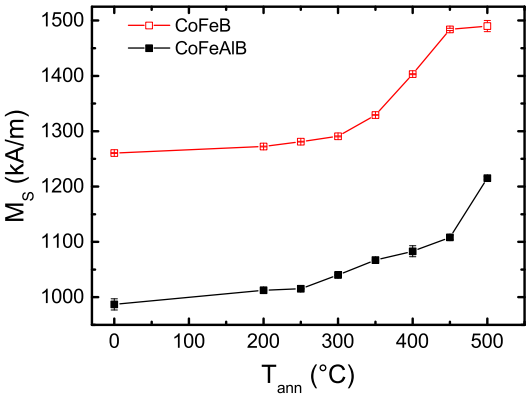

Fig. 1: Evolution of the saturation magnetization for CoFeB and CoFeAlB with the annealing temperature T_{ann}.

Figure 1 shows the obtained values for M_S for all samples from the Kittel fit [6] to the dependence of the FMR frequency on the external magnetic field. In the case of the CoFeAlB compound, a strong reduction of M_S compared to CoFeB is observed and the relative difference is maintained for all T_{ann}. Significantly, the increase in M_S starts for values of T_{ann} lower than expected from the appearance of the characteristic CoFe diffraction peaks in the XRD data. For CoFeB a saturation value around $M_S \approx 1500$ kA/m is reached at $T_{ann} = 450°C$. This is compatible with values reported for CoFe (1350-1700 kA/m) [7, 8] and CoFeB (1350-1500 kA/m) [8, 9]. On the contrary, for CoFeAlB the introduction of Al reduces the value of M_S of the samples and the annealing does not recover to CoFe-like values.

Furthermore, from the linear dependence of this linewidth on the FMR frequency, the Gilbert damping parameter is extracted (as exemplarily shown for the CoFeAlB alloy in the inset) and the results are shown in Fig. 2. For $T_{ann} < 350°C$, where the amorphous phase is still dominating, almost no difference between both alloys is observed. With increasing T_{ann}, the damping increases for both alloys but the evolution is different. For CoFeAlB, the increase starts almost abruptly at $T_{ann} = 400°C$, reaches a maximum of $\alpha = 0.02$ and then decreases again to $\alpha = 0.012$ for $T_{ann} = 500°C$. In contrast, for CoFeB, α increases continously with T_{ann} and increases steadily with higher T_{ann}. In fact, due to the large linewidths reached for $T_{ann} = 500°C$, the value of α cannot be properly estimated and only a lower limit of 0.03-0.04 and a upper bound of 0.05-0.06 can be given. This situation is represented by the dashed line in Fig. 2. It is important to note here that when the crystallization process is fulfilled (i.e. for $T_{ann} = 500°C$), α is much lower for the Al doped alloy. This is relevant for the application in tunneling junctions where a dominant (100) crystallization is required for the presence of the spin filtering effect causing large magnetoresistance values.

The increase of α for both alloys is detected after the first arising of the peaks in the XRD measurements (not shown here). This might appear to be contradictory since an improvement in crystalline order is usually related to a reduction of the damping. However, two points modify this view. First, it is not only an incremental improvement of the crystalline structure occurring in this case, but a complete transition from an amorphous phase to a polycrystalline phase. Thus, a priori it is difficult to predict which one will have lower damping properties. Second and more important, the damping properties of a thin film are very strongly influenced by the homogeneity (structural and chemical) of the sample. At the same time, it is already known that in CoFeB films, the crystallization process starts and evolves in a non-homogenous way. The MgO layer(s) act as a seed for the nucleation of the crystallization process which then advances towards the rest of the film. The same can happen when other seed layers are used. This has been, for instance, reported in [5, 10, 11]. This results in the fact that, although the XRD signal of the crystalline peaks increases when the

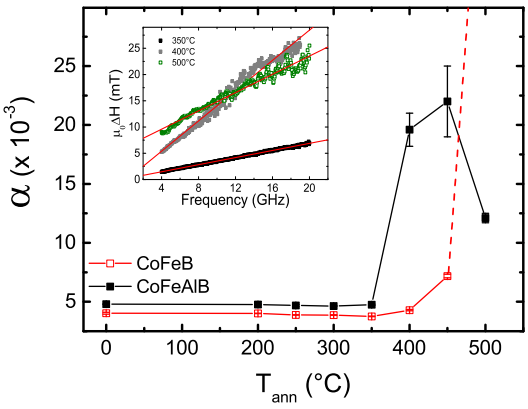

Fig. 2: Gilbert damping parameter α dependence on the annealing temperature T_{ann}. The inset shows the linear dependence of the linewidth on the frequency exemplarily for CoFeAlB annealed at 350°C, 400°C and 500°C. The lines are linear fits. The α value for $T_{ann} = 500°$ is only a rough estimation since the large linewidth value does not allow for a better estimation.

crystallization starts, the damping increases also due to a larger inhomogeneity in the film.

In addition to the change of M_S and α by the Al doping, the exchange constant A_{ex} is a critical parameter that is strongly influenced by the introduction of Al. The determination of A_{ex} can be achieved via the dependence of the frequency of the perpendicular standing spin-wave (PSSW) modes on the external static magnetic field [12]. As shown in previous works [4, 13], it is possible to observe the PSSW modes in metallic films with a standard VNA-FMR setup. However, the signal is strongly reduced compared to the FMR peak. For the samples presented here, the PSSW peak could not be observed for $T_{ann} > 400°C$ since the increased damping leads to a broadening and lowering of the peak which prevents the estimation of A_{ex}. For this reason, BLS spectroscopy is used for the measurement of the frequency position of the PSSW modes.

Figure 3 shows the evolution of A_{ex} upon annealing for both alloys. The error bars are the result of considering the fit error and an error of ± 1 nm in the thickness of the films. For the films dominated by the amorphous phase, A_{ex} is much lower for CoFeAlB which is also compatible with the lower M_S. However, as the crystallization evolves, A_{ex} increases stronger than for CoFeB and the same value is obtained for the fully crystallized films. This fact points to a similar role of Al and B during the crystallization process: when the CoFe crystallites form, the light atoms are expelled forming a Al-B-rich matrix embedding the magnetic crystallites or diffuse to the CoFe(Al)B/MgO interface or to the MgO layer itself. This explains also the similar evolution observed in the XRD data. The lower maximal magnetization obtained for the CoFeAlB can be explained by the reduced CoFe content but also a certain number of residual Al and B atoms in the crystallites, which may differ for both alloys.

The A_{ex} values for as-deposited CoFeB films are very similar to those in previous reports [4,13,14]. Concerning the values for the crystallized samples, a comparison with literature has to be made with caution since the properties are strongly dependent on the B content and on the ratio between Co and Fe as well as on the exact annealing conditions. Nevertheless, the maximal value and the evolution with T_{ann} for CoFeB is similar to the ones reported by some of the authors [4]. In addition, results for alloys with the same B content are compatible with our data [15]. CoFeB films with reduced B content show larger values [8]. The same is true for CoFe alloys with values between 3.84-2.61$\times 10^{-11}$ J/m depending on the exact stoichiometry [7, 8].

In summary, the presented experimental results show that CoFeAlB is a good candidate as an alternative to CoFeB for spin torque switching devices due to the strong reduction of M_S for different annealing temperatures without a strong increase in the damping parameter. Even more, the damping parameter is reduced also for CoFeAlB for the largest annealing temperature used in this work. Furthermore, the results reveal a larger thermal robustness of the damping properties in CoFeAlB

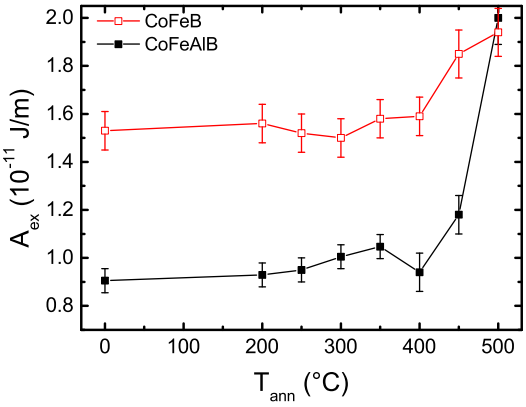

Fig. 3: Dependence of the exchange constant A_{ex} on the annealing temperature T_{ann} for CoFeB and CoFeAlB.

compared to CoFeB.

Financial support by M-era.Net through the HEUMEM project, by the DFG in the framework of the Collaborative Research Center TRR 173 Spin+X and by the JSPS Core-to-Core Program is gratefully acknowledged.

References

[1] A. Conca, T. Nakano, T. Meyer, Y. Ando, B. Hillebrands, *CoFeAlB alloy with low damping and low magnetization as a candidate for spin transfer torque switching*, J. Appl. Phys. **122**, 073902 (2017).
[2] Z. Diao, Z. Li, S. Wang, Y. Ding, A. Panchula, E. Chen, L.-C. Wang, Y. Huai, *Spin-transfer torque switching in magnetic tunnel junctions and STT-RAM*, J. Phys. D: Appl. Phys. **19**, 165209 (2007).
[3] A. Conca, S. Keller, L. Mihalceanu, T. Kehagias, G.P. Dimitrakopulos, B. Hillebrands, E.Th. Papaioannou, *Study of fully epitaxial Fe/Pt bilayers for spin pumping by FMR spectroscopy*, Phys. Rev. B **93**, 134405 (2016).
[4] A. Conca, E.Th. Papaioannou, S. Klingler, J. Greser, T. Sebastian, B. Leven, J. Lösch, B. Hillebrands, *Annealing influence on the Gilbert damping parameter and the exchange constant of CoFeB thin films*, Appl. Phys. Lett. **104**, 182407 (2014).
[5] C.Y. You, T. Ohkubo, Y.K. Takahashi, K. Hono, *Boron segregation in crystallized MgO/amorphous-$Co_{40}Fe_{40}B_{20}$ thin films*, J. Appl. Phys. **104**, 033517 (2008).
[6] C. Kittel, *On the theory of ferromagnetic resonance absorption*, Phys. Rev. **73**, 155 (1948).
[7] X. Liu, R. Sooryakumar, C.J. Gutierrez, G.A. Prinz, *Exchange stiffness and magnetic anisotropies in bcc $Fe_{1-x}Co_x$ alloys*, J. Appl. Phys. **75**, 7021 (1994).
[8] C. Bilzer, T. Devolder, J.-V. Kim, G. Counil, C. Chappert, S. Cardoso, P.P. Freitas, *Study of the dynamic magnetic properties of soft CoFeB films*, J. Appl. Phys. **100**, 053903 (2006).
[9] X. Liu, W. Zhang, M.J. Carter, G. Xiao, *Ferromagnetic resonance and damping properties of CoFeB thin films as free layers in MgO-based magnetic tunnel junctions*, J. Appl. Phys. **110**, 033910 (2011).
[10] Y. Lu, B. Lépine, G. Jézéquel, S. Ababou, M. Alnot, J. Lambert, A. Renard, M. Mullet, C. Deranlot, H. Jaffrès, F. Petroff, J.-M. George, *Depth analysis of boron diffusion in MgO/CoFeB bilayer by x-ray photoelectron spectroscopy*, J. Appl. Phys. **108**, 043703 (2010).
[11] T. Miyajima, T. Ibusuki, S. Umehara, M. Sato, S. Eguchi, M. Tsukada, Y. Kataoka, *Transmission electron microscopy study on the crystallization and boron distribution of CoFeB/MgO/CoFeB magnetic tunnel junctions with various capping layers*, Appl. Phys. Lett. 94, 122501 (2009).
[12] S.O. Demokritov, B. Hillebrands, *Spin Dynamics in Confined Magnetic Structures I*, Springer, Berlin, (2002).
[13] A. Conca, J. Greser, T. Sebastian, S. Klingler, B. Obry, B. Leven, B. Hillebrands, *Low spin-wave damping in amorphous $Co_{40}Fe_{40}B_{20}$ thin films*, J. Appl. Phys. **113**, 213909 (2013).
[14] J. Cho, J. Jung, K.-E.Kim, S.-I. Kim, S.-Y. Park, M.-H. Jung, C.-Y. You, *Effects of sputtering Ar gas pressure in the exchange stiffness constant of $Co_{40}Fe_{40}B_{20}$ thin films*, J. of Magn and Magn. Mat. **339**, 36 (2013).
[15] A. Helmer, S. Cornelissen, T. Devolder, J.-V. Kim, W. van Roy, L. Lagae, C. Chappert, *Quantized spin-wave modes in magnetic tunnel junction nanopillars*, Phys. Rev. B **81**, 094416 (2010).

4.19 Magneto-plasmonic interaction in YIG/Au hybrid nanostructures

S.D. Pappas, P. Lang, M. Schweizer, B. Hillebrands, and E.Th. Papaioannou

In collaboration with Ken-ichi Uchida, National Institute for Materials Science, Tsukuba, Ibaraki 305-0047, Japan

Strong localization of light, enabled by surface plasmons, increases the magneto-optical response of ferromagnetic materials [1–3]. In this work, we reveal the enhancement of the longitudinal magneto-optical effect in the ferromagnetic dielectric bismuth substituted yttrium iron garnet (Bi-YIG), induced by localized surface plasmons (LSPs) in gold nanoparticles (AuNPs). The magneto-plasmonic interactions were studied with the aid of a spectroscopic magneto-optical Kerr effect (MOKE) setup operating in the longitudinal mode, in combination with an optical spectrophotometer. The spectroscopic MOKE measurements were performed with the aid of a selectively filtered supercontinuum laser source. The comparison of the experimental results reveals a large enhancement of the longitudinal magneto-optical signal for the sample containing AuNPs close to the LSP resonances. Furthermore, we fitted computationally the experimental data, in order to estimate the localized plasmonic effects on the magneto-optical parameters.

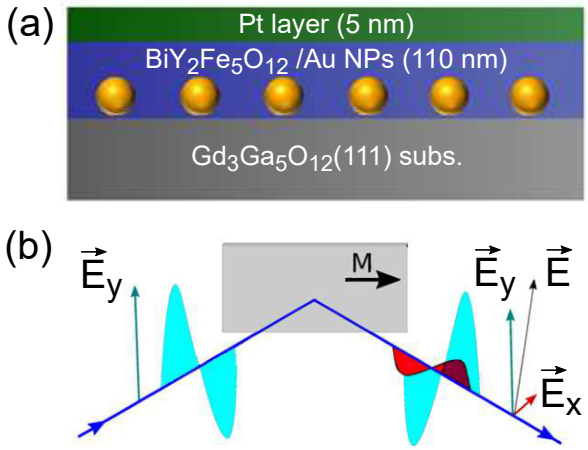

Fig. 1: (a) Schematic illustration of the sample used in the present study. (b) Scheme of the longitudinal MOKE geometry used to record the Kerr rotation of the Pt/$BiY_2Fe_5O_{12}$/(AuNPs) samples.The Kerr rotation induced by the sample is recorded for a range of different wavelengths of the incident light.

The Bi-YIG samples used in our study were produced by means of a metal-organic decomposition (MOD) method [4]. The topology of the examined samples is presented in Fig. 1 (a). The samples consist of AuNPs fabricated on top of a single crystalline GGG (111) substrate by post heating of a thin continuous Au film. Subsequently, on top of the AuNPs layer, the $BiY_2Fe_5O_{12}$ film is deposited. Finally, a Pt layer covers the whole structure. The deposition procedure is described in detail in Ref. [5]. Additionally, a second sample fabricated in the exact same procedure and settings, containing no AuNPs however, was also used as a reference. In Fig. 1(b) the geometry of the longitudinal MOKE (LMOKE) method is schematically shown. In the LMOKE mode, the magnetization (M) of the sample lies on the sample plane as well as on the plane of incidence of the laser light. The incoming laser light can be either s- or p- polarized. In Fig. 1(b) only the case of a measurement performed with s-polarized light is presented for simplicity. The Kerr rotation induced by the ferromagnetic sample is measured by means of a Wollaston prism in combination with a balanced photodiode setup. The setup is fully automated and, upon proper calibration, it can provide the magneto-optical Kerr rotation in absolute values. The probing light in the range of

550 - 900 nm was provided by a supercontinuum laser light source (SuperK Extreme) which was properly monochromatized by an acousto-optical tunable filter.

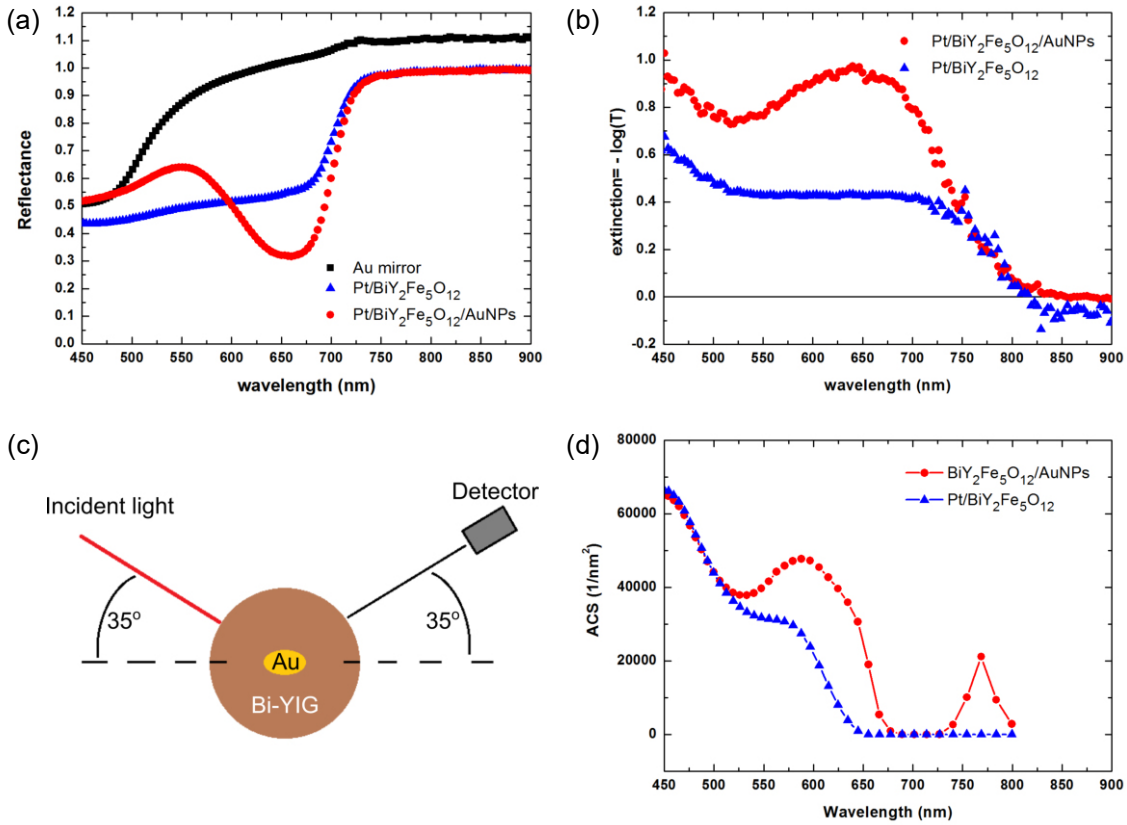

Fig. 2: (a) Reflectivity measurements of the $Pt/BiY_2Fe_5O_{12}$/(AuNPs) samples. The reflectivity measurement of an Au mirror is used as a reference. (b) Extinction plot as a function of wavelength for the same samples as in (a). (c) Schematic view of the geometry of the model used in the CST simulations. The simulated ellipsoidal Au NP has a major and a minor axis of 60 and 30 nm respectively. The NP is surrounded by a Bi-YIG shell with a radius of 110 nm. (d) Simulated absorption cross section for the system shown in (c).

Reflectance and transmittance measurements were conducted for both samples (reference sample and the sample containing AuNPs). A microspectrophotometer which consists of an optical microscope combined with a photodiode array detector was used for this purpose. As a reference for the reflection mode, a flat Au thin film mirror was used. In Fig. 2(a) the reflectance of the examined samples as well as the reflectance of the Au mirror as a function of wavelength is plotted. By comparing the spectra, a relatively sharp minimum of the reflectivity for the sample containing AuNPs occurs in the wavelength region of 600 -700 nm. The response of the sample containing no AuNPs is relatively flat in the same wavelength region. The extinction spectra (Fig. 2(b)) of the same samples show a similar behavior, namely the curve corresponding to the sample containing AuNPs exhibits a peak in the same wavelength region as for the reflectance curve. These features can be attributed to the excitation of LSPs in this specific wavelength region. In the wavelength region where the plasmonic resonance occurs, photons couple effectively to surface plasmons which are localized in the Au nanoparticle (resonance effect). Through this mechanism, optical energy is converted to phonons due to ohmic losses in the metal. Thus, the absorption (extinction) is increased and the scattered radiation (and consequently the reflectance) from the nanoparticle is

reduced.

To investigate the role of the shape of the AuNPs on the enhanced electromagnetic field distribution, induced by LSPs, we performed numerical calculations. These calculations were based on the Finite Integration Technique (FIT) method, by using the Computer Simulation Technology (CST) software. Our effort to reproduce qualitatively the experimental data is summed in Fig. 2(c) and Fig. 2(d). The geometry of the model is presented in Fig. 2(c). We modeled the AuNPs by ellipsoids encapsulated in a shell of $BiY_2Fe_5O_{12}$. The material properties used for the simulations, like the dielectric tensor of $BiY_2Fe_5O_{12}$ and Au, were obtained from already existing literature [6, 7]. The geometry used to build the model is based on the MOKE geometry used to perform our magneto-optical experiments. The calculated Absorption Cross Section (ACS) which is shown in Fig. 2(d) reveals also the existence of a strong peak in the wavelength region close to the experimental. From the Near Field image (not shown here) we observe indeed a strong enhancement of the electric field close to the AuNP, in the wavelength region of about 600 - 650 nm.

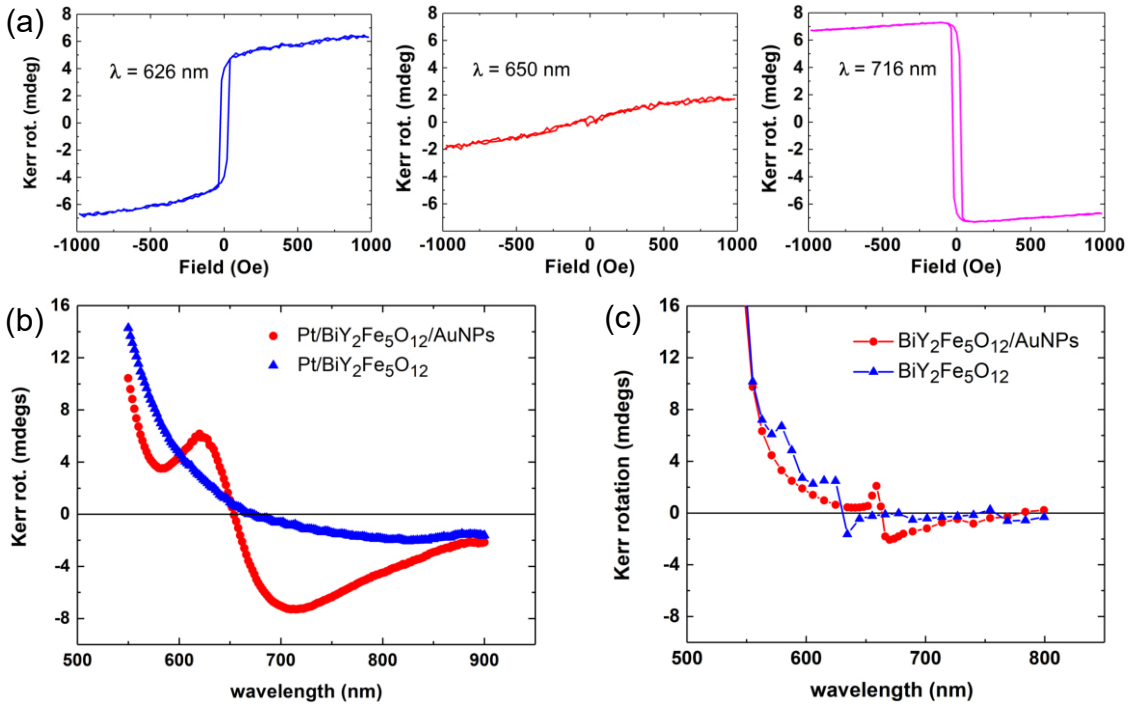

Fig. 3: (a) Magnetic loops recorded in the longitudinal mode for the Pt/$BiY_2Fe_5O_{12}$/AuNPs sample at three different wavelengths. The Kerr rotation is measured in absolute values. (b) Dependence of the Kerr rotation as a function of wavelength recorded for the samples with (red bold circles) and without (blue triangles) AuNPs. (c) CST simulation of the Kerr rotation for the sample containing AuNPs. The simulation is made for a Bi-YIG extended slab containing (not containing) embedded AuNPs. The detection geometry is described schematically in Fig. 2c.

We used MOKE spectroscopy in order to study the effect of LSPs on the magneto-optical response of the $BiY_2Fe_5O_{12}$ film. For this purpose, the Kerr rotation, induced by the magnetic sample when it is fully saturated along one of the directions shown in Fig. 1 (b), is recorded as a function of wavelength. In Fig. 3 (a) the magnetic loops recorded in the LMOKE mode at three different wavelength values, are presented. These measurements correspond to the sample with AuNPs.

The direction of the magnetic loop is connected with the sign of the Kerr rotation. We observe that for $\lambda = 650$ nm the magneto-optical response of the hybrid $BiY_2Fe_5O_{12}$/AuNPs film becomes zero. Although the material looks non-ferromagnetic from its magnetic response, in reality the magneto-optical response is minimum - to - zero. The dependence of the Kerr rotation as a function of the wavelength for both of the samples (with and without AuNPs) is shown in Fig. 3(b). For both of the samples exists a certain value of wavelength for which the response becomes zero. For the sample containing AuNPs, however, the magneto-optical response is strongly altered in the optical region where the resonant phenomena take place, by the presence of the LSPs. Two sharp features are located at about 625 nm and at 700 nm, where a quite strong enhancement with negative sign occurs. By this experiment, a large intensification of the LMOKE response for the hybrid $BiY_2Fe_5O_{12}$/AuNPs is revealed. Fig. 3(c) shows the simulated Kerr rotation by using the CST software for the geometry shown in Fig. 2(c). For the simulation, the dielectric tensor of $BiY_2Fe_5O_{12}$/AuNPs was used. The values of the diagonal and off-diagonal elements were taken from [7]. The magneto-optic activity is attributed to the off-diagonal elements of the dielectric tensor. Indeed, the numerical data reveal a sign change of the Kerr rotation in the region close to 600 nm. In the future, the numerical calculations will help us to reveal if the observed enhanced magneto-optic activity is attributed to a possible alteration induced on the dielectric tensor of $BiY_2Fe_5O_{12}$ caused by the intensified electric field of the LSPs, or if it is simply attributed to the alteration of the light scattering from AuNPs close to the resonant wavelength.

The enhancement of the magneto-optical effects in ferromagnetic materials, induced by plasmonic resonances, can have a big impact in device applications such as optical magnetic storage. As a step forward, engineering of the magneto-plasmonic structures can be used in order to control the magneto-optical response.

The collaborative research center SFB TRR 173: SPIN+X Project B07 and the Carl Zeiss Foundation are gratefully acknowledged.

References

[1] V. I. Belotelov, I. A. Akimov, M. Pohl, V. A. Kotov, S. Kasture, A. S. Vengurlekar, A. V. Gopal, D. R. Yakovlev, A. K. Zvezdin and M. Bayer, *Enhanced magneto-optical effects in magnetoplasmonic crystals*, Nature Nanotechnology **6**, 370 (2011).

[2] E. Th. Papaioannou, V. Kapaklis, E. Melander, B. Hjörvarsson, S. D. Pappas, P. Patoka, M. Giersig, P. Fumagalli, A. Garcia-Martin and G. Ctistis, *Surface plasmons and magneto-optic activity in hexagonal Ni anti-dot arrays*, Optics Express **19**, 23867 (2011).

[3] M. Rollinger, P. Thielen, E. Melander, E. Östman, V. Kapaklis, B. Obry, M. Cinchetti, A. Garcia-Martin, M. Aeschlimann, and E. Th. Papaioannou, *Light localization and magneto-optic enhancement in Ni antidot arrays*, Nano Lett. **16**, 2432 (2016).

[4] K. Uchida, H. Adachi, D. Kikuchi, S. Ito, Z. Qiu, S. Maekawa and E. Saitoh, *Generation of spin currents by surface plasmon resonance*, Nat. Commun. **6**, 5910 (2015).

[5] H. Uchida, Y. Masuda, R. Fujikawa, A. V. Baryshev,and M. Inoue, *Large enhancement of faraday rotation by localized surface plasmon resonance in Au nanoparticles embedded in Bi:YIG film*, J. Magn. Magn. Mat. **321**, 843 (2009).

[6] V. Doormann, J. P. Krumme, and C. P. Klages, *Measurement of the refractive index and optical absorption spectra of epitaxial bismuth substituted yttrium iron garnet films at uv to near-ir wavelengths*, Appl. Phys. A **34**, 223 (1984).

[7] S. Wittekoek, T. J. A. Popma, J. M. Robertson, and P. F. Bongers, *Magneto-optic spectra and the dielectric tensor elements of bismuth-substituted iron garnets at photon energies between 2.2 and 5.2 eV*, Phys. Rev. B **12**, 2777 (1975).

4.20 Evolution of the interfacial perpendicular magnetic anisotropy constant of the Co2FeAl/MgO interface upon annealing

A. Conca, B. Hillebrands

In collaboration with A. Niesen, G. Reiss, Center for Spintronic Materials and Devices, Physics Department, Bielefeld University, Germany.

In order to achieve efficient spin torque switching, materials with a certain set of properties are required. These properties are a combination of low damping and low magnetization, together with the presence of a robust perpendicular magnetic anisotropy (PMA). Additionally, these materials should show a high spin polarization and compatibility with standard tunneling barrier materials such as MgO or $MgAl_2O_4$. For the PMA properties of thin Heusler films, the interface-induced perpendicular anisotropy plays a critical role and its strength is given by the value of the perpendicular interfacial anisotropy constant $K_S^{\perp}$. The interfacial properties, and therefore the value of the constant, are strongly modified by the exact conditions of the annealing treatment for the stack, which is required to improve the crystalline order of the Heusler films [2, 3] and to achieve large TMR values. The alloy Co_2FeAl belongs to the materials for which large TMR [4] has been reported, and low damping [5–7] and large PMA [6] have been found. In this work, we study the evolution of $K_S^{\perp}$ with annealing in systems with a MgO interface by measuring different thickness series. Since the in-plane anisotropies and the Gilbert damping parameter change with varying thickness and annealing temperature, also their evolution is reported. The relevance of the study is not limited to Co_2FeAl but it is a model for all TMR systems with Co-based Heusler alloys and an interface with a MgO tunneling barrier.

Thickness series (7-80 nm) of Co_2FeAl (CFA) epitaxial films were prepared at the Bielefeld University and a microstrip-based VNA-FMR setup was used to study their magnetic properties. The stack layer structure is MgO(100)(subs)/ MgO(5)/CFA(d)/MgO(7)/Ru(2) with $d = 7, 9, 11, 15, 20,$ 40 and 80 nm. Rf-sputtering was used for MgO and dc-sputtering for the other materials. The values of the annealing temperature for the two series with thermal treatment are 320°C and 450°C. The layer stacking is symmetrical around CFA so that a similar interface is expected for both sides.

From the dependence of H_{FMR} on the resonance frequency f_{FMR}, the effective magnetization M_{eff} is extracted using a fit to Kittel's formula [9]. For a more detailed description of the FMR measurement and analysis procedure please see Ref. [10]. M_{eff} is related to the saturation magnetization of CFA by

$$M_{\mathrm{eff}} = M_{\mathrm{s}} - H_K^{\perp} = M_{\mathrm{s}} - \frac{2K_S^{\perp}}{\mu_0 M_{\mathrm{s}} d} \quad , \tag{1}$$

where $K_S^{\perp}$ is the perpendicular surface (or interfacial) anisotropy constant.

Fig. 1 shows the dependence of M_{eff} on $1/d$ for the three CFA series. The lines are a fit to Eq. 1. Let us first discuss the case of the as-deposited series shown in Fig. 1a. An almost constant value for M_{eff} is observed for the low thickness range (15-7 nm) where the interface properties should become dominating. The fit gives a value for $K_S^{\perp}$ of 0.03 ± 0.1 mJ/m^2 compatible with zero (hollow values in Fig. 1 not considered for the fit). This implies that it is not possible to obtain a stable perpendicular magnetization orientation for any thickness value based only on the interface effect.

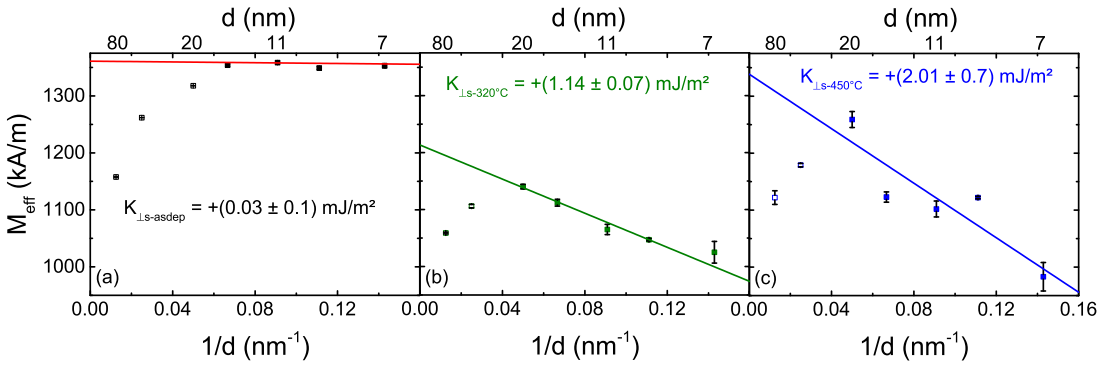

Fig. 1: Dependence of M_{eff} extracted from the Kittel fit on the inverse thickness $1/d$ for three sample series: (a) as-deposited, (b) annealed at 320°C, (c) annealed at 450°C. The lines are a fit to Eq. 1, the hollow data points were not considered.

Concerning the relative decrease of M_{eff} for large thicknesses, we attribute this to a inhomogeneous magnetization state which is sometimes observed in thick films [12].

Figs. 1b and 1c show the evolution of the situation when the annealing step is applied. The interface properties change with the thermal treatment and $K_S^{\perp}$ increases to a value of 1.14 ± 0.07 mJ/m^2 for the 320°C case and of 2.01 ± 0.7 mJ/m^2 for 450°C. The larger error bar in the later value is due to a larger scattering of values for M_{eff}. A recent study of the perpendicular anisotropy properties on CFA thin films has been published where a novel TiN buffer layer is employed [1]. In-plane and out-of-plane hysteresis loops are used to determine the value of $K_S^{\perp}$ instead of the FMR measurements used here. However, the largest obtained values for $K_S^{\perp}$ are in both in accordance with ours (0.86 ± 0.16 mJ/m^2). For comparison it has to be taken into account that due to the presence of two CFA/MgO interfaces, the values presented here are expected to be a factor two larger. Both values are then in good agreement.

First principle calculations of $K_S^{\perp}$ for stress-free CFA/MgO interfaces [13] have provided a value for $K_S^{\perp}$ of 1.31 mJ/m^2 for Co-terminated interfaces while FeAl-termination does induce in-plane orientation. This value is in agreement with our results considering that our values must be divided by two in order to take into account that two CFA/MgO interfaces are present in our system. In any case, our results are more compatible with a Co-termination at the MgO interfaces following this calculation. Other experimental results using XMCD attribute, contrarily to the previous calculation, a PMA contribution to the Fe atoms at the interface [14]. The exact atomic origin of the PMA is, thus, still under discussion.

From the extrapolation of the linear fits to $M_{\text{eff}} = 0$ it is possible to extract the thickness at which the interfacial perpendicular anisotropy is able to stabilize an out-of-plane configuration by overcoming the demagnetization field and allowing the magnetic easy axis to be out-of-plane. This thickness is 1.2 nm and 1.7 nm for 320°C and 450°C annealing temperature, respectively.

Figure 2 shows the dependence of the Gilbert damping parameter α on the thickness d for the as-deposited samples and the annealed series. For the three series we observe a minimum in the α value for $d = 40$ nm. The smallest value obtained for this series is $\alpha = 2.8 \pm 0.1 \cdot 10^{-3}$. The smallest reported value [11] is around $1 \cdot 10^{-3}$ but for films annealed at 600°C. The damping increases for lower annealing temperatures, up to values similar to the ones reported here at ∼450°C.

The reasons for the increased damping are different for the thicker and the thinner films. Concern-

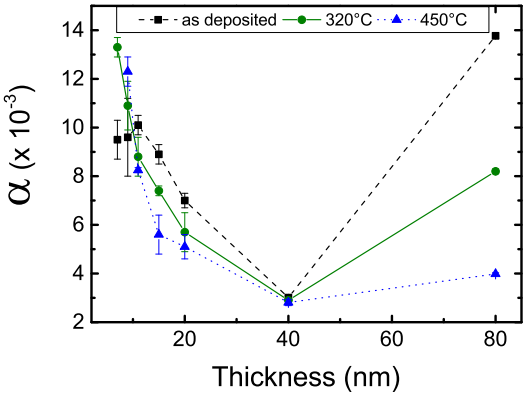

Fig. 2: Dependence of the Gilbert damping parameter α on the thickness d for three sample series: as-deposited, annealed at 320°C, and annealed at 450°C.

ing the large damping value for the 80 nm samples, it is a common behavior in soft magnetic thin films that the damping increases strongly with thickness starting at a certain value. An example of this can be seen for NiFe in the literature [12]. In this case the damping of the films strongly increases starting at $d = 90$ nm. The reason for that is a non-homogeneous magnetization state for thicker films which open new loss channels in addition to two-magnon scattering responsible for Gilbert-like behavior in in-plane magnetized films. Nevertheless, the value of α decreases with the annealing temperature pointing to a overall improvement of the uniformity of the film and of the crystalline order.

For the thinner samples down to 11 nm we also observe a reduction of α upon annealing, however this situation is inverted for $d < 11$ nm and provides a hint to one of the possible reasons for the increase of damping with decreasing thickness. When the thickness is reduced and the effect of the interface anisotropy is becoming larger the magnetization state is becoming more inhomogeneous due to the counterplay between the demagnetization field and the anisotropy field. However, this alone cannot explain the α increase since this is also observable in the as-deposited sample series where $K_S^{\perp} \approx 0$, although to a lower degree, and additional effects, e.g. due to roughness, seem to play also a role.

The in-plane anisotropies were studied by measuring the dependence of the resonant field H_{FMR} on the azimuthal angle ϕ. The results for the anisotropy constants K_b and K_u from the fits are plotted in Fig. 3. For the calculation of the anisotropy constant the magnetization values obtained from the fits in Fig. 1 are used. For K_b we observe a different thickness dependence for the as-deposited series and the series annealed at 320°C compared to the series annealed at 450°C. The value of K_b shows minor variation for the as-deposited samples with a small reduction for the thinner films. The evolution is similar for the 320°C case. On the contrary, the anisotropy constant increases continuously and strongly with decreasing thickness in the annealed series. However, the values converge for thick films and for 80 nm the difference vanishes. This points to a important role of the stress in the films, which normally relaxes with thickness, in the evolution of K_b. The absolute values are in concordance with literature data [8]. The values of K_u are one order of magnitude smaller and the absolute values and the thickness dependence are very similar for the three cases. A slight reduction with decreasing thickness is observed.

In summary, we measured the evolution of the interface induced perpendicular anisotropy for epitaxial CFA/MgO interfaces and we observed a strong increase with the annealing temperature up to a value of $K_S^{\perp} = 2.01 \pm 0.7$ mJ/m^2 for an annealing temperature of 450°C. A stabilization of a perpendicular magnetization orientation is then expected for films thinner than 1.7 nm. We studied the thickness dependent magnetic properties of CFA for as-deposited and annealed series. We ob-

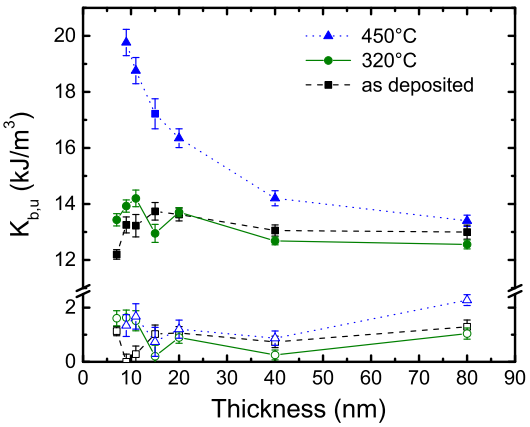

Fig. 3: Dependence of the in-plane biaxial anisotropy constant K_b (filled points) and the in-plane uniaxial anisotropy constant K_u (hollow points) on the thickness d for the as-deposited and the annealed series.

tained minimum values for α for a thickness of 40 nm for all series and a different evolution with annealing for thinner or thicker films. We correlate this with interface and bulk changes upon annealing, respectively. The study of the in-plane anisotropy constant shows a much larger thickness dependence on the annealed samples compared to the as-deposited ones.

Financial support by M-era.Net through the HEUMEM project is gratefully acknowledged.

References

[1] A. Niesen, J. Ludwig, M. Glas, R. Silber, J.-M. Schmalhorst, E. Arenholz, G. Reiss, *PMA of TiN buffered Co_2FeAl/MgO bilayers*, J. Appl. Phys. **121**, 223902 (2017).
[2] M. Cinchetti, J-P. Wüstenberg, M. Sánchez Albaneda, F. Steeb, A. Conca, M. Jourdan, M. Aeschlimann, *Towards a full Heusler alloy showing room temperature half-metallicity at the surface*, J. Phys. D: Appl. Phys. **40**, 1544 (2007).
[3] A. Conca, M. Jourdan, H. Adrian, *Epitaxial $Co_2Cr_{0.6}Fe_{0.4}Al$ thin films and magnetic tunnelling junctions*, J. Phys. D: Appl. Phys. **40** 1534 (2007).
[4] W. Wang, H. Sukegawa, R. Shan, S. Mitani, K. Inomata, *Giant TMR up to 330% at room temperature in sputter deposited $Co_2FeAl/MgO/CoFe$ magnetic tunnel junctions*, Appl. Phys. Lett. **95**, 182502 (2009).
[5] S. Mizukami, D. Watanabe, M. Oogane, Y. Ando, Y. Miura, M. Shirai, T. Miyazaki, *Low damping constant for Co_2FeAl Heusler alloy films and its correlation with density of states*, J. Appl. Phys. **105**, 07D306 (2009).
[6] Y. Cui, B. Khodadadi, S. Schäfer, T. Mewes, J. Lu, S.A. Wolf, *Interfacial perpendicular magnetic anisotropy and damping parameter in ultra thin Co_2FeAl films*, Appl. Phys. Lett. **102**, 162403 (2013).
[7] Y. Cui, J. Lu, S. Schäfer, B. Khodadadi, T. Mewes, M. Osofsky, S.A. Wolf, *Magnetic damping and spin polarization of highly ordered B2 Co_2FeAl thin films*, J. Appl. Phys. **116**, 073902 (2014).
[8] M. Belmeguenai, H. Tuzcuoglu, M.S. Gabor, T. Petrisor, Jr., C. Tiusan, D. Berling, F. Zighem, T. Chauveau, S.M. Chérif, P. Moch, *Co_2FeAl thin films grown on MgO substrates: Correlation between static, dynamic, and structural properties*, Phys. Rev. B **87**, 184431 (2013).
[9] C. Kittel, *On the theory of ferromagnetic resonance absorption*, Phys. Rev. **73**, 155 (1948).
[10] A. Conca, S. Keller, L. Mihalceanu, T. Kehagias, G.P. Dimitrakopulos, B. Hillebrands, E.Th. Papaioannou, *Study of fully epitaxial Fe/Pt bilayers for spin pumping by FMR spectroscopy*, Phys. Rev. B **93**, 134405 (2016).
[11] S. Mizukami, D. Watanabe, M. Oogane, Y. Ando, Y. Miura, M. Shirai, T. Miyazaki, *Low damping constant for Co_2FeAl Heusler alloy films and its correlation with density of states*, J. Appl. Phys. **105**, 07D306 (2009).
[12] Y. Chen, D. Hung, Y. Yao, S. Lee, H. Ji, C. Yu, *Ferromagnetic resonance study of thickness-dependent magnetization precession in $Ni_{80}Fe_{20}$ films*, J. Appl. Phys. **101**, 09C104 (2007).
[13] R. Vadapoo, A. Hallal, H. Yang, M. Chshiev, *First-principles investigation of magnetocrystalline anisotropy at the L21 full Heusler/MgO interfaces and tunnel junctions*, Phys. Rev. B **94**, 104418 (2016).
[14] Z. Wen, J.P. Hadorn, J. Okabayashi, H. Sukegawa, T. Ohkubo, K. Inomata, S. Mitani, K. Hono, *Interdiffusion in epitaxial ultrathin Co_2FeAl/MgO heterostructures with interface-induced perpendicular magnetic anisotropy*, Appl. Phys. Express **10**, 013003 (2017).

Chapter 5: Publications

Most publications can be downloaded from http://www.physik.uni-kl.de/hillebrands.

5.1 Submitted

1. *Optimized spintronic terahertz emitters based on epitaxial grown Fe/Pt layer structures*
   G. Torosyan, S. Keller, L. Scheuer, R. Beigang, and E. Th. Papaioannou
   submitted, arXiv:1707.08894v2

2. *Evolution of the interfacial perpendicular magnetic anisotropy constant of the Co_2FeAl/MgO interface upon annealing*
   A. Conca, A. Niesen, G. Reiss, and B. Hillebrands
   submitted, arXiv:1708.01126

3. *Reconfigurable nano-scale spin-wave directional coupler*
   Q. Wang, P. Pirro, R. Verba, A. Slavin, B. Hillebrands and A.V. Chumak
   submitted, arXiv:1704.02255

4. *Auto-oscillations in YIG/Pt microstructures driven by the spin Seebeck effect*
   V. Lauer, M. Schneider, T. Meyer, C. Dubs, P. Pirro, T. Brächer, F. Heussner, B. Lägel, V. I. Vasyuchka, A. A. Serga, B. Hillebrands and A.V. Chumak
   submitted, arXiv:1612.07305

5. *Low-damping transmission of spin waves through YIG/Pt-based layered structures for spin-orbit-torque applications*
   D. A. Bozhko, A. A. Serga, M. Agrawal, B. Hillebrands, and M. P. Kostylev
   submitted, arXiv:1603.09201

5.2 In press

1. *Temporal evolution of the spin-wave intensity and phase in a local parametric amplifier*
   T. Brächer, F. Heussner, T. Meyer, T. Fischer, M. Geilen, B. Heinz, B. Lägel, B. Hillebrands and P. Pirro
   accepted by J. Magn. Magn. Mat.

5.3 Published

1. *A switchable spin-wave signal splitter for magnonic networks*
   F. Heussner, A. A. Serga, T. Brächer, B. Hillebrands, and P. Pirro
   Appl. Phys. Lett. **111**, 122401 (2017)

2. *Parallel pumping for magnon spintronics: Amplification and manipulation of magnon spin currents on the micron-scale*
   T. Brächer, P. Pirro, and B. Hillebrands
   Physics Reports **699** 1 (2017)

3. *Experimental investigation of the temperature-dependent magnon density and its influence on studies of spin-transfer-torque-driven systems*
   T. Meyer, T. Brächer, F. Heussner, A. A. Serga, H. Naganuma, K. Mukaiyama, M. Oogane, Y. Ando, B. Hillebrands, and P. Pirro
   IEEE Magn. Lett. **699**, 318005 (2017)

4. *Topical Review: The 2017 magnetism roadmap*
   D. Sander, S. O. Valenzuela, D. Makarov, C. H. Marrows, E. E. Fullerton, P. Fischer, J. McCord, P. Vavassori, S. Mangin, P. Pirro, B. Hillebrands, A. D. Kent, T. Jungwirth, O. Gutfeisch, C. G. Kim, and A. Berger
   J. Phys. D :Appl.Phys. **50**, 363001 (2017)

5. *CoFeAlB alloy with low damping and low magnetization as a candidate for spin transfer torque switching*
   A. Conca, T. Nakano, T. Meyer, Y. Ando, and B. Hillebrands
   J. Appl. Phys. **122**, 073902 (2017)

6. *Relative weight of the inverse spin-Hall and spin-rectification effects for metallic polycrystalline Py/Pt, epitaxial Fe/Pt, and insulating YIG/Pt bilayers: Angular dependent spin pumping measurements*
   S. Keller, J. Greser, M. R. Schweizer, A. Conca, V. Lauer, C. Dubs, B. Hillebrands, and E. Th. Papaioannou
   Phys. Rev. B **96**, 024437 (2017)

7. *Spin-electromagnetic waves in planar multiferroic multilayers*
   A. A. Nikitin, A. B. Ustinov, V. V. Vitko, A. A. Nikitin, A. V. Kondrahov, P. Pirro, E. Lähderanta, B. A. Kalinikos, and B. Hillebrands
   J. Appl. Phys. **122**, 014102 (2017)

8. *Spin waves for interconnect applications*
   F. Ciubotaru, O. Zografos, G. Talmelli, C. Adelmann, I. P. Radu, T. Fischer, A. Chumak, P. Pirro, B. Hillebrands, and T. Devolder
   Interconnect Technology Conference (IITC), 2017 IEEE International

9. *Inversion of the domain wall propagation in synthetic ferrimagnets*
   A. Hamadeh, P. Pirro, J. P. Adam, Y. Lu, M. Hehn, S. Petit Watelot, and S. Mangin
   Appl. Phys. Lett. **111**, 022407 (2017)

10. *Magnonics: spin waves connecting charges, spins and photons*
    A. V. Chumak and H. Schultheiss
    J. Phys. D: Appl. Phys. **50**, 300201 (2017)

11. *Spin-pumping through a varying-thickness MgO interlayer in Fe/Pt system*
    L. Mihalceanu, S. Keller, J. Greser, D. Karfaridis, K. Symeonidis, G. Vourlias, T. Kehagias, A. Conca, B. Hillebrands, and E. Th. Papaioannou
    Appl. Phys. Lett. **110**, 252406 (2017)

12. *All-optical observation and reconstruction of spin wave dispersion*
    Y. Hashimoto, S. Daimon, R. Iguchi, Y. Oikawa, K. Shen, K. Sato, D. Bossini, Y. Tabuchi, T. Satoh, B. Hillebrands, G. Bauer, T. Johansen, A. Kirilyuk, T. Rasing, and E. Saitoh
    Nat. Commun. **8**, 15859 (2017)

13. *Bottleneck accumulation of hybrid magnetoelastic bosons*
D. A. Bozhko, P. Clausen, G. A. Melkov, V. S. Lvov, A. Pomyalov, V. I. Vasyuchka, A. V. Chumak, B. Hillebrands, and A. A. Serga
Phys. Rev. Lett. **118**, 237201 (2017)

14. *Magnonic crystals for data processing*
A. V. Chumak, A. A. Serga, and B. Hillebrands
J. Phys. D: Appl. Phys. **50**, 244001 (2017)

15. *Lack of correlation between the spin mixing conductance and the ISHE-generated voltages in CoFeB/Pt,Ta bilayers*
A. Conca, B. Heinz, M. R. Schweizer, S. Keller, E. Th. Papaioannou, and B. Hillebrands
Phys. Rev. B **95**, 174426 (2017)

16. *Damping of parametrically excited magnons in the presence of the longitudinal spin Seebeck effect*
T. Langner, A. Kirihara, A. A. Serga, B. Hillebrands, and V. I. Vasyuchka
Phys. Rev. B **95**, 134441 (2017)

17. *Voltage-controlled nano-scale reconfigurable magnonic crystal*
Q. Wang, A. V. Chumak, L. Jin, H. Zhang, B. Hillebrands, and Z. Zhong
Phys. Rev. B **95**, 134433 (2017)

18. *Experimental prototype of a spin-wave majority gate*
T. Fischer, M. Kewenig, D. A. Bozhko, A. A. Serga, I. I. Syvorotka, F. Ciubotaru, C. Adelmann, B. Hillebrands, and A. V. Chumak
Appl. Phys. Lett. **110**, 152401 (2017)

19. *Temporal evolution of auto-oscillations in a YIG/Pt microdisc driven by pulsed spin Hall effect-induced spin-transfer torque*
V. Lauer, M. Schneider, T. Meyer, Th. Brächer, P. Pirro, B. Heinz, F. Heussner, B. Laegel, M. C. Onbasli, C. A. Ross, B. Hillebrands, and A. V. Chumak
IEEE Magn. Lett. **8**, 3104304 (2017)

20. *Creation of unidirectional spin-wave emitters by utilizing interfacial Dzyaloshinskii-Moriya interaction*
T. Brächer, O. Boulle, G. Gaudin, and P. Pirro
Phys. Rev. B **95**, 064429 (2017)

21. *Magnetization switching diagram of a perpendicular synthetic ferrimagnet CoFeB/Ta/CoFeB bilayer*
O. Koplak, A. Talantsev, Y. Lu, A. Hamadeh, P. Pirro, T. Hauet, R. Morgunov, and S. Mangin
J. Magn. Magn. Mat. **433**, 91 (2017)

22. *Perpendicularly magnetized CoFeB multilayers with tunable interlayer exchange for synthetic ferrimagnets*
P. Pirro, A. Hamadeh, M. Lavanant-Jambert, T. Meyer, B. Tao, E. Rosario, Y. Lu, M. Hehn, S. Mangin, and S. Petit-Watelot
J. Magn. Magn. Mat. **432**, 260 (2017)

5.4 Ph.D. thesis

1. *Spinkalorischer Transport mit Magnonen in YIG und YIG/Pt-Bilagenschichten*
   Thomas Langner, TU Kaiserslautern, January 2017

2. *Spin transport in magnon and magnon-phonon gases and condensates*
   Dmytro Bozhko, TU Kaiserslautern, January 2017

3. *Spin orbit torque driven spin wave dynamics in microstructured Heusler magnon conduits*
   Thomas Meyer, TU Kaiserslautern, October 2017

5.5 Diploma thesis

1. *Charakterisierung von Rückwärts-Volumen-Spinwellenmoden in mikrostrukturierten Wellenleitern für die mechanische Detektion des Magnon-Drehimpulses*
   Moritz Geilen, TU Kaiserslautern, January 2017

2. *Herstellung und Untersuchung der Magnetisierungsdynamik in einzelnen Yttrium-Eisen-Granat Mikrostrukturen*
   Björn Heinz, TU Kaiserslautern, January 2017

5.6 Bachelor thesis

1. *Untersuchung der Spinwellenanregung in Permalloy-Strukturen mit verschiedenen Anregungsgeometrien*
   David Alexander Breitbach, TU Kaiserslautern, September 2017

Chapter 6: Conferences, Workshops, Schools, Seminars

(shown in chronological order)

6.1 Invited talks

6.1.1 International conferences and workshops

B. Hillebrands:
Compensation of spin-wave damping in magnetic metals and insulators
13th 4th JSPS Core-to-Core workshop on "New Concept Spintronic Devices", Sendai, Japan, November 2016

A. A. Serga:
Spin Transport using magnon gases
International School and Conference on Nanoscience and Quantum Transpor, Kyiv, Ukraine, November 2016

A. A. Serga:
Kinetic instability, Bose-Einstein condensation, and magnon supercurrents in YIG films
Spin Coherence, Condensation, and Superfluidity, Moorea, French Polynesia, Februar 2017

A. A. Serga:
Accumulation of hybrid magneto-elastic quasi-particles in a ferrimagnet
Spin Mechanics 4, Lake Louise, Canada, Februar 2017

A. A. Serga:
Bose-Einstein magnon condensation and bottleneck accumulation of magneto-elastic bosons in yttrium-iron-garnet films
5th International Conference on Oxide Materials for Electronic Engineering - Fabrication, Properties and Application, Lviv, Ukraine, Februar 2017

P. Pirro:
Magnonic spin transport: from fundaments to prototypes
Magnetization dynamics in nano objects, Nancy, France, May 2017

P. Pirro:
Designing magnonic transport
Optomagnonics, Erlangen, Germany, June 2017

E. Papaioannou:
Efficient THz spintronic emitters based on epitaxially grown Fe/Pt bilayers
New concepts on spintronic Devices, 5th Core-to-Core Workshop, York, England, June 2017

D. A. Bozhko:
Direct observation of dipolar-exchange magnon and phonon spectra in arbitrarily magnetized yttrium-iron-garnet films
New concepts on spintronic Devices, 5th Core-to-Core Workshop, York, England, June 2017

B. Hillebrands:
Physics and applications of focused spin-wave beams and caustics
SpinTech Conference, Fukuoka, Japan, June 2017

E. Papaioannou:
Magneto-plasmonic enhancement in 0-,1- and 2-D structures
META'17, 8th International Conference on Metamaterials, Photonic Crystals and Plasmonics, Incheon-Seoul, Korea, July 2017

V. Vasyuchka:
Spin transport using magneto-elastic bosons
SPICE Young Research Leaders Group Workshop: Insulator spintronics strong-coupling, coherence and entanglement, Mainz, Germany, July 2017

B. Hillebrands:
Magnonics in spin textured materials
Spin Dynamics in Nanostructures, Gordon Research Conference Les Diablerets, Switzerland, July 2017

A.V. Chumak:
Nano-scaled magnon transistor
3rd MagIC 2017 - Magnetism, Interactions and Complexity: multifunctional aspects of spin wave dynamics, Poznan, Poland, July 2017

B. Hillebrands:
Non-local detection of magnon supercurrents
Magnonics Conference, Oxford, UK, August 2017

P. Pirro:
Spin waves for data processing and logic
1st Paris-Saclay Workshop on Spintronics, Paris, France, September 2017

A.V. Chumak:
Spin-wave dynamics in yttrium iron garnet nano-structures
Workshop on "Spins, Waves and Interactions", Greifswald, Germany, September 2017

E. Papaioannou:
Magneto-plasmonic metamaterials
Euromat 2017, Thessaloniki, Greece, September 2017

M. Mohseni:
Design of band structure and spin-wave non-reciprocity in bilayer systems
One day workshop on magnetic nano objects, Nancy, France, October 2017

T. Brächer:
Short-waved magnon excitation and detection in ultra-thin Ta/CoFeB/MgO waveguides
One day workshop on magnetic nano objects, Nancy, France, October 2017

B. Hillebrands:
Advanced magnonics
Spin, charge and energy transport in novel materials, Hvar, Croatia, October 2017

6.1.2 Invited colloquia and seminar talks

P. Pirro:
Spin waves as a model system for wave physics
MPI for the physics of Light, Erlangen, Germany, November 2016

B. Hillebrands:
Advanced magnonics
Max-Born Institutskolloquium, Berlin, Germany, May 2017

A. A. Serga:
Spin transport by a supercurrent in a room-temperature magnon Bose-Einstein condensate
Center for Theoretical Physics at Physics Department of the New York City College of Technology of the City University of New York (CUNY), New York, USA, May 2017

A. V. Chumak:
Spin-wave logic devices
Laboratory of Nanoscale Magnetic Materials and Magnonics, EPFL, Lausanne, Switzerland, June 2017

B. Hillebrands:
Advanced magnonics
Abschlusskolloquium SFB 668, Hamburg, Germany, June 2017

A. A. Serga:
Kinetic instability, Bose-Einstein condensation, and magnon supercurrents in YIG films
Physics and Astronomy, CEMPS, University of Exeter, Exeter, United Kingdom, August 2017

B. Hillebrands:
Magnonen für den Computer von übermorgen?
Vortrag jDPG, TU Kaiserslautern, Germany, October 2017

D. A. Bozhko:
Magnonic supercurrents
Joint SFB689 and SFB1277 Seminar, Regensburg, Germany, October 2017

6.1.3 Lectures at schools

A.V. Chumak:
Spin-wave logic devices
Lecture for MAINZ School of Excellence, Mainz, Germany, November 2016

P. Pirro:
Spin waves and magnon spintronics
Magnetism: From Fundamentals to Spin based Nanotechnology, Bad Honnef, Germany, September 2017

A.V. Chumak:
Spin-wave logic devices
MAINZ Summer School "New directions in spintronics research: Spin phenomena and devices", Beijing, China, September 2017

6.2 Contributed talks and posters

6.2.1 Conferences and workshops

A. Conca, T. Nakano, T. Meyer, Y. Ando, and B. Hillebrands :
Comparative study of CoFeAlB and CoFeB FMR properties for spin torque devices
4th JSPS Core-to -Core Workshop on "New-Concept Spintronic Devices", Sendai, Japan, November 2016

A. Conca, S. Keller, B. Heinz, L. Mihalceanu, M. R. Schweizer, T. Kehagias, G. P. Dimitrakopulos, E. Papaioannou, and B. Hillebrands:
Spin mixing conductance in epitaxial and polycrystalline FM/Pt,Ta bilayers (FM= Fe, CoFeB)
MMM 2016, New Orleans, USA, November 2016

S. Keller, J. Greser, M. R. Schweizer, B. Hillebrands, and E. Th. Papaioannou:
The role of magnetic anisotropy on spin pumping revealed in epitaxial Fe/NM (Pt, Pd, Au) systems
MMM 2016, New Orleans, USA, November 2016

T. Langner, A. A. Serga, A. Kirihara, B. Hillebrands, and V. I. Vasyuchka:
Influence of a thermal gradient on parametrically excited magnons in YIG/Pt bilayers
633. Wilhelm und Else Heraeus-Seminar "Spin Orbit Dynamics", Bad Honnef, Germany, January 2017

L. Mihalceanu, D. A. Bozhko, T. Langner, V. I. Vasyuchka, A. A. Serga, and B. Hillebrands:
Relaxation parameter of parametrically excited magnons in the wide temperature range
633. Wilhelm und Else Heraeus-Seminar "Spin Orbit Dynamics", Bad Honnef, Germany, January 2017

T. Meyer, P. Pirro, T. Brächer, F. Heussner, A. A. Serga, H. Naganuma, K. Mukaiyama, M. Oogane, Y. Ando, and B. Hillebrands:
Revealing of decaying spin waves as the main source of heating in spin-transfer torque driven Cr|Heusler|Pt waveguides
633. Wilhelm und Else Heraeus-Seminar "Spin Orbit Dynamics", Bad Honnef, Germany, January 2017

T. Meyer, P. Pirro, T. Brächer, F. Heussner, A. A. Serga, H. Naganuma, K. Mukaiyama, M. Oogane, Y. Ando, and B. Hillebrands:
Revealing of decaying spin waves as the main source of heating in spin-transfer torque driven Cr|Heusler|Pt waveguides
Spin mechanics 4, Lake Louise, Canada, February 2017

M. Geilen, T. Meyer, P. Pirro, J. Losby, M. Freeman and B. Hillebrands:
Characterization of backward volume spin waves in microstructured waveguides for the mechanical detection of the magnon angular momentum
Spin mechanics 4, Lake Louise, Canada, February 2017

F. Heussner, T. Fischer, A. A. Serga, B. Hillebrands, and P. Pirro:
Frequency-division multiplexer for magnonic logic networks
Spin+X retreat, Bad Dürkheim, Germany, March 2017

M. Mohseni, Q. Wang, B. Hillebrands, P. Pirro:
Non-reciprocal spin-wave edge modes
Spin+X retreat, Bad Dürkheim, Germany, March 2017

T. Fischer, A. Friedel, D. Breitbach, B. Lägel, B. Hillebrands, G. von Freymann, and A. V. Chumak:
Nano-Structuring of nm-thick YIG films
Spin+X retreat, Bad Dürkheim, Germany, March 2017

M. Kewenig, T. Fischer, D. A. Bozhko, P. Pirro, B. Hillebrands, A. A. Serga, C. Dubs, I. I. Syvorotka, and A. V. Chumak:
Realization of a spin-wave majority gate
Spin+X retreat, Bad Dürkheim, Germany, March 2017

V. Lauer, M. Schneider, T. Meyer, C. Dubs, P. Pirro, T. Brächer, F. Heussner, B. Lagel, V. I. Vasyuchka, A. A. Serga, B. Hillebrands, A. V. Chumak:
Auto-oscillations in YIG/Pt nanostructures driven by the spin Seebeck effect
Intermag 2017, Dublin, Ireland, April 2017

J. Greser, S. Keller, M. Schweizer, H. Stopfel, V. Kapaklis and E. Th. Papaioannou:
Spin pumping near the magnetic phase transition in doped Pd(Fe) layers
Intermag 2017, Dublin, Ireland, April 2017

T. Fischer, F. Heussner, S. Jaiswal, G. Jakob, M. Kläui, B. Hillebrands, and P. Pirro:
Spin waves in CoFeB thin films dominated by Dzyaloshinskii-Moriya interaction
Intermag 2017, Dublin, Ireland, April 2017

Q. Wang, P. Pirro, R. Verba, A. Slavin, B. Hillebrands, A. V. Chumak:
Reconfigurable nano-scale spin-wave directional coupler
Intermag 2017, Dublin, Ireland, April 2017

D. A. Bozhko, A. J. E. Kreil, A. A. Serga, and B. Hillebrands:
Magnon density control of room-temperature supercurrents in Yttrium Iron Garnet films
Intermag 2017, Dublin, Ireland, April 2017

Q. Wang, P. Pirro, B. Hillebrands, and A. V. Chumak:
Nano-scaled magnon transistor based on three-magnon splitting
Intermag 2017, Dublin, Ireland, April 2017

T. Brächer, M. Fabre, T. Meyer, T. Fischer, S. Auffret, O. Boulle, U. Ebels, P. Pirro, and G. Gaudin:
Excitation and detection of short-waved spin waves in ultrathin Ta/CoFeB/MgO-layer system suitable for spin-orbit-torque magnonics
Intermag 2017, Dublin, Ireland, April 2017

A. Conca, T. Nakano, T. Meyer, Y. Ando, and B. Hillebrands:
Comparative study of CoFeAlB and CoFeB FMR properties for spin torque devices
Intermag 2017, Dublin, Ireland, April 2017

T. Noack, T. Langner, F. Heussner, V. Lauer, V. I. Vasyuchka, B. Hillebrands, A.A. Serga:
Thickness dependent temporal evolution of the spin Seebeck effect in platinum-covered YIG films
Spincaloritronics VIII, Regensburg, Germany, June 2017

T. Langner, A. A. Serga, A. Kirihara, B. Hillebrands and V. I. Vasyuchka:
Influence of a thermal gradient on parametrically excited magnons in YIG/Pt bilayers
Spincaloritronics VIII, Regensburg, Germany, June 2017

F. Heussner, T. Fischer, A. A. Serga, B. Hillebrands, and P. Pirro:
Frequency-division multiplexer for magnonic logic networks
York-Tohoku-Kaiserslautern Research Symposium on "New-Concept Spintronics Devices", 5th Core-to-Core Workshop, York, England, June 2017

V. Lauer, M. Schneider, T. Meyer, C. Dubs, P. Pirro, T. Brächer, F. Heussner, B. Lagel, V. I. Vasyuchka, A. A. Serga, B. Hillebrands, A. V. Chumak:
Auto-oscillations in YIG/Pt nanostructures driven by the spin Seebeck effect
York-Tohoku-Kaiserslautern Research Symposium on "New-Concept Spintronics Devices", 5th Core-to-Core Workshop, York, England, June 2017

T. Fischer, T. Koike, H. Inaba, A. Friedel, D. Breitbach, M. Kewenig, D. A. Bozhko, A. A. Serga, I. Y. Syvorotka, B. Hillebrands, M. Oogane, Y. Ando, and A. V. Chumak:
$Co_2Mn_{0.4}Fe_{0.6}Si$ for Spin-Wave Logic Applications
York-Tohoku-Kaiserslautern Research Symposium on "New-Concept Spintronics Devices", 5th Core-to-Core Workshop, York, England, June 2017

Q. Wang, R. Verba, M. Kewenlg, P. Pirro, B. Heinz, T. Meyer, C. Dubs, T. Brächer, and A. V. Chumak:
Spin-wave pinning conditions in nanoscale waveguide
MagIC Conference 2017, Pozan, Poland, July 2017

L. Mihalceanu, V. I. Vasyuchka, D. A. Bozhko, T. Langner, B. Hillebrands, A. A. Serga:
Temperature dependent realxation of dipolar-exchange magnons in yttrium-iron-garnet films
SPICE Workshop Topology Matters, Mainz, Germany, July 2017

F. Heussner, T. Fischer, A. A. Serga, B. Hillebrands, and P. Pirro:
Frequency-division multiplexer for magnonic logic networks
Magnonics 2017, Oxford, England, August 2017

M. Schneider, V. Lauer, T. Meyer, C. Dubs, P. Pirro, T. Brächer, F. Heussner, B. Lägel, V. I. Vasyuchka, A. A. Serga, B. Hillebrands, A. V. Chumak:

Auto-oscillations in YIG/Pt nanostructures driven by the spin Seebeck effect
Magnonics 2017, Oxford, England, August 2017

Q. Wang, T. Brächer, P. Pirro, and A. V. Chumak:

Nano-scaled magnon transistor based on three-magnon splitting
Magnonics 2017, Oxford, England, August 2017

M. Kewenig, T. Fischer, D. A. Bozhko, P. Pirro, B. Hillebrands, A. A. Serga, C. Dubs, I. I. Syvorotka, and A. V. Chumak:

Realization of a spin-wave majority gate
Magnonics 2017, Oxford, England, August 2017

A. A. Serga, D. A. Bozhko, G. A. Melkov, V. S. L'vov, A. Pomyalov, and B. Hillebrands:

Spin transport by magneto-elastic bosons in yttrium-iron-garnet films
Magnonics 2017, Oxford, England, August 2017

D. A. Bozhko, G. A. Melkov, V. S. Lvov, A. Pomyalov, V. I. Vasyuchka, A. V. Chumak, B. Hillebrands, and A. A. Serga:

Bottleneck accumulation of hybrid magneto-elastic bosons
Magnonics 2017, Oxford, England, August 2017

H. Yu. Musiienko-Shmarova, D. A. Bozhko, V. Tyberkevych, A. N. Slavin, P. Pirro, I. I. Syvorotka, B. Hillebrands, and A. A. Serga:

Dipolar-exchange magnon and phonon spectra in arbitrarily magnetized yttrium-iron-garnet films
Magnonics 2017, Oxford, England, August 2017

A. A. Serga, D. A. Bozhko, H. Yu. Musiienko-Shmarova, V. S. Tiberkevich, A. N. Slavin, I. I. Syvorotka, B. Hillebrands:

Direct observation of dipolar-exchange magnon and phonon spectra in obliquely magnetized YIG films
MAGNET 2017 - 5th Italian Conference on Magnetism, Assisi, Italy, September 2017

A. A. Serga, B. Hillebrands:

Non-local measurements of a supercurrent spin transport in a room temperature Bose-Einstein magnon condensate
TR49 Annual Retreat, Walldorf, Germany, September 2017

A. J. E. Kreil, D. A. Bozhko, B. Hillebrands, A. A. Serga:

Supercurrents in thermal gradients
TR49 Annual Retreat, Walldorf, Germany, September 2017

L. Mihalceanu, V. I. Vasyuchka, D. A. Bozhko, T. Langner, B. Hillebrands, A. A. Serga:

Temperature dependent realxation of dipolar-exchange magnons in yttriu,-iron-garnet films
TR49 Annual Retreat, Walldorf, Germany, September 2017

H. Yu. Musiienko-Shmarova, D. A. Bozhko, A. J. E. Kreil, V. S. Lvov, A. Pomyalov, B. Hillebrands, and A. A. Serga:

From kinetic instability to Bose-Einstein condensation and magnon supercurrents
TR49 Annual Retreat, Walldorf, Germany, September 2017

T. Brächer, M. Fabre, T. Meyer, T. Fischer, S. Auffret, O. Boulle, U. Ebels, P. Pirro, and G. Gaudin:

Excitation and detection of short-waved spin waves in ultrathin Ta/CoFeB/MgO-layer system suitable for spin-orbit-torque magnonics
Colloque Louis Néel, Paris, France, September 2017

S. Keller, L. Scheuer, G. Torosyan, T. Kehagias, B. Hillebrands, R. Beigang, E. Th. Papaioannou:

MBE epitaxial grown Fe/Pt bilayers for the optimization of inverse spin Hall effect and of THz emission
MBE Austrian 2017, Wien, Austria, September 2017

T. Fischer, F. Heussner, S. Jaiswal, G. Jakob, M. Klaui, B. Hillebrands, and P. Pirro:

Spin waves in CoFeB thin films dominated by Dzyaloshinskii-Moriya interaction
MAINZ Student Retreat, Amsterdam, Netherlands, October 2017

6.2.2 Contributions to the DPG Frühjahrstagung

17 contributions: DPG Frühjahrstagung, Dresden, Germany, March 2017

6.2.3 Schools

A. J. E. Kreil, D. A. Bozhko, B. Hillebrands, A. A. Serga:

Supercurrents in thermal gradients
SFB/TR 49 International School on Real and Synthetic Magnetism, Tutzing, Germany, March 2017

H. Yu. Musiienko-Shmarova, D. A. Bozhko, V. Tyberkevych, A. N. Slavin, P. Pirro, I. I. Syvorotka, B. Hillebrands, and A. A. Serga:

Direct observation of dipolar-exchange magnon and phonon thermal spectra in arbitrarily magnetized yttrium-iron-garnet films
SFB/TR 49 International School on Real and Synthetic Magnetism, Tutzing, Germany, March 2017

P. Frey, D. A. Bozhko, V. I. Vasyuchka, A. A. Serga, and B. Hillebrands:

Progress in wavevector-resolved Brillouin light scattering spectroscopy of magnon gases and condensates
SFB/TR 49 International School on Real and Synthetic Magnetism, Tutzing, Germany, March 2017

T. Noack, D. A. Bozhko, V. I. Vasyuchka, B. Hillebrands, and A. A. Serga:

Electrical detection of magnon Bose-Einstein-condensates
SFB/TR 49 International School on Real and Synthetic Magnetism, Tutzing, Germany, March 2017

P. Frey, D. A. Bozhko, V. I. Vasyuchka, A. A. Serga, and B. Hillebrands:
Progress in wavevector-resolved Brillouin light scattering spectroscopy of magnon gases and condensates
IEEE Magnetics Society Summer School 2017, Santander, Spain, June 2017

T. Noack, T. Langner, V. Lauer, F. Heussner, A. A. Serga, B. Hillebrands, and V. I. Vasyuchka :
Spectral properties of the longitudinal spin-Seebeck effect
IEEE Magnetics Society Summer School 2017, Santander, Spain, June 2017

T. Fischer, F. Heussner, S. Jaiswal, G. Jakob, M. Kläui, B. Hillebrands, and P. Pirro:
Spin waves in CoFeB thin films dominated by Dzyaloshinskii-Moriya interaction
MAINZ Summer School "New Directions in Spintronics Research", Beijing, China, September 2017

6.3 Annual group retreat

In 2017 our group organized a three-day retreat at the Kurhaus am Trifels, Annweiler. We have had two days of intense scientific discussion and 22 presentations by our group members and guests. Prof. Dr. Paul Lukowicz from DFKI Kaiserslautern gave a fascinating evening talk on Artificial Intelligence. On the first day, the group members participated in a soft skill seminar on Scientific writing held by Dr. Natalie Struve.

6.4 Other meetings and trade fairs

A. A. Serga:
Transport and electric control of Bose-Einstein condensation of magnons
InSpin final review meeting, Brussels, Belgium, April 2017

M. Mohseni, B. Hillebrands, P. Pirro:
Results on YIG/Py and YIG strip edge
MAGMATCH meeting, Strasbourg, France, May 2017

Appendix: Impressions from 2017

Christmas celebration, 20.12.2016

Ph.D. defense Dr. Dmytro Bozhko, 27.01.2017

Ph.D. defense Dr. Thomas Langner, 03.03.2017

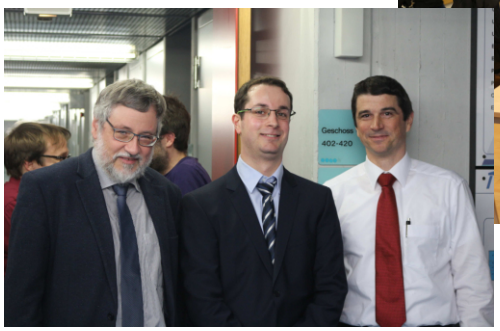

DPG Frühjahrstagung in Dresden, 19.-24.03.2017

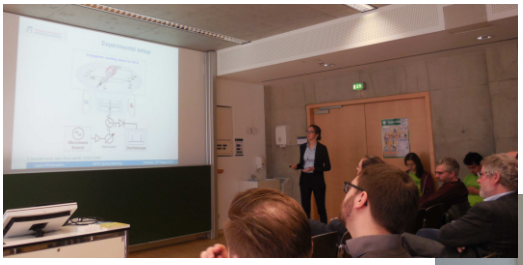

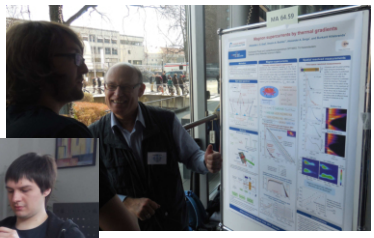

Group excursion, 06.07.2017

Juniorprofessur celebration Jun.- Prof. Dr. Andrii Chumak, 14.07.2017

Schülerinnentag, 28.09.2017

Group retreat, 09.-11.10.2017

Ph.D. defense Dr. Thomas Meyer, 11.10.2017

60. Birthday celebration Sibylle Müller, 16.10.2017

60. Birthday celebration Prof. Dr. Burkard Hillebrands, 27.10.2017

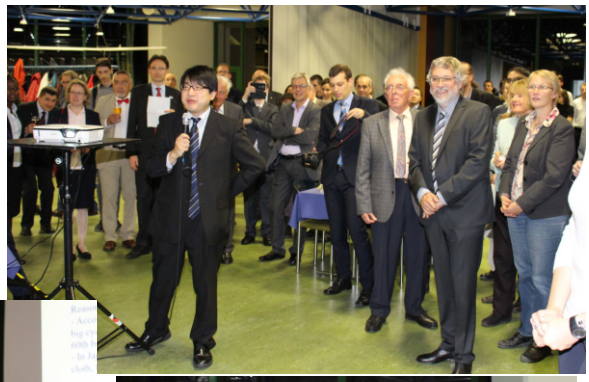

Prof. Dr. Burkard Hillebrands
Fachbereich Physik
Landesforschungszentrum OPTIMAS
Technische Universität Kaiserslautern, Germany
P.O. Box 3049
67653 Kaiserslautern
Phone: +49 631 205-4228
Fax: +49 631 205-4095
hilleb@physik.uni-kl.de
www.physik.uni-kl.de/hillebrands/

TECHNISCHE UNIVERSITÄT
KAISERSLAUTERN